University of Rhode Island
DigitalCommons@URI

Open Access Dissertations

1996

The Rock Magnetic Properties, Grain Size and Mineral Composition of Winborne Dust and Sediment in the North Pacific Ocean

Eve Maureen Arnold
University of Rhode Island

Follow this and additional works at: https://digitalcommons.uri.edu/oa_diss

Terms of Use
All rights reserved under copyright.

Recommended Citation
Arnold, Eve Maureen, "The Rock Magnetic Properties, Grain Size and Mineral Composition of Winborne Dust and Sediment in the North Pacific Ocean" (1996). *Open Access Dissertations.* Paper 815.
https://digitalcommons.uri.edu/oa_diss/815

This Dissertation is brought to you by the University of Rhode Island. It has been accepted for inclusion in Open Access Dissertations by an authorized administrator of DigitalCommons@URI. For more information, please contact digitalcommons-group@uri.edu. For permission to reuse copyrighted content, contact the author directly.

THE ROCK-MAGNETIC PROPERTIES, GRAIN SIZE AND MINERAL COMPOSITION OF WINDBORNE DUST AND SEDIMENT IN THE NORTH PACIFIC OCEAN

BY

EVE MAUREEN ARNOLD

A DISSERTATION IN PARTIAL FULFILLMENT OF THE REQUIREMENTS

FOR THE DEGREE OF

DOCTOR OF PHILOSOPHY

IN

OCEANOGRAPHY

UNIVERSITY OF RHODE ISLAND

1996

DOCTOR OF PHILOSOPHY DISSERTATION

OF

EVE MAUREEN ARNOLD

APPROVED:

Dissertation Committee

Major Professor

DEAN OF THE GRADUATE SCHOOL

UNIVERSITY OF RHODE ISLAND

1996

Abstract

Dust, uplifted by wind from the continents, and transported through the atmosphere, leaves a geologic record across the earth; in loess deposits on the continents, red clays on the ocean floors and on the polar ice caps. If we can interpret the paleoclimatic and paleometeorology information preserved in these deposits, we can learn how continental climate and atmospheric circulation have varied over the course of time. Continental climate information is preserved in the composition of the dust. The mineral phases that comprise the surface of the continents are dictated by the geology of the parent rocks, but more importantly, the soils formed by the weathering of these continental rocks are extremely sensitive to the climate variables precipitation, temperature and seasonality. Records of atmospheric circulation processes are preserved in the spatial distribution patterns, flux and particle size of the deposited eolian material. In order to exploit the global paleoclimate and paleometeorology records, the relationships between the continental dust source areas, the transport process and the resulting deposits must be quantified.

In this work, sediments and aerosols from the North Pacific Ocean are studied. The North Pacific contains the most spatially and temporally contiguous record of eolian material, transported from the deserts of northern Asia by the zonal westerly winds for millions of years. Aerosols, collected from research vessels in the North Pacific, surface sediments from across the entire ocean basin, and a sediment core from the central North Pacific were analyzed for rock-magnetic properties, grain size and mineralogy. This study provides a data set of geological measurements that are directly related to atmospheric processes, recent sedimentation, and eolian sedimentation over the last 8 million years.

The aerosol samples record both the source region and transport history of the continental dust. Atmospheric dust concentrations are highest for those samples with the shortest transport time from Asia to the open ocean. Asian dust samples are characterized by high dust concentrations, fine grain size, and high concentrations of 2-20μm quartz and <2μm kaolinite. High latitude, Aleutian/Alaskan dust is characterized by low dust concentrations, coarse grain size and is relatively enriched in plagioclase and magnetic material. The aerosol is compositionally fractionated during the transport process, becoming relatively enriched in clay minerals at the expense of primary minerals.

The surface sediments from the North Pacific preserve the relationships between transport process and physical characteristics observed for the aerosols. The rock magnetic properties, grain size and mineralogy of the aerosols are the same as the eolian surface sediments. The sediments display a steady decrease in the grain size across the entire basin, and the composition is fractionated towards a higher coercivity, and a plagioclase-depleted and kaolinite- and chlorite- enriched composition with increasing distance from the source area.

The eolian dust preserved in the down-core sediments records the onset of major eolian sedimentation to this region 3.8 million years ago. When the flux increased, the rock magnetic grain size increased, the composition of the minerals shifted from a kaolinite-enriched mineralogy to a chlorite enriched mineralogy, suggesting aridification of the source region and acceleration of atmospheric transport.

Acknowledgments

You know you may have been in school too long when your advisor is promoted to full professor, assistant dean, interim dean, and dean during your tenure as a graduate student. And still manages to have time to take her graduate student to the Newport Jazz Festival. Margaret Leinen is a remarkable person and an incredible role model, scientist and friend. What a good idea it was to come here and work with her.

My committee members John King, John Merrill and Tom Rockett provided guidance, good ideas, humor and support throughout the entire dissertation process.

The captain, crew and technicians of the SEDCO/BP471 a.k.a. the JOIDES Resolution, provided a lovely sediment core and a great cruise. My fellow shipboard scientists were a pleasure to work with. The Ocean Drilling Program and the Joint Oceanographic Institutes provided a fellowship and post cruise funding to support the study of the sediments recovered at ODP Site 885/886.

The atmospheric chemistry group at GSO devoted an incredible effort toward getting this geologist out of the mud and into the light. Maggie Peacock worked with me to develop the technique for the analysis of the mineralogy of "real" atmospheric samples. Rich Arimoto got sucked into the interdisciplinary vortex of the aerosol paper and gave unstintingly of his time, samples and data. Barbara Ray, Neil Tindale, Bob Duce, Hal Maring, Suilou Huang, Ruth Platner, and Ursula Tomza also made contributions to the data and lab work required for this study.

Frank Kyte provided many surface sediment samples. The National Science Foundation supported the aerosol and surface sediment research through a grant to

M. Leinen and J. Merrill (ATM 91- 02385). The GSO Alumni Association also provided support for some experimental work on aerosol processing.

Friends at GSO who watched and helped this whole saga unfold, Ann Isley, Alex Isern, Kathy Dadey, Kay Ho, John Kiddon, Norm and Amy Farris, Frank Hall and Terri King, kept the learning process interesting, fun or possible (depending on the day). Chris Knowlton, the last remaining Margaret student, who has struggled with me these last days to keep the lab equipment running long enough to finish this work (and with undaunted cheerfulness), has my undying gratitude.

Support on the non-GSO side of life came from Hilton and Adrienne Potter who provided a great place to live, and Amanda Wright, Mike Brennan and the Fourth of July crowd, who provided lot of fun, love and support.

Mom and Dad, thanks for everything. We did it.

Preface

This dissertation is presented in manuscript format, and consists of three chapters.

Chapter 1, entitled "Paleoenvironmental variation based on the mineralogy and rock-magnetic properties of sediment from Sites 885 and 886" presents research conducted for the Ocean Drilling Program for the Leg 145 North Pacific transect. The manuscript is co-authored by Margaret Leinen and John King, and is in press in the ODP scientific results volume 145. The manuscript presents the paleoenvironmental variation inferred from mineralogy and rock magnetism for a core recovered from the central basin of the North Pacific Ocean.

Chapter 2, entitled "Rock-magnetic properties, mineralogy and grain size of mineral aerosol collected over the North Pacific Ocean: relation to meteorology and implications for the interpretation of eolian sediments" presents research conducted on aerosols collected over the North Pacific Ocean. An abbreviated form of the manuscript will be submitted to the Journal of Geophysical Research, and it is prepared in that format. Co-authors for this manuscript are Margaret Peacock, John Merrill, Margaret Leinen and John King. The manuscript investigates the relationship between aerosol geological measurements, standard atmospheric analyses and meteorology.

Chapter 3, entitled "Rock-magnetic properties, mineralogy and grain size of North Pacific surface sediments: relation to present day eolian transport processes and implications for the interpretation of ancient sediment" presents research on a suite of surface sediment sample from the North Pacific. The manuscript will be submitted to the Journal of Geophysical Research, and it is prepared in that format.

Co-authors for this manuscript are Margaret Leinen, John Merrill, and John King. The manuscript investigates the relationship between the compositional, particle size and rock-magnetic variation of sediments with eolian transport processes. The sediments properties are compared with aerosol measurements, linking the recent sediment record to the present-day meteorology.

These three manuscripts are linked in that they transfer what we presently know about the atmospheric transport of continental dust to recent sedimentary processes and the ancient record of eolian sediment.

Table of Contents

Abstract	ii
Acknowlegments	iv
Preface	vi
Table of Contents	viii
List of Tables	xi
List of Figures	xiii

Chapter 1: Paleoenvironmental variation based on the mineralogy and rock-magnetic properties of sediment from Sites 885 and 886.

Abstract	1
Introduction	1
Methods	3
Results	7
Discussion	16
Summary	22
Acknowledgments	22
References	23

Chapter 2: Rock-magnetic properties, mineralogy and grain size of mineral aerosol collected over the North Pacific Ocean: relation to meteorology and implications for the interpretation of eolian sediments

Abstract	65
Introduction	66
Aerosol transport	66

Composition of aerosols 68
Grain size 71
Rock magnetics 72
Methods 74
Sampling 74
Meshes 75
Pumped samples 76
Sample processing 78
Meshes 78
Pumped samples 78
Analytical techniques 79
Rock magnetics 79
Grain size 80
Mineralogy 81
Air mass trajectories 81
Results 82
Meshes 82
Mineralogy 84
Meshes 84
Pumped samples 86
Air mass trajectories 90
Discussion 93
Comparison with other aerosol studies 93
Meshes vs. pumped samples 94
Aerosols vs. air mass trajectories 95
Implications for the interpretation of eolian sediments 100

Conclusions 101

Acknowledgments 102

References 103

Chapter 3: Rock-magnetic properties, mineralogy and grain size of North Pacific surface sediments: relation to meteorology and implications for the interpretation of eolian sediments

Abstract 186

Introduction 186

Sediment transport 187

Composition 190

Grain size 190

Rock magnetics 191

Methods 192

Rock magnetics 193

Grain size 194

Mineralogy 195

Results 195

Rock magnetics 195

Grain size 198

Mineralogy 199

Discussion 200

Conclusions 203

Acknowledgments 205

References 206

Bibliography 293

List of Tables

Chapter 1

Table 1. Precision, expressed as percent relative error of mineral peak areas. 26

Table 2. Stratigraphic parameters and mass accumulation rates for Holes 885A and 886B. 27

Table 3. Rock-magnetic measurements for Holes 885A and 886B. 31

Table 4. Normalized mineral peak areas for the <2 μm fraction of Holes 885A and 886B. 37

Table 5. Normalized mineral peak areas for the 2-20 μm fraction of Holes 885A and 886B. 41

Chapter 2

Table 1. Sampling locations for aerosol mesh samples. 108

Table 2. Sampling locations for pumped aerosol samples. 109

Table 3. Sample mass for aerosol mesh samples. 110

Table 4. Rock magnetism measurements for aerosol mesh samples. 111

Table 5. Mineralogy for aerosol mesh samples. 113

Table 6. Mineralogy for pumped aerosol samples. 116

Table 7. Replicate comparisons (p-values) for pumped aerosol samples. 117

Table 8. Elemental analyses and mass median diameter for pumped aerosol samples . 118

Table 9. Trajectory synthesis for the Moana Wave aerosol samples. 119

Table 10. Trajectory synthesis for the ADIOS aerosol samples. 125

Table 11. Regression coefficients between transport time and mineralogy. 129

Chapter 3

Table 1. Sample Locations. 210

Table 2. Rock magnetism measurements. 214

Table 3. Particle size measurements. 221

Table 4. Mineralogy measurements. 225

List of Figures

Chapter 1

Figure 1. Rock-magnetic parameters vs. composite depth for Holes 885A and 886B. 46

Figure 2. Mineral peak area for the <2 μm terrigenous size fraction vs. composite depth for Holes 885A and 886B. 48

Figure 3. Mineral peak area for the 2-20 μm terrigenous size fraction vs. composite depth for Holes 885A and 886B. 50

Figure 4. Peak area ratios for the <2 μm terrigenous size fraction vs. composite depth for Holes 885A and 886B. 52

Figure 5. Peak area ratios for the 2-20 μm terrigenous size fraction vs. composite depth for Holes 885A and 886B. 54

Figure 6. Less than 2 μm quartz peak area and low frequency susceptibility vs. composite depth for Hole 885A. 56

Figure 7. The S-ratio and 2-20μm illite/quartz ratio vs. composite depth for Hole 885A. 58

Figure 8. Mass accumulation rates for different sedimentary components vs. age for Holes 885A and 886B. 60

Figure 9. Accumulation rate of magnetic susceptibility and HIRM vs. age for Holes 885A and 886B. 62

Figure 10. Accumulation rates for the <2 μm minerals vs. age for Holes 885A and 886B. 64

Chapter 2

Figure 1. Location of aerosol samples. 131

Figure 2. Dust concentration for mesh samples. 133

Figure 3. Grain size for mesh samples. 135

Figure 4. Rock magnetism concentration properties for mesh samples. 137
Figure 5. Rock magnetism grain size properties for mesh samples. 139
Figure 6. Rock magnetism composition properties for mesh samples. 141
Figure 7. <2μm mineral composition for mesh samples. 143
Figure 8. 2-20μm mineral composition for mesh samples. 145
Figure 9. Bulk mineral composition for mesh samples. 147
Figure 10. Bulk mineral composition for pumped samples. 149
Figure 11. Mineral composition for cascade impactor stages. 151
Figure 12. Ash, aluminum and sodium concentration for pumped samples. 153
Figure 13. Ash, aluminum and sodium concentration for cascade impactor stages. 155
Figure 14. Ash residue vs. aluminum for all samples, high vols. and cascade impactors. 157
Figure 15. Ash residue vs. sodium for all samples, high vols. and cascade impactors. 159
Figure 16. Aerosol transport time from various continental areas for Moana Wave samples. 161
Figure 17. Aerosol transport time from various continental areas for ADIOS samples. 163
Figure 18. Residual ash from pumped samples and dust concentration from mesh samples. 165
Figure 19. <2μm mesh mineralogy and bulk pumped sample mineralogy. 167
Figure 20. 2-20μm mesh mineralogy and bulk pumped sample mineralogy. 169
Figure 21. Mass median diameter for cascade impactor samples calculated from aluminum mass distribution and Elzone geometric mean diameter for mesh samples. 171

Figure 22. Mass median diameter for cascade impactor samples calculated from iron mass distribution and Elzone geometric mean diameter for mesh samples. 173

Figure 23. Mesh dust concentration as a function of transport time from various continental regions for both cruises. 175

Figure 24. Mesh grain size as a function of transport time from various continental regions for both cruises. 177

Figure 25. Dust concentration vs. geometric mean grain size for all mesh samples. 179

Figure 26. Mesh rock magnetism as a function of transport time from various continental regions for both cruises. 181

Figure 27. Mesh <2μm mineralogy as a function of transport time from various continental regions for both cruises. 183

Figure 28. Mesh 2-20μm mineralogy as a function of transport time from various continental regions for both cruises. 185

Chapter 3

Figure 1. Spatial distribution of low frequency susceptibility. 232

Figure 2. Spatial distribution of SIRM. 234

Figure 3. Spatial distribution of HIRM. 236

Figure 4. Spatial distribution of X_{arm}. 238

Figure 5. Spatial distribution of Xarm/X. 240

Figure 6. Spatial distribution of S-ratio. 242

Figure 7. Spatial distribution of median grain size. 244

Figure 8. Spatial distribution of >63μm size fraction weight percent. 246

Figure 9. Spatial distribution of 20-63μm size fraction weight percent. 248

Figure 10. Spatial distribution of 2-20μm size fraction weight percent. 250

Figure 11. Spatial distribution of <2μm size fraction weight percent. 252
Figure 12. Spatial distribution of <2μm smectite concentration. 254
Figure 13. Spatial distribution of <2μm illite concentration. 256
Figure 14. Spatial distribution of <2μm kaolinite concentration. 258
Figure 15. Spatial distribution of <2μm chlorite concentration. 260
Figure 16. Spatial distribution of <2μm quartz concentration. 262
Figure 17. Spatial distribution of <2μm plagioclase concentration. 264
Figure 18. Spatial distribution of 2-20μm smectite concentration. 266
Figure 19. Spatial distribution of 2-20μm illite concentration. 268
Figure 20. Spatial distribution of 2-20μm kaolinite concentration. 270
Figure 21. Spatial distribution of 2-20μm chlorite concentration. 272
Figure 22. Spatial distribution of 2-20μm quartz concentration. 274
Figure 23. Spatial distribution of 2-20μm plagioclase concentration. 276
Figure 24. Rock magnetism concentration properties vs. longitude. 278
Figure 25. S-ratio vs. longitude. 280
Figure 26. Grain size parameters vs. longitude. 282
Figure 27 Sediment weight percent by size class vs. longitude. 284
Figure 28. <2μm smectite, illite and kaolinite vs. longitude. 286
Figure 29. <2μm chlorite, quartz and plagioclase vs. longitude. 288
Figure 30. 2-20μm smectite, illite and kaolinite vs. longitude. 290
Figure 31. 2-20μm chlorite, quartz and plagioclase vs. longitude. 292

Chapter 1:

Paleoenvironmental variation based on the mineralogy and rock-magnetic properties of sediment from sites 885 and 886

Abstract

Variation in the mineralogy and rock magnetic properties of Site 885 and 886 sediments can be explained by changing environmental conditions in the sediment source areas and sediment column. Climatic variations produce changes in the mineralogy and magnetics at these sites consistent with aridification of the Asian source area and cooling forced by tectonic activity. Asian aridification is noted by gradual reduction of a kaolinite-rich mineral assemblage from the late Miocene to an abrupt mineralogy change at 3.8 Ma to a chlorite- and illite-rich mineral assemblage. At the same time, the eolian mass accumulation rate and ferrimagnetic grain size increases. This event precedes the onset of Asian loess deposition by over 1 m.y., but it is consistent with a coupled environmental mechanism that explains the rapid onset of loess sedimentation at 2.5 Ma. Both the mineralogy and rock magnetics are overprinted with a diagenetic signal that suggests the sediments proximal to Sites 885 and 886 may have been suboxic to anoxic in the early Pliocene.

Introduction

The pelagic sediments preserved near Ocean Drilling Program (ODP) Holes 885A and 886B in the North Pacific Ocean are largely eolian in origin (Griffin et al., 1968; Leinen, 1989; Kyte et al., 1993); thus, variations in the properties of these sediments are related to variations in atmospheric transport patterns. The present upwind source region for these eolian sediments is Asia,

and the sediments record both past climatic variation and tectonic activity from this continent. In addition, the terrigenous material may have been subjected to sediment reworking and diagenetic alteration. By examining a variety of parameters, we can attempt to deconvolve this climate-tectonic-transport-preservation signal into its individual components and learn something about the variation of each through time.

In this paper, we examine the downcore variation in mineralogy and rock-magnetic measurements to infer the paleoenvironmental conditions responsible for sedimentation proximal to Sites 885 and 886. The composition and concentration of terrigenous material preserved in deep-sea sediment are related to weathering, transport, and depositional processes as well as postdepositional alteration of continental material. Mineralogical composition is related to parent-rock composition as well as regional climate. Paleoclimatologists and atmospheric scientists have established that the mineralogy of present-day aerosols is related to the source area (M. Leinen et al., unpubl. data; J. Merrill et al., unpubl. data) and that the mineralogy of aerosols collected over the North Pacific is the same as that of surface sediments from eolian deposits (Blank et al., 1985). Furthermore, downcore variation in mineralogy has demonstrated a consistent relationship with other paleoclimate proxies and has allowed paleoclimatologists to interpret variation in past climates in the Asia-North Pacific region (Leinen, 1985, 1989; Schramm, 1989).

In an analogous manner, rock-magnetic studies have also been used to trace atmospheric samples to their source area (Oldfield et al., 1985) and to infer changes in atmospheric input to deep-sea sediments through time (Robinson, 1986; Doh et al., 1988). In addition to compositional information, rock-magnetic properties are also useful proxies for the concentration and grain size of

terrigenous deep-sea sediments. Finally, the rock-magnetic properties are very sensitive to reduction diagenesis, so that we can control for postdepositional alteration of the sediment.

The rock-magnetic analyses are nondestructive, so we were able to analyze the same samples for mineralogy. Because the mineralogy of atmospheric aerosols has been identified with broad regional source areas, we can use this information to interpret the mineralogy signal in deep-sea sediments if we can confirm that the original mineralogy has not been modified by transport, deposition, or postdepositional modification. Bulk mineralogy can be altered by transport and deposition because mineralogy varies with grain size. As material travels through the atmosphere and falls through the water column, large particles fall out more quickly than the fine fraction. In addition, winnowing of deep-sea sediments can result in size fractionation. The coarse fraction of terrigenous material is relatively concentrated in primary minerals such as quartz and plagioclase, whereas the clay minerals dominate the fine fraction. We control for this by examining the mineralogy in separate size classes in the deep-sea sediments. Diagenetic alteration may be discerned by comparing the mineralogy record with the rock-magnetic properties; divergence of these two signals may indicate either a postdepositional modification of the sediment or a change in source.

Methods

Samples were collected at 150 cm intervals from Holes 885A and 886B with an aluminum sampling tool designed to collect undisturbed sediment; they were then extruded into 5-cm^3 plastic cubes for rock-magnetic analyses. In addition, ODP paleomagnetic samples (7 cm^3), collected at 150-cm intervals,

were also used. Sample spacing for the rock-magnetic study is approximately 75 cm, and 150 cm for the mineralogical analyses.

Susceptibility (X_{lf}, X_{hf}) was measured on a Bartington Instruments susceptibility meter at 0.47 and 4.7 kHz. The reported value (in $10^{-6}m^3/g$) is the average of three replicates. The samples were demagnetized in a 100-mT alternating field. Anhysteretic remanent magnetization (ARM) was induced in a 0.1-mT steady field superimposed on a 100-mT alternating field. The ARM was measured on a cryogenic magnetometer, and the reported value (in $10^{-6}Am^2/g$) is the average of duplicate measurements. The X_{arm} was calculated by dividing ARM by the steady field (reported in $10^{-6}m^3/g$). The final set of magnetic measurements were saturated isothermal remanent magnetization (SIRM) and isothermal remanent magnetization ($IRM_{-0.3T}$). Samples were saturated in a 1.2 T field and measured on a cryogenic magnetometer. Samples were then placed in reverse fields of 0.3 T and the magnetization remeasured. The values reported (in $10^{-6}Am^2/g$) are averages of duplicate measurements. The frequency ratio (X_{hf}/X_{lf}), the grain size parameter (X_{arm}/X_{lf}), and the compositional parameters (S [$S = IRM_{-0.3T}/SIRM$] and HIRM [$HIRM = \{IRM_{-0.3T} + SIRM\}/2$]) were calculated from the primary measurements. Further explanation of these variables and their applications may be found in the "Results" section (this chapter). Readers unfamiliar with rock-magnetic techniques are referred to King et al. (1989).

Samples were freeze-dried, weighed, and wet sieved at 63 μm; the >63 μm and <63 μm were then dried and weighed. The <63 μm fraction was treated to remove biogenic silica using a NaOH procedure (see Snoeckx, this volume). The NaOH procedure removes more amorphous material than other common extraction techniques, but does not alter the relative proportion of the various mineral

phases. Iron oxides were removed using the oxalic acid extraction technique of Landa and Gast (1973). Sediments were saturated with $MgCl_2$, to reduce d-spacing variability caused by cation differences; they were then rinsed with warm deionized water, dried, and weighed. Sediments were wet sieved at 20 μm with the aid of a sonic dismembrator, and the <20 μm fraction was split into 2-20 μm and <2 μm size fractions by means of centrifugation. The 2-20 μm size fraction was spiked with a 10% by weight Al_2O_3 internal standard and the <2 μm fraction was spiked with a 10% talc internal standard. Samples were homogenized by grinding in a mortar and pestle under acetone, air dried, suspended in a deionized water slurry, and drawn onto duplicate (one air-dried, one glycolated) silver filters for X-ray analysis.

The X-ray analysis was run from 2° to 30°2Θ at 45 kV and 40 mA at 2° 2Θ/min using Cu-kα radiation. Peak areas for smectite, illite, kaolinite, chlorite, quartz, and plagioclase were determined using Scintag DMS software. Precision of the peak areas is listed in Table 1. These precisions were calculated by comparing the area under the mineral curves between the glycolated and unglycolated samples. Smectite cannot be compared in this manner. Replicate scans and peak area resolution for this mineral were performed; the error for smectite determination is high (in excess of ~30% for both size fractions). The relative proportion of kaolinite and chlorite was determined by the relative proportions of the kaolinite [002] and chlorite [004] peak areas. Mineral peak areas were normalized to the internal standard peak areas.

Sites 885 (44°41'N, 168°16'E) and 886 (44°41'N, 168°14'E) were drilled at about 5700 m water depth in the North Pacific red clay province. A total of 59 m of sediments were cored at Hole 885A and 69 m at Hole 886B. Three stratigraphic sedimentary units were recognized at each site: (I) Pleistocene to late Pliocene

reddish brown to brown red clay; (II) late Pliocene to late Miocene diatom ooze and (III) a lower brown clay unit, originally dated as late Miocene (Rea, Basov, Janecek, Palmer-Julson, et al., 1993), but now recognized as older; late Miocene to late Cretaceous in Hole 886C (Ingram, this volume).

Table 2 lists the stratigraphic parameters for Holes 885A and 886B. Correlation between and composite depth of Holes 885A and 886B is detailed in Dickens et al. (this volume); all depths in this report are composite depths derived from that model. The depth intervals (in meters composite depth) for Unit I are 0-23.5 mcd; for Unit II, 23.5 to ~52 mcd, and for Unit III, >52 mcd. The age models used in this report are derived from the magnetic reversal stratigraphy listed in Dickens et al. (this volume). These ages are in agreement with the Radiolaria stratigraphy reported by Morely (this volume). Ages derived from ichthyolith strontium isotopic ratios (Ingram, this volume) indicate slightly younger sediments in the lower Unit II samples, but older sediment in the Unit III sediments than in the magnetic age model. Hiatuses and low sedimentation rates explain the discrepancy between the Unit III ages. Because the radiolarian ages agree with the paleomagnetic estimates, the Sr data were not incorporated into the age model for this study.

The sedimentation rate is estimated by linear interpolation between each magnetic datum obtained from the composite depth model. It is important to recognize that the linear sedimentation rates (LSRs) derived from the composite depth section may be higher than those derived from the original cores. This discrepancy is cause for some concern when trying to estimate mass accumulation rates (MARs), as the seismic records indicate that the Site 885 sediment is indeed thinner than Site 886 (Rea, Basov, Janecek, Palmer-Julson, et al., 1993). Most of the difference appears to occur in the lower brown clay of Unit III. The

LSRs derived from the composite depth model are comparable with those derived from the original depths from Hole 886B for all stratigraphic units. However, the LSR for Hole 885A Unit I is lower (0.48 cm/k.y.) than the Unit I LSR estimated from the composite depth model (0.67 cm/k.y.). A comparison of depth intervals between susceptibility datum for Holes 885A and 886A indicates equal LSRs in the top 10 m of these cores. Thus, it appears reasonable to apply the same LSRs to both sites for the upper two units, because the difference in the LSR estimates may be explained by coring gaps or drilling disturbance.

Dry bulk density (DBD) was estimated for each sample based on the dry weights of the constant volume magnetic cubes. The percent terrigenous is operationally defined as the <63 μm material remaining after the biogenic silica and iron-oxide removals, expressed as a weight percent of the total original sample. The 2-20 μm and <2 μm percentages are the weight percents of the total original sample for each size class after chemical treatment. The bulk mass accumulation rate (MAR) is the product of the LSR and DBD. The terrigenous, 2-20 μm, and <2 μm MARs are the product of the bulk MAR and the respective weight percent for each sedimentary component. The accumulation rates for the rock-magnetic properties are the product of the rock magnetic measurement and the bulk MAR. The accumulation of the <2 μm minerals is the product of the normalized peak area and the <2 μm MAR.

Results

Figure 1 illustrates the rock magnetic parameters plotted vs. composite depth, and Table 3 lists the magnetic measurements for Holes 885A and 886B. The low-frequency susceptibility (Fig. 1A) is primarily a measure of the concentration of magnetic iron oxides and is used as a proxy for the concentration

of terrigenous material. Susceptibility is highest in stratigraphic Unit III, the lower brown clay unit, suggesting a large iron-oxide component in these sediments, which grades monotonically to low values in the lower part of Unit II, the diatom ooze (~46 mcd). Susceptibility remains low throughout the diatom ooze and increases at the base of Unit I, the upper red clay unit (~24 mcd). There are large-amplitude peaks superimposed on the general upcore increase in susceptibility, coincident with the ash layers described in the initial reports (Rea, Basov, Janecek, Palmer-Julson, et al., 1993).

The frequency dependence of the susceptibility (X_{hf}/X_{lf}) is used to identify the presence of very fine (submicrometer), viscous, superparamagnetic grains. Should the contribution of such grains be large (low X_{hf}/X_{lf} ratios), the susceptibility concentration proxies and grain-size parameters derived from these values will no longer be related to the concentration and grain size of terrigenous materials, as superparamagnetic materials make a disproportionately large contribution to the susceptibility. Figure 1B illustrates the frequency dependence of the susceptibility; the frequency dependence in the lower and upper red clay units is relatively uniform and low, indicating that the application of the magnetic proxies for terrigenous material is appropriate in these intervals. The diatom ooze unit displays a more variable frequency dependence signal, largely because of the low concentration of terrigenous material combined with a negative contribution of the biogenic silica to the susceptibility signal, resulting in a frequency ratio of two very small numbers. However, there does not appear to be a large viscous superparamagnetic contribution in this stratigraphic unit; again, the application of the magnetic parameters as terrigenous proxies is appropriate.

Anhysteretic remanent magnetization, expressed as X_{arm} (Fig. 1C), is another measure of iron-oxide concentration, but it is also affected by the domain

state of the magnetic minerals. The domain state of magnetic material is related to the iron-oxide particle grain size, which, in turn, may be related to the terrigenous grain size, if fine magnetic particles are not randomly incorporated into larger terrigenous grains. The iron-oxide grain size is related to the terrigenous grain size because magnetic particles such as magnetite and hematite, derived from continental source areas, are subject to the same transport processes as the alumino-silicate grains. Smaller magnetic grains yield a larger X_{arm} signal. The X_{arm} mimics the upcore pattern observed for the susceptibility in the lower clay and diatom units, but reaches a broad maximum between 10 and 20 mcd in Unit I before decreasing toward the top of the core. This decrease at the top of the core indicates either a decrease in concentration of magnetic material, in conflict with the susceptibility signal, or an increase in the magnetic grain size. Examination of the ratio X_{arm}/X_{lf} (Fig. 1D) indicates that the latter explanation is more likely.

The ratio X_{arm}/X_{lf} is inversely related to the ferrimagnetic iron-oxide grain size and is independent of magnetic concentration. The X_{arm}/X_{lf} ratio monotonically increases from the base of stratigraphic Unit III to the base of stratigraphic Unit II, indicating a general ferrimagnetic-iron-oxide grain-size decrease throughout the lower brown clay unit. The ratio abruptly increases and becomes more variable at the base of Unit II. The high variability in this unit is related to the low magnetic mineral concentration in the diatom ooze; however, a few comments may be made about the overall grain-size pattern. In general, the diatom ooze contains the finest grain size of all sediments from Holes 885A and 886B. There is an interval of low X_{arm}/X_{lf} between 34 and 30 mcd, indicating a relatively coarse magnetic grain size, and a sharp peak in the grain-size ratio at ~28-30 mcd, indicating a very fine magnetic grain size. Above ~28 mcd, the grain-size ratio decreases and becomes less variable throughout the remainder of the

diatom ooze and in all of stratigraphic Unit I. This pattern of variation suggests a general increase in the ferrimagnetic grain size toward the top of the core.

The S-ratio ($IRM_{-0.3T}/SIRM_{1.2T}$) is a parameter sensitive to the composition of magnetic minerals. Magnetic minerals such as magnetite are easily magnetized, whereas minerals such as hematite require stronger magnetic fields to saturate them. Thus, the ratio of the proportion of magnetization stripped off of the magnetically saturated sample in a reverse field of 0.3 T is related to the proportion of "hard" to "soft" magnetic material present in a sample. Figure 1E shows the S-ratio for Sites 885 and 886. The small-amplitude, high-frequency variability in Hole 885A sediments is a systematic laboratory error; one batch of samples was not completely saturated. The S-ratio is relatively uniform and high in the lower brown clay unit and in the lower part of the diatom unit, indicating a constant magnetic mineral composition throughout this interval. Low S-ratios are observed from 29 to 35 mcd; this is the same interval as the low X_{arm}/X_{lf} ratios described earlier. The remainder of the diatom ooze unit and the upper red clay unit indicates a gradual evolution toward a slightly harder coercivity toward the top of the core.

HIRM ($[IRM_{-0.3T} + SIRM]/2$; Fig. 1F) is used to estimate the concentration of hard magnetic material in the sediment. HIRM occurs at moderate concentrations in the lower brown clay unit and decreases to uniformly low values in the diatom ooze. The concentration of hard magnetic minerals (such as goethite or hematite) does not explain the large magnetic concentrations indicated by the susceptibility or X_{arm} signal in Unit III. Thus, the magnetic carrier in these sediments must also include a softer component, such as magnetite. The concentration of hard-coercivity material begins to increase at the base of the uppermost red clay unit and displays a high-amplitude variability superimposed on

a general HIRM increase throughout this unit. This increase in HIRM tracks the increase in susceptibility; thus, the magnetic carrier in this unit is harder than the sediments in the lower brown clay unit.

Figures 2 and 3 illustrate the mineralogy for the <2 μm and 2-20 μm terrigenous material at Holes Sites 885A and 886B. Mineralogy was run at twice the sampling interval as the rock-magnetic measurements. A study to derive weighting factors for the 2-20 μm size fraction has not yet been completed, so normalized peak areas are presented instead of absolute weight percent (Tables 4-5). The absolute values of the peak areas are only comparable for the individual mineral within each size fraction. Relative change is directly comparable among all minerals and size classes.

Smectite is produced by continental weathering processes, weathering of volcanogenic material, and authigenic formation in the sediment column; so the interpretation of this mineral group is complex. However, Chamley (1989) states that most of the smectite in pelagic deep-sea sediments may be interpreted as continental weathering products. The concentration of smectite is relatively uniform in the <2 μm size fraction in both cores and through all units (Fig. 2A). For the 2-20 μm size fraction (Fig. 3A), smectite shows about a threefold increase in peak area between approximately 25 and 35 mcd and is relatively uniform and present in equal amounts in both stratigraphic clay Units I and III.

Illite is a ubiquitous terrigenous weathering product, generally associated with cool, dry environments, that is unlikely to form authigenically in the relatively thin sediments near Holes 885A and 886B. For both size fractions, there is a relative increase in illite weight percent centered on about 30 mcd (Figs. 2B and 3B). The magnitude of the increase is largest in the 2-20 μm size fraction and

smallest in the <2 μm size fraction. The <2 μm size fraction demonstrates the greatest variability in illite throughout all depths, and there is some suggestion of an illite increase in the upper 10 m of the Unit I red clay. The 2-20 μm size fraction has uniform and approximately equal illite concentrations in the upper and lower clay units.

Kaolinite is a terrigenous weathering product usually associated with strong hydrolysis. The error associated with kaolinite determination in this study is large due to the generally low kaolinite concentration in this study area, so only general comments may be made about variations in this mineral group. Kaolinite is present in highly variable amounts in all units for the <2 μm size fraction (Fig. 2C). The 2-20 μm size fraction contains a significant, but highly variable amount of kaolinite in only the diatom ooze unit (Fig. 3C).

Chlorite is a mineral phase that is usually used to indicate mechanical weathering of terrigenous sediments as it is highly susceptible to hydrolysis. The <2 μm fraction (Fig. 2D) shows low variability and low concentrations in the lower brown clay unit and high variability in the diatom unit and the upper red clay unit. Chlorite concentrations increase in sediments shallower than 10 mcd. The chlorite concentration in the 2-20 μm size fraction (Fig. 3D) is low in the lower brown clay unit, and high and variable in the diatom ooze, where again a concentration peak is observed centered at about 30 mcd. The concentration of chlorite drops at the Unit I/II boundary, and the Hole 885A and 886B records diverge; the normalized peak areas are lower in Hole 885A than in Hole 886B. This divergence appears to be a systematic laboratory error.

Quartz is a primary mineral that is not formed authigenically on the seafloor. Both records (Figs. 2E and 3E) show a high variability, but uniform

proportion, of quartz throughout all units. Quartz concentrations seem to increase in sediments shallower than 10 mcd in the <2 μm fraction.

Plagioclase is also a primary mineral not authigenically formed on the seafloor. Figures 2F and 3F illustrate the plagioclase distribution in the Hole 885A and 886B sediments. Both records are variable throughout all units. The <2 μm fraction shows a slight upcore increase, while the 2-20 μm fraction is relatively uniform in concentration.

Another way to examine the mineralogy data is to look at relative change between mineral groups. The compositional changes between groups of minerals are indicative of either changing tectonics, climatic conditions, source area, or diagenetic processes. Figures 4 and 5 illustrate peak area ratios between pairs of minerals for the <2 μm and 2-20 μm size fractions. The ratio of kaolinite to illite varies as a function of the amount of source area hydrolysis, which is related to rainfall. Kaolinite formation is favored in temperate, well-drained soils, whereas illite is a ubiquitous clay mineral associated with cooler, drier climates. The <2 μm fraction is highly variable throughout sediments from both Holes 885A and 886B (Fig. 4A). The 2-20 μm size fraction (Fig. 5A) suggests an abrupt compositional change at the Unit II/III boundary. Unit III contains no kaolinite in this size fraction. There is a sharp increase to an overall maximum in the proportion of kaolinite at the bottom of Unit II, followed by a monotonic decline that reaches zero again at the base of Unit I.

The ratio of smectite/illite (S/I) is usually indicative of either volcanism or hydrolysis in deep-sea sediments. However, in this case (Figs. 4B and 5B), the large S/I ratios in Unit III is consistent with a large hydrothermal component in the lower brown clay unit (see Owen et al. this volume). The S/I ratio drops at the

base of Unit II and remains relatively constant throughout the remainder of the sediment column in the <2 μm and 2-20 μm fraction.

Kaolinite to quartz (Figs. 4C and 5C) is the ratio of a hydrolysis sensitive mineral to a primary mineral. In both size fractions, K/Q is generally low in Unit III, reaches a maximum at about 30 mcd, and decreases toward the top of the core. This variation is more pronounced in the 2-20 μm size fraction, where K/Q goes to zero at the Unit I/II boundary.

The illite/quartz (Figs. 4D and 5D) ratios display decreasing values in the <2 μm fraction from the bottom to the top of Unit III; I/Q is relatively uniform in the 2-20 μm fraction of this interval. In both size fractions, the lower part of Unit II displays uniform ratios; there is a peak in this ratio centered at about 30 mcd. This peak is much more pronounced in the 2-20 μm size fraction. The ratio decreases slightly in both size fractions from the bottom to the top of the upper red clay unit.

In both size fractions, chlorite/quartz ratios (Figs. 4E and 5E), indicative of mechanical weathering, are generally very small in lower clay Unit III, show a slight increase at the Unit II/III boundary, and another small step up at ~45 mcd. There is a sharp peak in this ratio centered at approximately 30 mcd, followed by uniform values throughout the remainder of the diatom unit and Unit I.

Finally, we compare the rock-magnetic properties to the mineralogy, to examine how the two covary. Figure 6 illustrates the low-frequency susceptibility and the <2 μm quartz peak area plotted vs. composite depth. The two variables covary in the upper red clay and diatom ooze units. However, the signals decouple at the Unit II/III boundary. This decoupling of the signal implies that the sedimentary material in Unit III is from a different source than the terrigenous material in Unit I.

Figure 7 illustrates the illite/quartz ratio and the S-ratio plotted as a function of composite depth. These variables strongly correspond at about 30 mcd. Illite/quartz increases occur at the same place that the rock magnetic parameter, S, indicates a shift from low to high coercivity iron-oxide mineralogy.

Figures illustrating the mass accumulation rates (MARs) of different parameters over time are useful here because the diatom ooze represents a large dilutional component to the terrigenous sediments proximal to Sites 885 and 886. Figure 8 illustrates the MARs of the bulk sediment, terrigenous fraction, and the 2-20 μm and <2 μm fractions of the sediment used for mineralogical analysis. There is offset in the terrigenous MARs of Holes 885A and 886B in the upper clay unit. This could be the result of either systematic laboratory error, sediment winnowing, or focusing differences between the two sites. Because there are no systematic offsets in the primary rock magnetic parameters, or in the bulk MARs, we think the former is the case. Snoeckx and Rea (this volume) provide a detailed interpretation of the eolian accumulation at Sites 885 and 886. For the parameters presented, we display only the upper two units for the mass accumulation discussion; we have few samples from the lower clay unit, and the ages of these sediments are uncertain.

Figure 9 displays the magnetic concentration parameters plotted as accumulation rates vs. age. The magnetic-iron-oxide concentration parameters (X_{lf} and HIRM) track the terrigenous MARs. These records show a small, LSR-controlled peak at the base of Unit II (~7.5 Ma), low accumulation and low variability through the middle part of this unit, followed by an abrupt increase in accumulation at ~3.8 Ma, which continues through all of Unit I.

Figure 10 illustrates the accumulation rates for the mineral phases identified in the <2 μm size fraction. With the exception of kaolinite, which increases in the Unit II diatom ooze in the 2-20 μm size fraction, the <2 μm patterns are identical with the larger size class, and are not illustrated. For all minerals, the accumulation rate has small peaks at the base of Unit II at ~7.5, 6.5 and 5.1 Ma and decreases to low values after 5 Ma. The MARs of the minerals stay low until an abrupt increase at about 3.8 Ma, which continues to increase throughout the late Pleistocene.

Discussion

There are several changes in the mineralogy and magnetic properties that imply varying environmental conditions at Sites 885 and 886. Unit III, the lower brown clay unit, is characterized by high concentrations of fine-grained ferrimagnetic iron oxides, that contain a softer magnetic carrier than the Unit I sediments, low bulk and terrigenous MARs, and a mineralogy characterized by a large proportion of smectite relative to the other units. Unit II, the diatom ooze, is marked by low magnetic-iron-oxide concentrations and fine grain sizes, moderate sedimentation rates, low bulk and terrigenous MARs, and an interval of anomalous mineralogy and magnetic composition centered at 30 mcd. The Unit I/II boundary is marked by a step up in the terrigenous MAR and magnetic-iron-oxide concentrations. These increases continue to the top of the core and are accompanied by an increase in the iron-oxide grain size, as well as an increase in the chlorite concentrations.

The potentially important sediment sources proximal to Site 885 and 886 now and in the past include eolian terrigenous and volcanogenic sediment, siliceous biogenic material, and hydrothermal precipitates. The rock-magnetic and

mineralogy measurements mimic the major lithological changes, which account for most of the variation observed for these parameters. There is close covariance of the mineralogy and magnetics in the upper two lithologic units (Fig. 6). The decoupling of the signal at the base of Unit II, specifically a drop in quartz concentration together with a sharp increase in the iron-oxide concentration, occurs at the same time as a shift toward a magnetic composition enriched (relative to the Unit I sediments) in a low-coercivity component. Large concentrations of iron oxides in deep-sea sediments are produced by hydrothermal, terrigenous sedimentary or volcanogenic processes. The sediment in Unit III is likely composed of a large hydrothermal component (see Owen et al. this volume). Hydrothermal sediment is characterized by a wide variety of magnetic carriers, such as magnetite, hematite or goethite, which were observed in shipboard smear-slide analyses (Rea, Basov, Janecek, Palmer-Julson, et al., 1993).

Although the magnetic composition of terrigenous material would depend on the source area composition, terrigenous material from a volcanogenic environment would be enriched in low-coercivity magnetic minerals. We hypothesize that the hydrothermal sediments in Unit III may also contain a small amount of eolian, andesitic, terrigenous material. Kyte et al. (1993) propose andesitic volcanism in western Mexico as a source for the Late Cretaceous terrigenous sediments identified in the bottom of Core LL44-GPC3. Plate tectonic calculations indicate that conditions may have been favorable for some andesitic eolian contribution in the past. The clay material in the top two units of the sediment column is likely from an Asian source, as indicated by the present location of the site and the covariance of the rock-magnetic and mineralogy

measurements. The increase in the importance of this eolian component is considered in the context of the climate and tectonic forces driving the signal.

There are two types of tectonic variation that we need to consider to interpret the mineralogical and rock magnetic signals from Holes 885A and 886B. The first is plate motion, which will influence the source contribution to the sediments. Based on the paleopole reconstruction of Sager and Pringle (1988), Holes 885A and 886B were located only 3° south of the present location at 45°N during the late Miocene deposition of sediments at the Unit II/III boundary (R. Larson, pers. comm., 1994), so plate motion should not complicate the interpretation of the eolian sediments above this interval. However, the basement at Sites 885 and 886 has been dated at ~80 Ma (Keller, this volume). Paleomagnetic plate rotations indicate that the plate was formed at about 16°N. Thus, we need to control for plate motion when interpreting the Unit III sediments. Low latitudes are influenced by easterly eolian transport from the North American continent. This supports our hypothesis for some supply of andesitic eolian material to the Unit III hydrothermal sediments.

Tectonic activity in the Asian source area, such as uplift of the Himalayan Mountains or Tibetan Plateau, could impact eolian sedimentation proximal to Sites 885 and 886 as a result of climatic forcing. Geological evidence indicates that uplift pulses are episodic (Copeland et al., 1990; Amano and Taira, 1992; Hovan and Rea, 1993), so the response in the sediment record would be abrupt if the uplift-induced climate forcing is linear. Uplift-forced climatic change (Kutzbach, et al., 1989; Ruddiman et al., 1989) is hypothesized to result in cooling of northern Asia and drying of the Eurasian interior. The impact on the eolian sediments in the North Pacific would be manifested as an increase in the mechanical weathering proxies such as in chlorite, quartz, illite, and plagioclase at the expense of

chemical weathering proxies such as kaolinite and smectite. This climatic change would also produce an increase in terrigenous MARs, as particle production increased because of source region aridification. At Holes 885A and 886B, the shift from a kaolinite-rich mineralogy in the diatom ooze unit to chlorite-rich sediments in the upper red clay unit, concomitant with an increase in the terrigenous MAR are supportive of dramatic environmental changes in Asia during the Pliocene.

The timing of this event in this region of the North Pacific is at about 3.8 Ma. Studies of present-day eolian transport identify the deserts of interior Asia as the source region for the loess deposits in China, as well as the North Pacific eolian sediments (Merrill et al., 1985, 1989). A study by Ding et al. (1992) reports the onset of major loess deposition in China at 2.5 Ma. These authors state that the eolian source areas began drying out during the mid to late Pliocene because of plateau uplift. This assertion is supported by the mineralogy in the North Pacific sediments; specifically, the monotonic decline in the concentration of kaolinite in the 2-20 μm fraction of the late Miocene to early Pliocene Unit II sediments.

Although the eolian source regions developed in the late Pliocene, the meteorological conditions were not favorable for deposition on the loess plateau at that time. The mechanism invoked by Ding et al. (1992) for the lack of loess deposition during the late Pliocene involves atmospheric circulation changes, inferred from the model of Kutzbach et al. (1989). The authors state that the 500 mb quasi-stationary trough presently located to the east of the loess plateaus of China was not as well developed during the late Pliocene as it is presently because the Tibetan Plateau elevation was not as high as it is today. Thus, eolian transport from the desert regions was mainly west to east, as opposed to the present northwesterly flow, and the air-mass subsidence over the loess plateau,

responsible for dust deposition there, was reduced compared with the present. These meteorological conditions would not preclude deposition of eolian material in the North Pacific; perhaps they even provided a more direct path between the deserts and the ocean than at the present time. The age offset between the onset of loess deposition in China at 2.5 Ma and the sudden increase in eolian deposition in the North Pacific at 3.8 Ma is consistent with the scenario proposed by these authors. The three small peaks in the MARs of the six mineral species in the lower part of Unit II at about 7.5, 6.5, and 5.1 Ma may also record smaller pulses of Asian aridification in the late Miocene.

Changes in the eolian transport and sediment deposition (current winnowing) in this region would be characterized by changes in the grain size and changes in the LSRs not accounted for by changing source strengths. Magnetic-iron-oxide grain sizes increase at the base of Unit I, and continue to increase throughout the unit. The increase can be explained by increasing transport speed of atmospheric circulation, caused by an increase in the pole-to-equator temperature gradient induced by glaciation. Snoeckx and Rea (this volume) provide a detailed analysis of this grain size variation at Sites 885 and 886. Changes in LSR are generally accounted for by the varying strengths of the terrigenous and biogenic accumulation in these cores. There may be hiatuses in lower clay Unit III, but we do not have the sample resolution in this interval to discern this activity.

Another prominent feature of the sediments at Sites 885 and 886 is the sharp signal in the rock magnetic parameters S and X_{arm}/X_{lf} coupled with the sharp change in mineralogy at 30 mcd (~4.7 Ma). This signal appears in the middle of the diatom ooze unit, during the period with the lowest accumulation of terrigenous sediments in the entire sediment column. The S-ratio and X_{arm}/X_{lf}

changes could be the result of diagenetic alteration of the magnetic signal. Iron oxides are soluble under reducing conditions, and the finest grains will be preferentially dissolved over coarser magnetic particles. The low X_{arm}/X_{lf} ratio between 30 and 34 mcd may be the result of such a grain-size modification. Furthermore, the sharp X_{arm}/X_{lf} peak at 28-30 mcd could be caused by single-domain magnetite produced by magnetotactic bacteria active at the redox boundary in the sediment at the time of reduction diagenesis. This hypothesis is corroborated by the low S-ratio in this interval. Fine magnetite is more susceptible to dissolution than hematite, and this selective dissolution has altered the bulk magnetic composition in this interval, reducing the proportion of low-coercivity material. The total organic carbon shows a small peak at this depth (885A, maximum = 0.14%, 886B, maximum = 0.25%; Rea, Basov, Janecek, Palmer-Julson, et al., 1993), although the organic carbon concentrations are extremely low (mean TOC = 0.10%) everywhere in the core. The mineralogical variation could suggest a change in source supply, but it is difficult to envision a process that would supply such a short and intense burst of unusual clay mineralogy in the middle of the Pacific Ocean, especially with no increase in the terrigenous MAR. Because the terrigenous material is present in such low concentrations, and is accumulating in such small amounts, the minerals may be especially susceptible to alteration in this interval. The signal here is probably diagenetic in origin, marked by the dissolution of fine X-ray amorphous clay material in a relatively acidic environment and the creation of transitional minerals during clay halmyrosis. Chamley (1989) proposes this explanation for mineralogical variations in sapropel layers in Eastern Mediterranean sediments. Although the organic carbon concentration here is obviously much lower than the sapropels in the Mediterranean, the very small concentrations of terrigenous material may render it more susceptible to

modification. The shape of the signal, with a sharp bottom and a gradational top, was also characteristic of the sapropel diagenetic modification.

Summary

The magnetic and mineralogy signals from the sediments at Sites 885 and 886 record variations in a number of environmental parameters through time. The relative terrigenous, biogenic silica, and hydrothermal source strengths account for most signal variations. There may be some North American eolian terrigenous component in the hydrothermal sediments in Unit III. The terrigenous component in the diatom ooze and the upper red clay is Asian eolian material. The terrigenous source-area climate and tectonic variations cause a change from a mineralogy rich in chemical weathering products to one rich in mechanical weathering products, at the same time that the accumulation rate and grain size of the terrigenous material increase. These changes are consistent with late Pliocene Tibetan Plateau uplift pulses and Asian aridification. Diagenetic processes recorded in the mineralogy and rock-magnetics indicate that sediments in this region of the North Pacific may have been suboxic to anoxic sometime in the early Pliocene.

Acknowledgments

Eve Arnold was supported by a JOI fellowship for this research. This study benefited from the kind assistance of the ODP staff and SEDCO crew aboard the JOIDES Resolution. Ms. Bonnie Wolfe assisted in the processing of the sediments. Jan Bloemendal made helpful suggestions on an early draft of the manuscript. Steve Hovan and Suzanne O'Connell reviewed the manuscript. We thank these individuals for their contributions.

References

Amano, K., and Taira, A., 1992. Two-phase uplift of the higher Himalayas since 17 Ma. Geology, 20:391-394.

Blank, M., Leinen, M., and Prospero, J.M., 1985. Major eolian inputs indicated by the mineralogy of aerosols and sediments in the western North Pacific. Nature, 314:84-86.

Chamley, H., 1989. Clay Sedimentology: Heidelberg (Springer-Verlag).

Copeland, P., and Harrison, T.M., 1990. Episodic uplift in the Himalayas revealed by $^{40}Ar/^{39}Ar$ analysis of detrital K-feldspar and muscovite, Bengal Fan. Geology, 18:354-357.

Ding, Z., Rutter, N., Jingtai, H., and Tungsheng, L., 1992. A coupled environmental system formed at about 2.5 Ma in east Asia. Palaeoceangr., Palaeoclimatol., Palaeoecol., 94:223-242.

Doh, S.J., King, J.W., and Leinen, M., 1988. A rock magnetic study of giant piston core LL44-GPC3 from the central North Pacific and its paleoceanographic implications. Paleoceanography. 3:89-111.

Griffin, J.J., Windom, H., and Goldberg, E.D., 1968. The distribution of clay minerals in the world ocean. Deep-Sea Res., 15:433-459.

Hovan, S., and Rea, D.K., 1992. The Cenozoic record of continental mineral deposition on Broken and Ninetyeast Ridges, Indian Ocean: southern African aridity and sediment delivery from the Himalayas. Paleoceanography, 7:833-860.

King, J.W., Bloemendal, J., and Gangemi, P. 1989. Paleomagnetic and rock-magnetic stratigraphy of ESOPE core 63, Southern Nares Abyssal Plain. In Schuttenhelm, R.T.E., Auffret, G.A., Buckley, D.E., Cranston, R.E., Murray, C.N., Shepard, L.E., Spijkstra, A.E. (Eds.), The ESOPE International Expedition, Geoscience Investigations of Two North Atlantic Abyssal Plains: Luxembourg (Office for official publications of the European community), 611-636.

Kutzbach, J.E., Guetter, P.J., Ruddiman, W.F., and Prell, W.L. 1989. Sensitivity of climate to late Cenozoic uplift in southern Asia and the American west: numerical experiments. J. Geophys. Res., 94:18393-18407.

Kyte, F.T., Leinen, M., Heath, G.R., and Zhou, L., 1993. Cenozoic sedimentation history of the central North Pacific: Inferences from the elemental geochemistry of Core LL44-GPC3. Geochim. Cosmochim. Acta, 57:1719-1740.

Landa, E.R., and Gast, R.G., 1973. Evaluation of crystallinity in hydrated ferric oxides. Clays Clay Minerals., 21:121-130.

Leinen, M., 1985. Quartz content of northwest Pacific Hole 576A and implications for Cenozoic eolian transport. In Heath, G.R., Burkle, L.H., et al., Init. Repts. DSDP, 86: Washington (U.S. Govt. Printing Office), 581-588.

———, 1989. The late Quaternary record of atmospheric transport to the Northwest Pacific from Asia. In Leinen, M., and Sarnthein, M. (Eds.), Paleoclimatology and Paleometeorology: Modern and Past Patterns of Global Atmospheric Transport: Dordrecht (NATO ASI Series), 693-732.

Merrill, J.T., Bleck, R., and Avila, L. 1985. Modeling transport to the Marshall Islands. J. Geophys. Res. 90:12927-12936.

Merrill, J.T., Uematsu, M., and Bleck, R. 1989. Meteorological analysis of long range transport of mineral aerosols over the North Pacific. J. Geophys. Res. 94:8584-8598.

Oldfield, F., Hunt, A., Jones., D.H., Chester, R., Dearing, J.A., Olsson, L., and Prospero, J.M. 1985. Magnetic differentiation of atmospheric dusts. Nature, 317:516-518.

Rea, D.K., Basov, I.A., Janecek, T.R., Palmer-Julson, A., et al., 1993. Proc. ODP, Init. Repts., 145: College Station, TX (Ocean Drilling Program).

Robinson, S.G., 1986. The late Pleistocene paleoclimatic record of North Atlantic deep-sea sediments revealed by mineral-magnetic measurements. Phys. Earth Planet. Int., 42:22-47.

Ruddiman, W.F., Prell, W.L. and Raymo, M.E. 1989. Late Cenozoic uplift in southern Asia and the American west: rationale for general modeling experiments. J. Geophys. Res. 94:18397-18391.

Sager, W.W., and Pringle, M.S., 1988. Mid Cretaceous to early Tertiary apparent polar wander path of the North Pacific. J. Geophys. Res. 93:11753-11771.

Schramm, C.T. 1989. Cenozoic climatic variation recorded by quartz and clay minerals in North Pacific Sediments. In Leinen, M., and Sarnthein, M. (Eds.), Paleoclimatology and Paleometeorology: Modern and Past Patterns of Global Atmospheric Transport: Dordrecht (NATO ASI Series), 805-839.

Table 1. Precision, expressed as relative error of mineral peak areas.

[redacted]	Smectite	Illite	Kaolinite	Chlorite	Quartz	Plagioclase
[redacted] µm	ND	2.3	11.2	2.9	7.6	2.2
2-20 µm	ND	1.3	33.3	0.4	3.0	2.5

Note: ND = not determined.

Table 2. Stratigraphic parameters and mass accumulation rates for holes 885A and 886B.

Core, section, interval (cm)	Depth (mbsf)	Composite depth (m)	Age (Ma)	LSR (cm/k.y.)	Dry bulk density (g/cm^3)	Bulk MAR ($g/cm^2/k.y.$)	Terrigenous MAR ($g/cm^2/k.y.$)	> 63µm MAR ($g/cm^2/k.y.$)	20-63 µm MAR ($g/cm^2/k.y.$)	2-20 µm MAR ($g/cm^2/k.y.$)	<2 µm MAR ($g/cm^2/k.y.$)
145-885A											
1H-1, 25	0.25	0.30	0.05	0.63	0.47	0.295	0.143	0.014	0.003	0.092	0.042
1H-1, 125	1.25	1.65	0.26	0.63	0.54	0.337	0.152	0.010	0.003	0.097	0.045
1H-2, 25	1.75	2.34	0.37	0.63	0.45	0.284	0.144	0.007	0.004	0.094	0.043
1H-2, 125	2.75	3.89	0.62	0.63	0.44	0.277	0.127	0.009	0.008	0.081	0.033
1H-3, 25	3.25	4.34	0.69	0.63	0.47	0.291	0.129	0.006	0.002	0.080	0.042
1H-3, 125	4.25	5.16	0.85	0.41	0.48	0.194	0.103	0.002	0.003	0.066	0.031
2H-1, 25	4.85	5.63	0.96	0.41	0.53	0.217	0.118	0.002	0.004	0.075	0.036
2H-1, 125	5.85	6.72	1.11	0.46	0.47	0.216	0.099	0.004	0.004	0.066	0.025
2H-2, 25	6.35	7.24	1.27	0.46	0.55	0.252	0.128	0.004	0.004	0.078	0.035
2H-2, 125	7.35	8.19	1.48	0.46	0.47	0.217	0.092	0.008	0.006	0.057	0.023
2H-3, 25	7.85	8.63	1.57	0.46	0.57	0.261	0.093	0.030	0.017	0.055	0.014
2H-3, 125	8.85	9.61	1.78	0.46	0.44	0.205	0.083	0.004	0.003	0.052	0.023
2H-4, 125	10.35	12.12	2.23	0.66	0.52	0.342	0.158	0.002	0.004	0.097	0.048
2H-5, 125	11.85	14.55	2.60	0.66	0.44	0.290	0.116	0.002	0.002	0.072	0.035
2H-6, 125	13.35	17.06	2.86	0.96	0.42	0.407	0.091	0.008	0.011	0.056	0.017
3H-1, 125	15.35	21.35	3.30	0.96	0.48	0.458	0.132	0.005	0.006	0.079	0.038
3H-2, 125	16.85	23.55	3.53	0.96	0.37	0.354	0.062	0.005	0.002	0.041	0.015
3H-3, 125	18.35	25.05	3.77	0.61	0.33	0.202	0.015	0.005	0.001	0.010	0.003
3H-4, 125	19.85	26.55	4.02	0.61	0.32	0.192	0.019	0.001	0.001	0.010	0.004
3H-5, 125	21.35	28.05	4.26	0.61	0.28	0.171	0.012	0.001	0.001	0.008	0.003
3H-6, 125	22.85	29.31	4.47	0.61	0.29	0.177	0.008	0.001	0.000	0.006	0.001
4H-1, 125	24.85	30.82	4.72	0.61	0.24	0.143	0.004	0.001	0.000	0.002	0.001
4H-2, 125	26.35	31.95	4.91	0.61	0.29	0.178	0.014	0.003	0.000	0.009	0.003
4H-3, 125	27.85	33.23	5.12	0.61	0.40	0.241	0.054	0.002	0.002	0.034	0.015

Table 2. Continued.

Core, section, interval (cm)	Depth (mbsf)	Composite depth (m)	Age (Ma)	LSR (cm/k.y.)	Dry bulk density (g/cm^3)	Bulk MAR ($g/cm^2/k.y.$)	Terrigenous MAR ($g/cm^2/k.y.$)	> 63µm MAR ($g/cm^2/k.y.$)	20-63 µm MAR ($g/cm^2/k.y.$)	2-20 µm MAR ($g/cm^2/k.y.$)	<2 µm MAR ($g/cm^2/k.y.$)
4H-4, 125	29.35	34.53	5.33	0.61	0.36	0.217	0.027	0.002	0.002	0.017	0.005
4H-5, 125	30.85	35.99	5.57	0.61	0.39	0.235	0.046	0.002	0.001	0.030	0.010
4H-6, 125	32.35	37.57	5.83	0.61	0.39	0.234	0.027	0.001	0.001	0.017	0.006
5H-1, 125	34.35	40.15	6.26	0.61	0.43	0.258	0.063	0.001	0.005	0.039	0.014
5H-2, 125	35.85	42.06	6.58	0.61	0.42	0.254	0.058	0.003	0.001	0.035	0.018
5H-3, 125	37.35	44.09	6.91	0.61	0.32	0.191	0.009	0.003	0.000	0.006	0.002
5H-4, 125	38.85	45.82	7.20	0.61	0.40	0.240	0.038	0.002	0.001	0.023	0.011
5H-5, 125	40.35	47.49	7.42	0.79	0.46	0.362	0.113	0.001	0.005	0.071	0.031
5H-6, 125	41.85	49.48	7.67	0.79	0.42	0.332	0.112	0.001	0.003	0.080	0.025
6H-1, 125	43.85	51.52	8.26	0.07	0.45	0.034	0.015	0.000	0.000	0.011	0.004
6H-2, 125	45.35	53.30	10.67	0.07	0.43	0.032	0.016	0.000	0.000	0.011	0.005
6H-3, 125	46.85	54.58	12.41	0.07	0.61	0.045	0.022	0.000	0.000	0.014	0.007
6H-4, 125	48.35	56.68	15.26	0.07	0.65	0.048	0.023	0.000	0.000	0.013	0.009
6H-5, 125	49.85	64.22	25.47	0.07	0.47	0.035	0.014	0.000	0.000	0.007	0.007
6H-6, 125	51.35	69.96	33.25	0.07	0.46	0.034	0.012	0.003	0.000	0.002	0.006
145-886B											
1H-1, 50	0.50	0.77	0.12	0.63	0.51	0.320	0.184	0.005	0.004	0.111	0.062
1H-2, 11	1.31	2.76	0.44	0.63	0.47	0.294	0.179	0.002	0.005	0.105	0.063
2H-1, 50	2.30	4.71	0.75	0.63	0.53	0.331	0.223	0.005	0.004	0.128	0.081
2H-2, 50	3.80	4.76	0.76	0.63	0.48	0.301	0.202	0.003	0.005	0.111	0.077
2H-3, 50	5.30	4.82	0.77	0.63	0.54	0.337	0.222	0.005	0.006	0.123	0.082
2H-4, 50	6.80	4.87	0.78	0.63	0.47	0.294	0.190	0.002	0.008	0.102	0.072
2H-5, 50	8.30	4.93	0.79	0.41	0.51	0.209	0.137	0.006	0.016	0.069	0.046
2H-6, 50	9.80	4.98	0.80	0.41	0.48	0.196	0.132	0.003	0.004	0.073	0.049
2H-7, 45	11.25	7.49	1.33	0.46	0.46	0.214	0.137	0.001	0.002	0.084	0.045

Table 2. Continued.

Core, section, interval (cm)	Depth (mbsf)	Composite depth (m)	Age (Ma)	LSR (cm/k.y.)	Dry bulk density (g/cm^3)	Bulk MAR ($g/cm^2/k.y.$)	Terrigenous MAR ($g/cm^2/k.y.$)	> 63µm MAR ($g/cm^2/k.y.$)	20-63 µm MAR ($g/cm^2/k.y.$)	2-20 µm MAR ($g/cm^2/k.y.$)	<2 µm MAR ($g/cm^2/k.y.$)
3H-1, 50	11.80	9.11	1.68	0.46	0.45	0.210	0.122	0.001	0.001	0.074	0.041
3H-2, 50	13.30	10.60	1.99	0.66	0.46	0.301	0.159	0.005	0.006	0.091	0.055
3H-3, 50	14.80	12.61	2.30	0.66	0.48	0.317	0.172	0.002	0.002	0.099	0.065
3H-4, 50	16.30	14.65	2.61	0.96	0.53	0.512	0.294	0.002	0.005	0.171	0.106
3H-5, 50	17.80	16.15	2.76	0.96	0.39	0.371	0.078	0.001	0.000	0.043	0.029
3H-6, 50	19.30	17.71	2.93	0.96	0.39	0.375	0.120	0.001	0.001	0.068	0.044
4H-1, 50	21.30	20.47	3.21	0.96	0.42	0.408	0.103	0.001	0.000	0.058	0.039
4H-2, 50	22.80	22.55	3.43	0.96	0.43	0.415	0.139	0.006	0.009	0.079	0.046
4H-3, 50	24.30	24.59	3.71	0.61	0.31	0.185	0.021	0.000	0.000	0.012	0.007
4H-4, 50	25.80	26.17	4.00	0.61	0.33	0.200	0.021	0.000	0.000	0.012	0.008
4H-5, 50	27.30	27.52	4.25	0.61	0.32	0.197	0.015		0.000	0.009	0.005
4H-6, 50	28.80	28.87	4.49	0.61	0.33	0.200	0.013	0.001	0.000	0.008	0.004
5H-1, 50	30.80	30.66	4.82	0.61	0.29	0.175	0.008	0.000	0.000	0.004	0.002
5H-2, 50	32.30	32.01	5.07	0.61	0.32	0.193	0.024	0.009	0.002	0.015	0.006
5H-3, 50	33.80	33.50	5.34	0.61	0.41	0.247	0.048	0.013	0.000	0.027	0.018
5H-4, 50	35.30	35.00	5.62	0.61	0.33	0.199	0.037	0.011	0.003	0.018	0.012
5H-5, 50	36.80	36.50	5.87	0.61	0.36	0.215	0.029	0.014	0.000	0.015	0.010
5H-6, 50	38.30	38.00	6.07	0.61	0.35	0.214	0.028	0.017	0.001	0.016	0.010
5H-7, 50	39.80	39.56	6.25	0.61	0.49	0.297	0.112	0.007	0.001	0.062	0.044
6H-1, 50	40.30	40.39	6.35	0.61	0.42	0.254	0.059	0.014	0.001	0.032	0.023
6H-2, 50	41.80	41.95	6.59	0.61	0.40	0.245	0.050	0.012	0.000	0.028	0.019
6H-3, 50	43.30	43.45	6.82	0.61	0.36	0.220	0.024	0.022	0.000	0.014	0.009
6H-4, 50	44.80	44.95	7.06	0.61	0.34	0.205	0.027	0.013	0.000	0.015	0.010
6H-5, 50	46.30	46.45	7.29	0.79	0.40	0.317	0.063	0.007	0.001	0.031	0.025
6H-6, 52	47.82	48.12	7.50	0.79	0.46	0.366	0.169	0.002	0.002	0.090	0.072

Table 2. Continued.

Core, section, interval (cm)	Depth (mbsf)	Composite depth (m)	Age (Ma)	LSR (cm/k.y.)	Dry bulk density (g/cm^3)	Bulk MAR ($g/cm^2/k.y.$)	Terrigenous MAR ($g/cm^2/k.y.$)	> 63µm MAR ($g/cm^2/k.y.$)	20-63 µm MAR ($g/cm^2/k.y.$)	2-20 µm MAR ($g/cm^2/k.y.$)	<2 µm MAR ($g/cm^2/k.y.$)
6H-7, 50	49.30	50.28	7.77	0.79	0.44	0.350	0.139	0.003	0.001	0.073	0.061
7H-1, 47	49.77	50.97	7.86	0.79	0.35	0.280	0.078	0.007	0.000	0.041	0.034
7H-2, 47	51.27	53.02	10.29	0.07	0.44	0.033	0.019	0.000	0.000	0.010	0.008
7H-3, 47	52.77	54.52	12.32	0.07	0.61	0.045	0.028	0.000	0.000	0.014	0.013
7H-4, 47	54.27	55.55	13.72	0.07	0.65	0.048	0.019	0.000	0.001	0.010	0.007
7H-5, 47	55.77	57.20	15.95	0.07	0.56	0.041	0.029	0.000	0.000	0.010	0.018
7H-6, 47	57.27	58.79	18.11	0.07	0.52	0.039	0.030	0.000	0.000	0.010	0.016
7H-7, 47	58.77	60.22	20.05	0.07	0.54	0.040	0.031	0.000	0.001	0.010	0.019
8X-1, 50	59.30	60.75	20.77	0.07	0.51	0.038	0.024	0.000	0.000	0.015	0.008

Note: LSR = linear sedimentation rate, and MAR = mass accumulation rate. Blank = no measurement.

Table 3. Rock-magnetic measurements for Holes 885A and 886B.

Core, section, interval (cm)	Depth (mbsf)	Composite depth (m)	Age (Ma)	X_{arm} ($\mu m^3/g$)	X_{lf} ($\mu m^3/g$)	X_{HF} ($\mu m^3/g$)	X_{lf}/X_{hf}	X_{arm}/X	SIRM ($\mu A/m^2/g$)	IRM-0.3T ($\mu A/m^2/g$)	S-ratio	HIRM ($\mu A/m^2/g$)
145-885A												
1H-1, 25	0.25	0.30	0.05	8.63	21.35	20.38	0.95	0.40	19089.01	-17098.30	0.84	548.22
1H-1, 50	0.50	0.61	0.10	10.96	10.20	9.70	0.95	1.07	19310.96	-17801.43	0.92	409.57
1H-1, 125	1.25	1.65	0.26	5.64	15.47	14.71	0.95	0.36	9846.23	-9007.93	0.89	364.38
1H-2, 25	1.75	2.34	0.37	11.27	17.67	16.70	0.95	0.64	17316.93	-16355.27	0.87	255.03
1H-2, 50	2.00	2.68	0.43	11.92	15.15	14.41	0.95	0.79	24327.92	-22350.27	0.92	591.38
1H-2, 125	2.75	3.89	0.62	14.90	27.68	26.30	0.95	0.54	30093.61	-27704.20	0.87	618.02
1H-3, 25	3.25	4.34	0.69	10.04	10.57	9.98	0.94	0.95	10533.99	-9561.91	0.87	264.01
1H-3, 50	3.50	4.49	0.72	13.62	7.22	6.79	0.94	1.89	13880.38	-12855.70	0.93	270.22
1H-3, 125	4.25	5.16	0.84	9.92	16.05	15.22	0.95	0.62	14526.08	-13440.03	0.88	302.44
2H-1, 25	4.85	5.63	0.93	12.89	25.96	24.18	0.93	0.50	23418.97	-20571.62	0.85	885.46
2H-1, 50	5.10	5.88	0.98	14.93	17.06	15.90	0.93	0.88	29727.07	-26390.47	0.89	963.87
2H-1, 125	5.85	6.72	1.16	9.91	13.45	12.64	0.94	0.74	11434.31	-10664.09	0.88	209.75
2H-2, 25	6.35	7.24	1.27	9.29	14.78	14.09	0.95	0.63	11428.79	-10541.48	0.88	282.89
2H-2, 50	6.60	7.49	1.33	14.92	8.57	8.07	0.94	1.74	15347.45	-14184.78	0.92	296.12
2H-2, 125	7.35	8.19	1.48	15.71	29.69	28.27	0.95	0.53	29959.48	-27774.38	0.89	598.97
2H-3, 25	7.85	8.63	1.57	14.70	37.85	35.59	0.94	0.39				
2H-3, 50	8.10	8.85	1.62	15.09	16.37	15.55	0.95	0.92	29044.66	-26869.97	0.93	602.79
2H-3, 125	8.85	9.61	1.78	11.14	13.64	12.78	0.94	0.82	13073.65	-11688.32	0.85	356.23
2H-4, 50	9.60	10.62	2.00	16.27	13.86	13.17	0.95	1.17	30615.47	-28372.14	0.93	533.10
2H-4, 125	10.35	12.12	2.23	10.94	12.08	11.36	0.94	0.91	9851.48	-8812.33	0.85	315.49
2H-5, 50	11.10	13.71	2.47	18.89	7.26	6.88	0.95	2.60	12673.33	-11872.81	0.94	210.26
2H-5, 125	11.85	14.55	2.60	14.00	8.33	7.72	0.93	1.68	7786.71	-7165.01	0.89	160.11
2H-6, 50	12.60	15.75	2.72	13.66	2.99	2.82	0.94	4.57	6506.05	-6093.87	0.94	95.74
2H-6, 125	13.35	17.06	2.86	15.14	16.91	16.02	0.95	0.90	19040.23	-17969.53	0.88	263.93
2H-7, 14	13.74	17.49	2.90	23.77	19.94	18.75	0.94	1.19	44978.16	-40598.85	0.90	1099.99

Table 3. Continued.

Core, section, interval (cm)	Depth (mbsf)	Composite depth (m)	Age (Ma)	X_{arm} ($\mu m^3/g$)	X_{lf} ($\mu m^3/g$)	X_{HF} ($\mu m^3/g$)	X_{lf}/X_{hf}	X_{arm}/X	SIRM ($\mu A/m^2/g$)	IRM-0.3T ($\mu A/m^2/g$)	S-ratio	HIRM ($\mu A/m^2/g$)
3H-1, 50	14.60	19.54	3.12	12.09	1.90	1.73	0.91	6.36	4774.84	-4542.89	0.95	48.96
3H-1, 125	15.35	21.35	3.30	16.14	6.44	5.90	0.92	2.51	6241.31	-5919.02	0.90	89.51
3H-2, 50	16.10	22.80	3.45	12.03	3.67	3.40	0.93	3.28	4685.27	-4432.47	0.95	95.46
3H-2, 125	16.85	23.55	3.53	11.74	2.62	2.31	0.88	4.48	3968.48	-3792.59	0.93	37.71
3H-3, 50	17.60	24.30	3.65	9.06	1.15	1.06	0.92	7.88	3719.09	-3603.49	0.97	22.78
3H-3, 125	18.35	25.05	3.79	5.20	1.20	1.12	0.94	4.33	2288.08	-2178.35	0.91	21.39
3H-4, 50	19.10	25.80	3.93	8.81	1.39	1.27	0.92	6.34	4065.74	-3908.50	0.96	30.81
3H-4, 125	19.85	26.55	4.07	8.19	1.36	1.17	0.86	6.02	2859.41	-2733.49	0.91	23.27
3H-5, 50	20.60	27.30	4.21	9.12	0.89	0.80	0.90	10.25	3398.41	-3304.30	0.97	17.25
3H-5, 125	21.35	28.05	4.34	7.30	0.90	0.80	0.89	8.11	2694.87	-2652.00	0.95	7.08
3H-6, 50	22.10	28.74	4.47	6.12	0.36	0.31	0.87	17.00	2207.82	-2154.20	0.98	11.13
3H-6, 125	22.85	29.31	4.57	5.29	0.31	0.31	1.00	17.06	2082.90	-2032.85	0.91	8.51
3H-7, 50	23.60	29.87	4.68	0.60	0.40	0.37	0.93	1.50	1367.68	-1194.65	0.87	32.66
4H-1, 50	24.10	30.25	4.75	0.11	-0.13	-0.12	0.93	-0.85	156.25	-129.25	0.83	4.88
4H-1, 125	24.85	30.82	4.85	0.05	-0.65	-0.42	0.65	-0.08	57.65	-43.38	0.74	1.96
4H-2, 50	25.60	31.38	4.96	0.12	-0.08	-0.14		-1.50	183.73	-151.26	0.82	5.89
4H-2, 125	26.35	31.95	5.06	4.01	1.31	1.22	0.93	3.06	4552.44	-4265.61	0.91	49.20
4H-3, 50	27.10	32.58	5.18	0.11	-0.09	-0.09	1.00	-1.22	244.51	-181.09	0.74	11.23
4H-3, 125	27.85	33.23	5.30	5.99	1.45	1.40	0.97	4.13	2496.23	-2312.26	0.89	42.75
4H-4, 50	28.60	33.88	5.42	0.09	0.05	0.00		1.80	197.96	-162.10	0.82	8.38
4H-4, 125	29.35	34.53	5.53	0.11	0.01	-0.02		11.00	241.65	-179.36	0.72	13.03
4H-5, 50	30.10	35.21	5.66	0.06	1.33	1.28	0.96	0.05	5004.97	-4840.52	0.97	38.20
4H-5, 125	30.85	35.99	5.79	8.71	2.65	2.55	0.96	3.29	4341.91	-4117.09	0.92	50.86
4H-6, 50	31.60	36.78	5.92	8.37	0.94	0.94	0.99	8.90	3932.85	-3823.59	0.97	23.75
4H-6, 125	32.35	37.57	6.02	7.35	2.00	1.83	0.92	3.68	2875.38	-2760.31	0.91	25.89
4H-7, 50	33.10	38.44	6.12	10.61	1.60	1.50	0.93	6.63	3955.20	-3799.69	0.96	37.39

Table 3. Continued.

Core, section, interval (cm)	Depth (mbsf)	Composite depth (m)	Age (Ma)	X_{arm} ($\mu m^3/g$)	X_{lf} ($\mu m^3/g$)	X_{HF} ($\mu m^3/g$)	X_{lf}/X_{hf}	X_{arm}/X	SIRM ($\mu A/m^2/g$)	IRM-0.3T ($\mu A/m^2/g$)	S-ratio	HIRM ($\mu A/m^2/g$)
5H-1, 50	33.60	39.40	6.23	21.14	3.95	3.68	0.93	5.35	7242.45	-6948.29	0.96	80.43
5H-1, 125	34.35	40.15	6.32	13.16	3.50	3.36	0.96	3.76	5710.37	-5404.26	0.90	76.13
5H-2, 50	35.10	40.99	6.44	8.21	0.85	0.70	0.83	9.66	2759.93	-2687.21	0.97	15.38
5H-2, 125	35.85	42.06	6.61	10.24	3.40	3.13	0.92	3.01	3959.29	-3712.31	0.90	60.35
5H-3, 50	36.60	43.23	6.79	15.80	3.13	2.87	0.92	5.05	5803.21	-5493.51	0.95	84.18
5H-3, 125	37.35	44.09	6.93	2.83	0.24	0.20	0.86	11.79	1026.12	-978.45	0.91	8.78
5H-4, 50	38.10	44.96	7.06	6.99	1.15	1.11	0.96	6.08	2935.40	-2834.67	0.97	20.92
5H-4, 125	38.85	45.82	7.20	7.35	2.13	1.96	0.92	3.45	2756.58	-2554.92	0.89	46.60
5H-5, 50	39.60	46.66	7.31	14.70	2.50	2.27	0.91	5.88	5134.13	-4889.39	0.95	56.85
5H-5, 125	40.35	47.49	7.42	14.49	6.45	5.95	0.92	2.25	6258.31	-5818.82	0.91	116.68
5H-6, 50	41.10	48.46	7.54	23.78	5.28	4.78	0.91	4.50	7885.38	-7486.78	0.95	103.83
5H-6, 125	41.85	49.48	7.67	14.86	6.06	5.60	0.92	2.45	5847.84	-5445.19	0.89	98.13
5H-7, 50	42.60	50.32	7.77	21.01	4.94	4.54	0.92	4.25	7309.48	-6894.98	0.94	107.38
6H-1, 50	43.10	50.84	7.84	14.93	3.36	3.07	0.91	4.44	5903.40	-5561.75	0.94	82.09
6H-1, 125	43.85	51.52	8.26	15.01	8.67	7.96	0.92	1.73	6564.84	-6108.52	0.89	121.04
6H-2, 50	44.60	52.61	9.74	27.25	16.74	15.67	0.94	1.63	36453.07	-32616.16	0.89	1020.26
6H-2, 125	45.35	53.30	10.67	27.53	11.94	10.81	0.91	2.31	8779.16	-8680.96	0.92	24.87
6H-3, 50	46.10	53.94	11.54	26.98	7.69	7.05	0.92	3.51	11360.63	-10914.93	0.96	95.92
6H-3, 125	46.85	54.58	12.41	27.13	17.88	16.24	0.91	1.52	8482.88	-8258.80	0.92	80.17
6H-4, 50	47.60	55.22	13.28	47.08	17.42	15.70	0.90	2.70	14663.52	-14295.08	0.97	133.31
6H-4, 125	48.35	56.68	15.26	37.98	28.36	25.65	0.90	1.34	11938.51	-11937.87	0.92	0.24
6H-5, 50	49.10	59.68	19.31	84.97	38.89	35.87	0.92	2.18	40982.34	-40176.91	0.98	204.72
6H-5, 125	49.85	64.22	25.47	54.57	41.99	38.80	0.92	1.30	23838.75	-23549.26	0.92	79.17
6H-6, 50	50.60	69.03	31.99	52.74	27.11	24.88	0.92	1.95	19382.38	-18731.67	0.97	192.50
6H-6, 125	51.35	69.96	33.25	18.32	26.06	24.39	0.94	0.70	8056.40	-7749.45	0.96	81.49
6H-7, 37	51.85	70.45	33.91	23.27	17.14	15.82	0.92	1.36	9258.05	-9114.78	0.98	33.78

Table 3. Continued.

Core, section, interval (cm)	Depth (mbsf)	Composite depth (m)	Age (Ma)	X_{arm} ($\mu m^3/g$)	X_{lf} ($\mu m^3/g$)	X_{HF} ($\mu m^3/g$)	X_{lf}/X_{hf}	X_{arm}/X	SIRM ($\mu A/m^2/g$)	IRM-0.3T ($\mu A/m^2/g$)	S-ratio	HIRM ($\mu A/m^2/g$)
145-886B												
1H-1, 50	0.50	0.77	0.12	9.35	10.37	9.93	0.96	0.90	17185.43	-15996.30	0.93	365.44
1H-2, 11	1.31	2.76	0.44	10.16	11.26	10.72	0.95	0.90	17444.17	-16151.21	0.93	409.86
2H-1, 50	2.30	4.71	0.75	14.10	10.73	10.14	0.95	1.31	17927.93	-16830.07	0.94	316.78
2H-1, 125	3.05	4.73	0.76	12.69	23.31	22.03	0.95	0.54	18983.51	-16927.93	0.89	703.91
2H-2, 50	3.80	4.76	0.76	10.61	9.94	9.46	0.95	1.07	14056.10	-12852.04	0.91	389.63
2H-2, 125	4.55	4.79	0.77	9.43	12.77	12.23	0.96	0.74	9530.20	-8647.33	0.91	309.59
2H-3, 50	5.30	4.82	0.77	12.41	9.12	8.63	0.95	1.36	14578.18	-13371.56	0.92	340.10
2H-3, 125	6.05	4.85	0.77	11.13	17.29	16.65	0.96	0.64	12194.59	-10986.74	0.90	427.40
2H-4, 50	6.80	4.87	0.78	16.98	22.33	21.32	0.95	0.76				
2H-4, 125	7.55	4.90	0.78	14.26	34.00	32.66	0.96	0.42	35309.86	-32072.44	0.91	957.76
2H-5, 50	8.30	4.93	0.79	12.44	12.85	12.33	0.96	0.97	18910.29	-17644.32	0.93	366.28
2H-5, 125	9.05	4.96	0.80	11.12	31.28	30.39	0.97	0.36	21191.52	-19599.23	0.92	602.74
2H-6, 50	9.80	4.98	0.80	12.56	8.79	8.29	0.94	1.43	16163.62	-14944.65	0.92	338.88
2H-6, 125	10.55	5.28	0.86	9.15	14.31	13.71	0.96	0.64	13160.71	-11398.96	0.87	551.41
2H-7, 45	11.25	7.49	1.33	12.75	9.24	8.63	0.93	1.38	16088.10	-14904.64	0.93	323.02
3H-1, 50	11.80	9.11	1.68	17.26	15.91	14.97	0.94	1.08	29031.97	-26521.77	0.91	690.77
3H-1, 125	12.55	9.83	1.83	11.33	13.99	13.32	0.95	0.81	16430.93	-14653.08	0.89	425.22
3H-2, 50	13.30	10.60	1.99	15.60	8.73	8.16	0.93	1.79	13796.14	-12691.30	0.92	320.15
3H-2, 125	14.05	11.56	2.14	11.32	9.56	8.99	0.94	1.18	8953.88	-8229.79	0.92	198.31
3H-3, 50	14.80	12.61	2.30	17.43	9.43	8.87	0.94	1.85	14687.23	-13732.89	0.94	304.93
3H-3, 125	15.55	13.67	2.46	15.80	10.86	10.34	0.95	1.45	10376.44	-9819.99	0.95	155.64
3H-4, 50	16.30	14.65	2.61	12.82	2.85	2.68	0.94	4.50	6286.19	-5977.47	0.95	71.35
3H-4, 125	17.05	15.40	2.69	14.45	8.65	8.14	0.94	1.67	7834.02	-7264.36	0.93	160.45
3H-5, 50	17.80	16.15	2.76	17.35	4.59	4.25	0.93	3.78	10103.46	-9426.28	0.93	158.27
3H-5, 125	18.55	16.90	2.84	13.74	13.93	13.33	0.96	0.99	18838.13	-17645.96	0.94	277.75

Table 3. Continued.

Core, section, interval (cm)	Depth (mbsf)	Composite depth (m)	Age (Ma)	X_{arm} ($\mu m^3/g$)	X_{lf} ($\mu m^3/g$)	X_{HF} ($\mu m^3/g$)	X_{lf}/X_{hf}	X_{arm}/X	SIRM ($\mu A/m^2/g$)	IRM-0.3T ($\mu A/m^2/g$)	S-ratio	HIRM ($\mu A/m^2/g$)
3H-6, 50	19.30	17.71	2.93	15.83	3.19	2.94	0.92	4.96	6085.17	-5831.82	0.96	64.42
3H-6, 125	20.05	18.75	3.03	11.64	5.09	4.81	0.94	2.29	5585.70	-5048.87	0.90	129.74
4H-1, 50	21.30	20.47	3.21	16.96	5.62	5.32	0.95	3.02	10604.85	-10294.70	0.97	80.19
4H-1, 125	22.05	21.51	3.32	11.68	2.80	2.58	0.92	4.17	4271.97	-4224.29	0.99	9.79
4H-2, 50	22.80	22.55	3.43	8.68	0.89	0.80	0.89	9.75	3189.68	-3120.39	0.98	12.69
4H-2, 125	23.55	23.66	3.54	10.28	2.36	2.18	0.92	4.36	4384.55	-4196.38	0.96	38.31
4H-3, 50	24.30	24.59	3.71	11.15	1.18	1.15	0.98	9.45	4056.34	-3926.32	0.97	25.75
4H-3, 125	25.05	25.50	3.87	7.70	3.28	3.13	0.95	2.35	7027.44	-6476.59	0.92	97.95
4H-4, 50	25.80	26.17	4.00	7.11	1.24	1.10	0.89	5.73	4612.98	-4508.74	0.98	20.32
4H-4, 125	26.55	26.85	4.12	6.96	0.68	0.59	0.87	10.24	2623.39	-2567.60	0.98	9.66
4H-5, 50	27.30	27.52	4.25	0.20	-0.12	-0.12	1.01	-1.67	256.05	-224.98	0.88	6.16
4H-5, 125	28.05	28.19	4.37	4.04	0.08	0.09	1.15	50.50	1498.50	-1431.61	0.96	11.33
4H-6, 50	28.80	28.87	4.49	0.07	-0.22	-0.27	1.23	-0.32	91.12	-72.59	0.80	3.22
5H-1, 50	30.80	30.66	4.82	6.58	2.69	2.57	0.95	2.45	11340.34	-10902.72	0.96	83.55
5H-1, 125	31.55	31.34	4.95	0.08	-0.29	-0.31	1.05	-0.28	129.30	-94.73	0.73	5.25
5H-2, 50	32.30	32.01	5.07	0.15	0.33	0.28	0.83	0.45	487.65	-401.00	0.82	21.22
5H-2, 125	33.05	32.75	5.21	0.08	0.00	-0.03	0.00		176.52	-125.29	0.71	9.77
5H-3, 50	33.80	33.50	5.34	8.32	3.98	3.82	0.96	2.09	13243.68	-12814.12	0.97	84.70
5H-3, 125	34.55	34.25	5.48	0.09	0.03	0.07	2.01	3.00	265.94	-202.86	0.76	15.89
5H-4, 50	35.30	35.00	5.62	6.65	0.84	0.79	0.94	7.92	3477.03	-3304.73	0.95	36.75
5H-4, 125	36.05	35.75	5.75	5.83	0.95	0.94	0.99	6.14	3552.57	-3381.03	0.95	33.45
5H-5, 50	36.80	36.50	5.87	9.61	2.86	2.67	0.93	3.36	6917.48	-6598.62	0.95	67.57
5H-5, 125	37.55	37.25	5.98	6.92	2.43	2.24	0.92	2.85	3034.91	-2854.74	0.94	45.93
5H-6, 50	38.30	38.00	6.07	10.54	3.05	2.95	0.97	3.46	8000.02	-7544.79	0.94	134.10
5H-6, 125	39.05	38.75	6.16	5.44	1.56	1.53	0.98	3.49	3406.59	-3234.32	0.95	48.48
5H-7, 50	39.80	39.56	6.25	14.63	2.64	2.39	0.91	5.54	5134.38	-4920.78	0.96	53.69

Table 3. Continued.

Core, section, interval (cm)	Depth (mbsf)	Composite depth (m)	Age (Ma)	X_{arm} ($\mu m^3/g$)	X_{lf} ($\mu m^3/g$)	X_{HF} ($\mu m^3/g$)	X_{lf}/X_{hf}	X_{arm}/X	SIRM ($\mu A/m^2/g$)	IRM-0.3T ($\mu A/m^2/g$)	S-ratio	HIRM ($\mu A/m^2/g$)
6H-1, 50	40.30	40.39	6.35	10.78	1.88	1.72	0.91	5.73	4030.02	-3825.57	0.95	49.61
6H-1, 125	41.05	41.20	6.47	6.94	1.32	1.20	0.91	5.26	2482.49	-2368.66	0.95	23.76
6H-2, 50	41.80	41.95	6.59	3.30	0.43	0.39	0.90	7.67	1429.96	-1406.73	0.98	5.07
6H-2, 125	42.55	42.70	6.71	8.10	2.00	1.87	0.93	4.05	2946.94	-2813.81	0.95	30.23
6H-3, 50	43.30	43.45	6.82	5.47	0.58	0.53	0.91	9.43	2355.29	-2242.49	0.95	22.90
6H-3, 125	44.05	44.20	6.94	3.27	0.15	0.10	0.70	21.80	1121.57	-1147.82	1.02	-3.94
6H-4, 50	44.80	44.95	7.06	11.00	1.85	1.72	0.93	5.95	4050.49	-3859.19	0.95	45.85
6H-4, 125	45.55	45.70	7.18	6.95	1.71	1.56	0.92	4.06	2528.16	-2382.24	0.94	34.45
6H-5, 50	46.30	46.45	7.29	22.24	5.24	4.84	0.92	4.24	7610.02	-7285.45	0.96	89.77
6H-5, 125	47.05	47.20	7.38	14.85	6.34	5.87	0.93	2.34	5929.67	-5548.89	0.94	109.11
6H-6, 52	47.82	48.12	7.50	15.92	4.06	3.72	0.92	3.92	6217.09	-5826.15	0.94	103.28
6H-6, 125	48.55	49.19	7.63	15.74	8.48	8.01	0.94	1.86	8553.62	-8049.89	0.94	138.80
6H-7, 50	49.30	50.28	7.77	12.70	2.46	2.29	0.93	5.16	4781.84	-4597.94	0.96	38.92
7H-1, 47	49.77	50.97	7.86	29.39	8.58	8.05	0.94	3.43	10269.02	-9895.73	0.96	99.26
7H-1, 125	50.55	52.11	9.06	20.91	9.36	8.60	0.92	2.23	7612.39	-7277.04	0.96	88.16
7H-2, 47	51.27	53.02	10.29	31.59	11.87	10.83	0.91	2.66	10230.93	-9924.38	0.97	111.66
7H-2, 125	52.05	53.80	11.35	28.92	13.24	12.21	0.92	2.18	9553.70	-9177.02	0.96	100.12
7H-3, 47	52.77	54.52	12.32	47.93	21.45	19.57	0.91	2.23	16079.16	-15695.98	0.98	150.50
7H-3, 125	53.55	55.30	13.38	36.20	24.57	22.56	0.92	1.47	12257.41	-11916.47	0.97	123.74
7H-4, 47	54.27	55.55	13.72	62.44	20.90	18.95	0.91	2.99	19881.76	-19313.51	0.97	189.67
7H-4, 125	55.05	56.33	14.77	48.78	35.41	32.42	0.92	1.38	17306.08	-16839.75	0.97	168.86
7H-5, 47	55.77	57.20	15.95	71.37	36.79	33.98	0.92	1.94	30391.77	-29341.97	0.97	329.42
7H-5, 125	56.55	58.14	17.23	55.03	50.35	46.72	0.93	1.09	23183.52	-22028.97	0.95	400.63
7H-6, 47	57.27	58.79	18.11	105.39	62.71	58.37	0.93	1.68				
7H-6, 130	58.10	59.55	19.14	65.62	84.80	79.70	0.94	0.77				
7H-7, 47	58.77	60.22	20.05	38.72	35.86	32.75	0.91	1.08	15423.40	-15155.70	0.98	82.57

Table 4. Normalized mineral peak areas for the <2 µm fraction of Holes 885A and 886B.

Core, section, interval (cm)	Depth (mbsf)	Composite depth (m)	Age (Ma)	Smectite peak area	Illite peak area	Kaolinite peak area	Chlorite peak area	Quartz peak area	Plagioclase peak area
145-885A									
1H-1, 25	0.25	0.30	0.05	0.11	0.37	0.08	0.19	0.51	0.15
1H-1, 125	1.25	1.65	0.26	0.16	0.72	0.00	0.47	0.98	0.23
1H-2, 25	1.75	2.34	0.37	0.30	0.50	0.24	0.09	0.76	0.04
1H-2, 125	2.75	3.89	0.62	0.22	0.44	0.12	0.18	0.68	0.19
1H-3, 25	3.25	4.34	0.69	0.08	0.55	0.09	0.21	1.01	0.28
1H-3, 125	4.25	5.16	0.85	0.04	0.78	0.16	0.48	1.76	0.22
2H-1, 25	4.85	5.63	0.96	0.07	0.67	0.00	0.40	0.97	0.05
2H-1, 125	5.85	6.72	1.11	0.03	0.45	0.02	0.14	0.61	0.17
2H-2, 25	6.35	7.24	1.27	0.18	0.76	0.07	0.14	0.89	0.12
2H-2, 125	7.35	8.19	1.48	0.20	0.38	0.07	0.11	0.44	0.10
2H-3, 25	7.85	8.63	1.57	0.00	0.30	0.11	0.07	0.58	0.14
2H-3, 125	8.85	9.61	1.78	0.09	0.41	0.04	0.25	0.78	0.20
2H-4, 125	10.35	12.12	2.23	0.02	0.44	0.03	0.15	0.48	0.10
2H-5, 125	11.85	14.55	2.60	0.06	0.57	0.09	0.13	0.53	0.11
2H-6, 125	13.35	17.06	2.86	0.00	0.44	0.06	0.06	0.80	0.17
3H-1, 125	15.35	21.35	3.30	0.17	0.35	0.17	0.03	0.71	0.13
3H-2, 125	16.85	23.55	3.53	0.09	0.43	0.05	0.14	0.50	0.05
3H-3, 125	18.35	25.05	3.77	0.20	0.43	0.09	0.08	0.27	0.13
3H-4, 125	19.85	26.55	4.02	0.15	0.41	0.08	0.09	0.39	0.01
3H-5, 125	21.35	28.05	4.26	0.22	0.48	0.18	0.10	0.56	0.09
3H-6, 125	22.85	29.31	4.47	0.00	0.28	0.05	0.18	0.32	0.07
4H-1, 125	24.85	30.82	4.72	0.00	0.64	0.09	0.29	0.38	0.04
4H-2, 125	26.35	31.95	4.91	0.15	0.34	0.19	0.03	0.36	0.07
4H-3, 125	27.85	33.23	5.12	0.37	0.57	0.10	0.17	0.56	0.11

Table 4. Continued.

Core, section, interval (cm)	Depth (mbsf)	Composite depth (m)	Age (Ma)	Smectite peak area	Illite peak area	Kaolinite peak area	Chlorite peak area	Quartz peak area	Plagioclase peak area
4H-4, 125	29.35	34.53	5.33	0.43	0.71	0.25	0.17	0.64	0.10
4H-5, 125	30.85	35.99	5.57	0.14	0.41	0.08	0.15	0.49	0.09
4H-6, 125	32.35	37.57	5.83	0.17	0.36	0.08	0.11	0.29	0.03
5H-1, 125	34.35	40.15	6.26	0.14	0.47	0.00	0.25	0.74	0.08
5H-2, 125	35.85	42.06	6.58	0.19	0.35	0.00	0.19	0.43	0.06
5H-3, 125	37.35	44.09	6.91	0.03	0.54	0.12	0.21	0.41	0.06
5H-4, 125	38.85	45.82	7.20	0.16	0.39	0.06	0.11	0.37	0.04
5H-5, 125	40.35	47.49	7.42	0.20	0.44	0.09	0.09	0.48	0.13
5H-6, 125	41.85	49.48	7.67	0.14	0.38	0.13	0.09	0.33	0.19
6H-1, 125	43.85	51.52	8.26	0.16	0.35	0.11	0.09	0.39	0.09
6H-2, 125	45.35	53.30	10.67	0.04	0.28	0.06	0.03	0.29	0.06
6H-3, 125	46.85	54.58	12.41	0.00	0.46	0.02	0.06	0.36	0.04
6H-4, 125	48.35	56.68	15.26	0.00	0.23	0.02	0.02	0.34	0.05
6H-5, 125	49.85	64.22	25.47	0.65	0.14	0.02	0.01	0.18	0.02
6H-6, 125	51.35	69.96	33.25	0.00	1.61	0.14	0.00	1.10	0.00
145-886B									
1H-1, 50	0.50	0.77	0.14	0.00	4.35	0.00	4.26	16.43	2.90
1H-2, 11	1.31	2.76	0.49	0.24	3.76	0.00	4.07	12.40	2.64
2H-1, 50	2.30	4.71	0.84	0.40	3.19	0.00	2.86	17.29	3.05
2H-2, 50	3.80	4.76	0.85	0.40	6.33	0.00	4.41	16.71	3.21
2H-3, 50	5.30	4.82	0.86	0.52	4.54	0.00	3.32	17.24	2.39
2H-4, 50	6.80	4.87	0.87	0.00	2.75	0.00	1.97	11.26	1.82
2H-5, 50	8.30	4.93	0.88	0.72	5.37	0.00	3.66	16.52	3.31
2H-6, 50	9.80	4.98	0.89	0.79	4.50	0.00	4.58	16.73	2.71
2H-7, 45	11.25	7.49	1.34	0.11	2.37	0.00	2.15	10.69	2.17

Table 4. Continued.

Core, section, interval (cm)	Depth (mbsf)	Composite depth (m)	Age (Ma)	Smectite peak area	Illite peak area	Kaolinite peak area	Chlorite peak area	Quartz peak area	Plagioclase peak area
3H-1, 50	11.80	9.11	1.63	1.70	6.95	0.00	5.41	25.88	5.16
3H-2, 50	13.30	10.60	1.89	0.00	2.68	0.00	1.37	9.87	3.76
3H-3, 50	14.80	12.61	2.25	0.09	4.57	0.00	2.09	12.85	2.61
3H-4, 50	16.30	14.65	2.61	0.29	4.97	0.00	2.60	18.48	2.10
3H-5, 50	17.80	16.15	2.76	0.00	3.79	0.00	2.60	11.45	2.19
3H-6, 50	19.30	17.71	2.93	0.00	3.72	0.30	2.42	11.72	2.40
4H-1, 50	21.30	20.47	3.21	0.70	5.31	0.49	2.37	13.19	2.11
4H-2, 50	22.80	22.55	3.43	0.01	3.30	0.00	1.64	13.82	2.33
4H-3, 50	24.30	24.59	3.69	1.06	5.96	0.77	2.34	14.59	1.87
4H-4, 50	25.80	26.17	3.95	0.00	4.61	0.71	2.21	10.77	2.22
4H-5, 50	27.30	27.52	4.18	1.79	10.99	1.95	5.70	16.84	3.07
4H-6, 50	28.80	28.87	4.40	0.00	4.81	0.00	4.07	9.92	1.76
5H-1, 50	30.80	30.66	4.69	0.20	4.70	0.10	2.54	9.84	2.13
5H-2, 50	32.30	32.01	4.92	1.54	3.77	0.00	1.89	8.97	4.57
5H-3, 50	33.80	33.50	5.16	0.18	3.18	0.00	2.09	13.50	2.49
5H-4, 50	35.30	35.00	5.41	1.56	5.26	0.00	4.48	16.17	3.23
5H-5, 50	36.80	36.50	5.66	0.70	6.82	1.30	2.13	13.91	2.25
5H-6, 50	38.30	38.00	5.91	0.00	3.56	0.00	1.87	9.95	2.26
5H-7, 50	39.80	39.56	6.16	0.74	6.68	1.21	2.63	18.63	2.67
6H-1, 50	40.30	40.39	6.30	0.02	5.01	1.21	1.63	13.33	2.25
6H-2, 50	41.80	41.95	6.56	0.00	3.32	0.00	2.49	12.47	2.19
6H-3, 50	43.30	43.45	6.81	0.08	4.21	0.00	3.25	13.77	2.10
6H-4, 50	44.80	44.95	7.05	0.00	3.40	0.32	2.04	13.36	2.43
6H-5, 50	46.30	46.45	7.30	0.24	4.82	0.44	1.65	14.80	1.92
6H-6, 52	47.82	48.12	7.58	0.00	2.60	0.71	0.81	11.48	1.25

Table 4. Continued.

Core, section, interval (cm)	Depth (mbsf)	Composite depth (m)	Age (Ma)	Smectite peak area	Illite peak area	Kaolinite peak area	Chlorite peak area	Quartz peak area	Plagioclase peak area
6H-7, 50	49.30	50.28	7.93	0.00	4.74	0.77	1.31	15.66	2.21
7H-1, 47	49.77	50.97	8.05	0.00	1.65	0.25	0.70	9.89	1.29
7H-2, 47	51.27	53.02	8.39	0.00	2.49	0.56	0.39	11.63	1.61
7H-3, 47	52.77	54.52	8.63	0.00	0.88	0.00	0.00	7.61	3.20
7H-4, 47	54.27	55.55	8.80	0.11	1.53	0.00	0.00	10.39	1.83
7H-5, 47	55.77	57.20	9.08	0.53	2.78	0.00	0.00	13.35	2.26
7H-6, 47	57.27	58.79	9.34	0.04	0.88	0.00	4.04	7.61	3.20
7H-7, 47	58.77	60.22	9.57	1.83	0.95	0.00	0.00	7.66	2.78
8X-1, 50	59.30	60.75	9.66	0.00	0.82	0.00	0.00	1.43	0.24

Note: peak area = peak area normalized to internal standard.

Table 5. Normalized mineral peak areas for the 2-20 μm fraction of Holes 885A and 886B.

Core, section, interval (cm)	Depth (mbsf)	Composite depth (m)	Age (Ma)	Smectite peak area	Illite peak area	Kaolinite peak area	Chlorite peak area	Quartz peak area	Plagioclase peak area
145-885A									
1H-1, 25	0.25	0.30	0.05	0.35	2.12	0.00	1.58	15.50	0.60
1H-1, 125	1.25	1.65	0.26	0.52	2.98	0.00	2.26	23.35	3.57
1H-2, 25	1.75	2.34	0.37	0.54	3.21	0.00	1.34	17.03	2.95
1H-2, 125	2.75	3.89	0.62	0.09	1.44	0.00	0.74	7.79	1.46
1H-3, 25	3.25	4.34	0.69	0.28	1.49	0.00	1.31	11.06	2.06
1H-3, 125	4.25	5.16	0.85	0.00	2.45	0.00	1.82	15.41	2.88
2H-1, 25	4.85	5.63	0.96	0.10	3.14	0.00	1.65	16.49	2.95
2H-1, 125	5.85	6.72	1.11	0.00	2.27	0.00	1.38	12.01	2.73
2H-2, 25	6.35	7.24	1.27	0.00	2.71	0.00	1.30	13.11	2.26
2H-2, 125	7.35	8.19	1.48	0.00	1.89	0.00	0.99	11.13	2.10
2H-3, 25	7.85	8.63	1.57	0.32	2.00	0.00	0.00	9.63	3.01
2H-3, 125	8.85	9.61	1.78	0.00	2.75	0.00	1.13	13.36	2.46
2H-4, 125	10.35	12.12	2.23	0.26	3.04	0.00	1.39	18.31	2.56
2H-5, 125	11.85	14.55	2.60	0.00	2.10	0.00	0.84	13.29	2.24
2H-6, 125	13.35	17.06	2.86	0.00	1.46	0.00	0.00	8.54	3.59
3H-1, 125	15.35	21.35	3.30	1.44	2.79	0.00	1.69	12.88	2.47
3H-2, 125	16.85	23.55	3.53	0.46	3.13	0.00	1.54	9.98	1.69
3H-3, 125	18.35	25.05	3.77	1.57	9.53	0.00	4.00	15.46	5.71
3H-4, 125	19.85	26.55	4.02	1.96	11.59	1.04	5.45	17.12	3.45
3H-5, 125	21.35	28.05	4.26	1.43	6.40	1.14	3.20	14.36	2.34
3H-6, 125	22.85	29.31	4.47	1.69	5.65	0.00	3.61	8.97	1.86
4H-1, 125	24.85	30.82	4.72	4.54	22.16	2.30	11.66	14.14	2.84
4H-2, 125	26.35	31.95	4.91	3.13	9.26	0.00	7.14	19.03	4.16
4H-3, 125	27.85	33.23	5.12	1.14	3.70	0.32	2.05	20.86	2.11

Table 5. Continued.

Core, section, interval (cm)	Depth (mbsf)	Composite depth (m)	Age (Ma)	Smectite peak area	Illite peak area	Kaolinite peak area	Chlorite peak area	Quartz peak area	Plagioclase peak area
4H-4, 125	29.35	34.53	5.33	0.68	7.23	0.45	3.46	25.46	3.25
4H-5, 125	30.85	35.99	5.57	0.93	2.84	0.00	1.15	11.57	1.94
4H-6, 125	32.35	37.57	5.83	0.74	4.14	0.26	2.00	13.18	1.88
5H-1, 125	34.35	40.15	6.26	0.29	2.90	0.00	1.91	12.98	1.97
5H-2, 125	35.85	42.06	6.58	0.03	4.05	0.00	2.26	15.30	3.04
5H-3, 125	37.35	44.09	6.91	1.10	6.48	1.06	3.58	12.86	1.66
5H-4, 125	38.85	45.82	7.20	0.00	3.32	0.51	1.43	13.77	1.85
5H-5, 125	40.35	47.49	7.42	0.00	3.18	0.00	1.40	15.35	2.48
5H-6, 125	41.85	49.48	7.67	0.08	2.80	0.00	1.36	10.17	1.51
6H-1, 125	43.85	51.52	8.26	0.00	2.60	0.51	0.78	11.94	2.02
6H-2, 125	45.35	53.30	10.67	0.52	2.61	0.28	0.50	12.65	2.06
6H-3, 125	46.85	54.58	12.41	0.00	2.78	0.34	0.00	10.76	2.04
6H-4, 125	48.35	56.68	15.26	0.64	3.13	0.00	0.00	14.13	2.71
6H-5, 125	49.85	64.22	25.47	1.38	2.46	0.00	0.34	13.11	0.81
6H-6, 125	51.35	69.96	33.25	0.00	2.49	0.38	0.00	1.35	0.25
145-886B									
1H-1, 50	0.50	0.77	0.14	0.00	4.35	0.00	4.26	16.43	2.90
1H-2, 11	1.31	2.76	0.49	0.24	3.76	0.00	4.07	12.40	2.64
2H-1, 50	2.30	4.71	0.84	0.40	3.19	0.00	2.86	17.29	3.05
2H-2, 50	3.80	4.76	0.85	0.40	6.33	0.00	4.41	16.71	3.21
2H-3, 50	5.30	4.82	0.86	0.52	4.54	0.00	3.32	17.24	2.39
2H-4, 50	6.80	4.87	0.87	0.00	2.75	0.00	1.97	11.26	1.82
2H-5, 50	8.30	4.93	0.88	0.72	5.37	0.00	3.66	16.52	3.31
2H-6, 50	9.80	4.98	0.89	0.79	4.50	0.00	4.58	16.73	2.71
2H-7, 45	11.25	7.49	1.34	0.11	2.37	0.00	2.15	10.69	2.17

Table 5. Continued.

Core, section, interval (cm)	Depth (mbsf)	Composite depth (m)	Age (Ma)	Smectite peak area	Illite peak area	Kaolinite peak area	Chlorite peak area	Quartz peak area	Plagioclase peak area
3H-1, 50	11.80	9.11	1.63	1.70	6.95	0.00	5.41	25.88	5.16
3H-2, 50	13.30	10.60	1.89	0.00	2.68	0.00	1.37	9.87	3.76
3H-3, 50	14.80	12.61	2.25	0.09	4.57	0.00	2.09	12.85	2.61
3H-4, 50	16.30	14.65	2.61	0.29	4.97	0.00	2.60	18.48	2.10
3H-5, 50	17.80	16.15	2.76	0.00	3.79	0.00	2.60	11.45	2.19
3H-6, 50	19.30	17.71	2.93	0.00	3.72	0.30	2.42	11.72	2.40
4H-1, 50	21.30	20.47	3.21	0.70	5.31	0.49	2.37	13.19	2.11
4H-2, 50	22.80	22.55	3.43	0.01	3.30	0.00	1.64	13.82	2.33
4H-3, 50	24.30	24.59	3.69	1.06	5.96	0.77	2.34	14.59	1.87
4H-4, 50	25.80	26.17	3.95	0.00	4.61	0.71	2.21	10.77	2.22
4H-5, 50	27.30	27.52	4.18	1.79	10.99	1.95	5.70	16.84	3.07
4H-6, 50	28.80	28.87	4.40	0.00	4.81	0.00	4.07	9.92	1.76
5H-1, 50	30.80	30.66	4.69	0.20	4.70	0.10	2.54	9.84	2.13
5H-2, 50	32.30	32.01	4.92	1.54	3.77	0.00	1.89	8.97	4.57
5H-3, 50	33.80	33.50	5.16	0.18	3.18	0.00	2.09	13.50	2.49
5H-4, 50	35.30	35.00	5.41	1.56	5.26	0.00	4.48	16.17	3.23
5H-5, 50	36.80	36.50	5.66	0.70	6.82	1.30	2.13	13.91	2.25
5H-6, 50	38.30	38.00	5.91	0.00	3.56	0.00	1.87	9.95	2.26
5H-7, 50	39.80	39.56	6.16	0.74	6.68	1.21	2.63	18.63	2.67
6H-1, 50	40.30	40.39	6.30	0.02	5.01	1.21	1.63	13.33	2.25
6H-2, 50	41.80	41.95	6.56	0.00	3.32	0.00	2.49	12.47	2.19
6H-3, 50	43.30	43.45	6.81	0.08	4.21	0.00	3.25	13.77	2.10
6H-4, 50	44.80	44.95	7.05	0.00	3.40	0.32	2.04	13.36	2.43
6H-5, 50	46.30	46.45	7.30	0.24	4.82	0.44	1.65	14.80	1.92
6H-6, 52	47.82	48.12	7.58	0.00	2.60	0.71	0.81	11.48	1.25

Table 5. Continued.

Core, section, interval (cm)	Depth (mbsf)	Composite depth (m)	Age (Ma)	Smectite peak area	Illite peak area	Kaolinite peak area	Chlorite peak area	Quartz peak area	Plagioclase peak area
6H-7, 50	49.30	50.28	7.93	0.00	4.74	0.77	1.31	15.66	2.21
7H-1, 47	49.77	50.97	8.05	0.00	1.65	0.25	0.70	9.89	1.29
7H-2, 47	51.27	53.02	8.39	0.00	2.49	0.56	0.39	11.63	1.61
7H-3, 47	52.77	54.52	8.63	0.00	0.88	0.00	0.00	7.61	3.20
7H-4, 47	54.27	55.55	8.80	0.11	1.53	0.00	0.00	10.39	1.83
7H-5, 47	55.77	57.20	9.08	0.53	2.78	0.00	0.00	13.35	2.26
7H-6, 47	57.27	58.79	9.34	0.04	0.88	0.00	4.04	7.61	3.20
7H-7, 47	58.77	60.22	9.57	1.83	0.95	0.00	0.00	7.66	2.78
8X-1, 50	59.30	60.75	9.66	0.00	0.82	0.00	0.00	1.43	0.24

Note: peak area = peak area normalized to internal standard.

Figure 1. Rock-magnetic parameters vs. composite depth for Holes 885A and 886B.

χ_{lf}
($10^{-6}m^3/g$)
0
100
A
(χ_{hf}/χ_{lf})
0.6
1.0
B
χ_{arm}
($10^{-6}m^3/g$)
0
100
C
χ_{arm}/χ_{lf}
0
32
D
S-ratio
0.6
1.0
E
HIRM
($10^{-6}A/m^2/g$)
0
100
Composite depth (m)
0
10
20
30
40
50
60
70
885A
886B
Unit I
Unit II
Unit III
Pleist.
Pliocene
Miocene

Figure 2. Mineral peak area for the <2 μm terrigenous size fraction vs. composite depth for Holes 885A and 886B.

Smectite (peak area)
Illite (peak area)
Kaolinite (peak area)
Chlorite (peak area)
Quartz (peak area)
Plagioclase (peak area)
Composite depth (m)
885A
886B
A
B
C
D
E
F
Unit I
Unit II
Unit III
Pleist.
Pliocene
Miocene

Figure 3. Mineral peak area for the 2-20 μm terrigenous size fraction vs. composite depth for Holes 885A and 886B.

Smectite
(peak area)
0
5.0
Illite
(peak area)
0
24
Kaolinite
(peak area)
0
3.0
Chlorite
(peak area)
0
12
Quartz
(peak area)
0
30
Plagioclase
(peak area)
0
6.0
Composite depth (m)
0
10
20
30
40
50
60
70
885A
886B
A
B
C
D
E
F
Unit I
Unit II
Unit III
Pleist.
Pliocene
Miocene

Figure 4. Peak area ratios for the <2 μm terrigenous size fraction vs. composite depth for Holes 885A and 886B.

Kaolinite/Illite
0
0.8
Smectite/Illite
0
5.0
Kaolinite/Quartz
0
1.0
Illite/Quartz
0
4
Chlorite/Quartz
0
1.6
Composite depth (m)
0
10
20
30
40
50
60
70
885A
886B
A
B
C
D
E
Unit I
Unit II
Unit III
Pleist.
Pliocene
Miocene

Figure 5. Peak area ratios for the 2-20 μm terrigenous size fraction vs. composite depth for Holes 885A and 886B.

Kaolinite/Illite
Smectite/Illite
Kaolinite/Quartz
Illite/Quartz
Chlorite/Quartz
0
0.4
2
0.2
1.6
1.0
885A
886B
Composite depth (m)
0
10
20
30
40
50
60
70
A
B
C
D
E
Unit I
Unit II
Unit III
Pleist.
Pliocene
Miocene

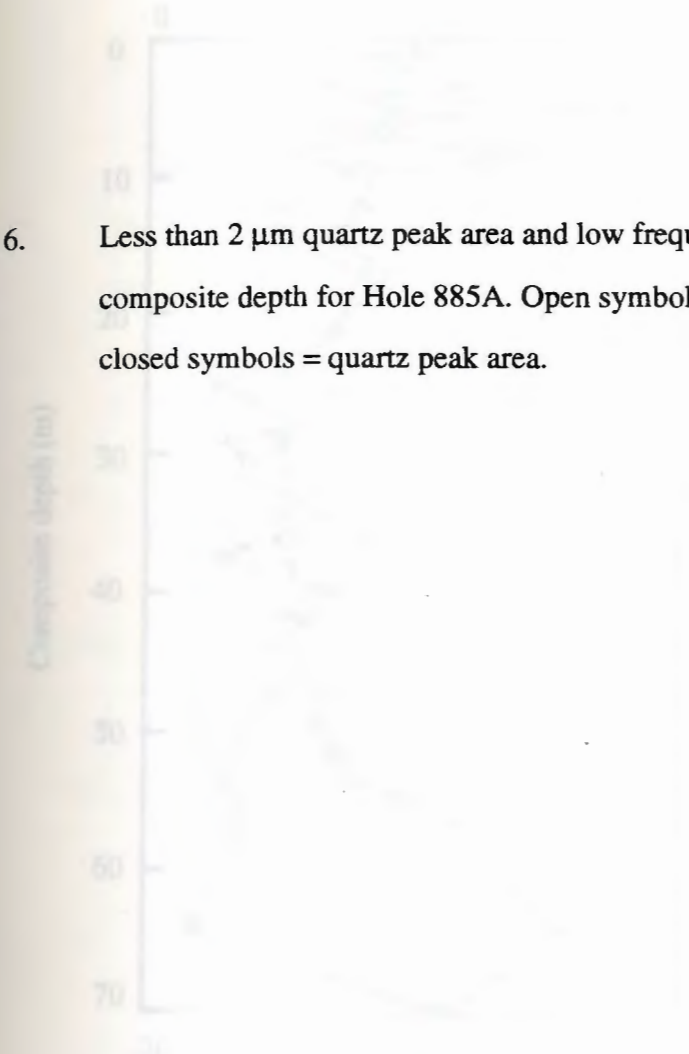

Figure 6. Less than 2 μm quartz peak area and low frequency susceptibility vs. composite depth for Hole 885A. Open symbols = susceptibility and closed symbols = quartz peak area.

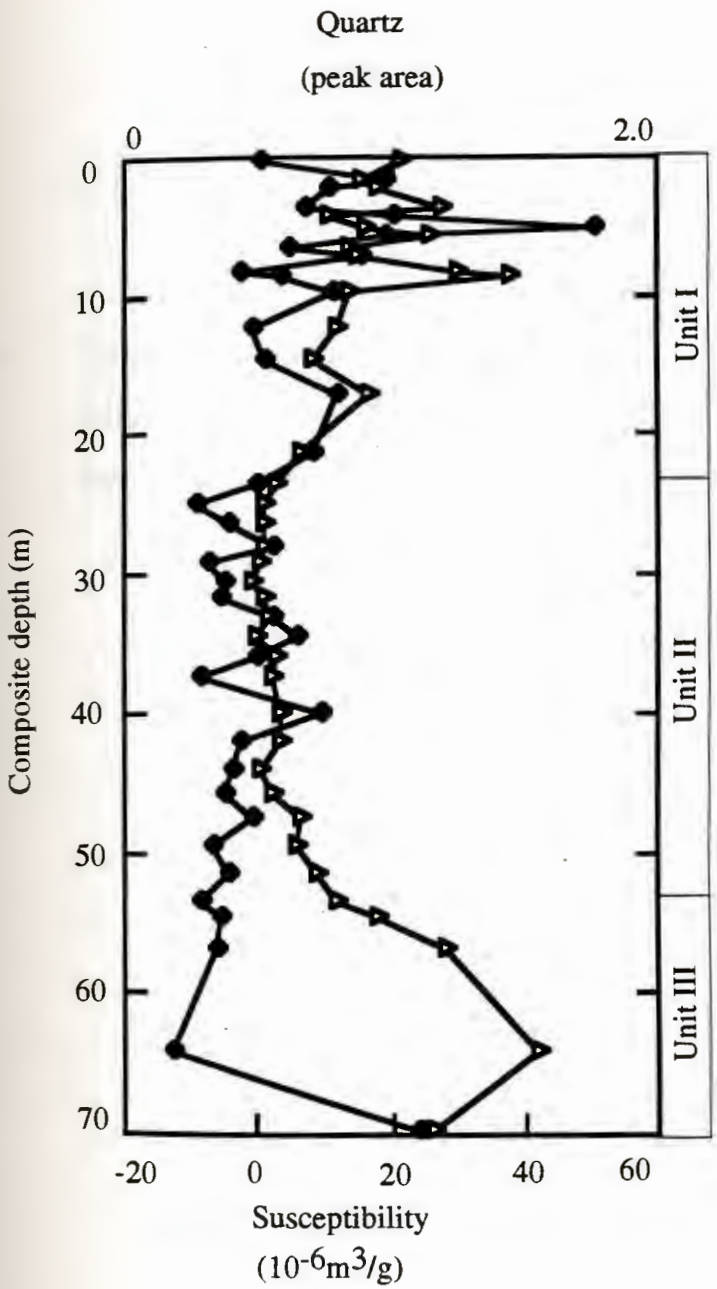
Quartz
(peak area)
0
2.0
0
10
20
30
40
50
60
70
Composite depth (m)
Unit I
Unit II
Unit III
-20
0
20
40
60
Susceptibility
(10-6m3/g)

Figure 7. The S-ratio and 2-20μm illite/quartz ratio vs. composite depth for Hole 885A. Open symbols = S-ratio and closed symbols = illite/quartz peak area.

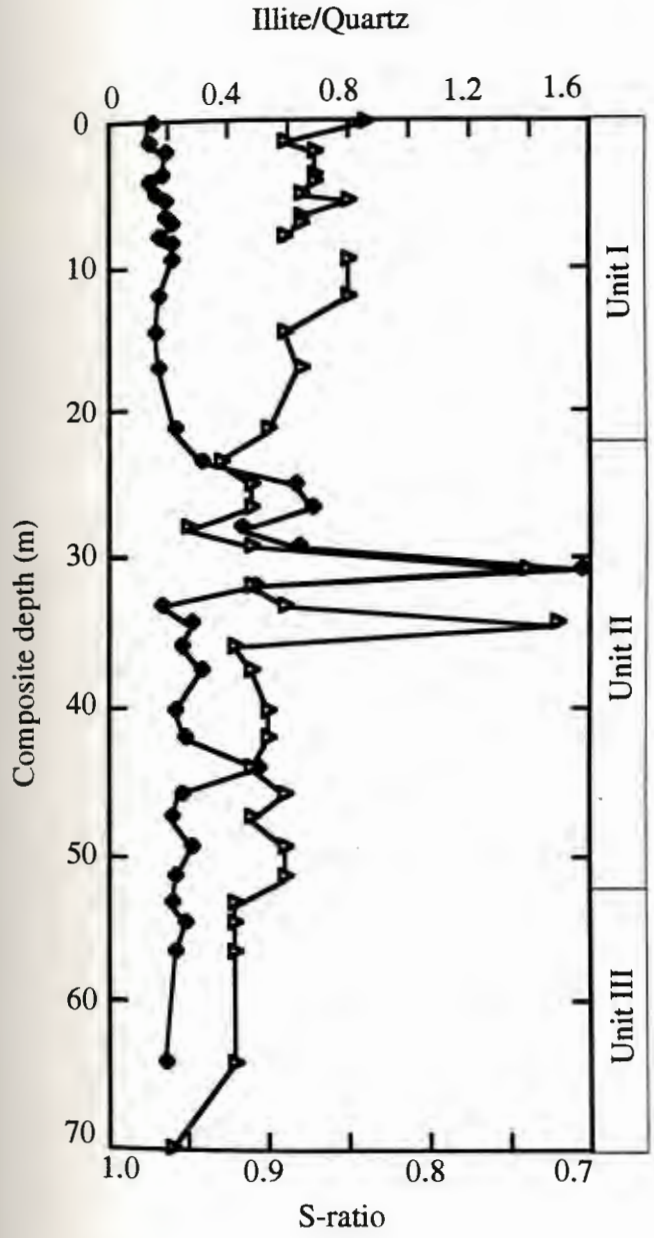
Illite/Quartz
0
0.4
0.8
1.2
1.6
Composite depth (m)
0
10
20
30
40
50
60
70
Unit I
Unit II
Unit III
1.0
0.9
0.8
0.7
S-ratio

Figure 8. Mass accumulation rates for different sedimentary components vs. age for Holes 885A and 886B.

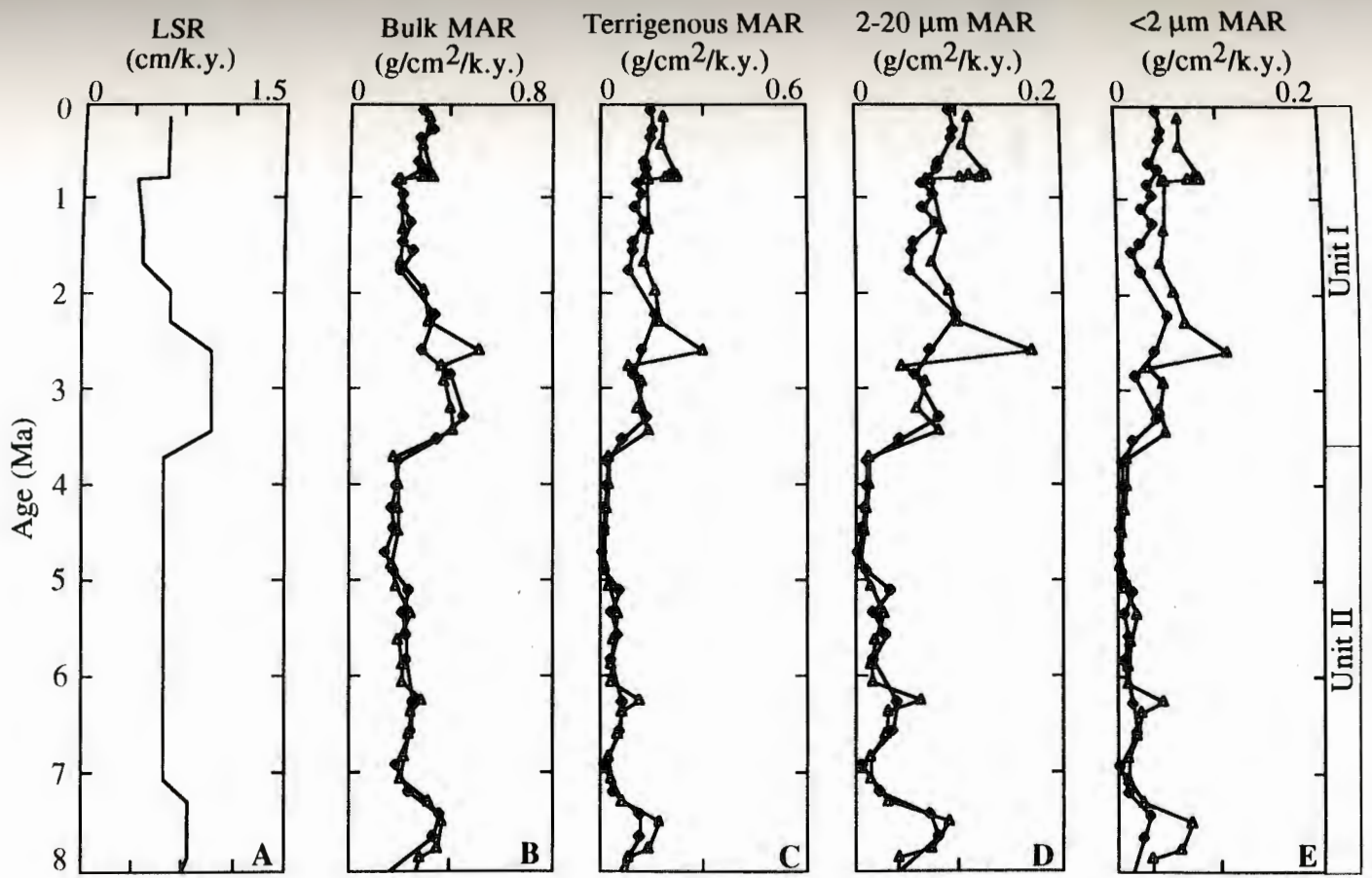
LSR
(cm/k.y.)
0
1.5
Bulk MAR
(g/cm2/k.y.)
0
0.8
Terrigenous MAR
(g/cm2/k.y.)
0
0.6
2-20 µm MAR
(g/cm2/k.y.)
0
0.2
<2 µm MAR
(g/cm2/k.y.)
0
0.2
Age (Ma)
0
1
2
3
4
5
6
7
8
A
B
C
D
E
Unit I
Unit II

Figure 9. Accumulation rate of magnetic susceptibility and HIRM vs. age for Holes 885A and 886B.

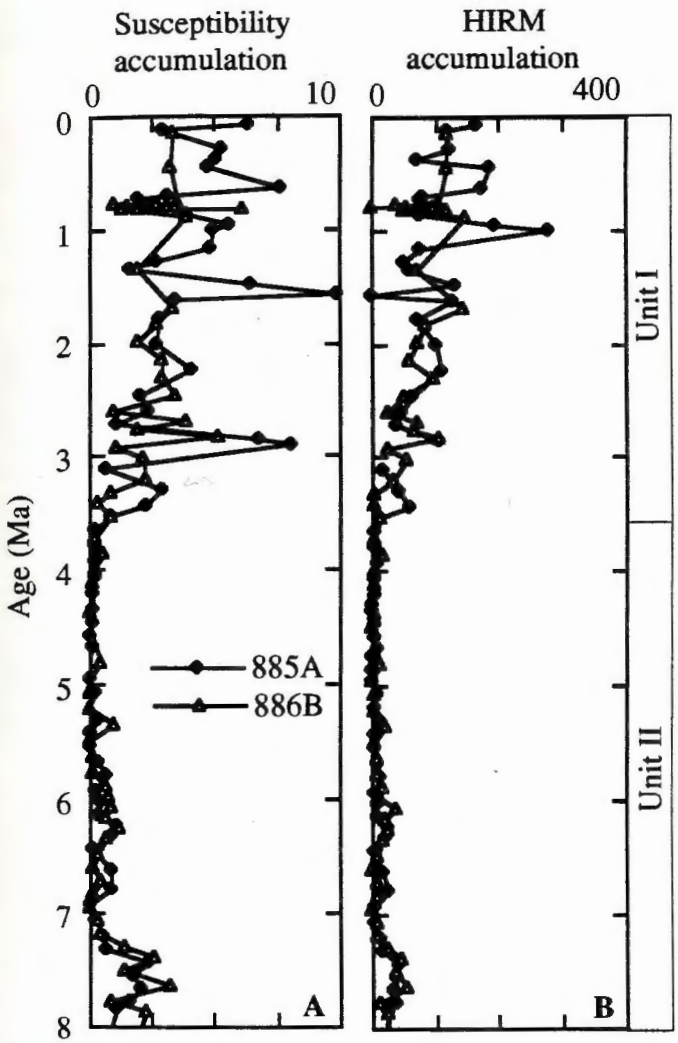
Susceptibility
accumulation
0
10
HIRM
accumulation
0
400
Age (Ma)
0
1
2
3
4
5
6
7
8
885A
886B
A
B
Unit I
Unit II

Figure 10. Accumulation rates for the <2 μm minerals vs. age for Holes 885A and 886B.

Smectite accumulation
0
0.02
Illite accumulation
0
0.04
Kaolinite accumulation
0
0.01
Chlorite accumulation
0
0.03
Quartz accumulation
0
0.08
Plagioclase accumulation
0
0.02
Age (Ma)
0
1
2
3
4
5
6
7
8
885A
886B
A
B
C
D
E
F
Unit I
Unit II

Chapter 2:

Rock-magnetic properties, mineralogy and grain size of mineral aerosol collected over the North Pacific Ocean: Relation to meteorology and implications for the interpretation of eolian sediments.

Abstract

This research quantifies the rock magnetic properties, grain size and mineralogy of a suite of North Pacific atmospheric samples using techniques developed for deep-sea sediment analysis; the measurements are then related to air-mass back trajectories. Aerosol samples were collected over the North Pacific Ocean using a variety of aerosol collection devices; high-volume bulk samplers, cascade impactors and nylon meshes. The mesh samples were analyzed using deep-sea sediment analytical techniques for rock-magnetism, quantitative mineralogy, and grain size. The pumped samples were analyzed for qualitative mineralogy and elemental composition by instrumental neutron activation analysis (INAA). Aerodynamic particle size is calculated from the Al mass distribution on cascade impactor stages.

The concentration, grain size and composition of the mineral aerosol collected by the various samplers are reproducible, and all display the same temporal variation. The atmospheric (INAA, aerodynamic particle size) analyses yield size and concentration information which is in good agreement with the analyses performed using standard deep-sea sedimentological techniques. Both data sets reveal that the aerosol physical characteristics are affected by both the source area and the transport pathway.

Introduction

Eolian deposition is the primary source of sediments in some regions of the Earth's oceans. Since the transport and deposition of eolian sediments are dependent upon source area climate and atmospheric circulation, these deposits are potentially a powerful tool for inferring climate changes through time. In order to fully exploit this paleoclimate record, it is necessary to determine how climate and atmospheric circulation processes control eolian transport and sedimentation. While there is a wealth of information for both aerosol and sediment composition and grain size, few studies in the North Pacific have analyzed both aerosol and sediment data in a strictly analogous manner. This research characterizes the mineralogy, rock-magnetism and grain size in a suite of North Pacific atmospheric samples using techniques normally employed for deep sea sediment analysis and relates the measurements to air-mass trajectories. The goal is to generate data from atmospheric samples that can be directly compared with the ancient eolian record.

Aerosol Transport

Many investigators have studied the contribution of continental material in the total particulate aerosol load presently found over the North Pacific Ocean (e.g. Parrington, et al., 1983; Parrington and Zoller, 1984). One of the most spatially and temporally complete suite of samples was collected as part of the SEAREX (sea-air exchange) program (Uematsu, et al., 1983 and 1985; Arimoto, et al., 1985; Duce, et al., 1980, 1983, and 1989, Prospero, 1989). This program monitored the aerosol concentration over the Pacific Ocean using a network of island and shipboard collection sites for periods of weeks to years. The goal of this program was to identify the sources, transport mechanisms and fluxes of material in the marine atmosphere.

Many results of the SEAREX and other long-term sampling programs are relevant for paleoclimate reconstructions. Continuous annual sampling demonstrated that atmospheric Al concentration, a measure of continental dust concentration, varies seasonally (Parrington, et al., 1983; Parrington and Zoller, 1984; Uematsu, et al., 1983; Duce, et al., 1980 and 1983). Peak aerosol Al concentrations in the North Pacific occur from February to June; the mineral concentration decreases by a factor of 2-12 during the July to January clean period. Periods of high atmospheric Al concentration are associated with Kosa events in Japan and dust storms in Asia (Uematsu, et al., 1983).

In addition to temporal variability, the atmospheric Al concentration varies spatially. In the North Pacific during 1981 through 1982, the largest Al concentrations occurred at high latitudes; mean values ranged from 0.89 $\mu g \cdot m^{-3}$ at Shemya (54°44'N) to 0.05 $\mu g \cdot m^{-3}$ at Fanning (3°55'N). This spatial trend in concentration is observed for the high-dust, clean periods and the average annual concentration (Uematsu, et al., 1983).

The seasonal and geographic trends noted for the mineral aerosol concentration are also observed in the measured or calculated depositional flux to the sea surface derived from Al concentration. The total aerosol flux is the sum of both the wet (75-85% of the total deposition) and dry deposition, and so varies with precipitation as well as dust concentration (Uematsu, et al., 1983 and 1985; Arimoto, et al., 1985). The calculated mineral aerosol flux is similar to the accumulation rate of eolian sediments in the North Pacific (Arimoto, et al., 1985; Uematsu, et al., 1983) with most of the annual dust deposition occurring during short term dust events.

Composition of aerosols

Since the goal of the SEAREX program was the estimation of the relative importance, transport mechanisms and flux to the ocean of all material in the marine atmosphere, and because the aerosols are collected in small quantities, elemental concentrations of the marine aerosol were the primary analytical tool. These elemental concentrations were compared with the typical elemental concentrations of sea salt, anthropogenic products and continental crust. The concentration of atmospheric Al was used as an index for the concentration of mineral aerosol, assuming the average crustal abundance of aluminum. Such normalizations are a common technique for distinguishing between various end-members, and the resulting information demonstrated the seasonal and spatial variability of mineral aerosol transport over the North Pacific and provided an approximation of the eolian flux to the sediments.

The interpretation of the Al concentration in deep sea sediments is more complex. Deep sea sediments are composed of aluminosilicates from different sources; eolian transport, hemipelagic and riverine input, authigenic formation and hydrothermal activity. Furthermore, aluminum is also incorporated into biogenic material (Murray and Leinen, 1993). Multivariate statistics can be employed to differentiate between various aluminum-bearing end-members and estimate their relative importance in deep sea sediment (Leinen, 1987, Leinen and Pisias, 1984). However, this type of statistical analysis precludes studying the compositional evolution of a single end-member source over time, a point that is usually of interest for paleoclimatic work.

A separate consideration is that the Al concentration of aluminosilicates is relatively invariant for some common clay minerals; for example, smectite, illite and

chlorite; each contain about 10% Al by weight. However, the Al concentration of kaolinite is about 20% and there is no Al in quartz, which is a very common constituent of soil-derived aluminosilicates. Thus, unless the aerosol source is homogenous, and there is no down wind fractionation of the mineralogy caused by particle size fractionation, the Al concentration may yield inaccurate estimates of mineral aerosol concentration. Finally, because variuos mineral phases are thermodynamically stable in different continental weathering environments, mineralogy is a compositional parameter which is particularly well suited for paleoclimatic work.

While there are many studies of the relationship between mineralogy and continental environments (Dixon and Weed, 1989, Chamley, 1989) as well as of mineralogy distributions in deep sea sediments (Goldberg, 1961; Biscaye, 1976; Heath and Pisias, 1979), there are relatively few studies of the mineral composition of aerosols collected over the North Pacific Ocean. This information is especially critical since aerosol samples can be related to specific meteorological conditions and to their continental source area with trajectory analysis, which would constrain the relationship between aerosol properties with transport and potential source areas.

Prospero and Bonatti (1969) studied the composition of dust in the eastern equatorial Pacific, using both elemental and X-ray diffraction techniques. The authors noted mineralogical differences across the intertropical convergence zone (ITCZ), but there was a lack of elemental variation across this boundary. Ferguson and others (1970) studied the mineralogy in both the clay and silt size aerosol collected in the eastern North Pacific, and concluded that the aerosols were mineralogically similar to eolian sediments from the North Pacific. Blank and others (1985) quantitatively determined the <2 μm size fraction mineralogy of a set of aerosols collected over the northwest Pacific and compared it with the mineralogy in the same size class of

eolian surface sediments. The concentrations of illite, kaolinite, chlorite, quartz, and plagioclase were statistically identical in the surface sediments and aerosols. Smectite concentrations were unequal, but the authors allow that this may be due to analytical and/or sampling variability as opposed to natural processes. Aerosols from both the western and eastern North Pacific margins were studied by Leinen, et al., (1994). The mineralogy of both the clay (<2 μm) and silt (2-20 μm) size fraction was determined; the same mineral phases were identified as in Blank's (1985) work. A companion study included an analysis of the synoptic meteorological conditions associated with the individual aerosol samples (Merrill, et al. 1994) which related the compositional variability of the aerosols to differences in air mass trajectory pathways. Different mineral assemblages were associated with different potential continental source areas. All the mineralogy work mentioned above used nylon meshes as the collection medium. Quantitative aerosol concentration cannot be determined using this technique (see methods).

Buat-Menard et al., (1983) used single particle analysis to identify the mineralogy of wet and dry bulk deposition samples from Enewetak. The authors detected differences between the rain and dry deposition mineralogy, but could not determine whether this variation was a function of the different sampling interval or fractionation by scavenging processes occurring during precipitation. While individual particle analysis provides aerosol mineralogy and grain size information, this technique is not practical for deep sea sediments. Again, the atmospheric concentration of the mineral aerosol can only be estimated qualitatively using this sampling technique.

Grain Size

Grain size is a commonly measured parameter of deep sea sediments and aerosols. The information is useful because grain size is an important control on the composition, chemical cycling, entrainment, transport and sedimentation of particles in both atmospheric and deep sea environments. Grain size measurements are generally made on the chemically isolated terrigenous fraction of deep sea sediment and represent individual aluminosilicate particle sizes (Rea, 1994, Rea and Hovan 1995). The grain size of sediment is usually measured with sieves, Stoke's settling or Elzone/Coulter counting equipment. Eolian deep sea sediment grain size measurements have been interpreted as a proxy for atmospheric transport vigor, based on the hypothesis that more turbulent and stronger atmospheric circulation can transport larger particles. Direct comparison of the sediment grain size with aerosol grain size is not straightforward; atmospheric scientists collect data representative of in situ particle size, which may consist of particle aggregates as well as individual aluminosilicate grains. A common sampling technique for estimating aerosol aluminosilicate grain size is fractionation with cascade impactors; these separate aerosol particles based on their aerodynamic particle size. Estimates of the aluminosilicate particle size are made by determining the mass of Al on each impaction stage and taking a geometric mean of the mass distributions over the range of size classes collected.

The mass median size distribution of aerosol particles containing Al was measured from cascade impactor samples collected during the 1979 SEAREX experiment at Enewetak (Duce et al., 1983). Samples from the second stage, with a mass median cutoff diameter of 3.0 μm, contained the highest concentration of Al during both the wet and dry seasons. The geometric mass median diameter ±1 standard deviation for these samples was 2.0 ± 4.8 μm (Arimoto, et al., 1985). A

similar study at American Samoa indicated a mean diameter of 1.9 ± 2.3 μm (Arimoto, et al., 1987). Both studies considered particles between median cutoff diameters of 7.4 and 0.49 μm. Total deposition (not size-fractionated) samples collected on several island locations in the North Pacific were studied by Uematsu and others (1985). The samplers (conical funnels) employed for total deposition have a larger cutoff diameter than the cascade impactors, but this cutoff has not been quantified. While the authors do not report the grain size distribution for the samples, they do include flux estimates for the <20 μm and <20 + ≥20 μm size fractions, which were separated using a 20 μm mesh. The authors state that the ≥ 20μm size fraction may account for up to 20 - 50% of the total dust flux, so it is clear that large size fractions should generally be included in analyses of atmospheric aerosols. In addition, these published estimates of dust flux suggest that the proportion of coarse material increases for samples collected at higher latitudes. Aerosol particles larger than 15μm were collected during the ADIOS (Asian Dust Input to the Oceanic System) experiment in 1986 (Betzer, et al., 1988). Analysis of 4 total deposition atmospheric samples using SEM/EDXA (scanning electron microscope/electron dispersive x-ray analysis) provided data on the 20-200 μm size range. The authors observed an increase in the number and mass flux of particles >75 μm coincident with the arrival of a dust plume from Asia. No information was given on the complete grain size range of the aluminosilicate aerosols.

Rock Magnetics

Rock magnetic parameters (susceptibility, anhysteretic remanent magnetization, isothermal remanent magnetization) are indicative of the concentration, grain size and composition of magnetic material (for example, magnetite and hematite) which occurs naturally in soils and soil-forming parent rocks. Rock magnetic measurements are commonly employed for the analysis of

sediments because they are a rapid, non-destructive means of estimating the concentration and grain size of the total terrigenous component of deep sea sediments (Robinson, 1986; Doh, et. al., 1988, Bloemendal and deMenocal, 1989). In addition, susceptibility can be measured on whole cores, providing a continuous proxy for terrigenous activity over time. Studies have used rock magnetization as a diagnostic tool for mineral aerosol origin (Oldfield, et al., 1985, Chester, et al., 1984) but no rock magnetization work on open ocean Pacific aerosols has been published.

From a paleoclimatologist's point of view, it is desirable to be able to interpret the sedimentological record in a way that can also be used to reconstruct atmospheric dust concentration. Even though atmospheric concentration is not a direct measure of deep sea sediment fluxes due to variable deposition processes, trends of sediment accumulation over time must be related to atmospheric concentration. One approach is to use a variety of collectors simultaneously, such as cascade impactors, high volume samplers and meshes, to integrate the elemental concentration information with composition and grain size sedimentological measurements. Cascade impactors or high volume samplers are commonly used to collect particles from a known volume of air, thus allowing an estimate of atmospheric aerosol concentration. However, the sample amounts are quite small, making it difficult to apply standard sedimentological techniques such as bulk X-ray diffraction. By integrating the results from a variety of collection devices, information useful to sedimentologists can be related to data gathered by atmospheric scientists.

This study quantifies the characteristics of the mineral aerosol collected over the open North Pacific Ocean using standard sedimentological techniques for mineralogy, particle size and rock magnetization determination. These measurements are readily accomplished on aerosol samples collected with meshes, due to the large sample mass of collected material. The mineralogy was determined by powder X-ray

diffraction using an internal standard in order to quantify the amount of each mineral phase present. Both the <2 μm and 2-20 μm size fraction mineralogy were determined for most samples. Elzone particle size is measured from 1 μm to 63 μm. Rock magnetization parameters, susceptibility (X), anhysteretic remanent magnetization (ARM) and isothermal remanent magnetization (IRM) are also determined for each of the samples. The measurements obtained for each sample are then compared with air mass trajectories, in order to relate the properties of the sample to the source areas and transport pathways.

The mineralogy measurements are also made on cascade impactor and high volume samples collected during one cruise. These mineralogy analyses are not quantified in terms of absolute weight percent, since no internal standard is used in the analysis. The cascade impactor sample mineralogy is determined for the different size classes collected on separate stages. Thus, both the high volume and cascade impactor sample mineralogy may be compared with the aluminum concentration in order to determine whether size fractionation of the mineralogy has any effect on the aluminum concentration in a sample. Finally, mass median diameter size estimates from the distribution of aluminum mass on the cascade impactors may be qualitatively compared with the particle size determination from the mesh samples. This set of comparisons will allow us to relate standard atmospheric analyses with standard sedimentology determinations.

Methods

Sampling

Aerosol sampling took place on 2 cruises in the North Pacific in the spring of 1986 and 1987 (Fig. 1). The first cruise was the May 1986 SEAREX expedition to the North Pacific. The cruise sailed from Hawaii to Kodiak, Alaska and returned to

Hawaii. The second cruise, part of the ADIOS expedition, also sailed from Hawaii in March and April of 1987, and occupied a single station at 26°N and 155°W. Both nylon mesh and pumped (either cascade impactors and/or high volume samplers) collection systems were deployed on each cruise.

All samples were collected during the springtime dust maximum in the Pacific; mesh samples were collected only during rain-free periods. Therefore, the variability of these few samples is not representative of the annual dust supply variability over the Pacific. However, the results of the SEAREX experiment indicate that the bulk of the annual aerosol transport to the North Pacific occurs during the springtime dust maximum. Thus, even though these samples do not illustrate the full annual range of aerosol variability over the central North Pacific, they do provide us with a longitudinal transect across the North Pacific during the springtime dust maximum.

Meshes

Paired $1m^2$ nylon meshes were used as an aerosol collection medium for the two North Pacific cruises (table 1). The meshes are monofilament nylon which sample by impaction. The sampling technique is passive; the air is not sieved, the mineral aerosol adheres to the dampened mesh. At each sample station two meshes were hung outboard of the research vessel where they were dampened by high relative humidity but not washed by waves. The meshes were deployed far forward of the ships' stacks in fair weather (no rain or fog) and only when the wind was off the bow of the ship. Any potential contamination of the meshes from stack gases or shipboard activity was recorded.

The mesh collection technique is useful for a sedimentological analysis; since large volumes of air are sampled, large numbers of particles may be collected rapidly.

From an atmospheric scientist's point of view, there are several limitations to the meshes. First, it is not possible to calculate atmospheric particle concentrations quantitatively, because there is no way to determine the volume of air sampled accurately. Additionally, the overall collection efficiency of the meshes is low (~30%) (Prospero and Nees, 1977). The efficiency likely varies with absolute wind speed and relative humidity. The collection efficiency of the meshes may vary with particle size so that the samples are not representative of the total aerosol, because they bias against fine particles (Prospero and Bonatti, 1969). Glaccum and Prospero (1980) found that the mineralogy of aerosols collected concurrently on pumped filter samplers and on meshes were compositionally identical. The one exception was microcline, but the authors assert that this difference was an artifact. There are no comparative studies of grain size or rock magnetism between meshes and other techniques. In summary, the meshes provide samples suitable for sedimentological analyses, but are a crude technique for quantitative atmospheric studies.

Fourteen mesh samples were collected on the research cruises. The sampling intervals ranged from 15 to 117 hours (Table 1). Eleven samples produced enough material for quantitative mineralogical analysis of both the <2 μm and 2-20 μm size fractions; the remaining 4 samples were quantitatively analyzed for mineralogy of the <20 μm size fraction. Twelve samples provided enough material for Elzone grain size analysis. All samples were subjected to rock-magnetism analysis.

Pumped Samples

High volume cascade impactors or bulk samplers were operated on both cruises (Table 2). The aerosol samplers were deployed on a tower located on the bow of the ship. Shipboard contamination was minimized for the SEAREX and ADIOS samples by the use of electronic controls which only pumped samples when the wind

was from a favorable direction. However, we report only on the results from cascade impactors and high volume samples from the May 1986 SEAREX cruise, because both elemental and mineralogy results have been generated for this sample set.

Bulk samples were collected on acid-washed Whatman 41 filters at a flow rate of 68 m^3/hr. High volume (68 m^3/hr) cascade impactor samples were collected with a modified six-stage Sierra model 235 impactor on the SEAREX cruise. This collector provides samples segregated into seven size classes based on aerodynamic equivalent diameter (AED). Cascade impactors collect samples by pumping air through a series of offset, slotted stages of decreasing slot width. Particles continue through the sampler until impacting on the stage with an aerodynamic cutoff diameter corresponding to the AED of the particle. Any particles too fine to be collected on the impactor stages are collected on a final cellulose filter. The instrumental configuration used on the SEAREX cruise may bias against particles greater than 10 μm, resulting in unreliable collection efficiency from stages 0 and 1 (Schneider, et al., 1990). The 50% aerodynamic cutoff diameters for each stage are:

Stage 0	16.8 μm	Stage 4	1.00 μm
Stage 1	9.3 μm	Stage 5	0.52 μm
Stage 2	3.63 μm	Backup	<0.52 μm
Stage 3	2.05 μm		

For both the high volume and cascade impactor samples, the impaction and filter substrates are acid-washed Whatman 41 cellulose filters. The cascade impactors and the bulk samplers are housed in separate plastic rain shelters during deployment. All impactor and filter substrates were handled in a clean room in the laboratory or a portable clean bench on board the research vessels. Personnel

responsible for collecting aerosols wore gloves and clean lab coats while loading and unloading filter cassettes at sea. Field blanks for both types of pumped samplers were obtained by loading cassettes with filter substrates and placing them in the rain shelter along with the active sampler. No air is drawn through the field blanks. The cellulose substrate used for filter and cascade impactor samples was stored in acid-washed plastic bags after being removed from the sampling cassette.

Sample Processing

Meshes

The aerosol particles are washed off the nylon mesh for analysis with repeated rinses of deionized water. Each duplicate sample mesh is processed separately. The rinse water is filtered onto pre-weighed 0.45 μm Nuclepore membranes, and the air-dried filter is re-weighed to determine the sample mass. The dried aerosol sample is scraped from the filter and stored in a vial for analysis. The large volume (> 1 liter) of water necessary to extract the aerosols from the mesh washes any sea salt from the sample. Bulk sample quantities ranged from 0.0047 g to 0.8852 g per mesh.

Pumped Samples

The cellulose substrate must be removed from the aerosol sample for X-ray diffraction analysis as the cellulose produces a high background on X-ray diffraction scans which interferes with the low intensity signal from the aerosol aluminosilicates. In addition, removal of the filter substrate concentrates the aerosol sample, which serves to intensify the aluminosilicate signal. Finally, by processing a larger portion of the filter than can be exposed to the x-ray beam at a single time, any effects from uneven distribution of particles on and within the filter substrate will be minimized.

The cellulose filter was oxidized by a low-temperature ashing technique. A 1 to 95 cm^2 section of cellulose filter or a single impaction substrate strip was cut with plastic scissors and placed in an acid-washed Teflon vial. The samples or blanks were combusted in a LFE Corporation model LTA-505 low temperature asher at 50 Watts, corresponding to a temperature below 100°C for 17 to 71 hours. After the cellulose was fully combusted, the residual material was mixed into a slurry with a small amount of deionized water. This slurry was pipetted onto a pre-weighed zero background quartz plate for X-ray diffraction analysis.

Analytical Techniques

Rock Magnetism

Samples were packed into 1.5 cm^3 Nalgene cylinders for analysis. Cotton was packed into the top of those vials with insufficient sample to fill the volume completely. Susceptibility was measured with a Bartington Instruments susceptibility meter at 0.47 (low frequency, X_{lf}) and 4.7 kHz (high frequency, X_{hf}). The reported value (in $\mu m^3/kg$) is the average of three replicates. The samples were demagnetized in a 100 mT alternating field. Anhysteretic remanent magnetization (ARM) was induced in a 0.1 mT steady field superimposed on a 100 mT alternating field. The ARM was measured on a cryogenic magnetometer, and the reported value (in $\mu Am^2/kg$) is the average of duplicate measurements. The X_{arm} was calculated by dividing ARM by the steady field (reported in $\mu m^3/kg$). The final set of magnetic measurements were saturated isothermal remanent magnetization (SIRM) and isothermal remanent magnetization ($IRM_{-0.3T}$). Samples were saturated in a 1.2 T field and measured on a cryogenic magnetometer. Samples were then placed in reverse fields of 0.3 T and the magnetization remeasured. The values reported (in $\mu Am^2/kg$) are averages of duplicate measurements. The frequency ratio (X_{hf}/X_{lf}),

the grain size parameter (X_{arm}/X_{lf}), and the compositional parameters (S [S = IRM$_{-0.3T}$/SIRM] and HIRM [HIRM ={IRM$_{-0.3T}$ + SIRM}/2]) were calculated from the primary measurements. Further explanation of these variables and their applications may be found in the results section. Readers unfamiliar with rock-magnetic techniques are referred to King et al. (1989).

Grain Size

The grain size distribution of the aerosol mesh samples was determined using a model 180 Elzone Particle Analyzer. Elzone analysis measures the volume of electrolyte displaced by a particle when it passes through a small orifice between two electrodes. The volume is converted to equivalent spherical diameter and the instrument is calibrated using latex spheres of a known diameter and volume. Samples were analyzed to provide a continuous grain size distribution (in equivalent spherical diameter) between 1 and 63 μm.

After the aerosol had been analyzed for rock-magnetism properties, it was wet-sieved at 63μm. The > 63μm samples were weighed and stored. The suspended <63 μm sediment was shaken and a subsample of this slurry was pipetted into a filtered solution of 4% sodium pyrophosphate and stirred continuously for analysis using a 120 μm diameter orifice tube. This procedure was repeated, sieving at 20 μm and using a 48 μm orifice tube to provide a more accurate measurement of the <20 μm size fraction. The 20-63 μm sieved size fraction was weighed and stored. The <20 μm size fraction was subsequently used for quantitative mineralogical analysis. 128 channels were measured for each orifice size and the results for both analyses were combined using a smoothing program to provide a continuous grain size profile.

Mineralogy

The <20 μm mesh aerosols were saturated with $MgCl_2$, to reduce d-spacing variability in clays with exchangeable cations; they were then rinsed with warm deionized water. The <20 μm fraction was split into 2-20 μm and <2 μm size fractions by centrifugation. The 2-20 μm and the <2 μm fractions were spiked with a 10% talc internal standard. Samples were homogenized by grinding in a mortar and pestle under acetone, air dried, suspended in a deionized water slurry, and drawn onto silver filters for X-ray analysis.

Both the mesh and pumped aerosol samples were X-rayed from 2° to 45°2Θ at 45 kV and 40 mA at 1° 2Θ per minute, using Cu-kα radiation. Peak areas for smectite, illite, kaolinite, chlorite, quartz, and plagioclase were determined using Scintag DMS software. The relative proportion of kaolinite and chlorite was determined by the relative proportions of the kaolinite [002] and chlorite [004] peak areas. Mineral peak areas were normalized to the internal standard peak areas for aerosol mesh samples.

Air Mass Trajectories

We used isentropic trajectory analysis to estimate the movement of the dust-laden air masses from which our samples were collected. This method provides a sample-specific assessment of potential source areas and transport pathways. The calculations are based on the global meteorological analysis of the National Meteorological Center. This is a gridded set of horizontal wind and geopotential height fields, at 2.5° latitude and longitude spacing, available twice daily. The winds are interpolated from the isobaric levels to isentropic surfaces at 5K intervals. A detailed description of this technique may be found in Merrill (1989). Examples of

the application of this technique to mineral aerosol transport are presented in Duce, et al., 1980; Uematsu, et al., 1983 and Merrill, et al., 1985, 1989 and 1994.

Results

Meshes

Table 3 shows the mass of dust collected on each mesh as well as the Elzone-determined geometric mean diameter for the aerosols. The aerosol mass recovered from the meshes ranged from 0.005 to 0.885 grams per mesh panel. Paired comparisons indicate that the replicate meshes collect dust in a reproducible manner at a 95% confidence limit for each cruise. Figure 2 shows the variation of the mass collected on each cruise, expressed as g/hr per sampler. The ADIOS cruise sampled a dust event which peaked during the second mesh sampling interval from March 30 through April 1, 1987. The magnitude of the time dependent variation in the collected dust mass is smaller for the Moana Wave cruise, and the concentration variation is related to different transport pathways, a function of the changing position of the ship as well as specific dust event (see section on air mass trajectory analysis).

The average grain diameter measured by Elzone (1 - 63 μm; Figure 3) showed no significant difference between replicate meshes on each cruise for paired comparisons at $a_{0.05}$. Samples with masses smaller than 20 mg of material per mesh were not analyzed for grain size. The ADIOS samples had finer geometric mean grain size (av. diameter = 3.72 ± 0.56 μm) and lower variability than the Moana Wave samples. There is a strong positive correlation ($R=0.90$, $r=<0.0001$) between the Elzone geometric mean grain size and the >63μm size fraction sieved off before Elzone analysis.

All of the primary rock magnetic measurements (low and high frequency susceptibility (X), anhysteretic remenant magnetism (X_{arm}) and isothermal remenant magnetism (SIRM)) are reproducible between replicate meshes for paired comparisons at $a_{0.05}$ (Table 4). These depend on the concentration of magnetic material in the aerosols. In the absence of superparamagnetic material, the susceptibility is largely independent of grain size over the grain size measured here; the magnitude of both X_{arm} and SIRM are grain size dependent, and will increase as the magnetic grain size decreases. Plots of the variation in these concentration measurements (fig. 4) indicate that the Moana Wave samples are more variable, while the ADIOS magnetic concentrations vary less. The X_{arm} and SIRM display the same general pattern as the susceptibility signal.

If samples have similar magnetic mineral composition, the grain size of the magnetic material may be estimated from the ratios of X_{arm}/X_{lf} and SIRM/ARM (fig. 5). This asumption is unlikely to be met in all cases. The rock magnetic grain size proxies are not correlated with the alumino-silicate grain size measurements. This poor match is likely a function of the detection limits for the Elzone, the variation in the magnetic grain size proxy with compositional changes, and the possibility that some of the aluminosilicate particles may be polymineralic fragments.

The compositional variations of the rock magnetic properties may be assessed using the S-ratio and the HIRM parameters (fig 6). The S-ratio ($IRM_{-0.3T}/SIRM_{1.2T}$) is sensitive to the composition of magnetic minerals because low coercivity, ferrimagnetic magnetic minerals such as magnetite are easily magnetized ("soft"), whereas high coercivity, antiferromagnetic ("hard") minerals such as hematite require stronger magnetic fields to saturate them. Thus, the ratio of the magnetization stripped off of the magnetically saturated sample in a reverse field of

0.3 T is related to the proportion of "hard" to "soft" magnetic material present in a sample. The ADIOS samples have the largest proportion of antiferromagnetic material. The Moana Wave samples trend toward higher values for meshes collected during the later part of the cruise. This suggests a relative increase in the ferrimagnetic concentration for these samples. HIRM ([IRM$_{-0.3T}$ + SIRM]/2) is used to estimate the concentration of high coercivity magnetic material in the aerosol. The variability of the HIRM (fig. 6) is comparable to the magnetic concentration parameters.

Mineralogy

Meshes

The mineralogy of the aerosols was determined for both the <2 μm and the 2-20 μm size fractions for most samples. Samples smaller than ~20 mg of material per mesh were not size-fractionated and the bulk sediment mineralogy was determined. The mineral phases quantified are smectite, illite, kaolinite, chlorite, quartz and plagioclase. For all analyses, paired comparisons indicate no statistically significant differences between replicate meshes at a = 0.05 (Table 5).

We wanted to use the mineralogy to: examine the relationship between source area and transport mechanism with compositional variation; compare our results to other studies; and, compare mineralogy of the pumped samples collected on the Moana Wave cruise. In light of these plans, we reduced the raw diffraction patterns in the following manner. The peak areas for each phase were normalized to the internal standard (10% talc) to correct for inter-sample differences in peak intensity. This normalization effects the variance between samples, but does not change the relative proportion of minerals within a sample. The normalized peak areas were multiplied by weighting factors derived for North Pacific deep sea sediments (Heath and Pisias,

1979), in order to estimate the absolute weight percent of each mineral phase present. While these weighting factors may not be accurate for aerosol samples, they allow us to compare the results of these analyses with previous studies of deep sea eolian sediment mineralogy and aerosol mineralogy. To facilitate comparison with other studies and with the pumped aerosol samples, the data are normalized to 100%. This expresses the data on an "amorphous-material-free" basis.

For both cruises and all size fractions, illite is the dominant mineral phase present in the aerosols. It accounts for 68% of the aerosol in the <2 μm size fraction and 49% of the 2-20 μm size fraction. The two samples that are not dominated by illite are the 2-20 μm size fraction of Moana Wave mesh 6, which is predominantly (44%) plagioclase, and the bulk analysis of Moana Wave mesh 7, which is predominantly (>50%) quartz. The latter is characterized by poor reproducibility between samples, although both replicates are dominated by quartz.

In the <2 μm size fraction, smectite comprises 3% of the diffracting material, chlorite 5% and kaolinite 9% (Table 5, Figure 9). The primary minerals quartz and plagioclase are present in approximately equal concentrations, 7.5% and 7% respectively. The 2-20 μm size fraction contains 2% smectite, 7% kaolinite and 5% chlorite (Table 5, Figure 8). The quartz and plagioclase concentrations are 19% and 18% respectively.

There are no significant mineralogical differences between the ADIOS and Moana Wave cruise samples. Another way to examine the mineralogy is to look at differences in the concentrations of the various mineral phases between the two size classes. The clay minerals smectite and illite are present in significantly higher concentrations (0.6% and 20% higher, respectively) in the < 2μm size fraction relative to the 2-20 μm size fraction for paired comparisons of all samples at a=0.05.

Quartz and plagioclase are concentrated 12% and 11% higher in the 2-20 μm size fraction than in the <2μm size fraction.

Pumped Samples

Samples from two cascade impactor and three high volume samplers which were analyzed for mineralogy from leg 1 of the Moana Wave cruise, and samples from two high volume samplers were analyzed from the second leg of the cruise. We were only able to analyze two cascade impactor samples due to the small number of filters remaining from the Moana Wave cruise. We chose these particular samples because they had both INAA elemental data and concurrently sampled high volume filters available for comparison. A suite of procedural and tower blank samples were processed in addition to the sample filters. The chemistry of cascade impactors and high volume samples collected over the same interval as the samples used for mineralogical analyses was determined by INAA (Arimoto, written communication). In addition, the mass median diameter of the aluminosilicate was estimated from the aluminum mass distribution on the cascade impactor stages (Arimoto, written communication). The average mineralogical concentration (Table 6, Figure 10) were calculated in the following manner. The mineral counts were multiplied by the Heath and Pisias (1979) weighting factors, and the data were normalized to 100. The application of the weighting factors is used to allow comparison of the pumped samples with the samples collected on the meshes. The measurements for each sample were then averaged, with high volume samples smaller than $4cm^2$ excluded from the averages. In order to generate a "total" mineralogy for cascade impactor samples 27 and 61, the values for each mineral phase for each stage were weighted by the proportion of ash from the stage, and the weighted values were summed for the cascade impactor. Variation of the mineralogy for each cascade impactor stage is illustrated in figure 11. Cascade impactor 27 demonstrates the expected variation of

composition with size; primary minerals dominate in stages 0 and 1, the coarsest size fraction collected, while the clay minerals become increasingly important in the smaller size fractions. Cascade impactor 61 is quite different; the primary minerals (quartz and plagioclase) comprise almost the entire composition for all of the collection stages. The only stage which contains appreciable clay mineral material is the backup filter (stage 6). In addition to the mineralogical data, the table includes the ashed residue mass from the filters, expressed in μg per cubic meter of air sampled.

In order to assess the significance of the replicate variability within each ashed sample, comparisons of all possible pairs were made using the non-parametric Wilcoxon signed rank test. The parameters tested were ashed weight in $\mu g/m^3$ and the peak height of each of the mineral phases smectite, illite, kaolinite, chlorite, quartz and plagioclase. The results are summarized in table 7, which contains the p-values for each of the paired comparisons. The tests were blocked by sample for all analyses, and the analysis was repeated for the cascade impactor samples, blocking for sample stage. Three of the five high volume samples contain replicates which are significantly different for one or more of the variables tested at a significance level of 0.05. However, the two samples, HV 43 and HV 197, which had large portions of the filter ashed ($95cm^2$ and $82.5cm^2$, respectively) were not significantly different for all comparisons made. Neither of the cascade impactors displayed significant differences at this level, even when blocked by stage.

In order to evaluate the effect of sample size on the reproducibility of the high volume samples, a paired comparison analysis of the ash concentration and mineral peak heights for sample aliquots >4 cm^2 was performed. Sample 23 only has two aliquots greater than 4 cm^2, so it cannot be included in this evaluation. For HV samples 7 and 181, the three parameters which were significantly different in the original statistical analysis were not significantly different at a=0.05 in the size >4

cm^2 subset (table 7). This analysis, together with the observation that the large aliquot samples HV 43 and HV 197 are not significantly different for all parameters suggests sample inhomogeneity is a problem for small high volume sample aliquots. These samples (<4 cm^2) were excluded from the data set.

Field blanks and procedural blanks were analyzed with the pumped samples. The ashed residue from all the blank samples was negligible. Peaks were present in some diffraction patterns from the field blank samples. However, the peaks were intermittent and the phases could not be conclusively identified. Common d-spacings included 6.33Å, 3.63Å and 3.18Å. Sodalite or a sodium - calcium sulfate phase have reflections at these d-spacings, but a multiple line match could not be made for any single sample. The d-spacing at 3.18Å overlaps with the d-spacing used to identify plagioclase, thus this mineral phase will be affected by these contaminating phases.

Low temperature oxidation of the cellulose substrate should not affect the aluminosilicate fraction of the aerosol. This assumption was assessed by running clay standards through the ashing procedure. A few milligrams of the clay standards montmorillonite (smectite), illite and kaolinite were run through the low temperature asher and there was no modification of the diffraction pattern in any of the standards. In addition to the clay standards, we ran two samples collected on the mesh samplers through the low temperature asher; the diffraction pattern of the aluminosilicate fraction was not affected by the ashing process.

The data may be compared with Arimoto's (written communication, 1995, Table 8) elemental data. The comparisons are not made on aliquots of the same samples, rather, they are made between samples that were collected over identical time intervals. In some cases, the INAA data for two samples are averaged together, weighted in proportion to the sampling interval, in order to cover the same time

interval as the samples analyzed for mineralogy. When this is the case, both sample identification numbers are listed on the figure. The variation of the elemental and ashed data is illustrated for the total samples (Fig. 12), and by stage for the two cascade impactors (Fig. 13). Linear regression analysis indicates that the aluminum concentration is correlated significantly with the ash concentration ($R^2 = 0.81$, $p < 0.01$) when all the analyzed samples are compared (the high volume analyses as well as the total cascade impactor stages). The aluminum to ash correlation is highest for the high volume sample subset ($R^2 = 0.94$, $p < 0.01$); the aluminum and ash in the cascade impactor samples are not correlated significantly ($R^2 = 0.16$, $p = 0.08$) when individual stages are compared. In contrast, sodium is not correlated significantly with the complete sample set ($R^2 = 0.09$, $p = 0.51$) and the high volume subset ($R^2 = 0.08$, $p = 0.65$), but is highly correlated ($R^2 = 0.91$, $p = <0.00$) for the cascade impactor stages (Figs.14 and 15). Al was not correlated with the concentration of any of the individual mineral phases.

The poor correlation of the Al with ash for the cascade impactors and the variable mineralogy replicates in the small aliquot high volume samplers may both be related to the variation of aerosol mineral composition with grain size. Primary minerals predominate in larger size fractions while clay minerals are concentrated in the finer size fractions in naturally occurring soil samples. In general, primary minerals have lower aluminum concentrations than clay minerals. Thus, cascade impactors, which fractionate the aerosols based on size, would not exhibit a linear relationship between aluminum and ashed weight over different stages. The clay minerals have positive correlation coefficients (and quartz and plagioclase negative correlation coefficients) with the aluminum concentration, but these correlations are not statistically significant at a=0.05. In the case of small aliquot high volume samples, the variable mineralogy replicates may be caused by the sparse distribution

on the filter of large (primary) mineral particles which are not as abundant as fine particles in the atmosphere.

The linear regression coefficients of ash vs. aluminum regression yield an aluminum concentration of 0.9 to 2.7 wt % (95% confidence interval) for all the pumped samples, and there is a positive intercept for the regression. Removing the mass contributed from sea salt, based on the sodium concentration, from the ashed residue does not significantly change the regression coefficients, but does eliminate the positive intercept. These regression coefficients are extremely low when compared with estimates of the average crustal abundance of aluminum (~8%). The aerosols may consist a mineral suite which is unusually low in aluminum, the residual may consist of some non-diffracting aerosol particulate besides aluminosilicate, or there may be differences between the ashed and INAA sample impactors. If the ash was dominated by material from the original filter, there should be no variation in residual ash concentration with impactor stage; all the filter substrates are identical. Furthermore, the ashed residual from blank samples is negligible. Thus, we rule out residual filter material as a significant contributor to the ashed mass, but we cannot account for the ash mass with measured aluminum concentration.

Air Mass Trajectories

Air mass trajectory calculations provide us with a semi-quantitative means of assessing potential dust source areas by tracing the pathway of an air parcel back in time. However, the calculations do not quantify the relative contribution of dust from any of the areas encountered, nor do they indicate whether the local meteorological conditions over the continents were appropriate for dust injection into the atmosphere at the time the air mass passed over the site. We will use the trajectory analysis

results to help explain the variability in the aerosol physical characteristics, based on the assumption that the properties of the mineral aerosol are dependent upon the source area and transport pathway.

Synthesis of the trajectory data together with the physical information is limited by the small number of aerosol samples. There are too few samples to perform any type of multivariate statistical analyses between source area, transport pathway, transport time and variation in the physical parameters. In order to compile the data into a format that is more easily interpreted on an individual sample basis, all trajectories available for each sample were reduced in the following manner. Continental source areas were divided into several broad categories; continental Asia, separated into the following latitude bands: >60°N, 50°N-60°N, 40°N-50°N, 30°N-40°N, 20°N-30°N, Japan, Kamchatka peninsula, Siberian peninsula (northeast of Kamchatka), Alaska, Aleutian islands, and Canada. There were no trajectories for the samples analyzed which crossed Asia south of 20°N, nor did any trajectories cross the continental United States. In the case where trajectories did not encounter any land masses, the designation open ocean is applied. For each trajectory, the time elapsed, in days, between the last time the air mass encountered a particular continental source area and the arrival over the sampling location is entered into the table. In the case of divergent airflow, the most direct (shortest transport) path to a source area is selected. The longitude for samples from Asia are in parentheses next to the transport time. Table 9 presents the compilation of the trajectory analyses for the Moana Wave cruise and table 10 for the ADIOS cruise.

There are some differences between the air mass trajectories for samples collected from the 1986 Moana Wave cruise compared with those from 1987 ADIOS cruise. This is illustrated, broken down by sample, in figures 16 and 17, which show the average transport time between the various source areas and the sampling

location. The figures display this information in three panels; the upper panel represents average transport time from all locations in continental Asia, the middle panel for other potential source regions adjacent to the western high latitude North Pacific and the bottom panel represents potential source regions adjacent to the eastern high latitude North Pacific. The potential source areas which the air parcels passed over were much more variable, and the flow more divergent, for the 1986 Moana Wave sampling compared with 1987 ADIOS cruise. This variability is largely a function of the location of the ship during sample collection. In 1986, the sampling took place from 25°N to 57°N and 150°W to 170°W, while in 1987, samples were collected at a single location; 25°N and 155°W. Samples from both cruises are typically characterized by flow from Asia and Japan, but the 1986 cruise samples are from a more northern Asian continental source, and also frequently include trajectories influenced by flow from the Kamchatka and Siberian peninsulas, the Aleutian island-arc chain and Alaska.

There are also important temporal changes in the transport time and potential source areas for each cruise. For the Moana Wave 1986 cruise, the most significant change is the drop in transport time from eastern source areas for the later part of the cruise. These short transport times from the Aleutian Islands and Alaska indicate a higher potential for these source areas to influence the physical characteristics of the aerosols. The shortest transport time from Asia, the most dust productive region which impacts the North Pacific, occurs during the sampling interval for HV7 and Mesh 1. Temporal changes in the ADIOS 1987 transport regime are much simpler than those for the Moana Wave cruise. The potential source areas do not appreciably change for the first four sampling intervals, but the transport time from Asia and Japan increases from 3 days at the beginning of the cruise to 8 days at the end. Mesh 5 is influenced by the most southerly Asian sources for both the Moana Wave and

ADIOS samples. Mesh 6 is influenced by the most northerly Asian sources for this cruise, as well as some transport from eastern source areas.

Discussion

Comparison with other aerosol studies

The majority of the chemistry work which has been performed on North Pacific mineral aerosols does not include a sample specific trajectory analysis, as performed in this work. Rather, the mineral concentration and grain size information is expressed as seasonal or latitudinal averages. Thus, direct comparison between this work and previous analyses is limited to comparing broad ranges of information.

For the pumped samples, the mineral aerosol concentration, based on an 8% Al concentration for mineral dust, and using the high volume and cascade impactor samples for the calculation (which was the value used in the previous studies), ranged from 4.1 $\mu g/m^3$ to 0.09 $\mu g/m^3$. These estimates are within the range of mineral aerosol concentrations previously published for North Pacific aerosols (Uematsu, et. al., 1983, and references therein). The grain size estimates, based on the cascade impactor aluminum and iron mmd range from 1.14 μm to 5.33 μm; Arimoto and others (1985) report a mmd, based on aluminum concentration, of 2.0 μm ± 4.8 μm for mineral aerosol samples collected at Enewetak. The Elzone geometric mean diameter of the mesh samples ranges from 3.06 μm to 7.62 μm. There are no previously published estimates of electronic particle size measurements for North Pacific aerosol to compare with the mesh samples. Comparison of the mineralogy results with previous aerosol mineralogy work is incorporated into the discussion of aerosol vs. air mass trajectories.

Meshes vs. Pumped Samples

The pumped and the mesh analyses can be compared in three ways; concentration, grain size and composition. These comparisons are necessarily qualitative because the mesh samples and pumped samples were not collected over exactly identical time intervals. Figure 18 shows the ashed weight from the pumped samples plotted with the dust mass collected on the meshes, expressed in g/hour per sampler for the mesh samples and in μg/m3 for the pumped samples. It is not possible to calculate the volume of air sampled by the meshes, thus there is no way to express the data in identical concentration units. However, the comparison of the mass collected per hour by each sampler type shows good temporal agreement in terms of mass variability. Qualitatively, both sample types record the same variation in dust loading; a high dust event at the beginning of leg 1 of the Moana Wave cruise, consistent with a short transport time from the major dust sources in Asia, decreasing to low, steady values for the remainder of the cruise, as the Asian transport time increases and less productive dust sources influence the air mass.

The differences in the analytical technique used for meshes and pumped aerosols precludes comparison of the absolute mineral phase concentrations. The mesh samples were size fractionated and spiked with an internal standard; the pumped samples were either bulk samples in the case of high volume samplers or the weighted sum across all stages for the cascade impactor stages. Again, we can only qualitatively compare temporal mineralogy variation. We plot the average mineralogy for each sample for the leg 1 Moana Wave samples. The figures depict the pumped samples vs. the <2 μm mesh mineralogy (fig. 19) and the pumped samples vs. the 2-20 μm mesh mineralogy (fig. 20). The samples at the beginning of the cruise, HV7 through Mesh 3, contain less plagioclase and more illite than samples HV43 through CI61, for both mesh mineralogy size fractions and for the pumped

samples. These mineralogy changes are both compositionally and temporally consistent with the increased influence of the Aleutian and Alaskan source areas on the later samples.

The mass median diameter (mmd) calculated from cascade impactor aluminum and iron concentration (written communication, Arimoto, 1995) and the Elzone determined geometric mean diameter from the mesh samples are illustrated in figures 21 and 22. There is poor agreement between these two estimates of particle size. While the pumped sample mmd based on the iron concentration is in good agreement with the mean grain size of the meshes during the beginning of the leg, the two grain size estimates diverge for samples CI39 through mesh 8. The pumped sample estimates decrease and the mesh sample size estimates increase compared with samples from the beginning of the leg. The rock magnetism particles size estimates, X_{arm}/X and SIRM/ARM, for the mesh samples demonstrate the same trend as the Elzone size analysis, even though the two size estimates are uncorrelated. The mineralogy of both pumped and mesh samples indicates a relative increase in the concentration of the primary minerals towards the later half of the cruise, and the air mass trajectory analysis indicates a change to short transport time to the Aleutians and Alaska, a potential source area dominated by physical weathering. These observations would generally support an increase in grain size for these samples. The pumped samplers may fail to collect the coarse grain size fraction efficiently, or variation in the percent Al and Fe with particle size may effect the mmd calculations.

Aerosols vs. Air Mass Trajectories

We can make some general statements about the expected effect of source area and transport pathway on the concentration, grain size and composition of the aerosols. Transport time will predictably effect all of the physical parameters. Dust

concentration and grain size will decrease with increasing transport time as particles settle out of the dust plume, with coarse particles sedimenting out more rapidly than fine particles. The composition of the aerosols will become increasingly dominated by clay minerals, as the coarser grained primary minerals settle out of the atmosphere with transport time. In addition to transport effects, all of the physical parameters will vary with changes in source area.

We test our predictions by examining the relationship between source area and transport time with the measured variables. The air masses pass over multiple source areas, at different speeds, on their way to the sampling stations. The small number of observations preclude statistically decoupling transport effects from source area effects with multivariate statistical analysis. In addition, it is not possible to completely isolate the effects of an individual source area with this data set, as the open ocean samples integrate many source areas, due to the long transit times.

The simplest transport effects to understand are the relationships between decreasing dust concentration and grain size with increasing transport time. Figure 23 illustrates the relationship between dust concentration and transport time for each sample, broken down by source area. For example, the three points at the highest dust concentration, 0.0125g/hr, represent ADIOS mesh 2. The air mass for this sample passed over Asia 4 days (top panel), over Japan 3.5 days (center panel) and over the Aleutians 2 days (bottom panel) prior to arriving at the shipboard sampling site. The samples from Asia show the predicted trend of decreasing dust concentration with increasing transport time. There is significant correlation between transport time from both Asian sources between 40-50°N ($r = -0.88$) and Japan source areas ($r = -0.84$) and dust concentration. Samples which are dominated by short transport Asian source area trajectories contain the highest dust loadings. Many of the samples with the lowest dust concentration had long transport times from Asia but passed over the

Aleutian islands, Alaska or the Siberian peninsula less than 4 days prior to arriving at the sampling station. However, these continental areas are not significant dust sources, especially in comparison with the deserts of northern Asia, so that even though the transit time from continent to sample station is small, the dust concentration remains low.

In addition to the correlation with transport from Asia and Japan, dust concentration is negatively correlated with 2-20 μm smectite and positively correlated with 2-20 μm quartz. These correlations could be the result of either mixing between different eolian source areas, or could be the result of transport driven mineral fractionation.

Figure 24 displays the grain size against transport time in the same manner as the previously discussed dust concentration. There is no clear relationship between grain size and transit time for any of the source areas. If anything, it appears that there is an increase in grain size with increasing transport time for Asian samples. However, if the grain size data are considered in the context of both the dust concentration and the source areas, a coherent picture emerges.

A plot of the grain size versus dust concentration (fig. 25) indicates that the grain size is largest for samples with the lowest dust concentration. The negative correlation between dust concentration and grain size is significant ($r = -0.61$), but only accounts for a third of the variance in the data set. Clearly, aerosol transport time from a single source is not dominating the grain size variability in this suite of samples. The samples with the coarsest grain size are not only among the those with the lowest dust concentration, but also the shortest transit time from the Aleutian/Canada/Alaska source areas. One scenario which explains both the grain size and dust concentration is that the Asian deserts provide a strong, fine grained

dust source while the Aleutians/Canada/Alaska contribute a coarse grained component in very low concentrations. Thus, the resultant grain size distribution is a function of mixing between the fine Asian source and the coarse Aleutian and North American sources. The grain size is also significantly correlated with plagioclase concentration in both size fractions, and negatively correlated with kaolinite concentration in both size fractions. This suggests mixing between a fine-grained kaolinite-rich Asian end member with a coarse-grained plagioclase-rich Aleutian/Alaska end member. These mineral associations are consistent with the geological differences between the high-latitude, volcanic, physically-weathered environment in the Aleutians and Alaska, contrasted with the deserts of northern Asia.

The rock magnetic properties of the aerosols plotted against transport time are illustrated in figure 26. For brevity, not all source areas are illustrated, only transport from Asia between 40-50°N, Japan and the Aleutian Islands. These are the three most common source areas, and they express most of the transport related variance in the data set. None of the rock magnetism parameters are significantly correlated with the transport time from any source area. The only significant correlations between the magnetic properties of the aerosols and the other measured parameters are positive correlations between both susceptibility and HIRM with plagioclase and negative correlations between these two magnetic parameters with illite. The correlation between magnetic concentration parameters and plagioclase is consistent with a volcanic source area, which would be typified by large concentration of magnetic minerals.

The comparison of the mineral phase concentration with transport time is illustrated in figures 27 and 28. These figures include mineralogy data from the western North Pacific (which have been normalized to 100%) from Leinen, et. al.,

1994. The collection techniques and analytical procedures used by Leinen, et al., 1994 were identical to those in this study. The samples from this previous study were collected from the margins of the North Pacific Ocean, thus transport time from the source areas is much shorter, and there is less mixing between multiple source areas. This affords us the opportunity to examine a broader range of transport times for the mineralogy data. The correlations between transport time and the mineralogy of the aerosols are presented in table 11; significant correlations (a=0.05) are highlighted in bold font. The source areas Siberia and Alaska had too few air mass trajectories to perform correlation analysis. The relationship between transport time and particle fractionation predicts that the concentration of the clay (primary) minerals should be positively (negatively) correlated with transport time, as the coarse grained primary minerals preferentially settle out with increasing time. This mechanism is consistent with the significant positive correlations for smectite, illite, chlorite, and negative correlations with quartz and plagioclase. Kaolinite, however, is negatively correlated with source areas from Japan and Asia in the <2μm size fraction, but is positively correlated with transport time for the Aleutian source area in the 2-20μm size fraction.

The alternative mechanism for this mineralogy variation is mixing between Asia/Japan source areas and high latitude Aleutian/Alaska/Canada source areas. The observed trends in mineralogy regressed against Asian transport predict that the high latitude source area would be relatively enriched in the clay minerals smectite, illite and chlorite and depleted in the primary minerals quartz and plagioclase as well as kaolinite clay. While most of these mineralogy differences between the two source areas are plausible, the requirement that plagioclase be depleted in the high source area is in conflict with both the grain size data and the geological differences between

these two source areas. Thus, we conclude that the mineralogy variation is the result of both mixing and transport driven mineral fractionation.

The measurements for the pumped samples were also evaluated against transport time from the different source areas. The mineralogy regression against transport time was performed separately because the pumped samples were not differentiated into separate size fractions for XRD analysis. Transport times from Asia (>60°N) and Japan are correlated with illite and inversely correlated with plagioclase for the pumped samples. Transport time from the Aleutians is correlated with kaolinite. The aerosol size, aluminum concentration and ash residual are not significantly correlated with transport time. There are fewer significant transport time - mineral phase correlations for the pumped samples, but the analysis demonstrates the same trends as that generated for the mesh samples.

Implications for interpretation of eolian sediments

The interpretation of paleoclimate and paleometeorology from eolian deep sea sediments generally includes the assumptions that the grain size is related to atmospheric transport vigor and the mineralogy is related to source area. While this data set is generally consistent with these assumptions, the relationship between atmospheric transport and aerosol physical properties is not that simple. The grain size is affected by variation in source area, and the mineralogy is fractionated by differential settling during transport. Thus, paleoclimate/meteorology studies of eolian sediments should include multiparameter analyses, as well as sample distributions on a large enough spatial scale to capture transport-related compositional and grain size gradients.

Conclusions

Atmospheric dust concentration and mineralogy data generated from mesh samplers, cascade impactors or high volume pumped samples are comparable, and all sampler types display the same temporal variation in the physical properties. However, aerosol size estimates generated by Elzone analysis for mesh samples and elemental mass distribution from cascade impactors, while comparable for fine grained samples, diverge for samples with large Elzone size estimates.

The concentration, grain size and composition of aluminosilicate aerosols collected over the North Pacific Ocean reflect variation in both the source area of the dust and atmospheric transport driven fractionation of the aerosol. While there is strong evidence for both transport and mixing influences on the composition and size of aluminosilicate mineral aerosol, a larger data set is required in order to estimate the relative importance of both processes.

This data set supports mixing between a dominant Asia dust source and a weak high latitude dust source, and transport driven fractionation of the aerosol. Asia is a strong, fine grained dust source which is relatively enriched in 2-20μm quartz and <2μm kaolinite. The high latitude source area is a weak, coarse-grained dust source which is relatively enriched in plagioclase and magnetic minerals.

Transport related mineral fractionation drives the mineralogy towards a clay mineral enriched and primary mineral depleted composition with increasing transport time. These trends are observed for all source areas studied, in both the mesh sample mineralogy and the data generated from cascade impactors and high volume samples.

Acknowledgments

This research was funded by NSF grant ATM 91-02385. Arnold and Peacock were also financially assisted by the Graduate School of Oceanography Alumni Association. Neil Tindale collected mesh samples aboard the ADIOS cruise. Ruth Platner performed the air mass trajectory calculations. Robert Duce and Richard Arimoto provided cascade impactor and high volume samples for X-ray diffraction analyses and unpublished INAA data. Barbara Ray and Noelle Lewis analyzed the INAA data and performed the mmd calculations. We thank all of these people and organizations for their substantial contributions to this research.

References

Arimoto, R., Duce, R. A., Ray, B. J., Hewitt, A. D. and Williams, J. 1987. Trace elements in the atmosphere of American Samoa: concentrations and deposition to the tropical South Pacific. Journal of Geophysical Research, 92.:8,465-8,479.

Arimoto, R., Duce, R. A., Ray, B. J. and Unni, C. K. 1985. Atmospheric trace elements at Enewetak atoll: 2. Transport to the ocean by wet and dry deposition. Journal of Geophysical Research, 90:2,391-2,408.

Betzer, P. R., Carder, K. L., Duce, R. A., Merrill, J. T., Tindale, N. W., Uematsu, M., Costello, D. K., Young, R. W., Feely, R. A., Breland, J. A., Bernstein, R. E. and Greco, A. M. 1988. Long-range transport of giant mineral aerosol particles. Nature, 336:568-571.

Blank, M., Leinen, M. and Prospero, J. M. 1985. Major Asian eolian inputs indicated by the mineralogy of aerosols and sediments in the western North Pacific. Nature, 314:84-86.

Bloemendal, J. and deMenocal, P. 1989. Evidence for a change in periodicity of tropical climate cycles at 2.4 Myr from whole-core magnetic suceptibility measurements. Nature, 342:897-900.

Buat-Menard, P., Ezat, U. and Gaudichet, A. 1983. Size distribution and mineralogy of aluminosilicate dust particles in tropical Pacific air and rain. 4th International Conference on Precipitation Scavenging, Dry Deposition, and Resuspension, November 28-December 3, 1982. Santa Monica, California. 8 pages.

Chamley, H. 1989. Clay Sedimentology. Springer-Verlag. Berlin. 623 pages.

Doh, S.-J., King, J. W. and Leinen, M. 1988. A rock-magnetic study of giant piston core LL44-GPC3 from the central North Pacific and its paleoceanographic implications. Paleoceanography, 3:89-111.

Duce, R. A. 1989. SEAREX: The Sea-Air Exchange Program. In: Riley, J. P. and Chester, R. Chemical Oceanography. Vol. 10. Academic Press Inc. San Diego. 404 pages.

Duce, R. A., Arimoto, R., Ray, B. J., Unni, C. K. and Harder, P. J. 1983. Atmospheric trace elements at Enewetak Atoll: 1, concentrations, sources and temporal variability. Journal of Geophysical Research, 88:5321-5342.

Duce, R. A., Unni, C. K., Ray, B. J., Prospero, J. M. and Merrill, J. T. 1980. Long-range transport of soil dust from Asia to the tropical North Pacific: temporal variability. Science, 209:1,522-1,524.

Ferguson, W. S., Griffin, J. J. and Goldberg, E. D. 1970. Atmospheric dusts from the North Pacific - a short note on a long-range eolian transport. Journal of Geophysical Research, 75:1137-1139.

Glaccum, R. A. and Prospero, J. M. 1980. Saharan aerosols over the tropical North Atlantic-mineralogy. Marine Geology, 37:295-321.

Heath, G. R. and Pisias, N. G. 1979. A method for the quatitative estimation of clay minerals in North Pacific deep-sea sediments. Clays and Clay Minerals, 27:175-184.

King, J. W., Bloemendal, J. and Gangemi, P. 1989. Paleomagnetic and rock-magetic stratigraphy of ESOPE core 63, southern Nares abyssal plain. 611-636. In:

Schuttenhelm, R. T. E., Auffret, G. A., Buckley, D. E., Cranston, R. E., Murray, C. N., Shepard, L. E. and Spijkstra, A. E. The ESOPE international expedition, geoscience investigations of two North Atlantic abyssal plains. Office for official publications of the European community. Luxembourg.

Leinen, M. 1987. The origin of paleochemical signatures in North Pacific pelagic clays: partitioning experiments. Geochimica et Cosmochimica Acta, 51:305-319.

Leinen, M. and Pisias, N. 1984. An objective technique for determining end-member compositions and for partitioning sediments according to their sources. Geochimica et Cosmochimica Acta, 48:47-62.

Leinen, M., Prospero, J. M., Arnold, E. and Blank, M. 1994. Mineralogy of aeolian dust reaching the North Pacific Ocean 1. Sampling and analysis. Journal of Geophysical Research, 99:10. 21,017-21,023.

Merrill, J., Arnold, E., Leinen, M. and Weaver, C. 1994. Mineralogy of aeolian dust reaching the North Pacific Ocean 2. Relationship of mineral assemblages to atmospheric transport patterns. Journal of Geophysical Research, 99:21,025-21,032.

Merrill, J. T. 1989. Atmopheric Long-range Transport to the Pacific Ocean. 15-49. In: Duce, R. A. SEAREX: The Sea/Air Exchange Program. Academic Press. San Diego. 404 pages.

Merrill, J. T., Bleck, R. and Avila, L. 1985. Modeling atmospheric transport to the Marshall Islands. Journal of Geophysical Research, 90:2,927-12,936.

Merrill, J. T., Uematsu, M. and Bleck, R. 1989. Meteorological analysis of long range transport of mineral aerosols over the North Pacific. Journal of Geophysical Research, 94:8584-8598.

Murray, R. W. and Leinen, M. 1993. Chemical transport to the seafloor of the equatorial Pacific Ocean across a latitudinal transect at 135°W: tracking sedimentary major, trace and rare earth element fluxes at the Equator and the intertropical convergence zone. Geochimica et Cosmochimica Acta, 57:4,141-4,163.

Oldfield, F., Hunt, A., Jones, M. D. H., Chester, R., Dearing, J. A., Olsson, L. and Propero, J. M. 1985. Magnetic differentiation of atmospheric dusts. Nature, 317:516-518.

Parrington, J. R. and Zoller, W. H. 1984. Diurnal and longer-term changes in the composition of atmospheric particles at Mauna Loa, Hawaii. Journal of Geophysical Research, 89:2,522-2,534.

Parrington, J. R., Zoller, W. H. and Aras, N. K. 1983. Asian dust: seasonal transport to the Hawaiian Islands. Science, 220:195-197.

Prospero, J. M. and Bonatti, E. 1969. Continental dust in the atmosphere of the eastern equatorial Pacific. Journal of Geophysical Research, 74:3362-3371.

Prospero, J. M. and Nees, R. T. 1977. Dust concentration in the atmosphere of the equatorial North Atlantic: Possible relationship to the Sahelian Drought. Science, 196:1196-1198.

Prospero, J. M., Uematsu, M. and Savoie, D. L. 1989. Mineral aerosol transport to the Pacific Ocean. 188-218. In: Duce, R. A. SEAREX: The Sea/Air Exchange Program. Academic Press. San Diego. 404 pages.

Rea, D. K. 1994. The paleoclimatic record provided by eolian deposition in the deep sea: the geologic history of wind. Reviews of Geophysics, 32:159 - 195.

Rea, D. K. and Hovan, S. A. 1995. Grain size distributions and depositional processes of the mineral component of abyssal sediments: lessons from the North Pacific. Paleoceanography, 10:251-258.

Robinson, S. G. 1986. The late Pleistocene palaeoclimatic record of North Atlantic deep-sea sediments revealed by mineral magnetic measurements. Physics of the Earth and Planetary Interiors, 42:22-47.

Schneider, B., Tindale, N. W. and Duce, R. A. 1990. Dry deposition of Asian mineral dust over the central North Pacific. Journal of Geophysical Research, 95:9,873-9,878.

Uematsu, M., Duce, R. A. and Prospero, J. M. 1985. Deposition of atmospheric mineral particles in the North Pacific Ocean. Journal of Atmospheric Chemistry, 3:123-138.

Uematsu, M., Duce, R. A., Prospero, J. M., Chen, L. Q. and Merrill, J. T. 1983. Transport of mineral aerosol from Asia to the North Pacific Ocean. Journal of Geophysical Research, 88:5343-5352.

Table 1. Sampling locations for aerosol mesh samples.

Cruise	Mesh	Start Date	Time	Position	Stop Date	Time	Position	Sample Time (hours)
Moana Wave	1	May 3, 1986	23:22	31°45'N, 156°26'W	May 5, 1986	04:05	32°59'N, 154°32'W	28.72
	2	May 5, 1986	04:05	32°59'N, 154°32'W	May 6, 1986	23:45	32°60'N, 153°09'W	43.67
	3	May 6, 1986	23:45	33°00'N, 153°09'W	May 9, 1986	01:31	32°43'N, 151°41'W	49.77
	4	May 9, 1986	01:31	32°43'N, 151°41'W	May 9, 1986	16:45	34°49'N, 150°19'W	15.38
	5	May 11, 1986	00:30	42°44'N, 151°02'W	May 12, 1986	17:09	43°52'N, 153°07'W	40.65
	6	May 15, 1986	20:44	49°29'N, 152°08'W	May 17, 1986	21:10	57°42'N, 152°05'W	48.43
	7	May 20, 1986	00:43	52°25'N, 154°20'W	May 21, 1986	10:21	47°40'N, 158°32'W	33.63
	8	May 27, 1986	23:54	35°47'N, 170°21'W	June 1, 1986	21:35	25°11'N, 154°55'W	117.68
Adios	1	March 25, 1987	14:33	25°55'N, 155°00'W	March 25,1987	20:10	25°57'N, 154°57'W	43.12
		March 30, 1987	12:30	26°00'N, 155°00'W	April 1, 1987	02:00	26°15'N, 155°00'W	-
	2	April 1, 1987	13:30	26°15'N, 155°26'W	April 4, 1987	11:10	26°14'N, 155°00'W	69.67
	3	April 4, 1987	11:15	26°14'N, 155°00'W	April 6, 1987	10:20	26°10'N, 154°50'W	47.08
	4	April 6, 1987	10:25	26°10'N, 154°50'W	April 10, 1987	10:55	26°04'N, 154°54'W	96.50
	5	April 10, 1987	10:55	26°04'N, 154°54'W	April 12, 1987	12:15	26°25'N, 154°55'W	49.33
	6	April 12, 1987	12:20	26°25'N, 154°55'W	April 15, 1987	12:45	25°54'N, 154°51'W	72.42

Table 2. Sampling locations for pumped aerosol samples.

Cruise	Sample	Start Date	Time	Position	Stop Date	Time	Position
Leg 1	HV1	May 1, 1986	13:09	25.74°N, 155.16°W	May 3, 1986	08:30	30.33°N, 157.82°W
	HV3, HV7*, CI9	May 3, 1986	21:01	31.21°N, 157.01°W	May 4, 1986	09:47	31.78°N, 156.41°W
	HV15, CI17	May 4, 1986	19:40	32.57°N, 155.67°W	May 6, 1986	10:30	33.16°N, 154.01°W
	HV21, CI25	May 6, 1986	11:36	33.16°N, 154.01°W	May 8, 1986	14:00	32.45°N, 152.37°W
	HV23*, CI27*	May 6, 1986	11:36	33.16°N, 154.01°W	May 13, 1986	10:03	44.70°N, 152.92°W
	HV31, CI33	May 8, 1986	18:14	32.74°N, 152.07°W	May 13, 1986	10:03	44.70°N, 152.92°W
	CI39, HV43*, HV45	May 13, 1986	11:52	44.70°N, 152.92°W	May 17, 1986	08:30	54.16°N, 152.08°W
	HV53, CI59, CI61*	May 19, 1986	16:16	54.11°N, 152.62°W	May 25, 1986	08:30	38.53°N, 167.99°W
Leg 2	HV181*	July 3, 1986	16:28	37.00°N, 168.20°W	July 9, 1986	10:00	33.00°N, 170.48°W
	HV177, CI183	July 3, 1986	16:28	37.00°N, 168.20°W	July 6, 1986	10:00	36.62°N, 168.98°W
	HV195, HV197*, CI199	July 6, 1986	13:51	37.45°N, 170.00°W	July 9, 1986	10:00	33.00°N, 170.48°W

HV = High volume sample
CI = Cascade impactor sample
* = analyzed for mineralogy

Table 3. Sample mass for aerosol mesh samples.

Cruise	Kite	Mesh	Exposure Time (Hours)	Total Weight (g)	Dust/hour (g/hr)	Geometric Mean Grain Diameter (μm)
Moana Wave	1	A	28.72	0.21346	0.00743	3.05
	1	B	28.72	0.22456	0.00782	3.07
	2	A	43.67	0.15191	0.00348	3.15
	2	B	43.67	0.08657	0.00198	3.10
	3	A	49.77	0.09028	0.00181	4.51
	3	B	49.77	0.11123	0.00223	4.07
	4	A	15.38	0.01642	0.00107	
	4	B	15.38	0.02246	0.00146	
	5	A	40.65	0.00474	0.00012	
	5	B	40.65	0.00693	0.00017	
	6	A	48.43	0.06032	0.00125	6.89
	6	B	48.43	0.05700	0.00118	7.58
	7	A	33.63	0.01017	0.00030	8.85
	7	B	33.63	0.01423	0.00042	6.40
	8	A	117.68	0.18034	0.00153	5.92
	8	B	117.68	0.15916	0.00135	5.00
ADIOS	1	A	43.12	0.41199	0.00955	3.15
	1	B	43.12	0.41021	0.00951	3.66
	2	A	69.67	0.88519	0.01271	2.94
	2	B	69.67	0.85981	0.01234	3.12
	3	A	47.08	0.28981	0.00616	3.76
	3	B	47.08	0.28734	0.00610	3.83
	4	A	96.50	0.07019	0.00073	4.48
	4	B	96.50	0.08405	0.00087	3.68
	5	A	49.33	0.09898	0.00201	4.30
	5	B	49.33	0.14353	0.00291	4.74
	6	A	72.42	0.14815	0.00205	3.61
	6	B	72.42	0.20657	0.00285	3.33
Averages						
Group			54	0.18949	0.00362	4.42
Moana Wave			47.24	0.08811	0.00210	5.13
ADIOS			63.02	0.32465	0.00565	3.72

Table 4. Rock magnetic measurements for aerosol mesh samples.

Cruise	Kite	Mesh	X_{lf} ($\mu m^3/g$)	X_{lf} ($\mu m^3/g$)	X_{lf}/X_{hf}	X_{arm} ($\mu m^3/g$)	X_{arm}/X	SIRM ($\mu A/m^2/g$)	IRM-0.3T ($\mu A/m^2/g$)	SIRM/ ARM	S-ratio	HIRM ($\mu A/m^2/g$)
Moana Wave	1	A	0.49	0.51	0.96	4.40	8.69	12426	-10762	35.51	0.87	832
	1	B	0.72	0.75	0.96	5.02	6.66	15569	-13994	39.00	0.90	788
	2	A	0.47	0.57	0.83	5.87	10.37	16050	-14372	34.36	0.90	839
	2	B	0.41	0.43	0.95	5.43	12.63	14438	-13119	33.43	0.91	660
	3	A	0.45	0.57	0.79	5.74	10.00	16329	-14599	35.75	0.89	865
	3	B	0.73	0.74	0.98	6.06	8.16	18483	-16563	38.29	0.90	960
	4	A	1.06	1.14	0.93	4.69	4.13	14794	-13354	39.59	0.90	720
	4	B	0.90	0.90	1.00	3.80	4.23	14753	-13088	48.81	0.89	833
	5	A	1.16	0.84		4.20	4.98	13508	-12354	40.43	0.91	577
	5	B	0.83	0.94	0.88	4.23	4.51	16291	-15445	48.41	0.95	423
	6	A	2.39	2.49	0.96	15.74	6.31	68838	-62631	54.96	0.91	3103
	6	B	3.20	3.32	0.96	19.18	5.78	78460	-74866	51.38	0.95	1797
	7	A	-0.84	-1.18	0.71	10.76	-9.15	29965	-27993	35.00	0.93	986
	7	B	-0.25	-0.25	0.99	13.58	-53.36	32079	-30928	29.68	0.96	575
	8	A	1.09	1.19	0.92	7.78	6.53	26093	-24090	42.12	0.92	1001
	8	B	1.14	1.15	0.99	7.08	6.17	25532	-24719	45.33	0.97	407

Table 4. Continued.

Cruise	Kite	Mesh	X_{lf} ($\mu m^3/g$)	X_{lf} ($\mu m^3/g$)	X_{lf}/X_{hf}	X_{arm} ($\mu m^3/g$)	X_{arm}/X	SIRM ($\mu A/m^2/g$)	IRM-0.3T ($\mu A/m^2/g$)	SIRM/ ARM	S-ratio	HIRM ($\mu A/m^2/g$)
ADIOS	1	A	1.64	1.70	0.97	7.30	4.30	30970	-26410	53.27	0.85	2280
	1	B	1.62	1.65	0.98	6.43	3.89	30660	-26013	59.88	0.85	2323
	2	A	0.90	0.94	0.96	4.74	5.04	15593	-13585	41.31	0.87	1004
	2	B	0.87	0.92	0.94	4.69	5.08	13720	-12876	36.74	0.94	422
	3	A	0.90	0.96	0.94	4.60	4.80	13016	-11267	35.56	0.87	875
	3	B	0.83	0.88	0.94	3.93	4.45	8288	-9155	26.49		
	4	A	0.26	0.30	0.85	4.02	13.23	10859	-9065	33.94	0.83	897
	4	B	0.00	0.25		4.18	17.01	11241	-9579	33.77	0.85	831
	5	A	0.46	0.46	1.01	4.70	10.29	11537	-10123	30.81	0.88	707
	5	B	0.22	0.29	0.76	4.33	14.80	13078	-11619	37.91	0.89	729
	6	A	0.20	0.20	1.00	5.76	28.28	10223	-9061	22.31	0.89	581
	6	B	0.29	0.21		6.27	29.31	10657	-9351	21.35	0.88	653
Averages												
Group			0.79	0.82	0.93	6.59	6.33	21195	-19321	38.76	0.90	988
Moana Wave			0.87	0.88	0.92	7.72	2.29	25851	-23930	40.75	0.92	960
Adios			0.68	0.73	0.94	5.08	11.71	14987	-13175	36.11	0.87	1027

Table 5. Mineralogy of aerosol mesh samples.

Cruise	Kite	Mesh	<2μm Smectite	<2μm Illite	<2μm Kaolinite	<2μm Chlorite	<2μm Quartz	<2μm Plagioclase
Moana Wave	1	A	2.49	68.97	12.87	4.56	5.17	5.94
	1	B	2.85	65.49	12.34	4.95	7.28	7.08
	2	A	2.69	70.10	10.54	3.81	7.02	5.85
	2	B	2.44	67.07	11.72	4.77	7.27	6.73
	3	A	3.84	76.99	8.69	4.42	3.31	2.74
	3	B	3.28	70.49	12.13	4.91	2.77	6.42
	4	A						
	4	B						
	5	A						
	5	B						
	6	A	2.43	56.28	0.00	5.65	9.54	26.10
	6	B	2.20	50.39	10.18	5.91	8.22	23.11
	7	A						
	7	B						
	8	A	4.73	68.16	8.65	6.11	5.77	6.57
	8	B	4.42	71.49	0.00	8.11	9.17	6.82
ADIOS	1	A	2.18	61.67	18.05	3.95	10.81	3.34
	1	B	3.44	79.37	0.00	7.21	9.99	0.00
	2	A	2.36	57.62	14.30	3.11	10.36	12.25
	2	B	2.45	53.94	16.30	2.79	9.48	15.04
	3	A	2.47	62.98	17.53	3.65	8.17	5.19
	3	B	3.67	62.76	13.04	3.86	7.22	9.45
	4	A	2.37	68.16	11.69	4.80	5.74	7.23
	4	B	2.55	67.46	12.25	5.07	6.56	6.11
	5	A	2.43	86.58	0.00	6.08	4.91	0.00
	5	B	3.10	82.77	0.00	7.43	6.70	0.00
	6	A	2.35	80.16	0.00	8.09	9.40	0.00
	6	B	0.97	70.21	16.23	3.38	9.21	0.00
Averages								
Group			2.81	68.14	9.39	5.12	7.46	7.09
Moana Wave			3.14	66.54	8.71	5.32	6.55	9.74
ADIOS			2.53	69.47	9.95	4.95	8.21	4.88

Table 5. Continued.

Cruise	Kite	Mesh	2-20μm Smectite	2-20μm Illite	2-20μm Kaolinite	2-20μm Chlorite	2-20μm Quartz	2-20μm Plagioclase
Moana Wave	1	A	2.23	60.58	0.00	5.62	18.80	12.76
	1	B	2.49	53.42	8.77	3.83	17.60	13.89
	2	A	2.69	54.25	8.89	3.61	17.01	13.56
	2	B	1.95	53.17	10.56	3.85	15.78	14.69
	3	A	2.61	62.37	6.35	4.95	12.37	11.35
	3	B	2.77	56.08	10.88	3.81	14.36	12.10
	4	A						
	4	B						
	5	A						
	5	B						
	6	A	1.20	32.80	0.00	4.53	17.44	44.03
	6	B	2.92	29.58	0.00	5.03	18.08	44.39
	7	A						
	7	B						
	8	A	1.81	40.70	11.87	5.76	20.90	18.94
	8	B	3.74	29.58	0.00	10.85	28.34	27.48
ADIOS	1	A	1.87	41.01	7.36	3.73	27.52	18.52
	1	B	1.37	34.75	14.15	3.02	25.43	21.28
	2	A	1.69	46.53	6.05	4.80	22.25	18.69
	2	B	1.61	45.15	4.11	3.62	26.14	19.37
	3	A	1.89	56.54	5.66	4.35	19.11	12.45
	3	B	0.86	43.09	8.53	3.64	22.73	21.15
	4	A	2.34	57.25	12.13	4.65	13.94	9.69
	4	B	2.89	60.20	10.52	4.74	11.97	9.69
	5	A	2.07	61.74	0.00	5.92	15.32	14.96
	5	B	1.97	51.51	8.35	3.95	19.32	14.89
	6	A	2.61	47.98	11.54	3.62	20.14	14.11
	6	B	2.47	48.80	7.17	4.29	21.91	15.36
Averages								
Group			2.18	48.50	6.95	4.65	19.38	18.33
Moana Wave			2.44	47.25	5.73	5.19	18.07	21.32
ADIOS			1.97	49.55	7.96	4.19	20.48	15.85

Table 5. Continued.

Cruise	Kite	Mesh	Bulk Smectite	Bulk Illite	Bulk Kaolinite	Bulk Chlorite	Bulk Quartz	Bulk Plagioclase
Moana Wave	1	A						
	1	B						
	2	A						
	2	B						
	3	A						
	3	B						
	4	A	3.00	70.65	0.00	5.50	9.77	11.08
	4	B	3.14	60.63	7.93	5.12	10.21	12.97
	5	A	7.04	91.85	0.00	0.00	1.10	0.00
	5	B	3.40	91.84	0.00	0.00	4.76	0.00
	6	A						
	6	B						
	7	A	12.53	0.00	0.00	0.00	87.47	0.00
	7	B	8.37	0.00	0.00	20.32	51.19	20.13
	8	A						
	8	B						
ADIOS	1	A						
	1	B						
	2	A						
	2	B						
	3	A						
	3	B						
	4	A						
	4	B						
	5	A						
	5	B						
	6	A						
	6	B						
Averages								
Group			6.25	52.50	1.32	5.16	27.42	7.36
Moana Wave			6.25	52.50	1.32	5.16	27.42	7.36
ADIOS								

Table 6. Mineralogy of pumped aerosol samples.

Sample	Stage	Sample Size (cm^2)	Weight (mg)	Ash ($\mu g/m^3$)	Smectite	Illite	Kaolinite	Chlorite	Quartz	Plagioclase
HV7		9.8	0.3	35.5	1.3	75.2	2.3	0.6	4.4	16.3
HV23		4.3	1.4	15.8	1.3	77.8	7.4	0.5	4.7	8.3
CI27			9.2	10.8	3.7	61.7	5.3	1.3	5.9	22.1
HV43		95.0	9.8	9.3	0.0	30.1	0.8	0.2	7.5	61.4
CI61			8.4	14.0	0.2	14.4	1.7	0.7	7.1	75.9
HV181		12.7	1.9	8.3	0.0	39.6	4.2	1.4	1.3	53.5
HV197		82.5	9.6	12.1	2.1	49.2	6.3	5.7	6.4	30.3
CI27	0		0.8	0.8	2.8	46.1	0.8	0.1	3.6	46.7
CI27	1		3.0	3.2	1.4	45.4	4.2	1.4	4.0	43.7
CI27	2		3.1	3.3	2.5	75.9	8.4	2.1	5.6	5.5
CI27	3		1.2	1.3	2.6	77.0	6.3	1.4	4.0	8.8
CI27	4		0.7	0.7	0.0	82.4	7.6	0.2	4.4	5.5
CI27	5		0.2	0.2	2.9	82.8	10.5	0.0	3.8	0.0
CI27	6	6.8	0.2	1.3	16.2	45.4	0.0	0.8	15.9	21.7
CI61	0		1.3	1.8	0.0	3.6	0.0	0.0	31.7	64.7
CI61	1		2.3	3.5	0.0	7.6	0.0	1.3	2.2	88.9
CI61	2		2.7	4.1	0.0	12.4	5.6	1.2	2.4	78.4
CI61	3		1.1	1.7	0.1	3.5	0.6	0.1	13.4	82.4
CI61	4		0.5	0.8	0.0	0.0	0.0	0.1	1.7	98.2
CI61	5		0.4	0.6	0.0	1.9	0.0	0.1	0.4	97.7
CI61	6	5.1	0.1	1.5	1.6	73.7	0.0	0.5	0.5	23.7

Table 7. Replicate comparisons (p-values) for pumped aerosol samples.

Replicate Comparison		Ash ($\mu g/m^3$)	Smectite	Illite	Kaolinite	Chlorite	Quartz	Plagioclase
Sample								
	HV7	0.11	0.11	0.23	0.82	0.00	0.99	0.17
	HV23	0.51	0.03	0.29	0.76	0.86	0.03	0.02
	CI27	0.39	0.21	0.28	0.50	0.31	0.29	0.47
	HV43	0.59		0.29	0.16	0.59	0.11	0.59
	CI61	0.77	0.50	0.22	0.42	0.48	0.29	0.79
	HV181	0.08	0.71	0.03	0.01	0.54	0.69	0.86
	HV197	0.59	0.29	0.11	0.16	0.59	0.11	0.11
Stage								
	0	0.47	0.56	0.47			0.72	0.27
	1	0.14		0.47		0.47	1.00	0.72
	2	0.72		0.47	0.14	0.29	0.14	0.27
	3	0.14	0.28	0.14	0.79	0.79	0.27	0.72
	4	1.00				0.79	0.47	0.47
	5	0.14						
Sample > $4cm^2$								
	HV7	0.59	0.16	0.59	1.00	0.16	0.41	0.59
	HV181	0.07		0.78	0.08	0.59	0.78	0.10

Table 8. Elemental analyses and mass median diameter for pumped aerosol samples (pers. comm., Arimoto, 1995).

Sample	Volume Air (m^3)	Al ($\mu g/m^3$)	Fe ($\mu g/m^3$)	Na ($\mu g/m^3$)	Cl ($\mu g/m^3$)	Mass Median Diameter (μm)
HV1	1978	0.280	0.153	2.240	2.010	
HV3	167	0.333	0.237	1.430		
CI9	172		0.160			
HV15	2528	0.104	0.069	3.030	3.200	
CI17	2672	0.075	0.051	2.402	3.776	4.94
HV21	2672	0.093	0.059	4.120	5.650	
CI25	3480	0.081	0.048	3.260	5.574	3.85
HV31	5631	0.136	0.092	1.710	2.460	
CI33	5283	0.147	0.086	1.434	2.295	4.54
CI39	3597	0.034	0.026	1.789	2.785	2.72
HV45	3417	0.046	0.028	2.340	2.890	
HV53	6307	0.026	0.019	4.040	6.300	
CI59	6624	0.029	0.015	2.012	3.244	2.59
HV67	3964	0.042	0.059	0.958	1.240	
CI73	4079	0.062	0.042	1.403	2.227	5.33
HV81	3161	0.061	0.046	1.910	2.000	
CI83	6513	0.086	0.035	1.408	2.109	3.78
HV89	3195	0.061	0.050	1.560	1.110	
HV177	3310	0.009	0.007	0.783	0.868	
CI183	3532	0.068	0.007	0.436	0.347	
HV195	3601	0.008	0.006	1.740	2.440	
CI199	3785	0.009	0.006	1.430	2.306	

Table 9. Trajectory synthesis for Moana Wave aerosol samples.

Mesh	Pumped Sample	Date	Time	Potential Temperature Surface (K)	Altitude (start to finish) (hPa)	Open ocean	Asia >60°	Asia >50°	Asia >40°	Asia >30°	Asia >20°
		3-May-86	00	290	550 to bl		(130)10	(120) 9	(130) 8		
K1	HV7	3-May-86	12	290	550 to bl				(140) 8		
K1	HV7	4-May-86	00	290	475 to bl		(100) 9	(130) 4	(120) 9		
K1		4-May-86	12	290	550 to bl		(120) 6	(130) 5	(140) 4		
K2		5-May-86	00	285	700 to bl						
K2		5-May-86	12	285	650 to bl						
K2	HV23/CI27	6-May-86	00	290	550 to bl						
K2	HV23/CI27	6-May-86	12	290	500 to bl						
K3	HV23/CI27	7-May-86	00	290	550 to bl						
K3	HV23/CI27	7-May-86	12	290	500 tobl		(140) 9				
K3	HV23/CI27	8-May-86	00	290	600 to bl						
K3	HV23/CI27	8-May-86	12	290	900 to bl						
K4	HV23/CI27	9-May-86	00	290	900 to bl						
K4	HV23/CI27	9-May-86	12	290	600 to bl		(140) 9				
	HV23/CI27	10-May-86	00	290	600 to bl	X					
	HV23/CI27	10-May-86	12	290	600 to bl	X					
K5	HV23/CI27	11-May-86	00	290	700 to bl	X					
K5	HV23/CI27	11-May-86	12	290	700 to bl	X					
K5	HV23/CI27	12-May-86	00	290	700 to bl	X					
K5	HV23/CI27	12-May-86	12	290	700 to bl	X					
	HV23/CI27	13-May-86	00	290/295	bl	X					
	HV43	13-May-86	12	290/295	bl	X					
	HV43	14-May-86	00	285	700 to bl	X					
	HV43	14-May-86	12	280	800 to bl			(130) 6			
K6	HV43	15-May-86	00	285	700 to bl			(130) 7			

Table 9. Continued.

Mesh	Pumped Sample	Date	Time	Potential Temperature Surface (K)	Altitude (start to finish) (hPa)	Open ocean	Asia >60°	Asia >50°	Asia >40°	Asia >30°	Asia >20°
K6	HV43	15-May-86	12	285	700 to bl			(130) 7			
K6	HV43	16-May-86	00	280	900 to bl						
K6	HV43	16-May-86	12	275	800 to bl						
K6	HV43	17-May-86	00	280	800 to 900						
K6		17-May-86	12	280	800 to 900						
		18-May-86	00	nd							
		18-May-86	12	nd							
		19-May-86	00	nd							
	CI61	19-May-86	12	nd							
K7	CI61	20-May-86	00	280	750 to 850						
K7	CI61	20-May-86	12	280	800 to 900						
K7	CI61	21-May-86	00	280	800 to bl						
	CI61	21-May-86	12	285	900 to bl						
	CI61	22-May-86	00	280	900to bl						
	CI61	22-May-86	12	285	700 to 900			(130) 9			
	CI61	23-May-86	00	295	500 to 700		(90) 8	(110) 6	(120) 5		
	CI61	23-May-86	12	290	900 to bl				(130) 6		
	CI61	24-May-86	00	280	800 to bl						
	CI61	24-May-86	12	285	700 to bl						
	CI61	25-May-86	00	295	600 to bl			(120) 8	(130) 6		
		25-May-86	12	300	900 to bl					(120) 9	
		26-May-86	00	300	700 to 900			(80) 10		(120) 9	
		26-May-86	12	295	bl to bl	X					
		27-May-86	00	295	bl	X					
		27-May-86	12	295	bl	X					

Table 9. Continued.

Mesh	Pumped Sample	Date	Time	Potential Temperature Surface (K)	Altitude (start to finish) (hPa)	Open ocean	Asia >60°	Asia >50°	Asia >40°	Asia >30°	Asia >20°
		27-May-86	00	300	700 to 900	X			(130)10		
K8		27-May-86	12	300	950 to bl	X					
K8		28-May-86	00	295	700 to bl			(120)10		(130)10	
K8		28-May-86	12	295	700 to bl				(130)10		
K8		29-May-86	00	295	900 to bl						
K8		29-May-86	12	295	500 to bl						
K8		30-May-86	00	295	500 to bl						
K8		30-May-86	12	295	650 to bl						
K8		31-May-86	00	nd							
K8		31-May-86	12	nd							
K8		1-Jun-86	00	nd							
K8		1-Jun-86	12	nd							

Table 9. Continued.

Mesh	Pumped Sample	Date	Time	Potential Temperature Surface (K)	Altitude (start to finish) (hPa)	Japan	Kamchatka	Siberia	Aleutians	Alaska	Canada
		3-May-86	00	290	550 to bl	7.0	5.5		4.0		
K1	HV7	3-May-86	12	290	550 to bl	8.0	6.0		4.0		
K1	HV7	4-May-86	00	290	475 to bl	8.5	5.0				
K1		4-May-86	12	290	550 to bl	4.0	3.5		2.0		6.0
K2		5-May-86	00	285	700 to bl			8.5	7.0		
K2		5-May-86	12	285	650 to bl					7.0	5.0
K2	HV23/CI27	6-May-86	00	290	550 to bl						6.0
K2	HV23/CI27	6-May-86	12	290	500 to bl				8.0		6.0
K3	HV23/CI27	7-May-86	00	290	550 to bl				8.0		8.0
K3	HV23/CI27	7-May-86	12	290	500 tobl	8.0	7.0		6.0		9.0
K3	HV23/CI27	8-May-86	00	290	600 to bl				10.0		
K3	HV23/CI27	8-May-86	12	290	900 to bl	9.0	6.0		4.5		
K4	HV23/CI27	9-May-86	00	290	900 to bl	10.0	6.5	9.0	5.5		
K4	HV23/CI27	9-May-86	12	290	600 to bl		6.5				
	HV23/CI27	10-May-86	00	290	600 to bl				8.0		
	HV23/CI27	10-May-86	12	290	600 to bl						
K5	HV23/CI27	11-May-86	00	290	700 to bl						
K5	HV23/CI27	11-May-86	12	290	700 to bl						
K5	HV23/CI27	12-May-86	00	290	700 to bl						
K5	HV23/CI27	12-May-86	12	290	700 to bl						
	HV23/CI27	13-May-86	00	290/295	bl						
	HV43	13-May-86	12	290/295	bl						
	HV43	14-May-86	00	285	700 to bl			4.0	2.0	3.0	
	HV43	14-May-86	12	280	800 to bl	5.5	4.5		1.0		
K6	HV43	15-May-86	00	285	700 to bl	6.5	5.5		2.0		

Table 9. Continued.

Mesh	Pumped Sample	Date	Time	Potential Temperature Surface (K)	Altitude (start to finish) (hPa)	Japan	Kamchatka	Siberia	Aleutians	Alaska	Canada
K6	HV43	15-May-86	12	285	700 to bl	6.5	5.0		2.0		
K6	HV43	16-May-86	00	280	900 to bl				1.0	2.0	
K6	HV43	16-May-86	12	275	800 to bl				0.5	1.0	
K6	HV43	17-May-86	00	280	800 to 900					1.0	
K6		17-May-86	12	280	800 to 900					3.0	
		18-May-86	00	nd							
		18-May-86	12	nd							
		19-May-86	00	nd							
	CI61	19-May-86	12	nd							
K7	CI61	20-May-86	00	280	750 to 850					5.0	
K7	CI61	20-May-86	12	280	800 to 900			3.0	0.5		
K7	CI61	21-May-86	00	280	800 to bl			3.0	1.0		
	CI61	21-May-86	12	285	900 to bl		7.0	5.0	3.0		
	CI61	22-May-86	00	280	900to bl			5.0	2.5		
	CI61	22-May-86	12	285	700 to 900		9.0	5.0	2.5		
	CI61	23-May-86	00	295	500 to 700	4.0					
	CI61	23-May-86	12	290	900 to bl	5.0					
	CI61	24-May-86	00	280	800 to bl			7.0		4.0	
	CI61	24-May-86	12	285	700 to bl			7.0	5.0	6.0	
	CI61	25-May-86	00	295	600 to bl	4.0					
		25-May-86	12	300	900 to bl	6.5					
		26-May-86	00	300	700 to 900	7.0					
		26-May-86	12	295	bl to bl						
		27-May-86	00	295	bl						
		27-May-86	12	295	bl						

Table 9. Continued.

Mesh	Pumped Sample	Date	Time	Potential Temperature Surface (K)	Altitude (start to finish) (hPa)	Japan	Kamchatka	Siberia	Aleutians	Alaska	Canada
		27-May-86	00	300	700 to 900	9.0					
K8		27-May-86	12	300	950 to bl						
K8		28-May-86	00	295	700 to bl	7.5			3.0		
K8		28-May-86	12	295	700 to bl	9.0			3.0		
K8		29-May-86	00	295	900 to bl				3.0	10.0	
K8		29-May-86	12	295	500 to bl				2.5	3.5	9.0
K8		30-May-86	00	295	500 to bl			10.0	3.5	5.0	
K8		30-May-86	12	295	650 to bl				2.5	4.0	
K8		31-May-86	00	nd							
K8		31-May-86	12	nd							
K8		1-Jun-86	00	nd							
K8		1-Jun-86	12	nd							

Table 10. Trajectory synthesis for ADIOS aerosol samples.

Mesh	Date	Time	Potential Temperature Surface (K)	Altitude (start-finish) (hPa)	Open ocean	Asia >60°	Asia >50°	Asia >40°	Asia >30°	Asia >20°
	25-Mar-87	00	300	500 to 850						
K1	25-Mar-87	12	300	500 to 850	X					
	26-Mar-87	00	300	600 to 850	X					
	26-Mar-87	12	295	400 to bl			(90) 10	(130) 8		
	27-Mar-87	00	295	350 to bl		(90) 10	(130) 3-10	(130) 3-10		
	27-Mar-87	12	290	600 to bl				(80-140) 4-10		
	28-Mar-87	00	nd							
	28-Mar-87	12	nd							
	29-Mar-87	00	nd							
	29-Mar-87	12	nd							
	30-Mar-87	00	290	bl	X					
K1	30-Mar-87	12	295	900 to 800	X					
K1	31-Mar-87	00	290	bl	X					
K1	31-Mar-87	12	290	500 to bl				(130) 3		
K1	1-Apr-87	00	285	600 to bl				(140) 3		
K2	1-Apr-87	12	290	600 to bl				(120) 3		
K2	2-Apr-87	00	285	500 to bl	X					
K2	2-Apr-87	12	290	750 to bl				(125) 4		
K2	3-Apr-87	00	290	700 to bl				(130) 5		
K3	3-Apr-87	12	290	700 to bl	X					
K3	4-Apr-87	00	290	700 to bl	X					
K3	4-Apr-87	12	290	650 to bl						
K3	5-Apr-87	00	290	700 to bl						
K3	5-Apr-87	12	295	600 to 900				(130) 7		
K3	6-Apr-87	00	295	500 to bl						

Table 10. Continued.

Mesh	Date	Time	Potential Temperature Surface (K)	Altitude (start-finish) (hPa)	Open ocean	Asia >60°	Asia >50°	Asia >40°	Asia >30°	Asia >20°
K4	6-Apr-87	12	295	500						
K4	7-Apr-87	00	295	450 to bl				(130) 8		
K4	7-Apr-87	12	295	900 to bl	X					
K4	8-Apr-87	00	295	900 to bl	X					
K4	8-Apr-87	12	295	900 to bl	X					
K4	9-Apr-87	00	295	900 to bl	X					
K4	9-Apr-87	12	295	900 to bl	X					
K4	10-Apr-87	00	295	900 to bl	X					
K5	10-Apr-87	12	300	700 to 850					(120) 9	(120) 9
K5	11-Apr-87	00	295	900 to bl	X					
K5	11-Apr-87	12	295	700 to bl					(130) 9	
K5	12-Apr-87	00	300	500 to 800	X		(120) 8			
K6	12-Apr-87	12	300	900 to 800	X					
K6	13-Apr-87	00	300	500 to 800			(120) 8			
K6	13-Apr-87	12	290	500 to bl				(140) 10		
K6	14-Apr-87	00	290	600 to bl			(120) 10	(140) 9		
K6	14-Apr-87	12	290	500 to bl						
K6	15-Apr-87	00	285	700 to bl						
K6	15-Apr-87	12	290	500 to bl		(150) 8				

Table 10. Continued.

Mesh	Date	Time	Potential Temperature Surface (K)	Altitude (start-finish) (hPa)	Japan	Kamchatka	Siberia	Aleutians	Alaska	Canada
	25-Mar-87	00	300	500 to 850	10.0					
K1	25-Mar-87	12	300	500 to 850						
	26-Mar-87	00	300	600 to 850						
	26-Mar-87	12	295	400 to bl	7.0					
	27-Mar-87	00	295	350 to bl		2.5				
	27-Mar-87	12	290	600 to bl	4.0					
	28-Mar-87	00	nd							
	28-Mar-87	12	nd							
	29-Mar-87	00	nd							
	29-Mar-87	12	nd							
	30-Mar-87	00	290	bl						
K1	30-Mar-87	12	295	900 to 800						
K1	31-Mar-87	00	290	bl						
K1	31-Mar-87	12	290	500 to bl	3.0					
K1	1-Apr-87	00	285	600 to bl	3.0					
K2	1-Apr-87	12	290	600 to bl	2.5			1.5		
K2	2-Apr-87	00	285	500 to bl				2.5		
K2	2-Apr-87	12	290	750 to bl	3.0					
K2	3-Apr-87	00	290	700 to bl	4.5					
K3	3-Apr-87	12	290	700 to bl						
K3	4-Apr-87	00	290	700 to bl						
K3	4-Apr-87	12	290	650 to bl	6.0					
K3	5-Apr-87	00	290	700 to bl	7.0					
K3	5-Apr-87	12	295	600 to 900	7.0					
K3	6-Apr-87	00	295	500 to bl	8.0					

Table 10. Continued.

Mesh	Date	Time	Potential Temperature Surface (K)	Altitude (start-finish) (hPa)	Japan	Kamchatka	Siberia	Aleutians	Alaska	Canada
K4	6-Apr-87	12	295	500	7.0					
K4	7-Apr-87	00	295	450 to bl	7.5					
K4	7-Apr-87	12	295	900 to bl						
K4	8-Apr-87	00	295	900 to bl						
K4	8-Apr-87	12	295	900 to bl						
K4	9-Apr-87	00	295	900 to bl						
K4	9-Apr-87	12	295	900 to bl						
K4	10-Apr-87	00	295	900 to bl						
K5	10-Apr-87	12	300	700 to 850	8.0					
K5	11-Apr-87	00	295	900 to bl						
K5	11-Apr-87	12	295	700 to bl	8.0					
K5	12-Apr-87	00	300	500 to 800	7.0					
K6	12-Apr-87	12	300	900 to 800						
K6	13-Apr-87	00	300	500 to 800	7.0					
K6	13-Apr-87	12	290	500 to bl	9.0	7.0				
K6	14-Apr-87	00	290	600 to bl	8.5			5.0		
K6	14-Apr-87	12	290	500 to bl		6.5				
K6	15-Apr-87	00	285	700 to bl				5.0		7.0
K6	15-Apr-87	12	290	500 to bl						

Table 11. Regression coefficients between transport time and mineralogy.

	Asia >60°N	Asia >50°N	Asia >40°N	Asia >30°N	Asia >20°N	Japan	Kamchatka	Aleutians	Canada
n	6	11	13	5	4	16	4	7	5
<2μm Smectite	0.83	0.52	0.55	0.80	0.97	0.67	-0.08	0.04	0.75
<2μm Illite	0.96	0.74	0.77	0.87	0.93	0.80	0.70	0.72	0.44
<2μm Kaolinite	-0.43	-0.65	-0.57	-0.93	-0.77	-0.65	-0.15	0.16	-0.74
<2μm Chlorite	0.86	0.83	0.74	0.95	0.97	0.74	0.16	-0.15	0.68
<2μm Quartz	-0.44	-0.24	-0.44	-0.83	-0.39	-0.63	-0.09	-0.60	-0.29
<2μm Plagioclase	-0.78	-0.54	-0.55	-0.85	-0.65	-0.54	-0.58	-0.66	-0.01
n	5	9	11	3	3	14	4	7	5
2-20μm Smectite	-0.36	-0.31	-0.23	0.97	0.95	-0.26	0.73	0.49	1.00
2-20μm Illite	0.96	0.49	0.63	0.00	0.80	0.71	0.23	0.70	-0.51
2-20μm Kaolinite	0.71	0.26	0.31	-0.89	-0.13	0.12	0.81	0.86	-0.10
2-20μm Chlorite	0.95	0.78	0.74	0.63	0.59	0.66	-0.91	-0.37	0.69
2-20μm Quartz	0.19	0.06	-0.11	0.58	0.56	-0.24	-0.03	-0.62	0.29
2-20μm Plagioclase	-0.77	-0.39	-0.47	-0.44	-0.68	-0.47	-0.40	-0.66	0.52

Figure 1. Location of aerosol samples.

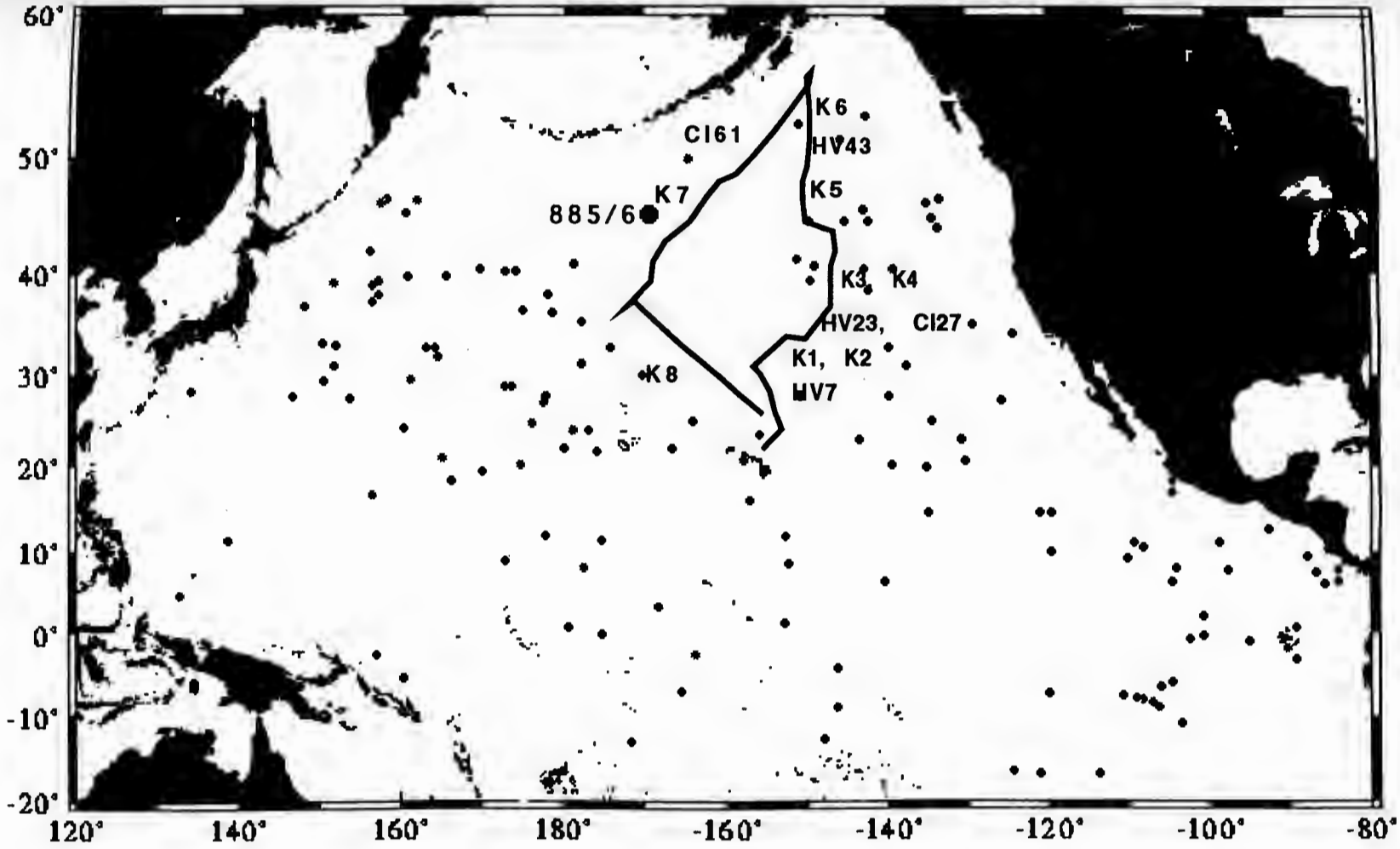
60°
50°
40°
30°
20°
10°
0°
-10°
-20°
120°
140°
160°
180°
-160°
-140°
-120°
-100°
-80°
K6
CI61
HV43
K5
K7
885/6
K3
K4
HV23,
CI27
K1, K2
K8
HV7

Figure 2. Dust concentration for mesh samples. Open symbols, mesh A, closed symbols, mesh B.

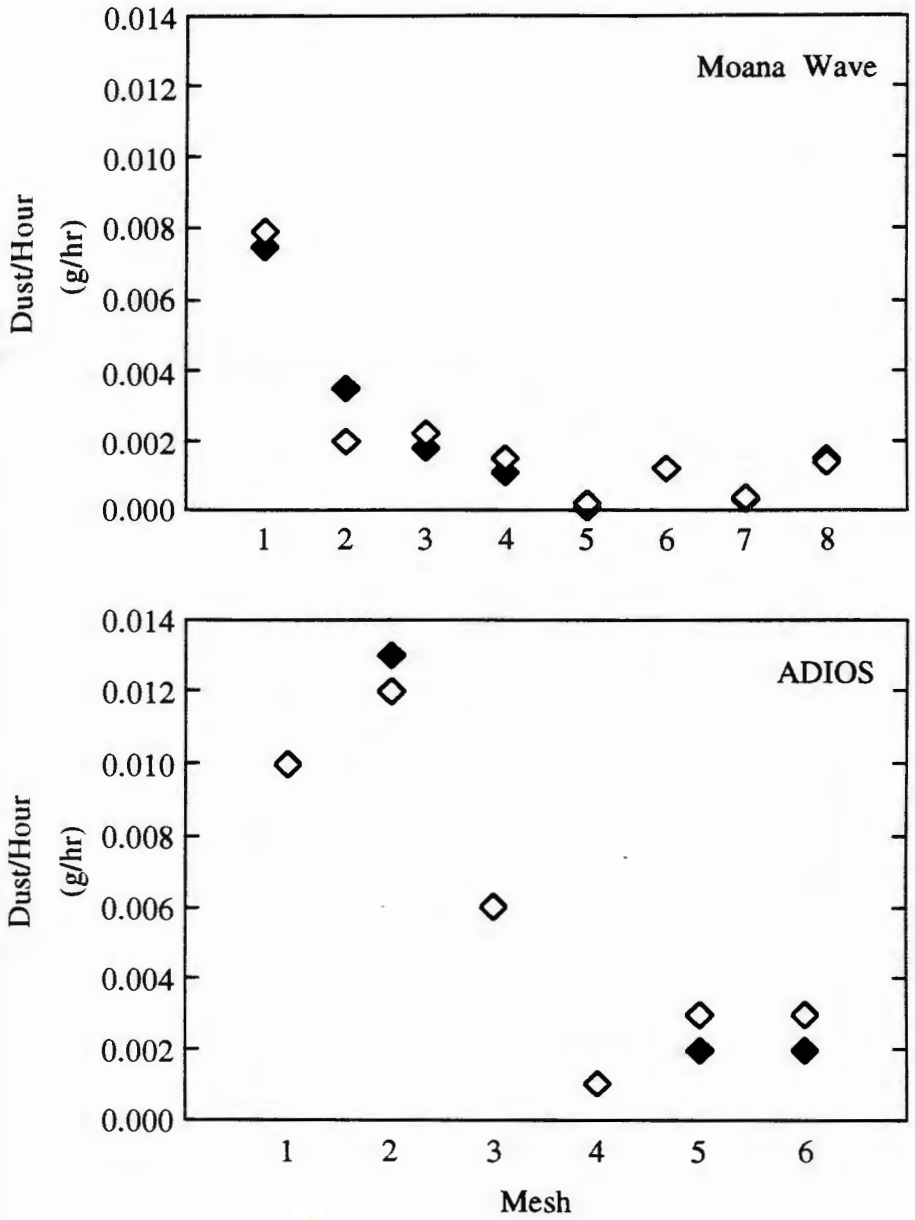
Moana Wave
Dust/Hour (g/hr)
0.014
0.012
0.010
0.008
0.006
0.004
0.002
0.000
1
2
3
4
5
6
7
8
ADIOS
Dust/Hour (g/hr)
0.014
0.012
0.010
0.008
0.006
0.004
0.002
0.000
1
2
3
4
5
6
Mesh

Figure 3. Grain size for mesh samples. Open symbols, mesh A, closed symbols, mesh B.

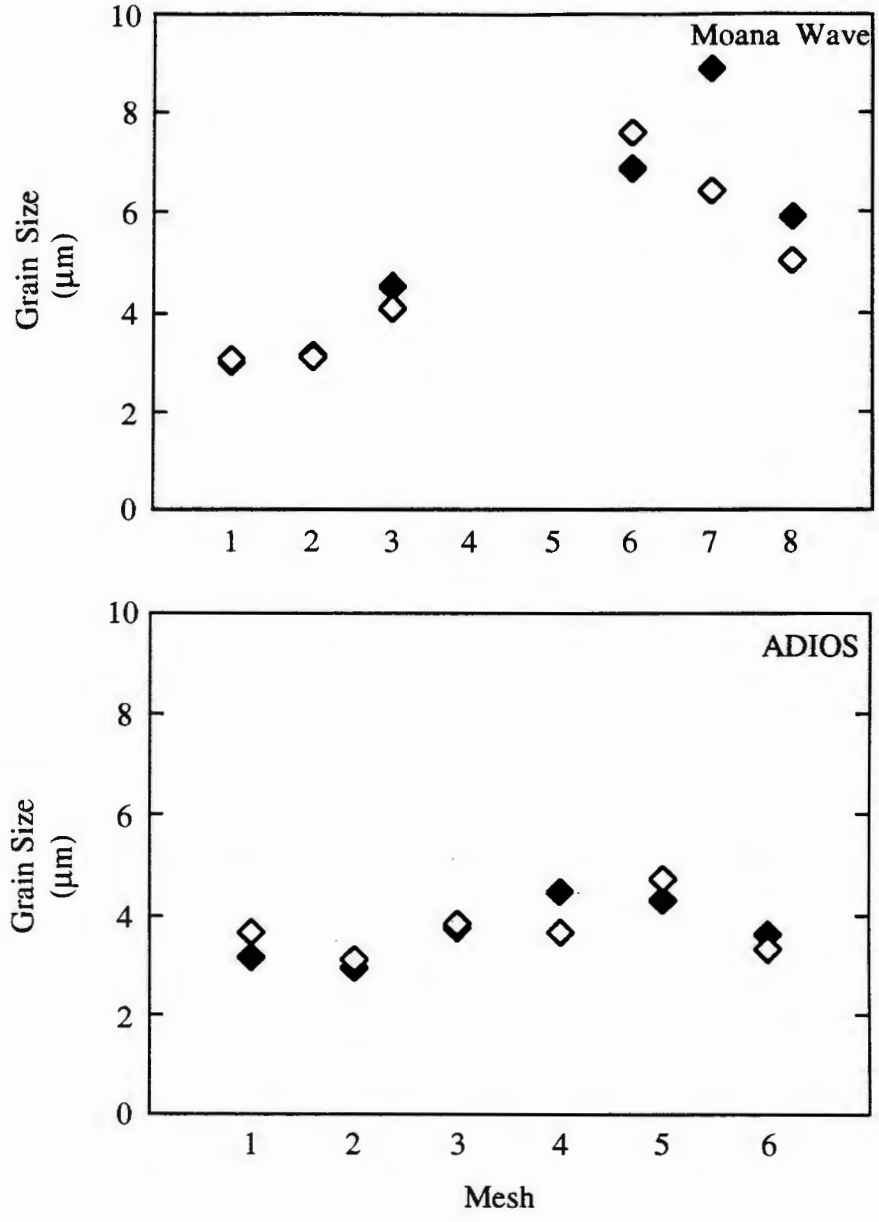
Moana Wave
Grain Size (μm)
10
8
6
4
2
0
1
2
3
4
5
6
7
8
ADIOS
Grain Size (μm)
10
8
6
4
2
0
1
2
3
4
5
6
Mesh

Figure 4. Rock magnetism concentration properties for mesh samples. Open symbols, mesh A, closed symbols, mesh B.

Susceptibility
(10-6m3/kg)
4
-2
1 2 3 4 5 6 7 8
Moana
Wave
Susceptibility
(10-6m3/kg)
4
-2
1 2 3 4 5 6
ADIOS
Mesh
SIRM
(10-3m3/kg)
80
0
1 2 3 4 5 6 7 8
Moana
Wave
SIRM
(10-3m3/kg)
80
0
1 2 3 4 5 6
ADIOS
Mesh
Xarm
(10-6m3/kg)
20
0
1 2 3 4 5 6 7 8
Moana
Wave
Xarm
(10-6m3/kg)
20
0
1 2 3 4 5 6
ADIOS
Mesh

Figure 5. Rock magnetism grain size properties for mesh samples. Open symbols, mesh A, closed symbols, mesh B.

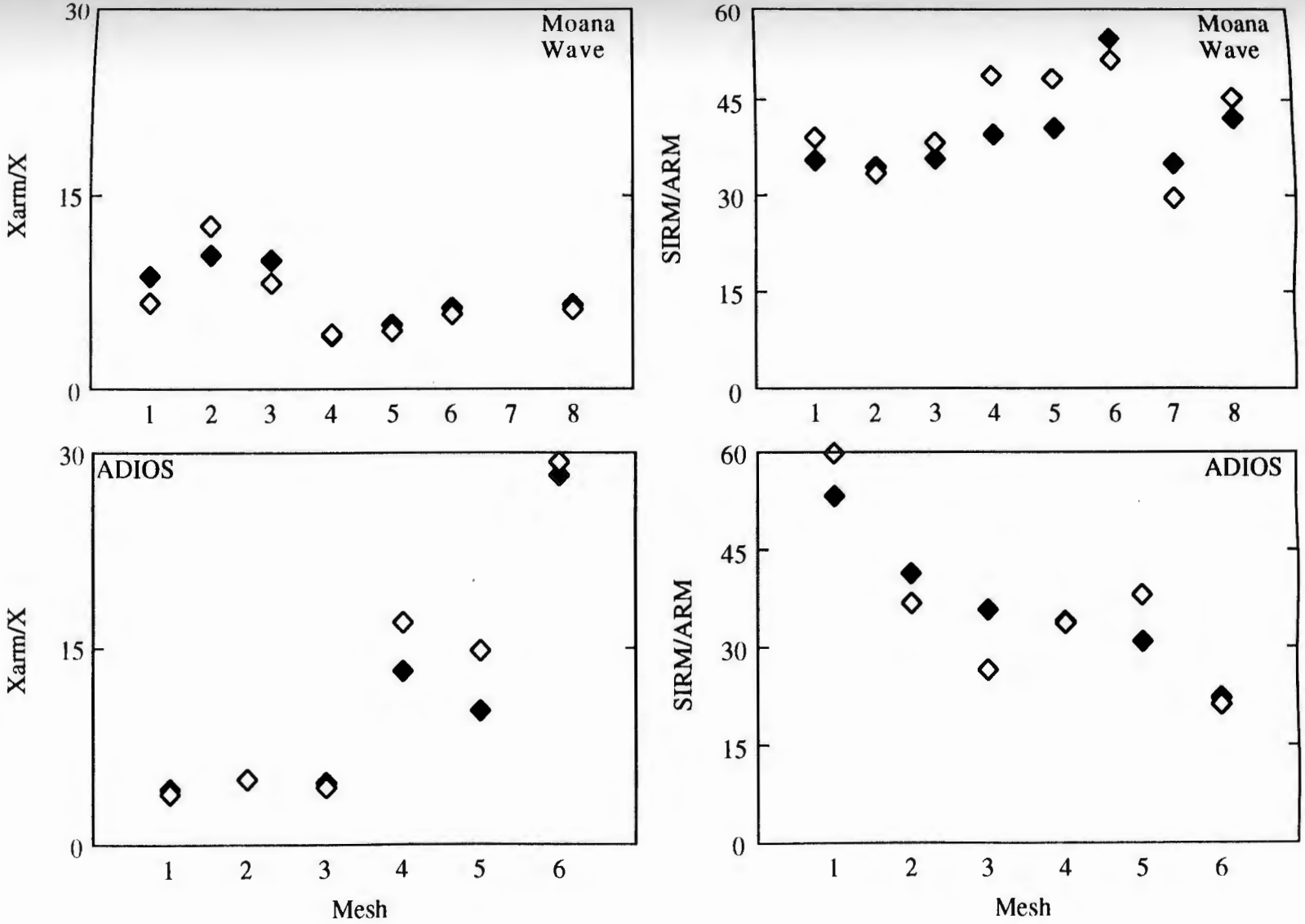
Moana
Wave
Xarm/X
SIRM/ARM
ADIOS
Mesh
0
15
30
45
60
1
2
3
4
5
6
7
8

Figure 6. Rock magnetism composition properties for mesh samples. Open symbols, mesh A, closed symbols, mesh B.

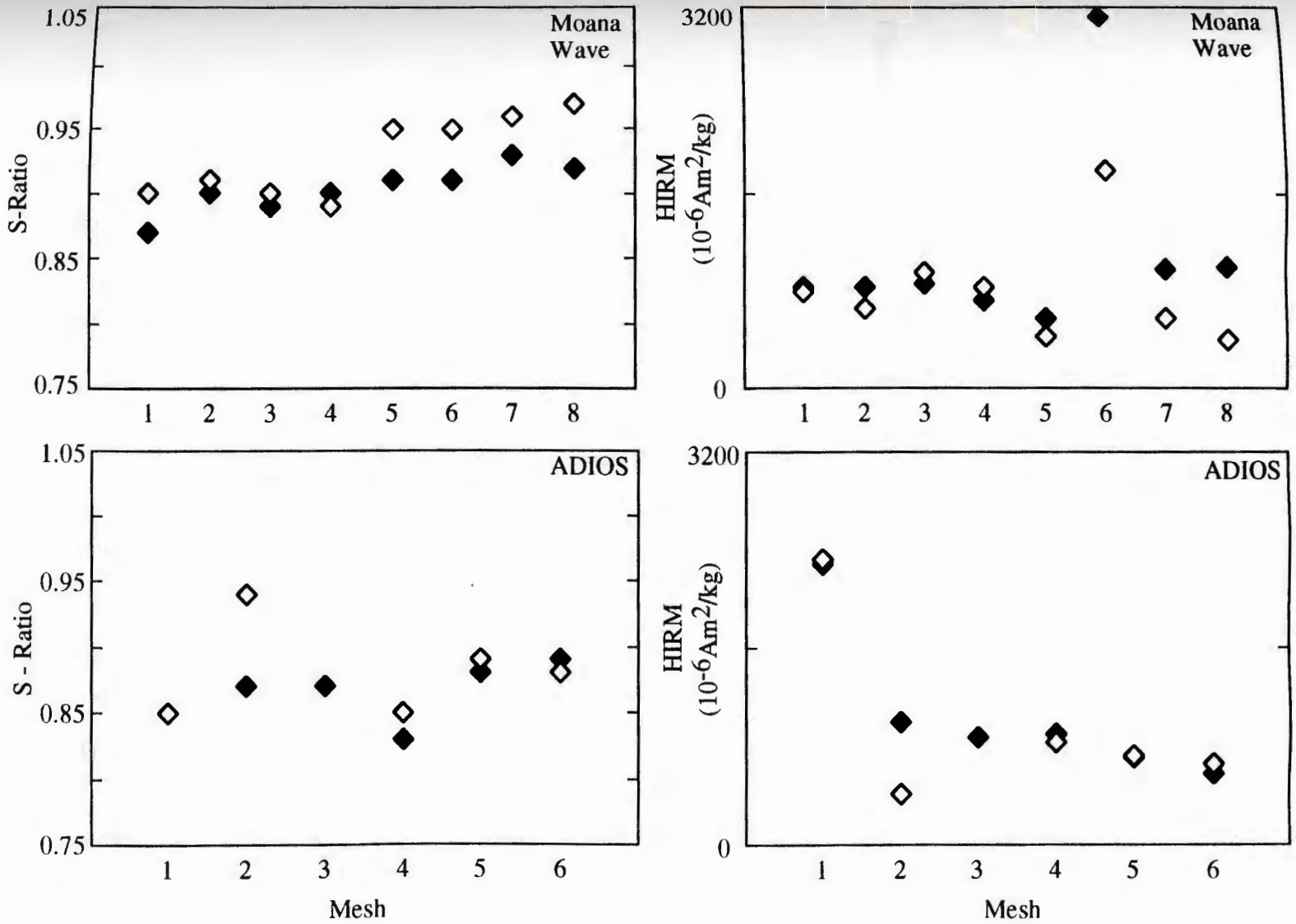
Moana
Wave
S-Ratio
1.05
0.95
0.85
0.75
1 2 3 4 5 6 7 8
HIRM
(10^{-6}Am^2/kg)
3200
0
ADIOS
S - Ratio
1 2 3 4 5 6
Mesh

Figure 7. <2μm mineral composition for mesh samples in weight percent.

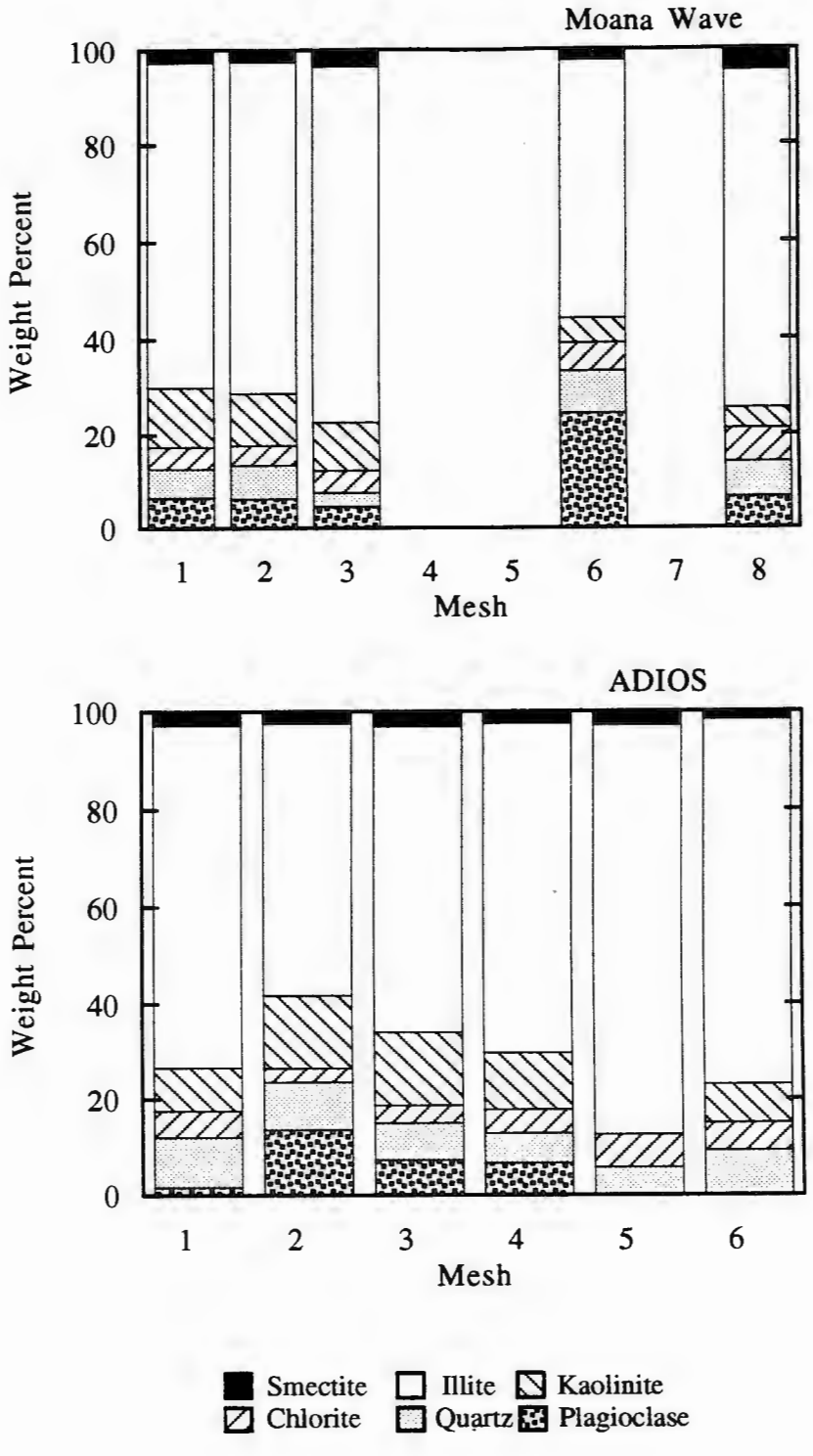
Moana Wave
Weight Percent
100
80
60
40
20
0
1
2
3
4
5
6
7
8
Mesh
ADIOS
Weight Percent
100
80
60
40
20
0
1
2
3
4
5
6
Mesh
Smectite
Illite
Kaolinite
Chlorite
Quartz
Plagioclase

Figure 8. 2-20μm mineral composition for mesh samples in weight percent.

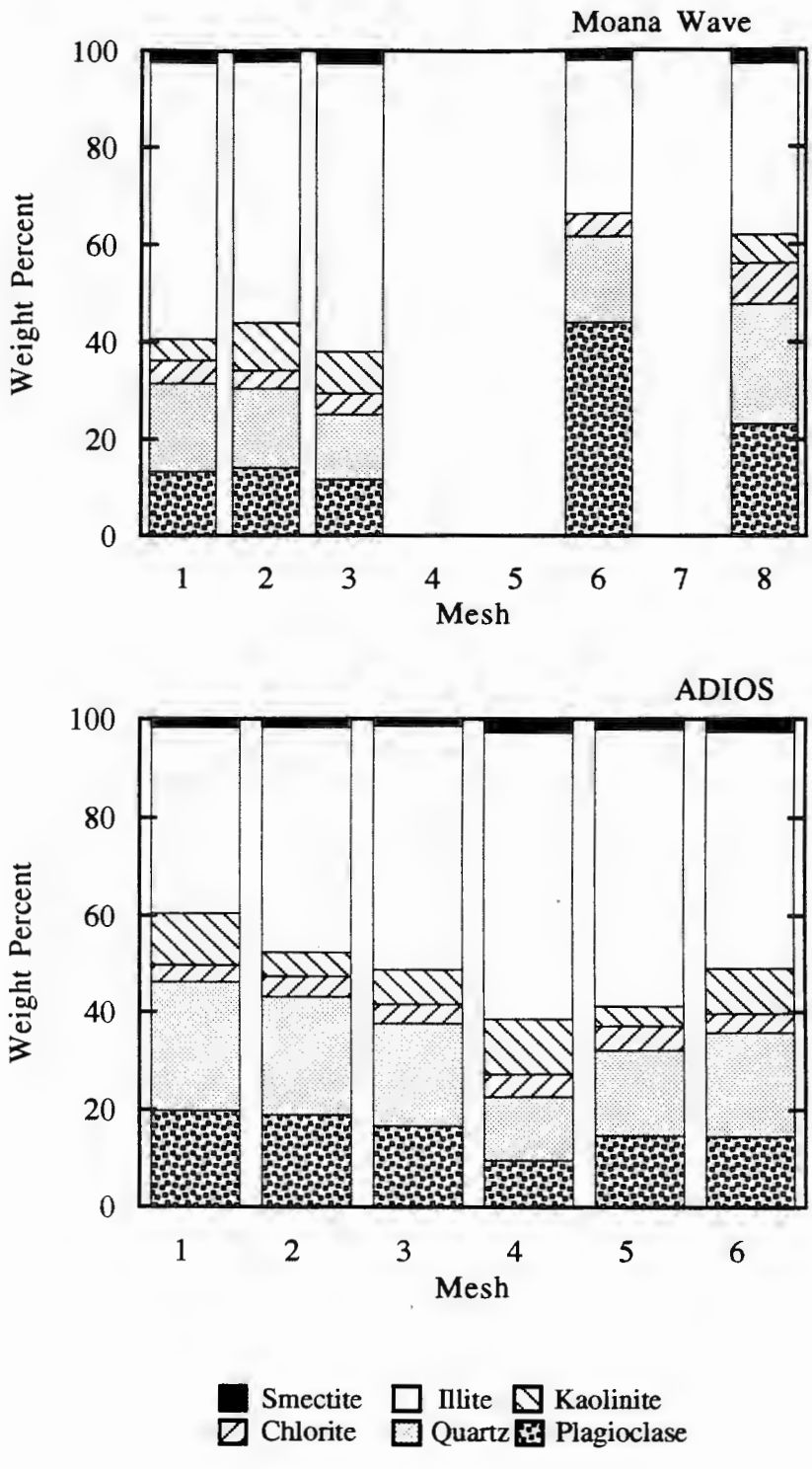
Moana Wave
Weight Percent
100
80
60
40
20
0
1
2
3
4
5
6
7
8
Mesh
ADIOS
Weight Percent
100
80
60
40
20
0
1
2
3
4
5
6
Mesh
Smectite
Illite
Kaolinite
Chlorite
Quartz
Plagioclase

Figure 9. Bulk mineral composition for mesh samples in weight percent.

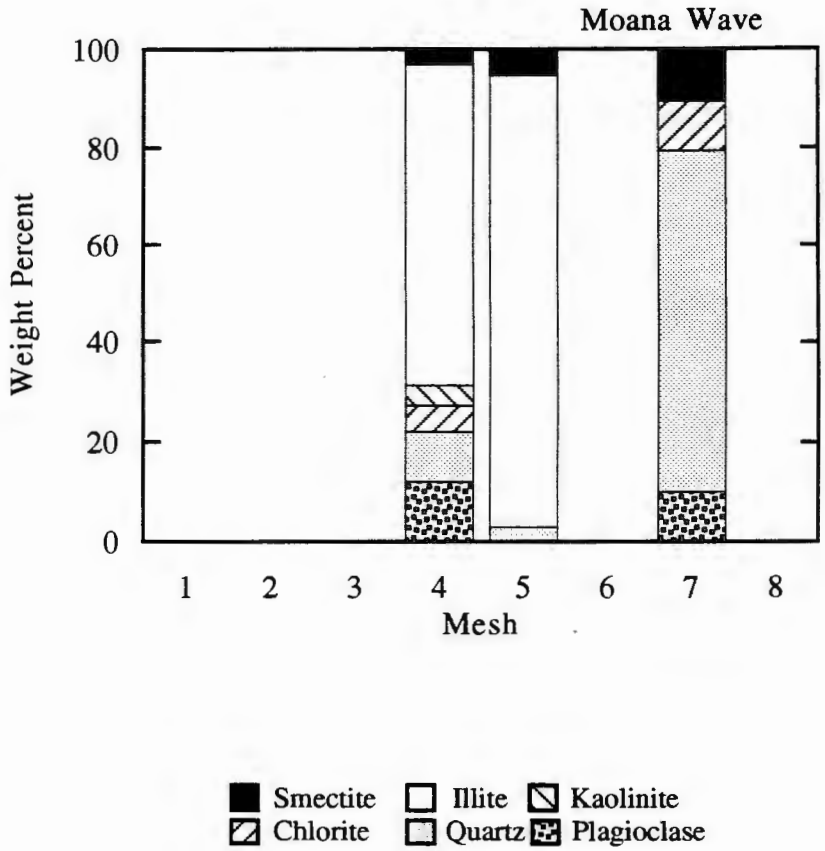
Moana Wave
100
80
60
40
20
0
Weight Percent
1
2
3
4
5
6
7
8
Mesh
Smectite
Illite
Kaolinite
Chlorite
Quartz
Plagioclase

Figure 10. Bulk mineral composition for pumped samples in weight percent.

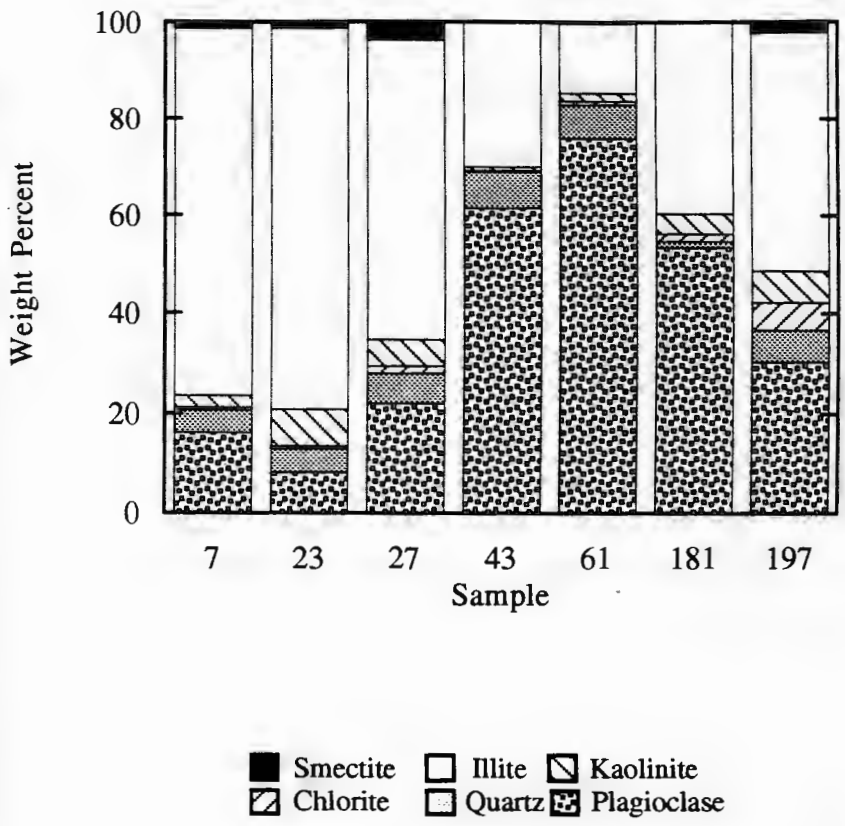
100
80
60
40
20
0
Weight Percent
7
23
27
43
61
181
197
Sample
Smectite
Illite
Kaolinite
Chlorite
Quartz
Plagioclase

Figure 11. Mineral composition for cascade impactor stages in weight percent.

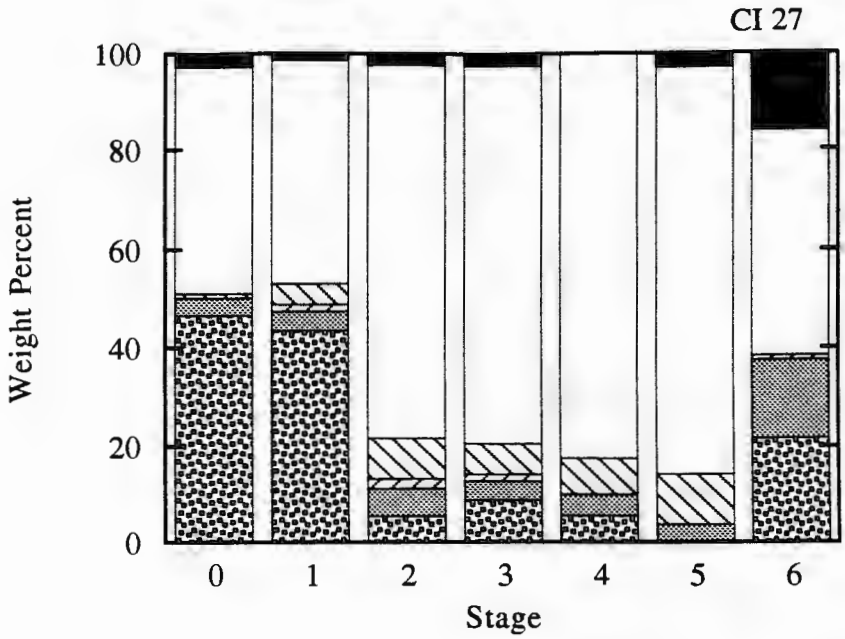
CI 27
Weight Percent
100
80
60
40
20
0
0
1
2
3
4
5
6
Stage

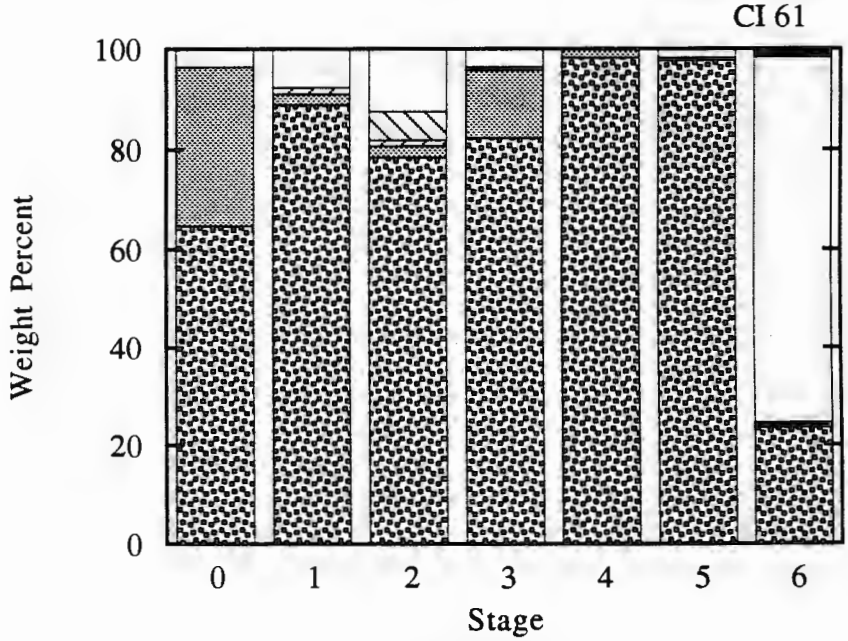
CI 61
Weight Percent
100
80
60
40
20
0
0
1
2
3
4
5
6
Stage

Smectite
Illite
Kaolinite
Chlorite
Quartz
Plagioclase

Figure 12. Ash, aluminum and sodium concentration for pumped samples.

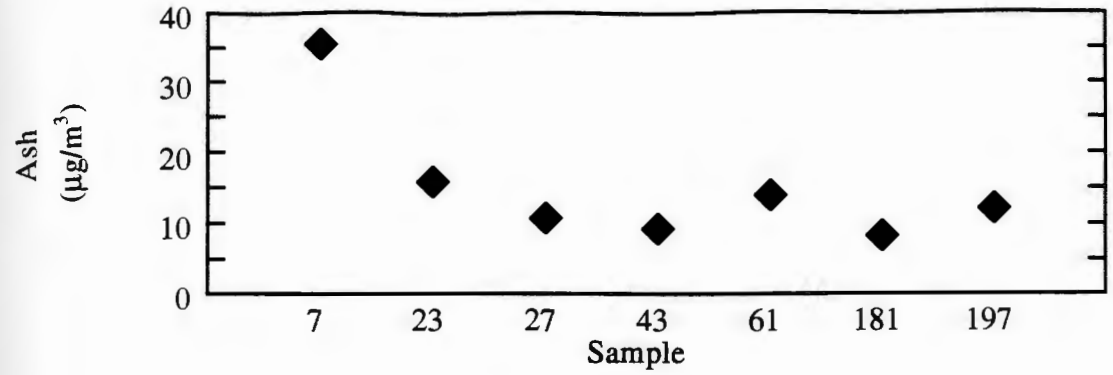
Ash
(µg/m3)
40
30
20
10
0
7
23
27
43
61
181
197
Sample

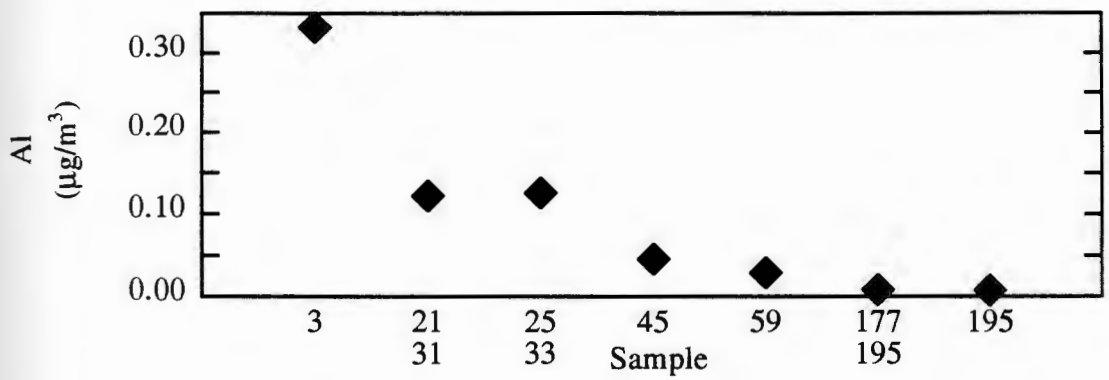
Al
(µg/m3)
0.30
0.20
0.10
0.00
3
21
31
25
33
45
59
177
195
195
Sample

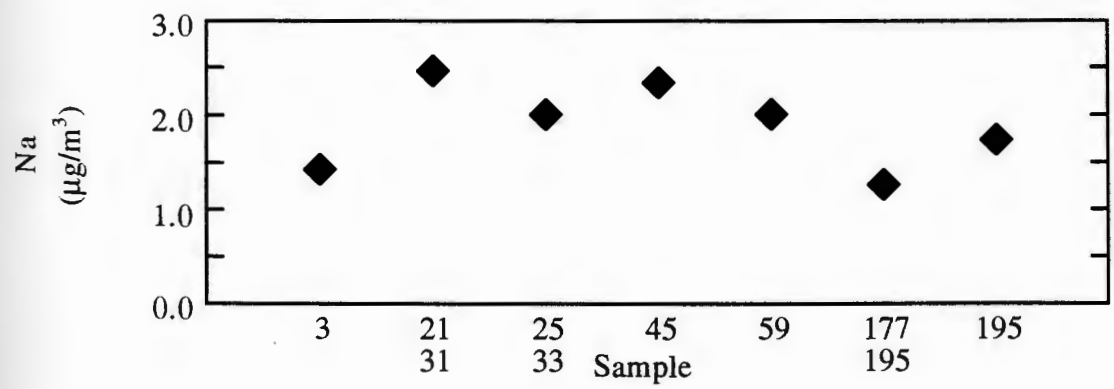
Na
(µg/m3)
3.0
2.0
1.0
0.0
3
21
31
25
33
45
59
177
195
195
Sample

Figure 13. Ash, aluminum and sodium concentration for cascade impactor stages.

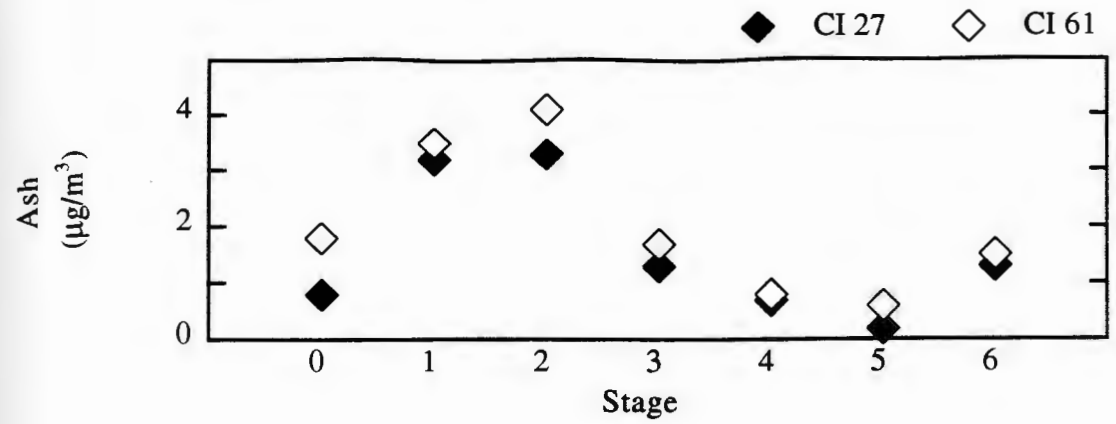
CI 27
CI 61
Ash (µg/m3)
4
2
0
0
1
2
3
4
5
6
Stage

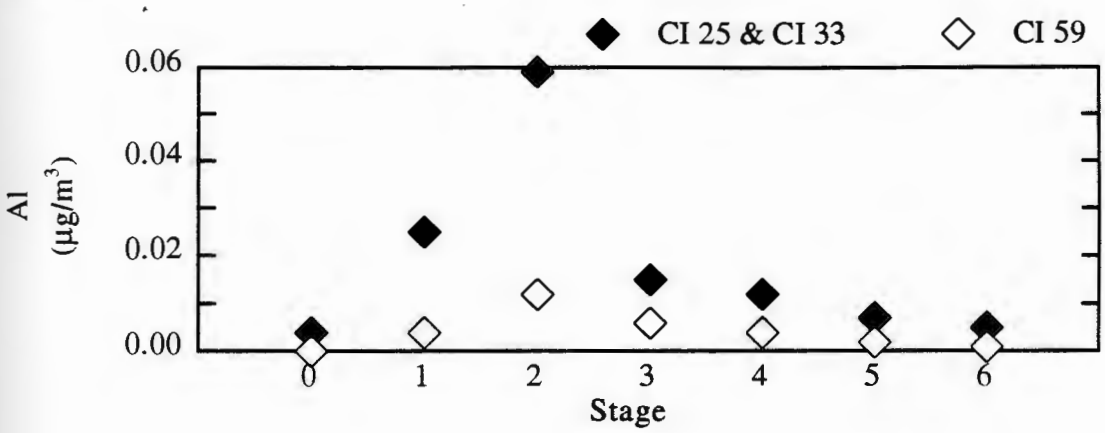
CI 25 & CI 33
CI 59
Al (µg/m3)
0.06
0.04
0.02
0.00
0
1
2
3
4
5
6
Stage

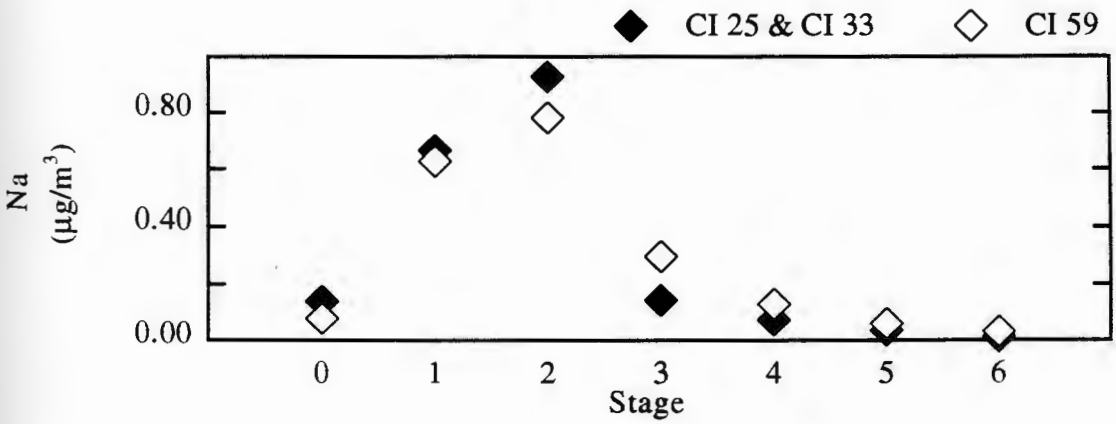
CI 25 & CI 33
CI 59
Na (µg/m3)
0.80
0.40
0.00
0
1
2
3
4
5
6
Stage

Figure 14. Ash residue vs. aluminum for all samples, high volume samples and cascade impactors.

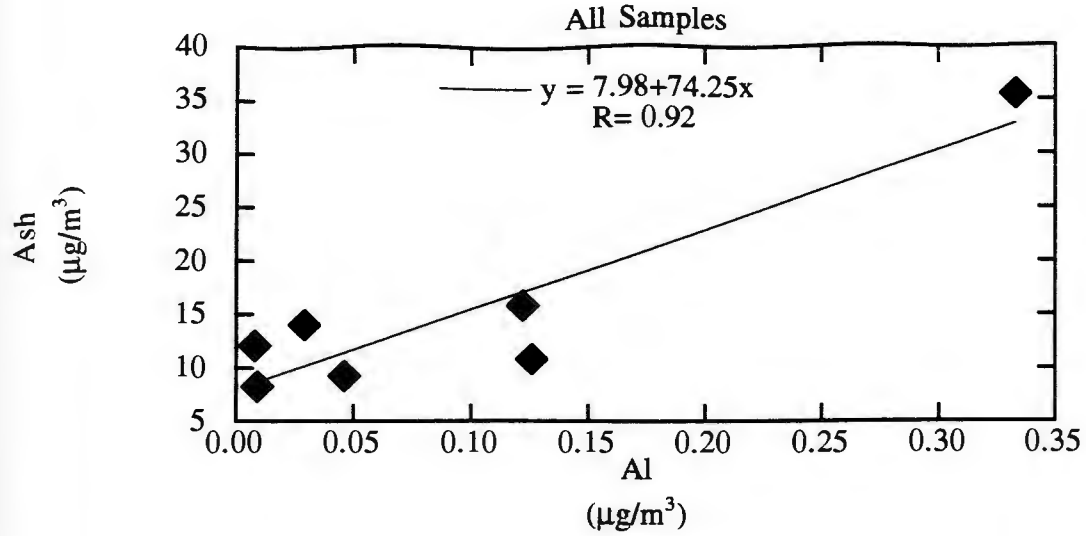
All Samples
y = 7.98+74.25x
R= 0.92
Ash
(µg/m3)
Al
(µg/m3)
40
35
30
25
20
15
10
5
0.00
0.05
0.10
0.15
0.20
0.25
0.30
0.35

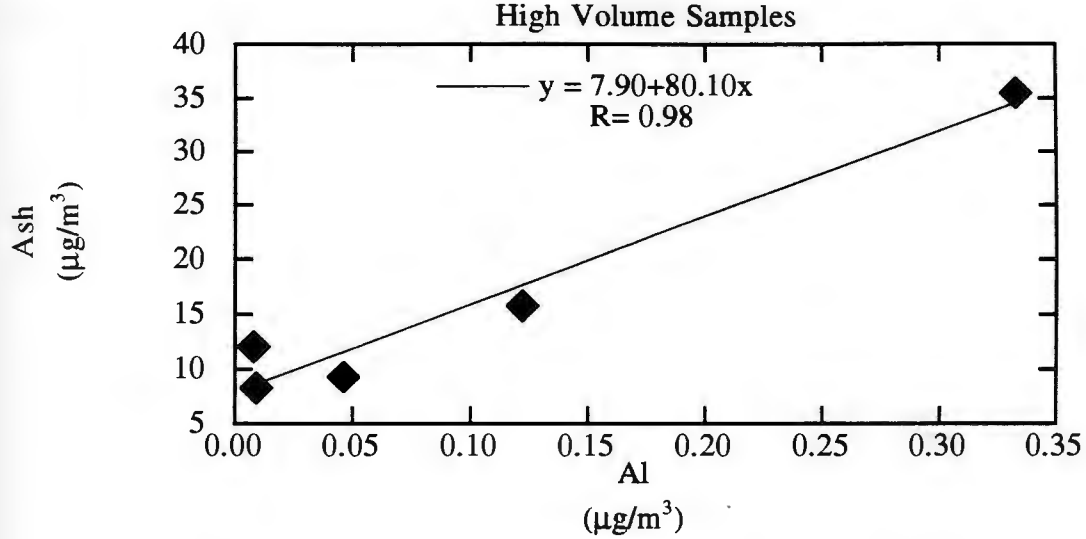
High Volume Samples
y = 7.90+80.10x
R= 0.98
Ash
(µg/m3)
Al
(µg/m3)
40
35
30
25
20
15
10
5
0.00
0.05
0.10
0.15
0.20
0.25
0.30
0.35

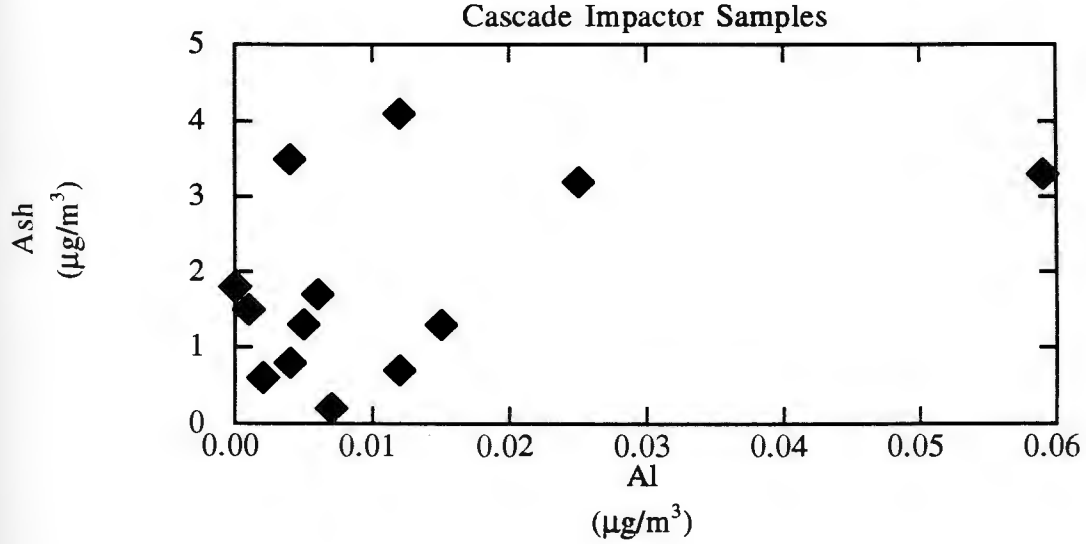
Cascade Impactor Samples
Ash
(µg/m3)
Al
(µg/m3)
5
4
3
2
1
0
0.00
0.01
0.02
0.03
0.04
0.05
0.06

Figure 15. Ash residue vs. sodium for all samples, high volume samples and cascade impactors.

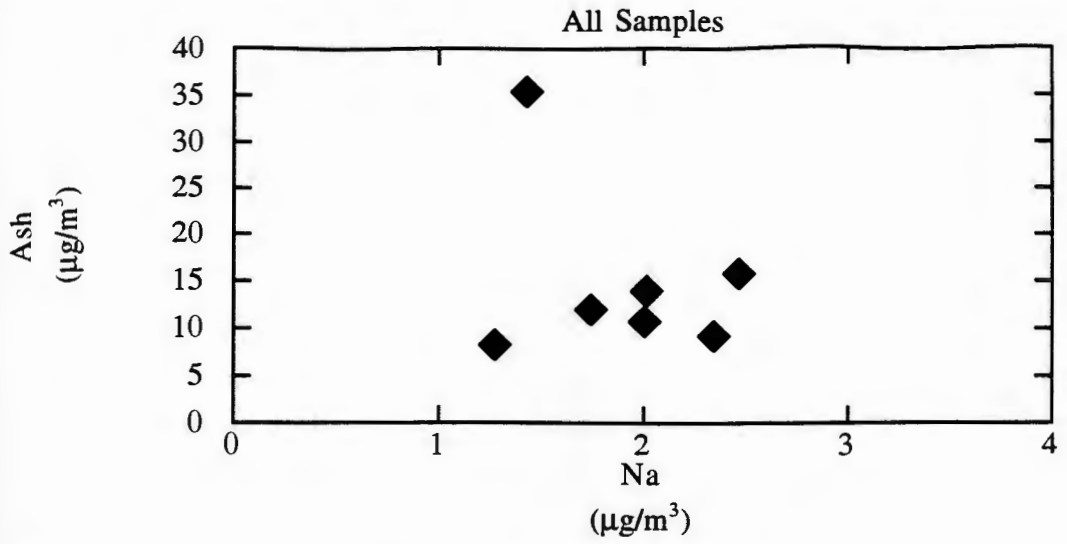
All Samples
Ash
(µg/m3)
40
35
30
25
20
15
10
5
0
0
1
2
3
4
Na
(µg/m3)

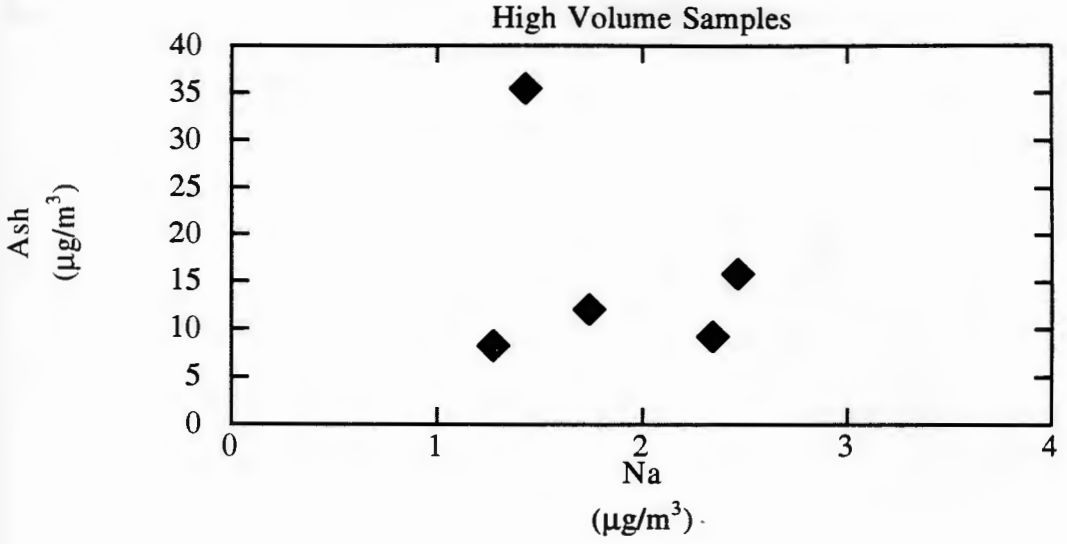
High Volume Samples
Ash
(µg/m3)
40
35
30
25
20
15
10
5
0
0
1
2
3
4
Na
(µg/m3)

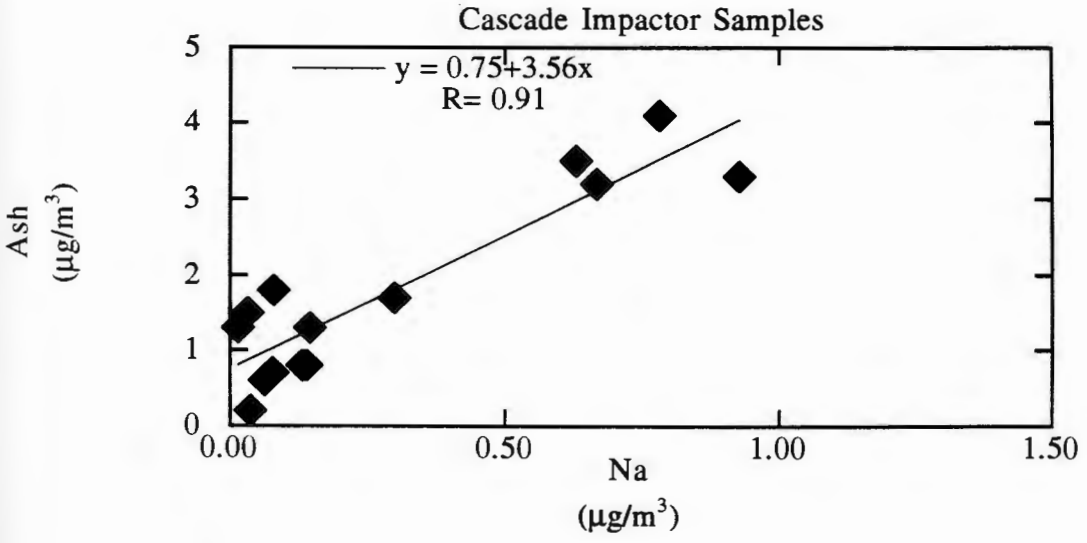
Cascade Impactor Samples
y = 0.75+3.56x
R= 0.91
Ash
(µg/m3)
5
4
3
2
1
0
0.00
0.50
1.00
1.50
Na
(µg/m3)

Figure 16. Aerosol transport time (in days) from various continental areas for the Moana Wave samples.

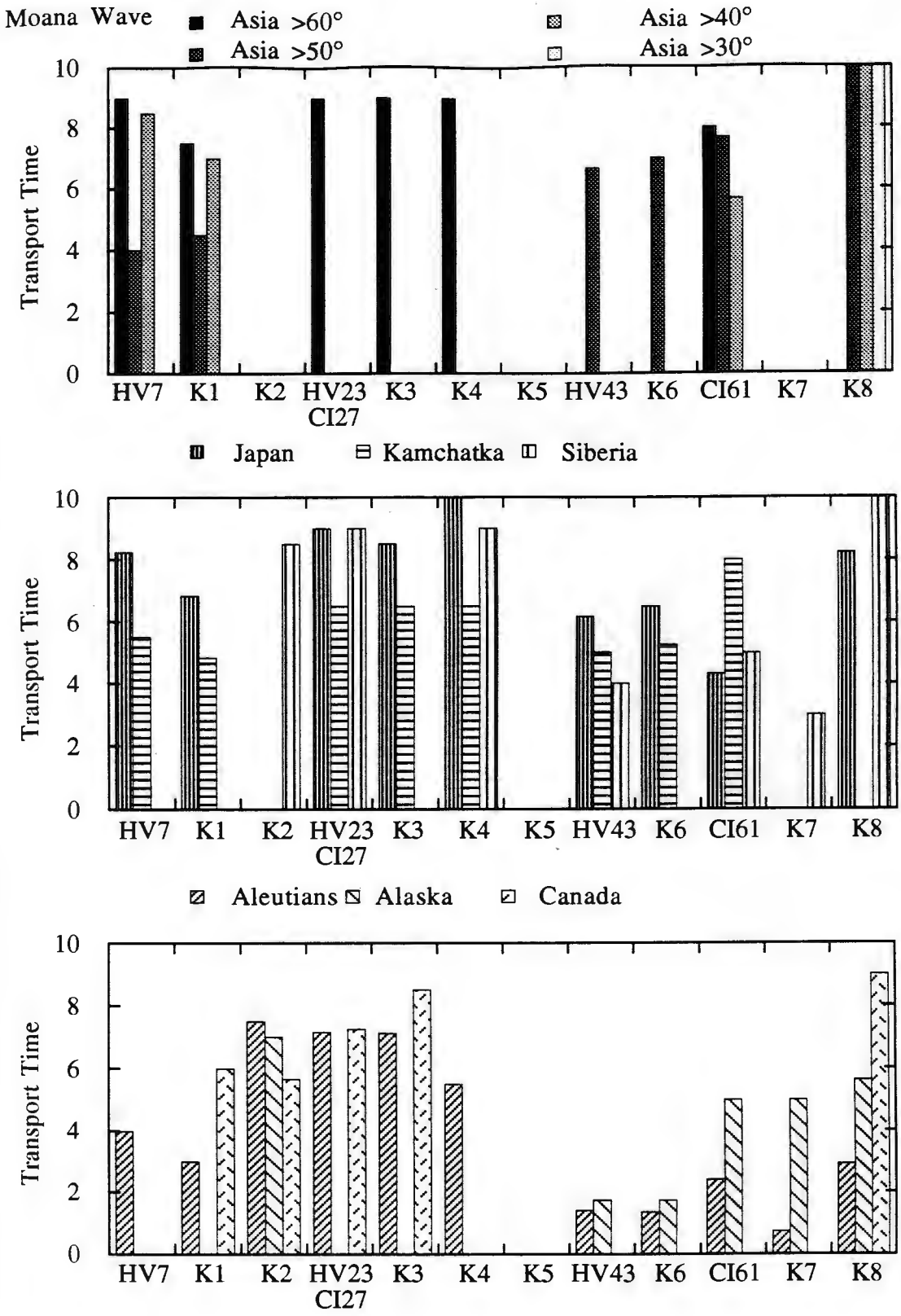
Moana Wave
Asia >60°
Asia >50°
Asia >40°
Asia >30°
Transport Time
10
8
6
4
2
0
HV7 K1 K2 HV23 CI27 K3 K4 K5 HV43 K6 CI61 K7 K8
Japan
Kamchatka
Siberia
Transport Time
10
8
6
4
2
0
HV7 K1 K2 HV23 CI27 K3 K4 K5 HV43 K6 CI61 K7 K8
Aleutians
Alaska
Canada
Transport Time
10
8
6
4
2
0
HV7 K1 K2 HV23 CI27 K3 K4 K5 HV43 K6 CI61 K7 K8

Figure 17. Aerosol transport time (in days) from various continental areas for the ADIOS samples.

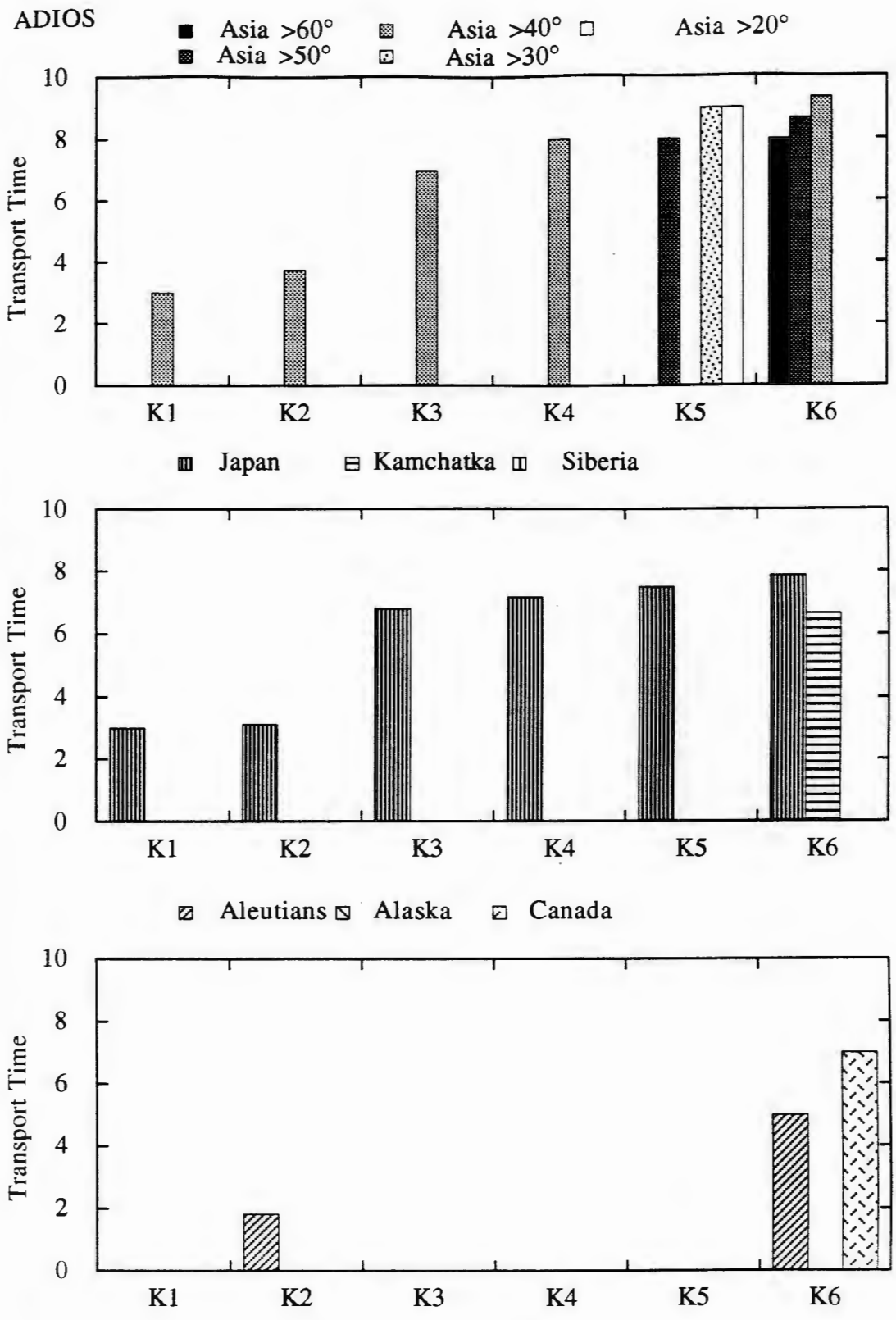
ADIOS
Asia >60°
Asia >50°
Asia >40°
Asia >30°
Asia >20°
Transport Time
10
8
6
4
2
0
K1
K2
K3
K4
K5
K6
Japan
Kamchatka
Siberia
Transport Time
10
8
6
4
2
0
K1
K2
K3
K4
K5
K6
Aleutians
Alaska
Canada
Transport Time
10
8
6
4
2
0
K1
K2
K3
K4
K5
K6

Figure 18. Residual ash from pumped samples and dust concentration from mesh (kite) samples.

Ash
(μg/m³)
5
10
15
20
25
30
35
40
HV7
Kite1
Kite 2
HV 23
CI 27
Kite 3
Kite 4
Kite 5
HV 43
Kite 6
CI 61
Kite 7
Kite 8
HV 181
HV197
0
0.001
0.002
0.003
0.004
0.005
0.006
0.007
0.008
Dust Concentration
(g/hr)
Pumped Samples
Kite

Figure 19. <2 μm mesh mineralogy and bulk pumped sample mineralogy.

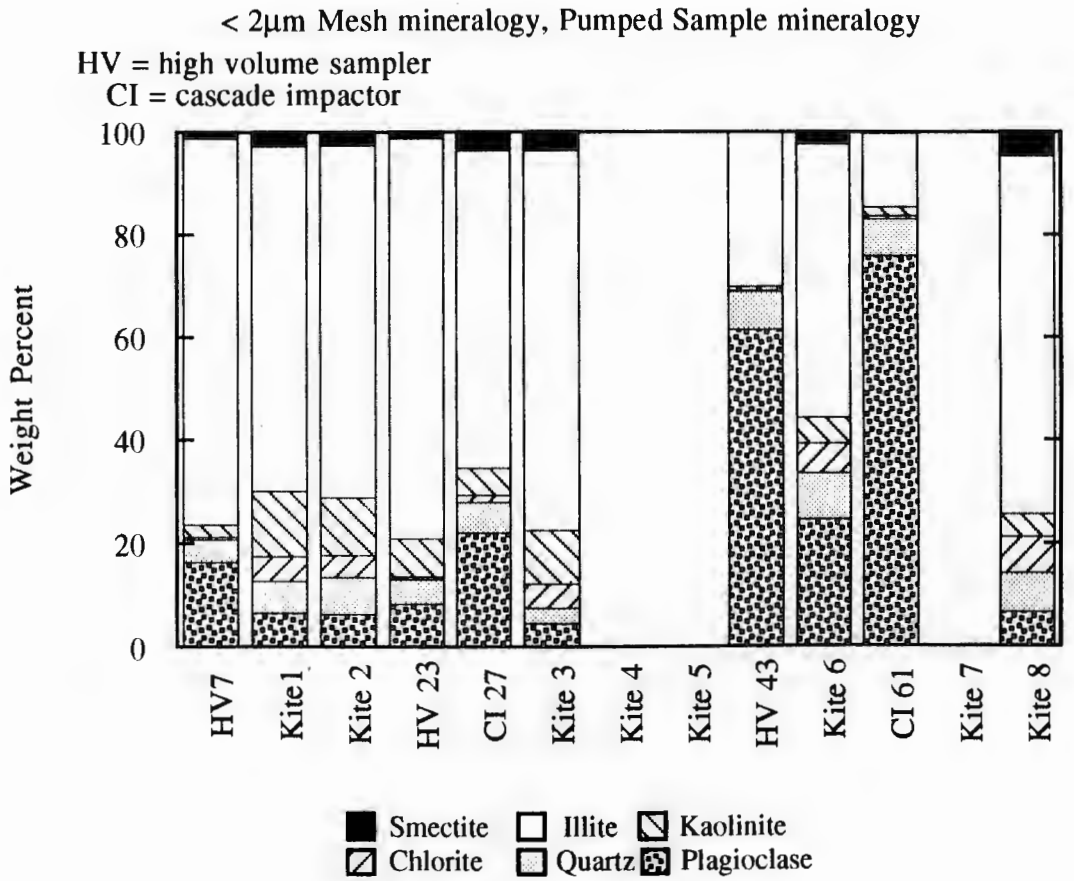
< 2µm Mesh mineralogy, Pumped Sample mineralogy
HV = high volume sampler
CI = cascade impactor
Weight Percent
100
80
60
40
20
0
HV7
Kite1
Kite 2
HV 23
CI 27
Kite 3
Kite 4
Kite 5
HV 43
Kite 6
CI 61
Kite 7
Kite 8
Smectite
Illite
Kaolinite
Chlorite
Quartz
Plagioclase

Figure 20. 2-20 μm mesh mineralogy and bulk pumped sample mineralogy.

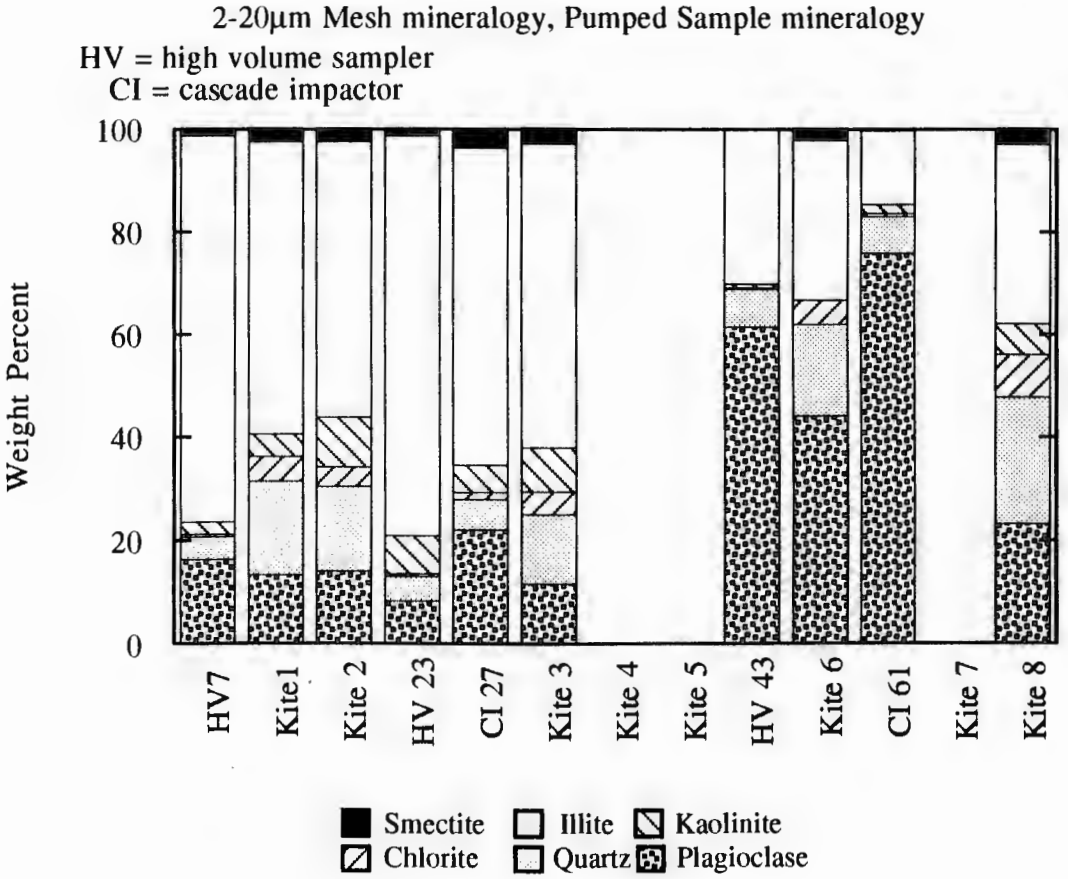
2-20μm Mesh mineralogy, Pumped Sample mineralogy
HV = high volume sampler
CI = cascade impactor
Weight Percent
100
80
60
40
20
0
HV7
Kite1
Kite 2
HV 23
CI 27
Kite 3
Kite 4
Kite 5
HV 43
Kite 6
CI 61
Kite 7
Kite 8
Smectite
Illite
Kaolinite
Chlorite
Quartz
Plagioclase

Figure 21. Mass median diameter for cascade impactor samples calculated from aluminum mass distribution and Elzone geometric mean diameter for mesh samples.

Mass Median Diameter (CI)
or
Geometric Mean Diameter (kites)
(μm)
2
3
4
5
6
7
8
CI9
Kite1
CI17
Kite2
CI25
Kite3
CI33
Kite4
Kite5
CI39
Kite6
CI59
Kite7
Kite8
Kite
Cascade Impactor (AI)

Figure 22. Mass median diameter for cascade impactor samples calculated from iron mass distribution and Elzone geometric mean diameter for mesh samples.

Mass Median Diameter (CI)
or
Geometric Mean Diameter (kites)
(μm)
2
3
4
5
6
7
8
CI9
Kite1
CI17
Kite2
CI25
Kite3
CI33
Kite4
Kite5
CI39
Kite6
CI59
Kite7
Kite8
Kite
Cascade Impactor (Fe)

Figure 23. Mesh dust concentration (g/hr) as a function of transport time from various continental regions for both cruises.

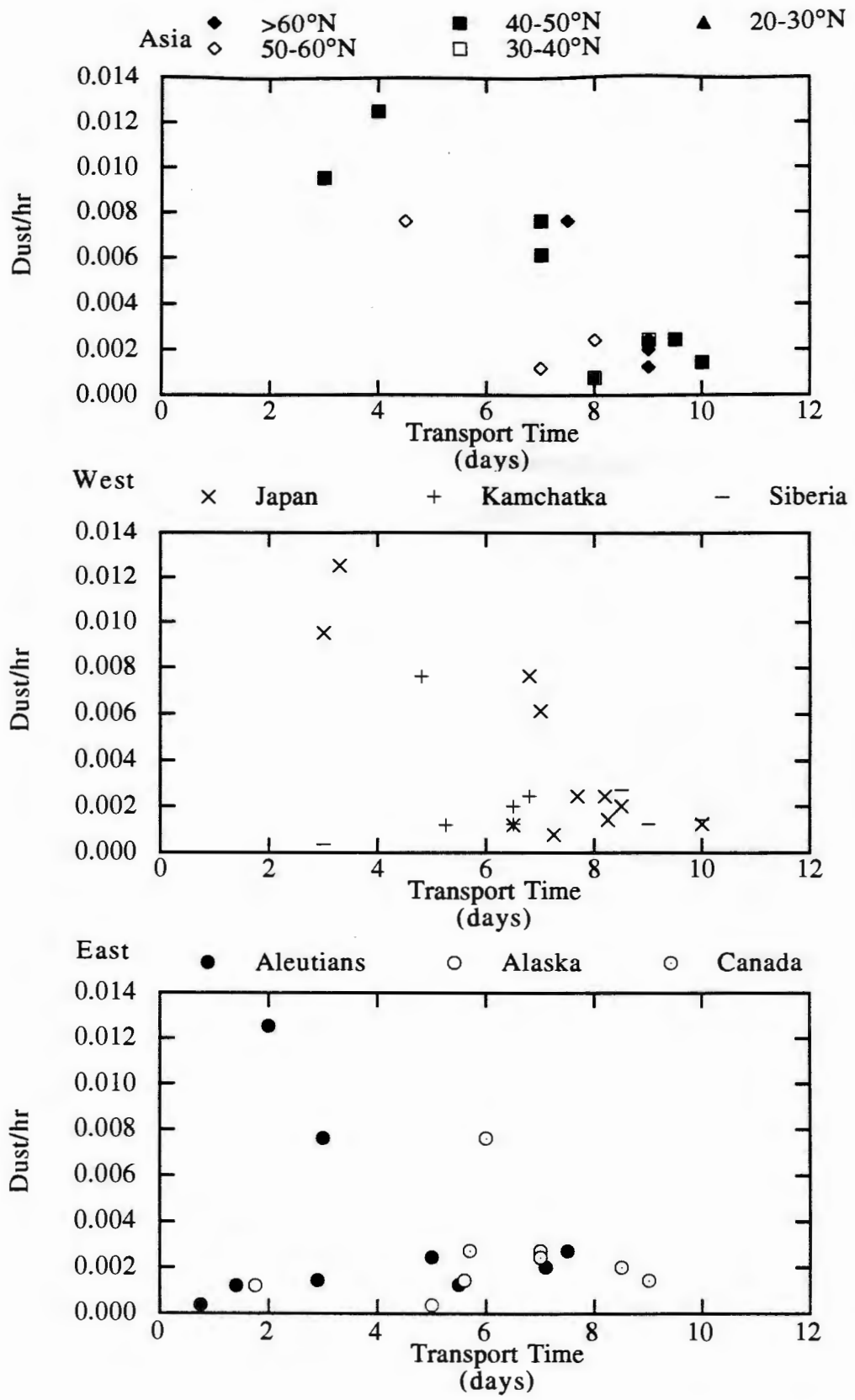
Asia
>60°N
50-60°N
40-50°N
30-40°N
20-30°N
Dust/hr
0.014
0.012
0.010
0.008
0.006
0.004
0.002
0.000
0
2
4
6
8
10
12
Transport Time
(days)
West
Japan
Kamchatka
Siberia
Dust/hr
Transport Time
(days)
East
Aleutians
Alaska
Canada
Dust/hr
Transport Time
(days)

Figure 24. Mesh grain size as a function of transport time from various continental regions for both cruises.

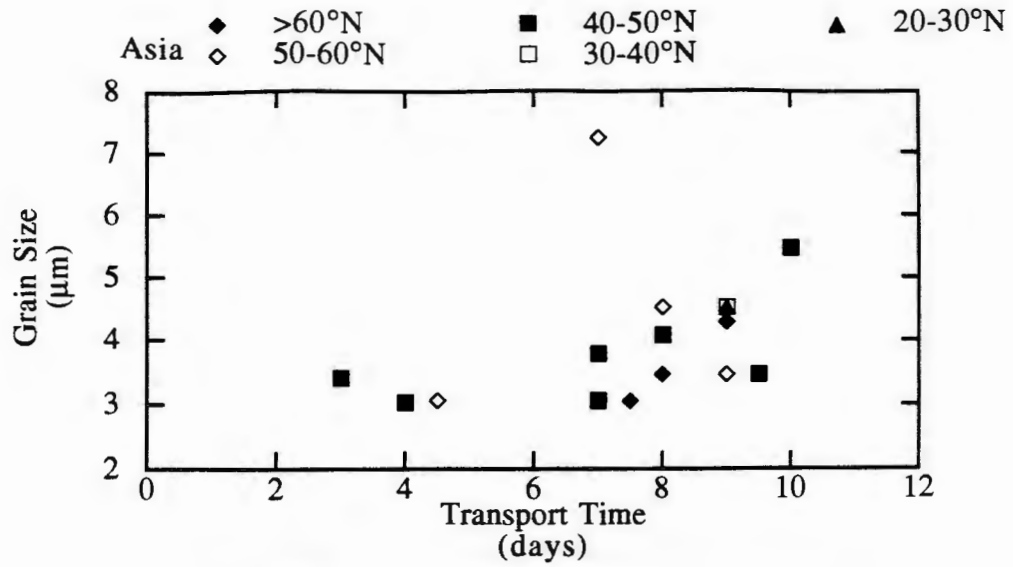
Asia
>60°N
50-60°N
40-50°N
30-40°N
20-30°N
Grain Size (µm)
Transport Time (days)

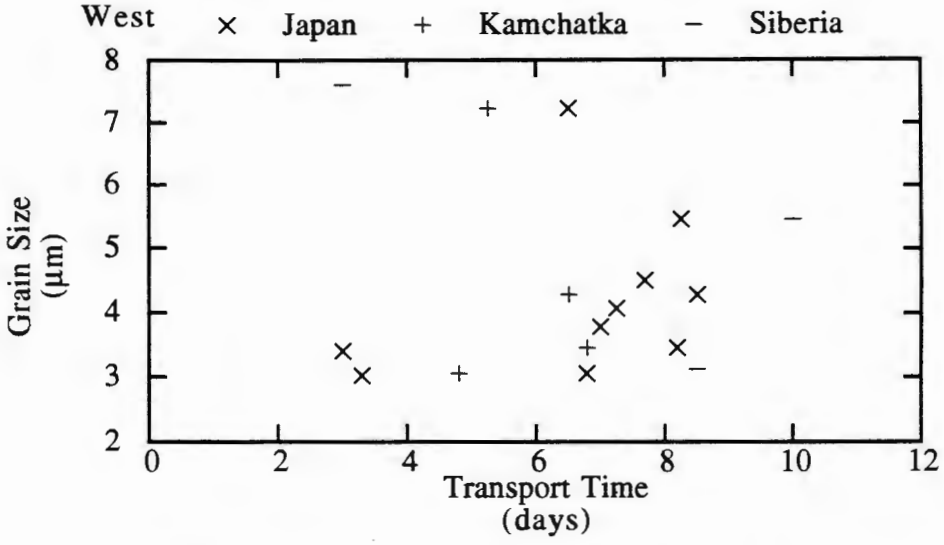
West
Japan
Kamchatka
Siberia
Grain Size (µm)
Transport Time (days)

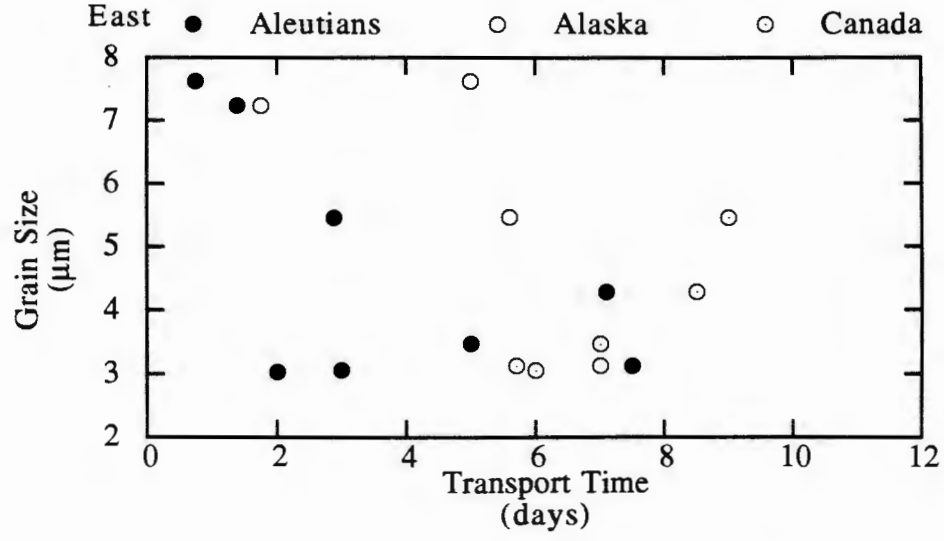
East
Aleutians
Alaska
Canada
Grain Size (µm)
Transport Time (days)

Figure 25. Dust concentration vs. geometric mean grain size for all mesh samples.

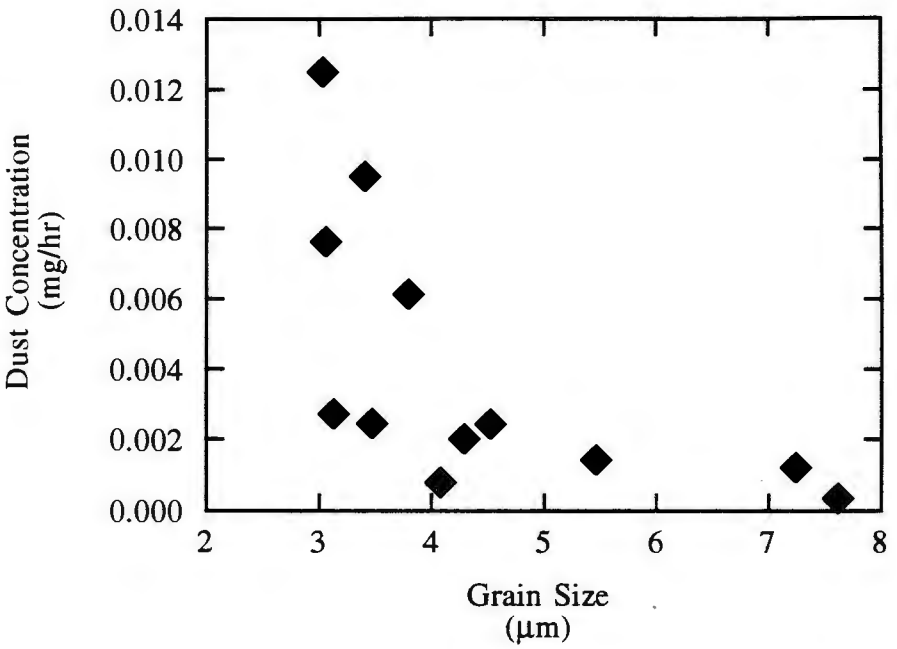
0.014
0.012
0.010
0.008
0.006
0.004
0.002
0.000
Dust Concentration
(mg/hr)
2
3
4
5
6
7
8
Grain Size
(μm)

Figure 26. Mesh rock magnetic properties as a function of transport time from various continental regions for both cruises.

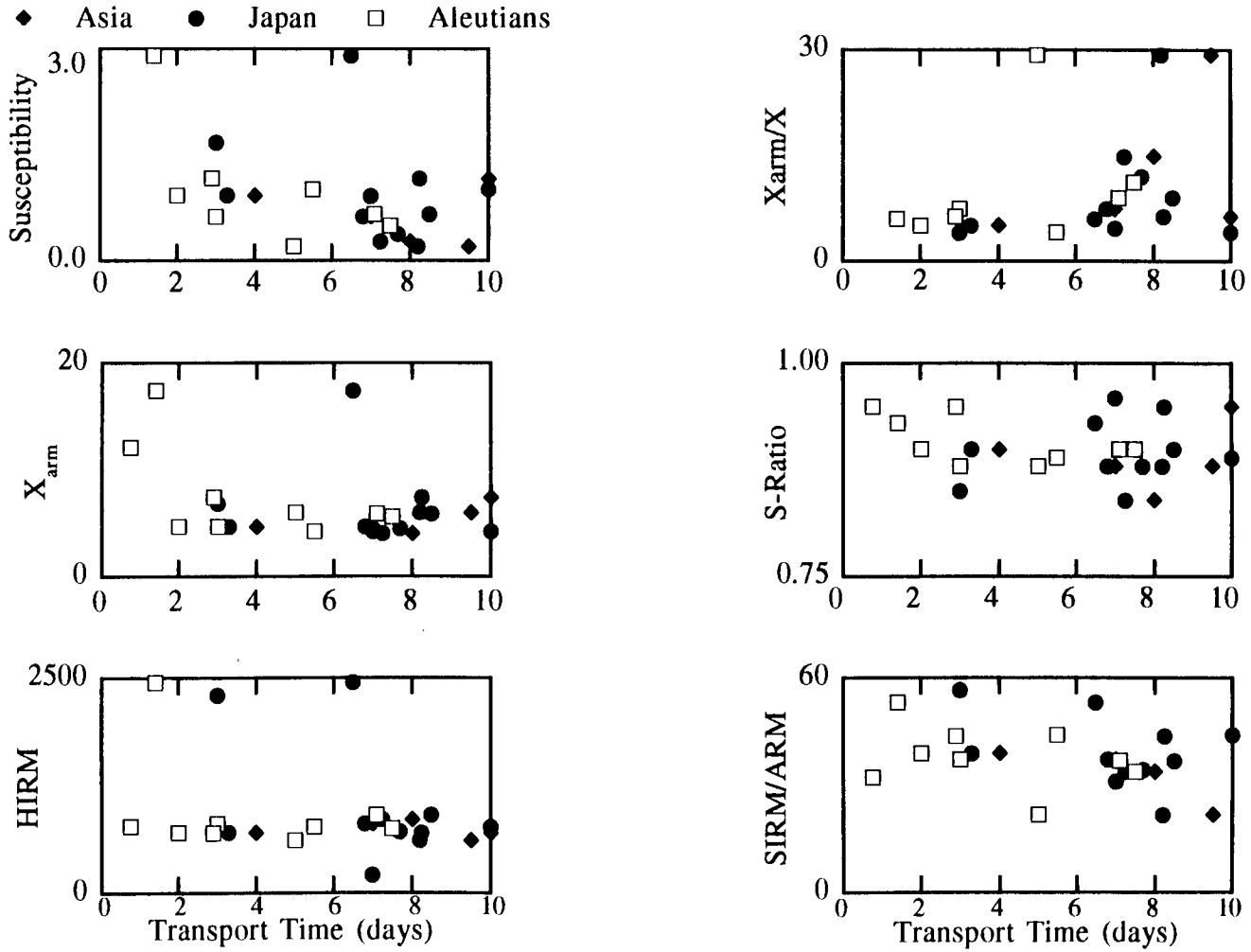
Asia
Japan
Aleutians
Susceptibility
3.0
0.0
Xarm/X
30
0
X_{arm}
20
0
S-Ratio
1.00
0.75
HIRM
2500
0
SIRM/ARM
60
0
0 2 4 6 8 10
Transport Time (days)

Figure 27. Mesh <2 μm mineralogy as a function of transport time from various continental regions for both cruises (open symbols) and from Leinen, et al., (1994; closed symbols).

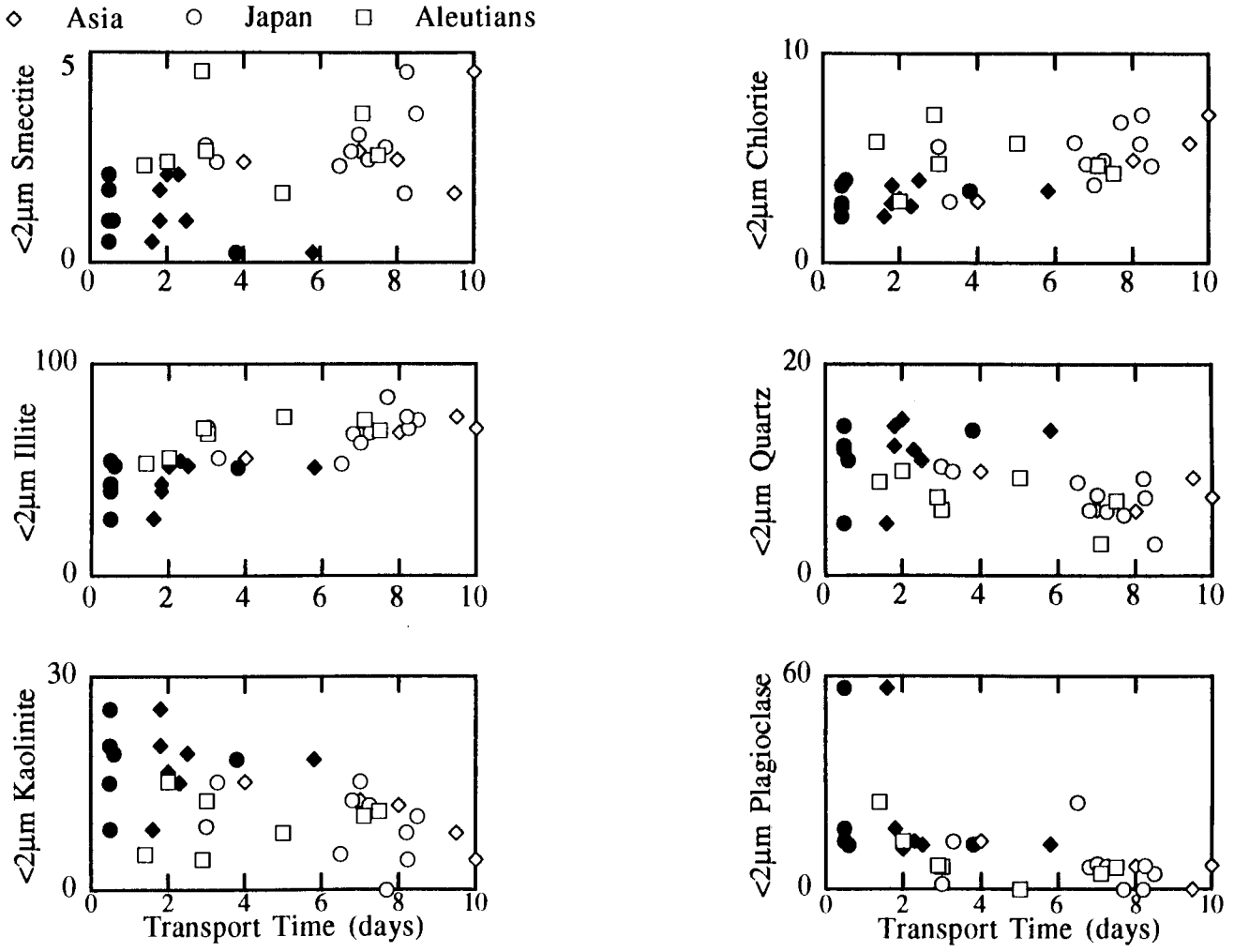
◇ Asia ○ Japan □ Aleutians
<2μm Smectite
<2μm Chlorite
<2μm Illite
<2μm Quartz
<2μm Kaolinite
<2μm Plagioclase
Transport Time (days)
Transport Time (days)

Figure 28. Mesh 2-20 μm mineralogy as a function of transport time from various continental regions for both cruises (open symbols) and from Leinen, et al., (1994; closed symbols).

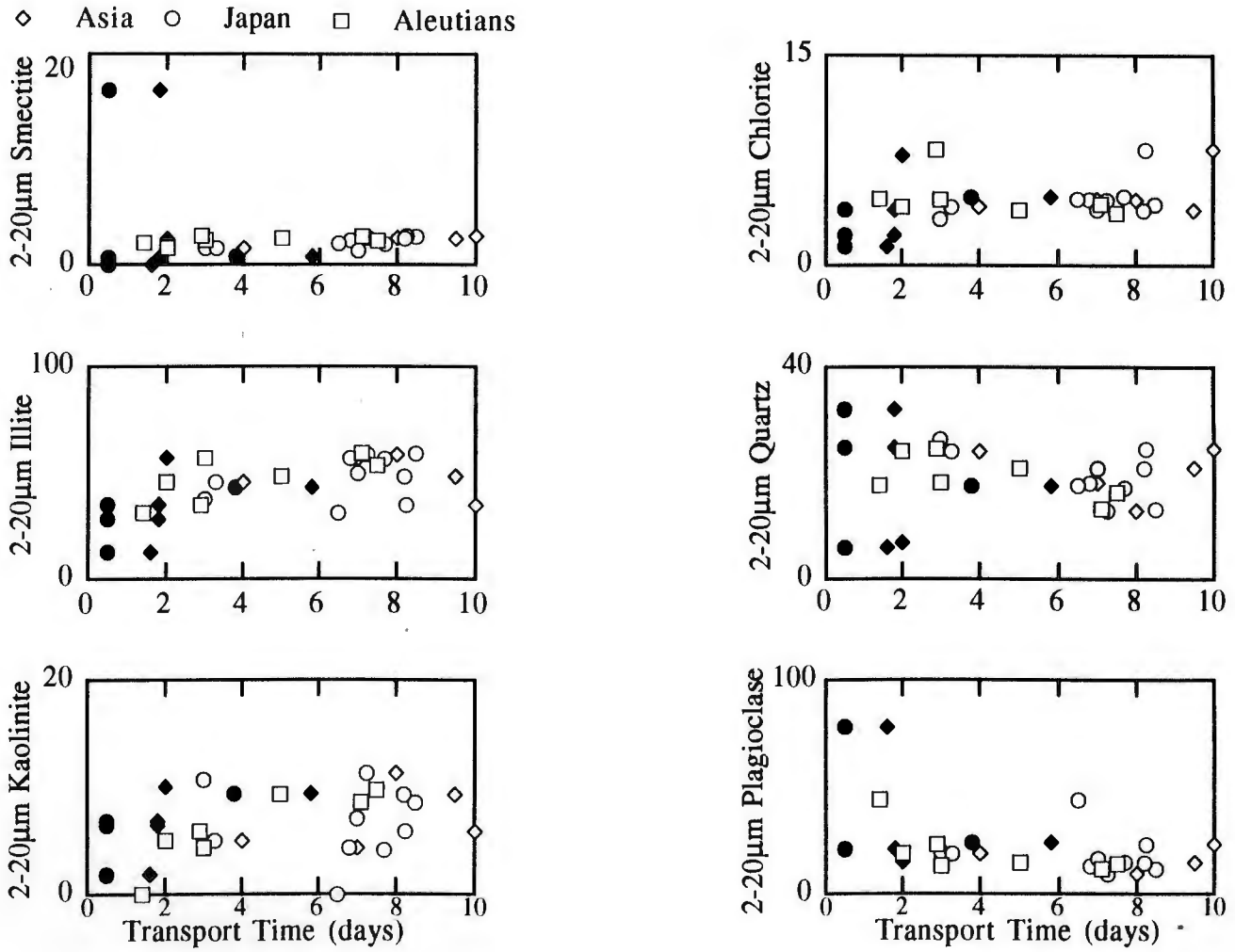
◇ Asia ○ Japan □ Aleutians
2-20µm Smectite
2-20µm Illite
2-20µm Kaolinite
2-20µm Chlorite
2-20µm Quartz
2-20µm Plagioclase
Transport Time (days)
Transport Time (days)

Chapter 3:

Rock-magnetic properties, mineralogy and grain size of North Pacific surface sediments: Relation to present day eolian transport processes and implications for the interpretation of ancient sediment

Abstract

The physical properties (rock magnetics, grain size and mineralogy) of eolian sediments are controlled by continental source area, weathering regime and geology, and atmospheric transport mechanisms. Here we present data for a suite of surface sediments spanning the North Pacific eolian province. The data are compared with aerosol rock magnetics, mineralogy and grain size determinations to provide a link between present day aerosol transport and eolian sediment physical properties.

North Pacific eolian sediments are strongly influenced by transport through the atmosphere from Asia to the ocean basin. The grain size and composition of the aerosol are fractionated during transport. The grain size steadily decreases across the entire North Pacific basin. The mineralogy is also fractionated, with decreasing plagioclase and increasing high coercivity minerals, kaolinite and chlorite concentration from Asia toward the center of the ocean. Paleoclimatic reconstructions based on mineralogy variability must consider the compositional fractionation of aerosols during transport, before inferring changes in source area climate or continental source region.

Introduction

Eolian sedimentation is the primary source of sediment in the central North Pacific Ocean. Since the composition and grain size of the eolian sediments depend

upon source area geology, weathering regime and atmospheric transport process, these deposits have been used by paleoclimatologists to infer changes in source area climatology and atmospheric circulation through time. These interpretations are based on research by both atmospheric scientists and geologists, which has largely been independently conducted. Thus, the integration of the observations generated by these two groups is complicated by different analytical techniques and research objectives. This research presents rock magnetic, mineralogy and grain size measurements determined from a suite of North Pacific surface sediments. These measurements are compared with identical analyses made for aerosols collected over the North Pacific Ocean. The goal of this research is to relate the physical characteristics of recent eolian sediments to present day source areas and atmospheric transport patterns in order to enhance paleoclimate reconstructions from ancient eolian sediments.

Sediment transport

The central North Pacific Ocean accumulates eolian sediment transported from the deserts of northern Asia and southwestern North America. Rex and Goldberg (1958) described the coincidence of high quartz concentration in surface sediments of the North Pacific with the peak in the mean zonal velocity of the geostrophic wind and the distribution of arid land area in the Northern Hemisphere. Subsequent research has demonstrated that the grain size (Dauphin, 1983; Rea and Hovan, 1995), composition (Windom, 1975; Griffin, et al., 1968; Leinen, et al., 1986) and flux (Leinen, 1989) distributions of surface sediment properties in the North Pacific Ocean display a pattern which is consistent with dust transport through the atmosphere from Asia. There is a maximum in the flux of quartz beneath the axis of the zonal westerlies, and the concentration decreases from west to east. Eolian material accumulates very slowly in the North Pacific Ocean. Present-day eolian

mass accumulation rates are highest between 38-40°N in the Northwest Pacific (~2,000 $mg/cm^{-2}/ky^{-1}$) and rates decrease to the east, north and south (Leinen, 1989). The decreases are related to distance from the major eolian source (arid regions of Asia) and the predominant transport pathway, high-altitude tropospheric westerlies associated with large storms (Leinen, 1989). Grain size also decreases from west to east, and the mineral distribution patterns mimic the trends displayed by the flux and grain size properties.

Atmospheric scientists have also studied dust transport from Asia into the North Pacific. Continuous sampling through an annual cycle, measured during the SEAREX program in the North Pacific, demonstrated that atmospheric Al concentration, a measure of continental dust concentration, varies seasonally (Parrington, et al., 1983; Parrington and Zoller, 1984; Uematsu, et al., 1983; Duce, et al., 1980 and 1983). Peak aerosol Al concentrations in the North Pacific occur from February to June; the mineral concentration decreases by a factor of 2-12 during the July to January clean period. Periods of high atmospheric Al concentration are associated with Kosa events in Japan and dust storms in Asia (Uematsu, et al., 1983).

In addition to temporal variability, the atmospheric Al concentration varies spatially. In the North Pacific during 1981 through 1982, the largest Al concentrations occurred at high latitudes; mean values ranged from 0.89 $\mu g \cdot m^{-3}$ at Shemya (54°44'N) to 0.05 $\mu g \cdot m^{-3}$ at Fanning (3°55'N). This spatial trend in concentration is observed for the high-dust, for clean periods and for the average annual concentration (Uematsu, et al., 1983).

The seasonal and geographic trends noted for the mineral aerosol concentration are also observed in the measured or calculated depositional flux derived from Al concentration. The total aerosol flux is the sum of both the wet (75-

85% of the total deposition) and dry deposition, and so varies with precipitation as well as dust concentration (Uematsu, et al., 1983 and 1985; Arimoto, et al., 1985). The calculated mineral aerosol flux is similar to the accumulation rate of eolian sediments in the North Pacific (Arimoto, et al., 1985; Uematsu, et al., 1983) with most of the annual dust deposition occurring during short term dust events.

Eolian dust can only dominate sedimentation in regions where the influence of the more rapidly accumulating sediment types is diminished. Other common sedimentation regimes in the North Pacific include downslope (turbidite) continental transport in the Alaskan abyssal plain, biogenic sedimentation in the equatorial region and North Pacific upwelling regions, hemipelagic sedimentation along the margins of the basin, ice rafting in the north, and volcanogenic contributions from the island arcs surrounding the North Pacific. Trenches on the western and northern borders and ridges on the eastern border prevent terrigenous material from being transported downslope into the central basin.

The water of the central gyre is unproductive and the mineral tests of biogenic materials which are produced are not preserved, since the sediment surface is well below the CCD in this region, and the bottom water is undersaturated with respect to silica. The contribution of hemipelagic material drops off rapidly with increasing distance from the continents, but this component is difficult to distinguish from eolian sediment because the lithogenic component of hemipelagic sedimentation contains the same mineral phases as the eolian component. Rea and Hovan (1995) have developed a technique for distinguishing between hemipelagic and eolian sedimentation based on the shape of the terrigenous grain size distribution; the hemipelagic sediment has a flatter distribution and is coarser grained compared with the eolian material. This technique can be used to determine the dominant sedimentary component, but cannot quantitatively partition the sediment into the two

sources. The other component which may contribute to the sediment in the central basin is ash derived from the circum-Pacific island arc chains; however, this component can be quantitatively distinguished from the eolian sediments by statistical partitioning based on chemical analyses (Weber, et al., 1995; Kyte, et al., 1993; Olivarez, et al., 1991). The samples studied in this research cover the full range of sedimentation regimes in the North Pacific Ocean, but primarily consist of samples from the central basin.

Composition

The average composition of the eolian <2 μm size class in the North Pacific red clays is 30-40% illite, 10-15% chlorite, 10-15% quartz, 10-15% plagioclase, 10-15% kaolinite and 0-5% smectite (Leinen, 1989). Quartz and illite concentrations are highest in a latitudinal band centered at ~30°N (Leinen, et al., 1986; Heath and Pisias, 1979; Griffin, et al., 1968). Chlorite concentrations are highest in the north. Kaolinite concentrations are high in latitudinal bands extending from the western and eastern borders into the center of the Pacific basin, but the distribution pattern does not display a continuous band across the ocean (Griffin, et al., 1968). Smectite concentrations are highest along the margins of the North Pacific basin (Griffin, et al., 1968).

Grain Size

J. Paul Dauphin studied the particle size distribution of quartz in the silt-size fraction of North Pacific surface sediments (Dauphin, 1983). Dauphin determined that the mass median diameter of the 2.5-68.3 μm size fraction decreased from 10 μm at 150°E to 7 μm at 140°W. The pattern of quartz grain size distribution shows the same latitudinal distribution as the quartz concentration in surface sediments; the latitudinal band of coarsest grain size is centered at ~30°N.

Rea and Hovan (1995) have measured the 1-30 μm grain size of 40 surface sediment samples in the North Pacific Ocean. In addition to the previously observed trend of decreasing grain size with increasing transport distance from Asia, the authors were able to discriminate between hemipelagic and eolian sediments based on the shape of the grain size distribution curve. Janecek (1985) determined the size of eolian surface sediment particles in the 1-16 μm size range. The median grain size decreased from 4 μm in the western Pacific (DSDP site 578) to 2.4 μm in the eastern Pacific (site LL44-GPC-3).

Rock magnetics

The are no maps of the surface sediment rock magnetic properties in the North Pacific. Rock magnetic measurements provide information on the phase, concentration and grain size of magnetic minerals, primarily iron oxides, in sediments. Since the iron oxide concentration, grain size and composition are highly correlated with the same parameters of the total aluminosilicate (terrigenous) component of sediments (Bloemendal and deMenocal, 1989), these measurements have been extensively used in down core studies to provide continuous proxies of terrigenous sedimentation through time. The measurements are non-destructive, rapid, and can be conducted on whole cores.

Doh and others (1988) used the rock-magnetism properties of sediment recovered from core LL-GPC3, located at 30°N and 157°W in the central North Pacific, to study the paleoceanographic changes of the eolian sediment deposited through time at this location. The authors were able to document changes in the iron oxide flux, composition and grain size based on the rock magnetic analyses which recorded the evolution of sedimentary processes through time. These analyses agreed well with previous studies of the terrigenous composition and grain size which

tracked the movement of the site from the easterly wind regime into the westerly wind regime of the North Pacific. In addition, the onset of northern hemisphere glaciation was expressed as increasing iron oxide grain size and flux, and changing iron oxide composition. This temporal variation in rock magnetic properties should be expressed as spatial variability in the surface sediments, and will be investigated as part of this research.

Here, we again measure the mineralogy and total terrigenous grain size as well as determine the spatial distribution patterns of rock magnetic properties (susceptibility, anhysteretic remanent magnetism and isothermal remanent magnetism) in North Pacific surface sediments. For the grain size and mineralogy, we include coarser size fractions than previous work; mineralogy is measured in both the <2 μm and 2-20 μm size fractions and grain size is determined over a 1 to 63 μm size range. We make all measurements on the same samples, so that we can characterize the covariation of the different sediment properties. We have analyzed a set of aerosol samples collected over the North Pacific Ocean using identical analytical techniques, for comparison with the surface sediments. The aerosol samples have been related to meteorological analyses which allows us to directly compare the physical properties with the source area and transport pathway of eolian sediments. The goal of this research is to provide an integrated data set which relates various eolian sediment proxies with present day eolian sedimentation processes.

Methods

The data set consists of a suite of 168 surface sediment samples collected from the North Pacific (Table 1). These samples are all dried powders, and some of the samples were disaggregated from pressed XRF pellets provide by Frank Kyte of University of California Los A.ngeles. Statistical analysis of the two subsets indicate

that there are no systematic differences in the dried powder vs. the material from the pellet samples.

Rock magnetics

Samples were packed into 1.5 cm^3 Nalgene cylinders for analysis. Cotton was packed into the top of those vials with insufficient sample to fill the volume completely. Susceptibility (X_{lf}, X_{hf}) was measured on a Bartington Instruments susceptibility meter at 0.47 and 4.7 kHz. The reported value (in $\mu m^3/kg$) is the average of three replicates. The samples were demagnetized in a 100 mT alternating field. Anhysteretic remanent magnetization (ARM) was induced in a 0.1 mT steady field superimposed on a 100 mT alternating field. The ARM was measured on a cryogenic magnetometer, and the reported value (in $\mu Am^2/kg$) is the average of duplicate measurements. The X_{arm} was calculated by dividing ARM by the steady field (reported in $\mu m^3/kg$). The final set of magnetic measurements were saturated isothermal remanent magnetization (SIRM) and isothermal remanent magnetization ($IRM_{-0.3T}$). Samples were saturated in a 1.2 T field and measured on a cryogenic magnetometer. Samples were then placed in reverse fields of 0.3 T and the magnetization remeasured. The values reported (in $\mu Am^2/kg$) are averages of duplicate measurements. The frequency ratio (X_{hf}/X_{lf}), the grain size parameter (X_{arm}/X_{lf}), and the compositional parameters (S [$S = IRM_{-0.3T}/SIRM$] and HIRM [$HIRM = \{IRM_{-0.3T} + SIRM\}/2$]) were calculated from the primary measurements. Further explanation of these variables and their applications may be found in the results section. Readers unfamiliar with rock-magnetic techniques are referred to King et al., (1989).

After the rock-magnetism was determined for the bulk samples, the samples were treated to remove biogenic calcite with a buffered acetic acid extraction.

Samples were then wet sieved at 63 μm; the >63 μm and <63 μm fractions were then dried and weighed. The <63 μm fraction was treated to remove biogenic silica using a sodium carbonate procedure. Iron oxides were removed using the oxalic acid extraction technique of Landa and Gast (1973). Sediments were saturated with $MgCl_2$, to reduce d-spacing variability caused by cation differences; they were then rinsed with warm deionized water.

Grain Size

The grain size distribution of the sediment samples was determined using a model 180 Elzone Particle Analyzer. Elzone analysis measures the volume of electrolyte displaced by a particle when it passes through a small orifice between two electrodes. The volume is converted to equivalent spherical diameter and the instrument is calibrated using latex spheres of a known diameter and volume. Samples were analyzed to provide a continuous grain size distribution (in equivalent spherical diameter) between 1 and 63 μm.

After the sediment had been processed to remove biogenic silica, calcium carbonate and iron oxides, the suspended <63 μm sediment is shaken and a subsample of this slurry is pipetted into a filtered solution of 4% sodium pyrophosphate and stirred continuously for analysis using a 120 μm diameter orifice tube. This procedure is repeated, sieving at 20 μm and using a 48 μm orifice tube to provide a more accurate measurement of the <20 μm size fraction. The 20-63 μm sieved size fraction is weighed and stored. The <20 μm size fraction is subsequently used for quantitative mineralogical analysis. 128 channels are measured for each orifice size and the results for both analyses are combined using a smoothing program to provide a continuous grain size profile between 1 and 63 μm.

Mineralogy

The <20 μm fraction was split into 2-20 μm and <2 μm size fractions by means of centrifugation. The 2-20 μm size and the <2 μm fraction was spiked with a 10% talc internal standard. Samples were homogenized by grinding in a mortar and pestle under acetone, air dried, suspended in a deionized water slurry, and drawn onto silver filters for X-ray analysis.

The samples were X-rayed from 2° to 32° 2Θ at 45 kV and 40 mA at 1° 2Θ per minute, using Cu-kα radiation. Peak areas for smectite, illite, kaolinite, chlorite, quartz, and plagioclase were determined using Scintag DMS software. The relative proportion of kaolinite and chlorite was determined by the relative proportions of the kaolinite [002] and chlorite [004] peak areas. Mineral peak areas were normalized to the internal standard peak areas and converted to mineral weight percent using the weighting factors of Heath and Pisias (1969).

Results

Rock magnetics

For all discussion, samples further south than 20°S are excluded from consideration, due to paucity of data below this latitude. The magnetic measurements are made on unprocessed samples, thus recording the influence of all the sedimentary processes effecting the sample site. The concentration of magnetic material in a sample is determined from the susceptibility (X) data, which is a measurement of the magnitude of the magnetic moment measured while the sample is in an magnetic field. This measurement is made at two frequencies, with differences in the high and low frequency susceptibility due to the contribution of ultra fine, or superparamagnetic, particles. The high frequency susceptibility (X_{hf}) and low

frequency susceptibility (X_{lf}) have means of 0.63± 0.65 and 0.66±0.67 $\mu m^3/kg$ (Table 2). The magnetic concentration is lowest along the equatorial region where terrigenous material is diluted with the high flux of biogenic (primarily calcium carbonate) sedimentation (Fig. 1). Susceptibility values are highest along the margins of the North Pacific and near the Hawaiian Islands, reflecting the strong input of highly magnetic volcanogenic material. Central basin values are intermediate to the other end members, reflecting a high concentration of terrigenous material but a smaller volcanogenic influence than near the margins.

The saturated isothermal remanent (SIRM) is the magnitude of the magnetic moment retained after the sample has been magnetically saturated in a strong magnetic field, and again is indicative of the concentration of the magnetic material in a sample. The mean SIRM for the North Pacific sediments is 14,397±14,240 $\mu Am^2/kg$. The spatial distribution of SIRM closely mimics the distribution of the susceptibility (Fig. 2).

The HIRM is the amount of remanent magnetism remaining after the magnetically saturated sample has been exposed to a weaker reversed field. This measurement depends both on the concentration and the coercivity (a function of the composition) of magnetic material. As an example, magnetite is a "soft" or low coercivity mineral; all of the induced magnetism from the SIRM is stripped off in the weaker reversed field. Conversely, hematite is a "hard" or high coercivity material. Since "hard" minerals are not easily magnetized, some of the magnetism from the saturation step is retained after exposure to the weaker reversed field. Thus, this measurement indicates the concentration of high coercivity material in the sediment. The mean HIRM is 425±579 $\mu Am^2/kg$. Again, the spatial distribution of the HIRM mimics the X_{lf} and the SIRM (Fig. 3).

The final magnetic concentration measurement is the anhysteretic remenant magnetism (ARM), here expressed in the same units as the susceptibility, as X_{arm}. This measurement is sensitive to both the concentration and the grain size of the magnetic material, with finer particles yielding a higher measurement than larger particles. The mean X_{arm} is 11.5±7.8 $\mu m^3/kg$. Unlike the previously discussed measurements of magnetic concentration, the highest values for X_{arm} occur in the central basin from the equator north to Hawaii (Fig. 4). These high X_{arm} values may reflect the presence of ultra-fine magnetic particles produced by sediment-dwelling magnetotactic bacteria for samples near the equator. The lowest X_{arm} values occur south of the equator and in the northwest quadrant of the central Pacific Ocean.

Since the X_{arm} values are sensitive to both magnetic concentration and magnetic particle size, normalizing these measurements to concentration will yield a parameter which is inversely proportional to magnetic particle size. A map of the spatial distribution of the ratio X_{arm}/X_{lf} is presented in figure 5. The bull's eye in the southeast quadrant of the map is located over the east pacific rise, and likely represents the magnetic signature of hydrothermal sediments, which would contribute very fine grained iron oxide particles to the sediment. In general, the X_{arm}/X_{lf} values of samples south of 10°N are high, indicating fine magnetic particle sizes. The ratio is low around the margins of the northern basin, consistent with a large contribution of coarse terrigenous and volcanogenic magnetic material.

The final magnetic parameter is the S-ratio, -IRM/SIRM, which is a compositional parameter expressing the proportion of high coercivity material in the sediment. Sediment containing a large proportion of high coercivity material, such as hematite, will have a lower S-ratio than sediments with a large proportion of low coercivity material such as magnetite. Samples with the lowest S-ratio are located in the central North Pacific (Fig. 6). The relatively high proportion of high coercivity

material in this region is related to the dominance of terrigenous sedimentation. Volcanogenic material has a high proportion of magnetite, but material from the deserts of northern Asia should have a higher proportion of hematite produced by the weathering conditions in this region.

Grain Size

The median grain size for the <63 μm terrigenous fraction of the samples is 6.1±4.6 μm (Table 3). The largest grain sizes are found on the southeast quadrant of the map area, from the spreading ridge/hydrothermal areas (Fig. 7). The grain size is large around the northern margins of the basin and near Hawaii, and the finest grain sizes are in the central North Pacific and along the equatorial region. The terrigenous grain size distribution in the open ocean is primarily a function of the transport distance from the various source areas.

Figures 8-11 illustrate the weight percent of each of the size classes >63 μm, 20-63 μm, 2-20 μm and <2 μm derived from the sample processing. The weight percentages are all relative to the calcium carbonate free weight, so that the residual is the amount of siliceous biogenic and iron oxide material extracted and material lost during sample processing. The >63 μm size fraction reflects a large input of either ice rafted or downslope transport in the Gulf of Alaska, a large grain size component near the spreading/hydrothermal regions in the southeast and a coarse grain size component, possibly biogenic silica tests to the south of the equator in the central basin. The high 20-63 μm percentage along the northern margins reflects the influence of the continents and volcanoes bordering the North Pacific, and again, there is a large grain size influence on the sediments from the spreading ridge in the southeast quadrant of the map area. The 2-20 μm weight percent is highest in the central northwestern basin of the Pacific, while the <2 μm size fraction is present in

highest concentration in the central northeastern basin.

Mineralogy

There are six mineralogy phases which were quantified in this study; smectite, illite, kaolinite, chlorite, quartz and plagioclase (Table 4). The average smectite concentration is 13.0±12.0 % and 5.2±5.3 in the <2 μm and 2-20 μm size fractions, respectively. In the <2 μm size fraction, the smectite concentrations are highest in the low latitudes; the northern margins display moderate values and the central basin contains the lowest smectite concentration (Fig. 12). The coarser size fraction smectite concentration is also highest in the low latitudes, with generally low concentrations everywhere else (Fig. 18). This distribution pattern indicates a large contribution of smectite from low latitude weathering of volcanic material in Central and South America, with easterly transport through the atmosphere into the ocean. The moderate smectite values along the northern margins reflect the dominance of volcanic input in this region. The low smectite concentrations in the central basin are consistent with a source area in the deserts of northern Asia.

The illite concentration in the North Pacific is 47±17% for the <2 μm size fraction and 31±14% for the 2-20 μm size fraction. Illite concentrations are highest in the central basin in both size fractions, consistent with dominantly terrigenous sedimentation from mid latitude continental areas (Figs. 13 and 19). For almost all <2 μm samples, illite is the dominant mineral phase. In the 2-20 μm size fraction either illite or plagioclase is present in the highest concentration.

Kaolinite is present in concentrations of 17±11% in the <2 μm size fraction and 8±7% in the 2-20 μm size fraction. The <2 μm size fraction displays moderate concentrations along the northern margin of the basin, and high concentration off the coast of Central and South America (Fig. 14). The 2-20 μm size fraction kaolinite is

most common off the coast of Central and South America (Fig. 20).

Chlorite ranges from 5±3% and 3±2% in the <2 μm and 2-20 μm size fractions, respectively. The highest chlorite values tend to occur near the northeast and eastern margin of the basin in the <2 μm size fraction (Fig. 15). The 2-20 μm chlorite concentration is high near the margins and in the region around the Hawaiian Islands (Fig. 21).

Quartz concentration in the <2 μm size fraction is 7±4%, while in the 2-20 μm size fraction, quartz concentrations are higher, 16±8%. The quartz concentration in both the <2 μm and the 2-20 μm size fraction is highest in the western mid-latitude portion of the Pacific Ocean (Figs. 16 and 22).

Plagioclase concentrations average 10±8% for the <2 μm size fraction and 36±13% in the 2-20 μm size fraction. There is a strong input of plagioclase along the northern margin of the Pacific, low concentrations in the central basin and intermediate values along the eastern equatorial region (Figs. 17 and 23). This is consistent with strong volcanogenic inputs from the island arc volcanoes in the north, moderate input from volcanoes along the edge of the Central and South America, and primarily terrigenous input in the central basin.

Discussion

The fundamental hypothesis investigated in this research is that the rock magnetics, grain size and mineralogy of the sediments are indicative of the sediment source area and the transport dynamics. One important question is whether each of the parameters convolve both the source signal and the dynamics, or whether some parameters are more sensitive to source region and other to transport process. When interpreting the eolian sediment record, particle size has been used as a measure of

transport vigor, and composition as an proxy for either changing source area or changing weathering regime in the same source area.

In order to investigate this problem, a series of plots were constructed illustrating the variation of the measured parameters with transport distance (longitude) from Asia. Additionally, the values of aerosol measurements are plotted at their sampling longitude for comparison with the sediment values. Coherent trends in these plots should be indicative of the influence of eolian transport process on the measured parameters for the sediments.

The susceptibility, SIRM and HIRM display rapidly decreasing magnetic concentration from 130°E to 160°E, reflecting the diminishing influence of hemipelagic/volcanogenic material with increasing distance from the continent (Fig. 24). X_{arm} values are much more scattered than the other magnetic concentration parameters, but are high between 140°E and 160°E, and show a general increase across the basin with increasing longitude. The average susceptibility and SIRM aerosol concentrations fall within the range of the sediment data, but the X_{arm} is much lower and the HIRM mean values are higher than those of the sediments. The higher HIRM values indicate that the aerosols are relatively enriched in high coercivity material relative to the sediments, while the X_{arm} observations suggest that the sediments are either magnetically coarser grained or contain less magnetic material than the sediment. The differences between the two groups could be due to a soluble iron oxide component, such as hematite coatings on the mineral particles. Thus, dissolution of hematite in the water column explains the higher HIRM values, but the X_{arm} values suggest that there must be preferential dissolution of large magnetic particles. However, the magnetic measurements are composites of all of the magnetic material in the sediment; the relationship between grain size and X_{arm} is different for different mineral phases. Thus, preferential dissolution of hematite could

produce the increase in X_{arm} and decrease in the HIRM aerosols required to bring the aerosols in line with the sediment observations.

Figure 25 shows the magnetic composition parameter S, plotted as a function of longitude. There is a general decrease in the ratio, indicating an increase in the relative proportion of high coercivity material with distance from the continent. This is consistent with both diminishing hemipelagic/volcanogenic input across the ocean, but likely also includes fractionation of the eolian aerosol during transport. As dense, magnetic particles preferentially settle out, the aerosol is enriched in fine grained aluminosilicates coated with high coercivity iron oxides. A large change in the proportion of high coercivity to low coercivity material is required to change the S-ratio, thus this observation is not necessarily in conflict with the mechanism proposed for explaining the discrepancy between the aerosol and sediment X_{arm} values.

The rock magnetic grain size proxy X_{arm}/X and the aluminosilicate geometric mean and median grain diameter are illustrated in figure 26. There is a steep decrease in grain size from 130°E to 160°E, followed by a small, but steady decline in grain size across the entire North Pacific basin. The aerosol measurement of X_{arm}/X fall well below the sediment values, and this again is explained by some dissolution of iron oxides in the ocean.

The aerosol Elzone particle size measurements fit the sediment observations. Figure 27 shows the variation of the weight percent of each of the sediment size fractions separated during sample processing. There is very little >63μm material in North Pacific surface sediments. The 20-63μm size fraction shows the same continentally influenced drop off between 130°E and 160°E observed in the previously discussed observations. The 2-20μm size class remains relatively constant, but the <2μm size class steadily increases across the basin. It has been suggested that

wind transported aluminosilicates achieve equilibrium with respect to the particle size and the zonal wind velocity after a few thousand kilometers (Janecek and Rea, 1985; Janecek and Rea, 1983; Rea and Janecek, 1982); this hypothesis is not supported by the sediment observations in this work.

Fractionation of aerosol mineralogy has been described by Johnson (1976), and in Chapter 2 of this dissertation, a decrease in the kaolinite, plagioclase and quartz concentrations, and an increase in the clay minerals smectite, illite and chlorite concentration with increasing transport time from Asia was noted. The sediment mineralogy data is plotted in figures 28 through 31. There are no clear trends in the mineralogy concentration with distance from Asia in the <2 μm size class; but the aerosols do show the same range of variability as the sediments. The 2-20 μm size fraction is characterized by flat distributions of smectite, illite and quartz across the North Pacific basin. Kaolinite and chlorite appear to increase in concentration, and plagioclase decreases in concentration from west to east across the basin. The aerosol data is in good agreement with the sediment mineralogy data.

Conclusions

The rock-magnetism, grain size and mineralogy of North Pacific surface sediments can be used to distinguish a variety a sedimentary processes. Hemipelagic and volcanogenic material fringe the northern margins of the basin and the region around Hawaii. These sediments are characterized by coarse-grained, highly-magnetic sediments, rich in smectite and plagioclase. The equatorial region is comprised of biogenic sediment which dilutes the small amount of terrigenous material transported through the atmosphere and into the oceans from the American continents. The sediment is characterized by low magnetic concentration, extremely small magnetic particle size, fine aluminosilicate particle size, and is rich in smectite.

The East Pacific Rise spreading/hydrothermal area is characterized by very large aluminosilicate particle size, very fine grained magnetic particle size, low magnetic concentration and unique mineralogy.

Large regions of the central basin are dominated by eolian terrigenous material transported through the atmosphere from the deserts of northern Asia. This sediment is characterized by intermediate magnetic concentration and particle size, very fine grained aluminosilicate particles and a mineralogy which is characteristic of terrigenous material.

Detailed examination of the eolian sediments indicate strong magnetic and grain size gradients from the Asia coast into the central basin. These strong gradients represent the border between the hemipelagic and volcanogenic sedimentation dominance to the west of 160°E and predominantly eolian sedimentation to the east. These same hemipelagic/volcanogenic gradients occur at about 45°N, but the southern boundary of the eolian province is poorly delineated.

There is good agreement between the magnetic concentration, the overall composition and particle size of eolian sediments and aerosols collected over the North Pacific Ocean. The eolian material is fractionated as it travels through the atmosphere. The aluminosilicate and magnetic particle size decreases across the North Pacific Basin. The aerosols are also compositionally fractionated during sediment transport; the S-ratio decreases, indicating a relative enrichment in high coercivity material with increasing distance from the source area. There is no coherent pattern in the <2μm mineralogy across the basin, but the 2-20μm size fraction demonstrates an increase in chlorite and kaolinite and a decrease in the plagioclase concentration across the basin.

The interpretation of ancient eolian sediments can be enhanced by utilizing

the observations from this research. Typically, changes in mineralogy are attributed to changes in source area or weathering regime in the source area. Here we see that the mineralogy can be changed by changing transport length (time), so that if mineralogy concentration changes coherently with grain size, the source area may not have changed. Similarly, the ratios between two minerals are frequently used to infer changes in source area. However, the gradients for each mineral phase are different, thus changing mineral ratios over time do not necessarily dictate climate or source area change. Again, controlling the interpretation of the mineralogy with grain size or rock magnetic data is required.

In order to appropriately interpret climate change from the mineralogy cores must be analyzed along the transport pathway. Changes in the mineralogy gradients between two cores over time are unambiguously due to either changing source region or source region climate. Furthermore, if the grain size gradient does not change, while the mineralogy gradient does, mineralogy can be related to source region climate change.

Acknowledgments

Frank Kyte supplied many of the surface sediments for this research. This research was supported by NSF grant ATM 91-02385.

References

Arimoto, R., Duce, R. A., Ray, B. J. and Unni, C. K. 1985. Atmospheric trace elements at Enewetak atoll: 2. Transport to the ocean by wet and dry deposition. Journal of Geophysical Research, 90:2,391-2,408.

Bloemendal, J. and deMenocal, P. 1989. Evidence for a change in periodicity of tropical climate cycles at 2.4 Myr from whole-core magnetic suceptibility measurements. Nature, 342:897-900.

Doh, S.-J., King, J. W. and Leinen, M. 1988. A rock-magnetic study of giant piston core LL44-GPC3 from the central North Pacific and its paleoceanographic implications. Paleoceanography, 3:89-111.

Duce, R. A., Arimoto, R., Ray, B. J., Unni, C. K. and Harder, P. J. 1983. Atmospheric trace elements at Enewetak Atoll: 1, concentrations, sources and temporal variability. Journal of Geophysical Research, 88:321-5342.

Duce, R. A., Unni, C. K., Ray, B. J., Prospero, J. M. and Merrill, J. T. 1980. Long-range transport of soil dust from Asia to the tropical North Pacific: temporal variability. Science, 209:1,522-1,524.

Griffin, J. J., Windom, H. and Goldberg, E. D. 1968. The distribution of clay minerals in the world ocean. Deep-Sea Research, 15:433-459.

Heath, G. R. and Pisias, N. G. 1979. A method for the quatitative estimation of clay minerals in North Pacific deep-sea sediments. Clays and Clay Minerals, 27:175-184.

Janecek, T. R. and Rea, D. K. 1983. Eolian deposition in the northeast Pacific Ocean: Cenozoic history of atmospheric circulation. Geological Society of America Bulletin, 94:730-738.

Johnson, L. R. 1976. Particle-size fractionation of eolian dusts during transport and sampling. Marine Geology, 21:M17-M21.

King, J. W., Bloemendal, J. and Gangemi, P. 1989. Paleomagnetic and rock-magetic stratigraphy of ESOPE core 63, southern Nares abyssal plain. 611-636. In: Schuttenhelm, R. T. E., Auffret, G. A., Buckley, D. E., Cranston, R. E., Murray, C. N., Shepard, L. E. and Spijkstra, A. E. The ESOPE international expedition, geoscience investigations of two North Atlantic abyssal plains. Office for official publications of the European community. Luxembourg.

Kyte, F. T., Leinen, M., Heath, G. R. and Zhou, L. 1993. Cenozoic sedimentation history of the central North Pacific: Inferences from the elemental geochemistry of core LL44-GPC3. Geochimica et Cosmochimica Acta, 57:1719-1740.

Landa, E. R. and Gast, R. G. 1973. Evaluation of crystallinity in hydrated ferric oxides. Clays and clay minerals, 21:121-130.

Leinen, M. 1989. The pelagic clay province of the North Pacific Ocean. 323-335. In: Winterer, E. L., Hussong, D. M. and Decker, R. W. The eastern Pacific Ocean and Hawaii. Geological Society of America. Boulder.

Leinen, M., Cwienk, D., Heath, G. R., Biscaye, P. E., Kolla, V., Thiede, J. and Dauphin, J. P. 1986. Distribution of biogenic silica and quartz in recent deep-sea sediments. Geology, 14:199-203.

Olivarez, A. M., Owen, R. M. and Rea, D. K. 1991. Geochemistry of eolian dust in Pacific pelagic sediments: implications for paleoclimatic interpretations. Geochimica et Cosmochimica Acta, 55:2147-2158.

Parrington, J. R. and Zoller, W. H. 1984. Diurnal and longer-term changes in the composition of atmospheric particles at Mauna Loa, Hawaii. Journal of Geophysical Research, 89:2,522-2,534.

Parrington, J. R., Zoller, W. H. and Aras, N. K. 1983. Asian dust: seasonal transport to the Hawaiian Islands. Science, 220:195-197.

Rea, D. K. and Hovan, S. A. 1995. Grain size distributions and depositional processes of the mineral component of abyssal sediments: lessons from the North Pacific. Paleoceanography, 10:251-258.

Rea, D. K. and Janecek, T. R. 1982. Late Cenozoic changes in atmospheric circulation deduced from North Pacific eolian sediment. Marine Geology, 49:149-167.

Rex, R. W. and Goldberg, E. D. 1958. Quartz contents of pelagic sediments of the Pacific Ocean. Tellus, 10:153-159.

Uematsu, M., Duce, R. A. and Prospero, J. M. 1985. Deposition of atmospheric mineral particles in the North Pacific Ocean. Journal of Atmospheric Chemistry, 3:123-138.

Uematsu, M., Duce, R. A., Prospero, J. M., Chen, L. Q. and Merrill, J. T. 1983. Transport of mineral aerosol from Asia to the North Pacific Ocean. Journal of Geophysical Research, 88:5343-5352.

Weber II, E. T., Owen, R. M., Dickens, G. R., Halliday, A. N., Jones, C. E. and Rea, D. K. 1996. Quantitative resolution of eolian continental crustal material and volcanic detritus in North Pacific surface sediment. Paleoceanography, 11:115-127.

Windom, H. L. 1975. Eolian contributions to marine sediments. Journal of Sedimentary Petrology, 45:520-529.

Table 1. Location of sediment samples.

[redacted] ID	Sample Name	Latitude + = North - = South	Longitude + = East - = West	Water Depth (m)	Sample Depth (cm)
	HILO 05G	22.95	-143.97	4850	3.5
2	PROA 132G	3.67	-168.37	5441	2.5
3	V3612 46G	32.68	163.53		3.0
4	PAPA 03 GC	14.80	-119.87	4218	1.5
5	ZETES III 11G	27.70	146.77		2.5
6	JYN IV 14G	22.02	-179.85		5.0
7	RC10 245	11.13	-98.73	3680	0.5
8	JYN IV 15G	21.90	-175.55		4.0
9	AKACARMNOVA	20.18	174.72		5.0
10	JYN II 47PG	14.65	-135.07		3.0
11	V21 065	23.97	-176.85	5365	1.0
12	JYN IV 06G	24.48	160.18		1.5
13	CARM 11G	16.87	156.78		5.0
14	HILO 12G	23.60	-156.08	4381	3.0
15	NOVA A1 2G	-13.02	-171.70		1.5
16	MSN 2G	23.25	-130.77	4950	1.0
17	RP20 C72	28.67	173.70		4.0
18	Y70 16P	45.00	-142.58	5189	4.0
19	Y70 1 9	45.00	-149.95		0.0
20	SCAN 13P	6.32	-140.32	5059	1.0
21	ARIES 40PG	29.66	160.99	5701	2.0
22	MEN 23G	40.63	-149.02	4810	5.0
23	MEN 26G	40.73	-139.37	4540	3.0
24	JYN II 12G	39.78	160.88	5510	5.0
25	V20 126TW	42.15	155.87	5515	1.0
26	MUK B1G	35.25	-129.27		5.0
27	LSDH 082G	8.98	173.02	5000	3.0
28	MEN 28G	38.67	-142.60	5270	2.5
29	RC10 167TW	33.40	150.38	6092	0.5
30	JYN IV 05G	27.70	153.95		5.0
31	MEN 25G	40.68	-142.87	4700	2.5
32	LSDH 103G	27.48	-125.82	4450	1.0
33	MSN 3G	20.02	-135.20	5220	1.0
34	V20 122TW	46.57	161.68	5563	1.0
35	V20 064	23.35	-155.87	4205	1.5
36	V20 079	46.83	-133.30	3711	0.5
37	ANTP 46PG	45.49	160.95	5736	5.0
38	JYN IV 10G	28.73	173.17		1.0
39	CUSP 11G	45.57	-143.18		5.0
40	V20 066	28.00	-151.17	5338	1.0
41	JYN II 06G	37.93	178.17	5250	5.0
42	JYN IV 12G	27.08	177.68		1.0
43	JYN II 20G	37.07	148.23	5730	3.5

Table 1. Continued.

Sample ID	Sample Name	Latitude + = North - = South	Longitude + = East - = West	Water Depth (m)	Sample Depth (cm)
44	V21 067	24.97	176.27	5879	1.0
45	ANTP 45PG	46.68	161.97	5676	3.0
46	Y70 1 7P	45.00	-145.40	4746	4.0
47	JETES 41G	31.02	-137.68		4.0
48	V20 147	4.65	132.78	3213	1.0
49	PAPA 04 GC	9.93	-119.70	4321	3.0
50	JYN II 08G	40.48	172.55	4250	5.0
51	MUK H19G	51.23	-145.67		5.0
52	V20 106	40.87	-178.47		1.0
53	V21 031	-1.83	-90.47	3334	1.0
54	V19 054	-17.03	-113.90	2964	0.0
55	V28 304TW	28.53	134.13	2942	0.5
56	RC11 174	52.58	-151.35	1618	1.0
57	RC13 108	-3.12	-89.42	3308	0.5
58	JYN II 07G	40.20	173.98	4340	1.5
59	V21 171TW	49.88	-164.95	5013	2.5
60	RC10 250	6.28	-84.32	1734	0.5
61	RC10 079	9.32	-110.55	3630	4.0
62	RC10 140	-2.65	156.98	1679	0.0
63	RC13 132	7.87	-97.66	3484	1.0
64	V20 080	46.50	-135.00	3801	0.5
65	AKACARNOVA9G	19.45	170.00		3.0
66	V28 235TW	-5.45	160.48	1746	1.0
67	JYN II 03G	30.32	-170.35	5490	3.0
68	V20 147TW	4.65	132.78	3213	0.5
69	JYN II 15G	38.22	157.27	5670	3.5
70	Y70 1 2 LD	44.98	-134.03		0.0
71	RC10 249	7.32	-87.05	3233	0.5
72	LSDH 089P	8.13	-177.17	5435	3.0
73	ARIES 49G	36.43	178.64	3902	3.5
74	BNFC 86PG	14.58	-121.07		1.0
75	KK74FFC76	6.55	-104.90		0.5
76	KK7401091C01	-0.20	-100.40		3.0
77	KK740109FFC12	2.33	-100.80		5.0
78	KK740109FFC77	8.12	-104.10		3.0
79	LSDH 087	11.50	177.80	5520	5.0
80	KK740109GCTG02	7.87	-104.30		4.5
81	Y71991M61	-5.95	-104.86	3512	4.0
82	BNFC 20PG	10.57	-108.40		1.0
83	CCTW 2GC	8.27	-104.09	3100	2.0
84	KK740109TC2	-0.33	-102.30		3.0
85	CARM 10G	18.49	166.00		1.0
86	AMPH 17GC	-7.98	-108.62	3200	2.5

Table 1. Continued.

Sample ID	Sample Name	Latitude + = North - = South	Longitude + = East - = West	Water Depth (m)	Sample Depth (cm)
87	RC12 027	7.75	-83.97	1683	0.5
88	JYN II 11G	39.93	165.53	5350	4.0
89	AMPH 18GC	-8.18	-108.18	3400	3.5
90	CCTW 1GC	8.27	-104.17	3280	4.0
91	KK740109PC004	2.37	-100.80		5.0
92	V3612 44	33.24	152.03		5.0
93	STYX 3FFGD	20.07	-130.07	4959	0.0
94	BNFC 01GC	18.30	-104.70		1.0
95	V3612 38P	39.29	151.50		5.0
96	RC15 065	-53.07	-78.95	4111	0.5
97	RC12 087	-2.30	-163.97	5243	0.5
98	V28 203	0.95	-179.42	3243	0.0
99	V28 304	28.53	134.13	2942	0.5
100	V21 059TW	20.92	-158.10	2992	0.5
101	RC10 108	-12.57	-148.20	4200	0.5
102	V21 059	20.92	-158.10	2992	0.5
103	RC15 052TW	-29.24	-85.99	3780	0.5
104	SCAN 59P	11.00	-175.18	4849	3.0
105	RC13 023	0.04	-175.06	5218	0.5
106	JYN II 14G	39.32	156.95	5635	3.0
107	JYN II 05G	35.42	-177.72	4320	1.0
108	RC15 061	-45.29	-77.21	2809	0.5
109	V24 095	27.60	177.77	5287	1.0
110	JYN IV 04G	29.30	150.70		4.0
111	RC12 032	13.00	-92.65	4034	0.5
112	JYN II 10G	40.50	169.80	5550	1.5
113	V15 053	-33.45	-73.67	3915	0.5
114	V21 172	47.67	-164.35	5198	1.0
115	WAH 2P	11.85	-152.95		1.0
116	HILO 03G	24.78	-134.52	4700	5.5
117	ZETES 05G	46.27	158.17	4714	2.0
118	V3612 32P	30.92	151.62		1.0
119	V20 129	37.68	156.58	5766	2.0
120	V20 102	31.18	-177.82	5216	1.0
121	BNFC 15P				1.0
122	MEN 21G	41.12	-151.37	5150	1.0
123	RC10 107	-8.83	-146.27	5127	0.5
124	MEN 22G	39.35	-149.93	5560	2.5
125	SHOW A 18G	23.63	-155.73		3.0
126	RC12 029	9.45	-88.03	3274	1.0
127	RC11 180	53.15	-142.90	3860	0.5
128	JYN IV 17G	21.65	-166.65		3.0
129	SCAN 09PG	19.87	-139.86	5176	3.0

Table 1. Continued.

Sample ID	Sample Name	Latitude + = North - = South	Longitude + = East - = West	Water Depth (m)	Sample Depth (cm)
130	ZETES 14G	25.14	-164.10		3.0
131	KK740109FFC17	-0.87	-95.40		4.0
132	V3612 51P	32.38	164.46		3.0
133	Y71754PCV	-10.99	-103.75	5343	4.0
134	V3612 47P	32.06	164.32		4.0
135	Y70 1 2PC	44.59	-134.00		0.0
136	CUSP 17G	36.10	-142.50		3.0
137	V21 029	0.95	-89.35	712	1.0
138	STYX 22G	15.82	-157.07	5310	0.0
139	V28 235	-5.45	160.48	1746	0.5
140	RC15 062	-45.28	-77.22		1.0
141	RC15 052	-29.24	-85.99	3780	0.5
142	SCAN 08P	28.19	-140.01	4794	2.0
143	SCAN 20P	24.10	-178.50	5604	3.0
144	SCAN 07PG	33.06	-140.01	5025	2.0
145	PAPA 103GC	17.45	-104.80	3052	2.5
146	WAH 4P	8.59	-152.50		2.0
147	BNFC 17PG1	11.18	-109.60		1.0
148	V3612 49P	32.24	164.16		3.0
149	JYN IV 07G	21.02	164.97		1.5
150	JYN II 04G	33.07	-174.25	5530	4.0
151	V18 349	6.07	-85.72	1818	0.5
152	ARIES 45PG	36.58	174.95	5195	2.0
153	7TOW186G	34.52	-124.50		3.0
154	RC13 063	1.35	-153.07	4420	0.5
155	RC10 106	-4.27	-146.47	4590	0.5
156	AMPH 24GC	-8.87	-106.42	3370	3.5
157	AMPH 12GC	-7.60	-110.97	3480	2.5
158	AMPH 22GC	-8.57	-107.20	3240	1.0
159	Y71992M62	-6.80	-106.11		4.0
160	RC08 094	-27.28	-102.08	3074	0.5
161	RC10 117	-6.82	-165.37	3523	0.5
162	RC12 225	-53.67	-123.13	2964	0.0
163	V19 064	-16.93	-121.20	3570	0.5
164	V19 065	-16.65	-124.38	3867	0.5
165	V21 045	-7.13	-119.90	4198	0.5
166	V28 203TW	0.95	-179.42	3243	0.5
167	V28 243	11.07	138.53	2129	0.0

Table 2. Rock magnetic measurements.

ID #	LF Susc. $\mu m^3/kg$	HF Susc. $\mu m^3/kg$	ARM $\mu Am^2/kg$	X_{arm} $\mu m^3/kg$	X_{arm}/X	SIRM $\mu Am^2/kg$	IRM-3T $\mu Am^2/kg$	S	HIRM $\mu Am^2/kg$
1	0.56	0.53	1188.71	14.93	26.59	13027	-12049	0.92	489
2	0.28	0.26	1652.49	20.76	74.03	8528	-8371	0.98	78
3	0.41	0.40	568.38	7.14	17.45	9955	-8875	0.89	540
4	0.42	0.41	1502.86	18.88	44.52	9132	-8494	0.93	319
5	1.06	1.02	869.06	10.92	10.33	27811	-25808	0.93	1001
6	0.37	0.37	915.05	11.50	30.68	7823	-6830	0.87	497
7	0.49	0.47	861.95	10.83	22.17	13056	-12492	0.96	282
8	0.39	0.37	911.18	11.45	29.08	7943	-6898	0.87	523
9	0.50	0.46	1318.23	16.56	32.87	8973	-8404	0.94	285
10	0.44	0.42	1551.31	19.49	44.40	9622	-8969	0.93	326
11	0.36	0.34	753.35	9.46	26.09	7734	-6853	0.89	441
12	0.58	0.55	895.03	11.24	19.53	11947	-10421	0.87	763
13	0.69	0.65	1599.68	20.10	28.93	13582	-13012	0.96	285
14	1.62	1.57	1624.32	20.41	12.60	49819	-46949	0.94	1435
15	0.29	0.27	955.13	12.00	41.42	6889	-6083	0.88	403
16	0.47	0.43	1130.53	14.20	30.37	8980	-7701	0.86	640
17	0.43	0.41	732.88	9.21	21.32	8125	-7240	0.89	443
18	0.55	0.52	781.84	9.82	17.99	14456	-13402	0.93	527
19	0.48	0.46	824.70	10.36	21.38	12854	-11988	0.93	433
20	0.37	0.30	2295.99	28.84	78.11	10791	-10386	0.96	203
21	0.58	0.55	718.23	9.02	15.49	12303	-11235	0.91	534
22	0.40	0.38	877.42	11.02	27.71	9527	-8501	0.89	513
23	0.47	0.44	973.44	12.23	26.28	9879	-8872	0.90	504
24	0.69	0.66	1111.67	13.97	20.30	18130	-17334	0.96	398
25	0.73	0.72	809.67	10.17	13.86	21121	-19913	0.94	604
26	0.53	0.51	908.48	11.41	21.49	10121	-9525	0.94	298

Table 2. Continued.

ID #	LF Susc. $\mu m^3/kg$	HF Susc. $\mu m^3/kg$	ARM $\mu Am^2/kg$	X_{arm} $\mu m^3/kg$	X_{arm}/X	SIRM $\mu Am^2/kg$	IRM-3T $\mu Am^2/kg$	S	HIRM $\mu Am^2/kg$
27	0.47	0.54	1501.45	18.86	40.44	13547	-13148	0.97	200
28	0.38	0.37	829.53	10.42	27.18	6909	-6139	0.89	385
29	0.99	0.96	793.78	9.97	10.06	30329	-28530	0.94	900
30	1.03	0.99	963.71	12.11	11.75	21113	-19146	0.91	983
31	0.39	0.37	898.60	11.29	28.64	8935	-7738	0.87	599
32	0.55	0.51	1252.98	15.74	28.72	10246	-9550	0.93	348
33	0.47	0.45	1180.92	14.84	31.64	10661	-9704	0.91	479
34	2.05	1.99	1418.68	17.82	8.71	52679	-51227	0.97	726
35	2.07	2.03				67763	-64718	0.96	1522
36	0.54	0.51	903.54	11.35	21.02	13503	-12826	0.95	338
37	2.44	2.39	856.39	10.76	4.41	40807	-39011	0.96	898
38	0.39	0.37	789.39	9.92	25.21	7918	-7054	0.89	432
39	0.54	0.53	739.10	9.29	17.08	14884	-14137	0.95	374
40	0.46	0.44	830.10	10.43	22.74	11446	-10464	0.91	491
41	0.39	0.37	735.67	9.24	23.67	10870	-10074	0.93	398
42	0.41	0.39	858.51	10.79	26.21	7862	-6927	0.88	467
43	1.53	1.49	1013.94	12.74	8.32	45533	-43331	0.95	1101
44	0.37	0.35	764.74	9.61	26.23	7298	-6562	0.90	368
45	1.57	1.53	1278.00	16.06	10.23	42370	-40759	0.96	806
46	0.69	0.66	834.89	10.49	15.11	18922	-17417	0.92	752
47	0.42	0.38	974.38	12.24	29.20	8109	-7418	0.91	345
48	0.32	0.30	322.16	4.05	12.57	5310	-5201	0.98	54
49	0.42	0.40	1545.03	19.41	46.19	9882	-9203	0.93	339
50	0.32	0.31	469.17	5.89	18.61	8359	-7840	0.94	259
51	1.16	1.15	532.57	6.69	5.78	19678	-19428	0.99	125
52	0.33	0.33	551.81	6.93	20.72	8312	-7853	0.94	229

Table 2. Continued.

ID #	LF Susc. $\mu m^3/kg$	HF Susc. $\mu m^3/kg$	ARM $\mu Am^2/kg$	X_{arm} $\mu m^3/kg$	X_{arm}/X	SIRM $\mu Am^2/kg$	IRM-3T $\mu Am^2/kg$	S	HIRM $\mu Am^2/kg$
53	0.54	0.53	470.08	5.91	10.86	14967	-14356	0.96	306
54	0.26	0.26	73.15	0.92	3.53	394	-349	0.89	22
55	0.60	0.59	331.61	4.17	6.90	10172	-9743	0.96	215
56	3.20	3.13	374.33	4.70	1.47	28100	-28158	1.00	-29
57	0.20	0.19	291.20	3.66	18.61	3556	-3409	0.96	74
58	0.46	0.44	844.41	10.61	23.17	11781	-10976	0.93	402
59	2.77	2.67	1800.39	22.62	8.17				
60	0.33	0.31	603.81	7.59	22.84	6797	-6471	0.95	163
61	0.42	0.40	1097.99	13.79	33.10	11444	-10479	0.92	483
62	0.31	0.30	280.37	3.52	11.43	6353	-6354	1.00	-1
63	0.59	0.58	645.95	8.11	13.69	6964	-6908	0.99	28
64	1.36	1.30	660.65	8.30	6.10	21712	-21357	0.98	177
65	0.48	0.45	1193.82	15.00	31.10	9574	-8836	0.92	369
66	0.37	0.35	308.92	3.88	10.59	7520	-7433	0.99	44
67	0.32	0.30	666.03	8.37	26.36	7086	-6268	0.88	409
68	0.35	0.34	405.36	5.09	14.69	6658	-6604	0.99	27
69	0.69	0.66	861.72	10.83	15.77	19863	-19145	0.96	359
70	0.90	0.88	789.31	9.92	11.01	16666	-18888	1.13	-1111
71	1.15	1.11	1266.68	15.91	13.88	15769	-15029	0.95	370
72	1.61	1.52	3268.82	41.07	27.02	25646	-25176	0.98	235
73	0.13	0.12	400.62	5.03	43.24	4101	-3686	0.90	208
74	0.40	0.38	1761.42	22.13	55.34	9870	-9328	0.95	271
75	0.20	0.19	599.64	7.53	38.64	5165	-4887	0.95	139
76	0.02	0.02	154.63	1.94	126.67	904	-863	0.95	21
77	0.02	0.02	91.70	1.15	70.11	866	-817	0.94	24
78	0.44	0.44	1147.10	14.41	32.68	10728	-9942	0.93	393

Table 2. Continued.

ID #	LF Susc. $\mu m^3/kg$	HF Susc. $\mu m^3/kg$	ARM $\mu Am^2/kg$	X_{arm} $\mu m^3/kg$	X_{arm}/X	SIRM $\mu Am^2/kg$	IRM-3T $\mu Am^2/kg$	S	HIRM $\mu Am^2/kg$
79	0.99	0.88	4027.45	50.60	57.34	16803	-16569	0.99	117
80	0.36	0.34	926.62	11.64	34.47	8683	-8179	0.94	252
81	0.05	0.05	227.74	2.86	60.81	1401	-1323	0.94	39
82	0.79	0.75	2246.81	28.23	37.87	20604	-19024	0.92	790
83	0.49	0.46	1154.06	14.50	31.23	12502	-12460	1.00	21
84	0.01	0.01	123.02	1.55	261.08	742	-706	0.95	18
85	0.51	0.46	1245.05	15.64	33.88	10470	-9567	0.91	452
86	0.03	0.03	94.39	1.19	42.37	478	-463	0.97	8
87	0.93	0.87	994.84	12.50	13.44	17044	-16420	0.96	312
88	0.67	0.63	954.82	12.00	17.88	18544	-17543	0.95	501
89	0.04	0.05	97.06	1.22	25.92	544	-522	0.96	11
90	0.56	0.53	1254.32	15.76	29.64	14605	-13900	0.95	353
91	0.03	0.02	164.53	2.07	93.19	1201	-1178	0.98	12
92	1.09	1.02	1119.43	14.06	13.80	31544	-29386	0.93	1079
93	0.45	0.41	1281.02	16.09	39.11	9070	-8309	0.92	380
94	2.48	2.40	911.68	11.45	4.77	44778	-42182	0.94	1298
95	0.75	0.70	920.69	11.57	16.46	18145	-16713	0.92	716
96	0.37	0.35	477.27	6.00	16.07	8086	-7664	0.95	211
97	0.39	0.33	1042.12	13.09	33.70	7890	-7494	0.95	198
98	0.04	0.04	66.58	0.84	22.21	444	-427	0.96	8
99	3.26	3.19	516.01	6.48	1.99	56412	-56167	1.00	123
100	2.71	2.63	2168.53	27.24	10.05	84834	-85010	1.00	-88
101	0.17	0.16	435.78	5.47	32.22	4849	-4632	0.96	108
102	1.83	1.78	1443.57	18.14	9.89	59503	-54868	0.92	2318
103	0.49	0.44	1255.18	15.77	32.26	12960	-12345	0.95	307
104	0.15	0.14	569.26	7.15	47.06	3583	-3356	0.94	113

Table 2. Continued.

ID #	LF Susc. $\mu m^3/kg$	HF Susc. $\mu m^3/kg$	ARM $\mu Am^2/kg$	X_{arm} $\mu m^3/kg$	X_{arm}/X	SIRM $\mu Am^2/kg$	IRM-3T $\mu Am^2/kg$	S	HIRM $\mu Am^2/kg$
105	0.23	0.20	895.43	11.25	48.05	4246	-3940	0.93	153
106	0.71	0.68	876.30	11.01	15.53	20040	-19090	0.95	475
107	0.28	0.26	762.88	9.58	34.59	6915	-6571	0.95	172
108	2.00	1.92	2049.68	25.75	12.87	84007	-77264	0.92	3371
109	0.34	0.33	632.34	7.94	23.29	7402	-6562	0.89	420
110	0.66	0.63	830.71	10.44	15.82	16007	-14818	0.93	595
111	1.42	1.37	825.33	10.37	7.28	29642	-26868	0.91	1387
112	0.48	0.46	910.97	11.44	23.75	12485	-11913	0.95	286
113	1.23	1.18	1026.39	12.89	10.52	39490	-37664	0.95	913
114	1.71	1.66	884.49	11.11	6.49	45469	-43420	0.95	1025
115	0.54	0.48	1763.45	22.15	40.95	17615	-16673	0.95	471
116	0.43	0.41	991.37	12.45	29.03	8342	-7523	0.90	410
117	1.25	1.22	1071.27	13.46	10.79	33860	-22697	0.67	5582
118	0.74	0.72	692.63	8.70	11.72	19211	-16229	0.84	1491
119	0.91	0.87	929.38	11.68	12.89	27583	-26249	0.95	667
120	0.32	0.30	590.73	7.42	23.55	7006	-6370	0.91	318
121	0.49	0.47	1369.14	17.20	34.88	13992	-13202	0.94	395
122	0.37	0.35	793.13	9.96	27.15	8996	-7867	0.87	565
123	0.88	0.87	2627.35	33.01	37.71	22516	-21611	0.96	453
124	0.35	0.33	821.68	10.32	29.21	7814	-6755	0.86	530
125	1.53	1.48	1610.50	20.23	13.26	48990	-45214	0.92	1888
126	1.26	1.22	1250.01	15.70	12.43	24302	-23663	0.97	319
127	1.73	1.65	1061.34	13.33	7.71	49457	-47088	0.95	1184
128	1.36	1.34	1634.12	20.53	15.06	40667	-37950	0.93	1358
129	0.86	0.75	2328.35	29.25	33.89	15262	-14644	0.96	309
130	0.60	0.56	1222.56	15.36	27.43	14603	-13622	0.93	490

Table 2. Continued.

ID #	LF Susc. $\mu m^3/kg$	HF Susc. $\mu m^3/kg$	ARM $\mu Am^2/kg$	Xarm $\mu m^3/kg$	Xarm/X	SIRM $\mu Am^2/kg$	IRM-3T $\mu Am^2/kg$	S	HIRM $\mu Am^2/kg$
131	0.03	0.02	226.09	2.84	134.64	1549	-1465	0.95	42
132	0.47	0.45	754.42	9.48	21.28	10526	-9565	0.91	481
133	0.76	0.73	2550.14	32.04	44.17	24513	-23462	0.96	526
134	0.43	0.40	668.81	8.40	20.93	9827	-9340	0.95	243
135	1.16	1.13	816.70	10.26	9.09	26688	-25803	0.97	443
136	0.37	0.35	988.17	12.41	35.95	7135	-6377	0.89	379
137	0.12	0.11	183.90	2.31	19.94	3170	-3003	0.95	84
138	3.95	3.91	2231.54	28.03	7.10				
139	0.25	0.25	238.79	3.00	11.78	5398	-5447	1.01	-24
140	1.68	1.65	1255.19	15.77	9.37	60021	-58118	0.97	952
141	0.64	0.59	1275.04	16.02	24.88	13083	-10383	0.79	1350
142	0.40	0.37	1036.14	13.02	35.10	7712	-6859	0.89	427
143	0.38	0.34	1064.10	13.37	39.29	8151	-7205	0.88	473
144	0.46	0.42	1336.90	16.80	39.58	8150	-7415	0.91	367
145	0.70	0.65	1277.14	16.04	24.62	15843	-14682	0.93	581
146	0.52	0.49	1722.55	21.64	44.44	10736	-10438	0.97	149
147	0.28	0.26	752.20	9.45	36.46	7911	-7335	0.93	288
148	0.44	0.40	710.86	8.93	22.06	10535	-9548	0.91	494
149	0.48	0.45	1036.74	13.02	27.19	8766	-7911	0.90	427
150	0.26	0.23	627.04	7.88	33.89	6664	-5723	0.86	471
151	0.24	0.23	388.66	4.88	20.18	3938	-3806	0.97	66
152	0.39	0.37	841.20	10.57	27.14	9154	-8540	0.93	307
153	0.27	0.26	757.17	9.51	36.35	5414	-4905	0.91	255
154	0.01	0.02	164.41	2.07	169.23	409	-433	1.06	-12
155	0.06	0.07	78.38	0.98	16.23	560	-655	1.17	-48
156	0.00	0.00	117.36	1.47	-688.04	491	-480	0.98	5

Table 2. Continued.

ID #	LF Susc. $\mu m^3/kg$	HF Susc. $\mu m^3/kg$	ARM $\mu Am^2/kg$	X_{arm} $\mu m^3/kg$	X_{arm}/X	SIRM $\mu Am^2/kg$	IRM-3T $\mu Am^2/kg$	S	HIRM $\mu Am^2/kg$
157	0.01	0.00	85.09	1.07	-221.95	388	-374	0.96	7
158	0.00	0.00	101.29	1.27	-1133.14	437	-420	0.96	8
159	0.00	0.00	133.25	1.67	1248.82	554	-527	0.95	13
160	0.07	0.06	187.51	2.36	31.98	809	-758	0.94	25
161	0.02	0.00	72.95	0.92	51.45	291	-292	1.00	-1
162	-0.02	-0.01	60.33	0.76	-36.59	150	-39	0.26	55
163	0.02	0.01	157.65	1.98	80.83	457	-430	0.94	14
164	0.11	0.10	251.02	3.15	29.54	1439	-1438	1.00	1
165	0.06	0.06	119.56	1.50	23.37	469	-490	1.05	-11
166	-0.02	-0.01	68.66	0.86	-49.78	444	-434	0.98	5
167	0.64	0.63	96.68	1.21	1.90	7504	-7757	1.03	-127

Table 3. Particle size measurements.

ID #	Median Grain Size (μm)	%>63μm	%20-63μm	%2-20μm	%<2μm
1	3.28	0.37	1.00	43.52	30.68
2	3.22	0.18	0.34	14.95	17.26
3	4.57	0.18	1.51	47.01	26.75
4	5.02	4.04	6.67	34.72	25.19
5	5.85	2.91	9.23	42.67	16.93
6	3.65	0.03	0.30	48.60	30.77
7	6.11	0.79	5.81	26.16	24.32
8	3.33	0.04	0.16	43.04	29.32
9	4.83	1.11	3.56	47.42	28.29
10	3.69	0.41	1.34	37.73	29.29
11	3.36	0.02	0.10	46.18	31.83
12	3.90	0.06	0.60	43.93	28.82
13	4.17	0.11	0.55	40.01	31.52
14	4.04	0.04	1.30	47.33	27.64
15	3.42				
16	3.43	0.12	0.31	43.00	28.53
17	3.87	0.07	0.47	49.77	27.57
18	3.92	0.08	1.61	41.33	31.65
19	3.96	0.05	0.69	43.31	26.32
20	3.17	2.18	0.48	18.19	18.67
21	4.07	0.11	1.89	47.48	26.59
22	3.72	0.24	0.63	48.33	23.53
23	3.53	0.29	0.48	45.38	26.82
24	4.25	0.08	2.05	41.99	19.02
25	7.31	1.86	6.68	27.32	8.95
26	3.33	0.14	0.24	34.89	32.98
27	7.28	0.84	5.52	44.54	8.34
28	3.46	0.26	0.26	43.73	30.08
29	7.24	0.80	6.96	39.96	14.22
30	4.74	0.54	4.94	46.30	23.20
31	3.27	0.20	0.39	43.23	28.32
32	4.20	0.10	0.50	42.60	30.48
33	3.10	0.02	0.13	42.68	32.39
34	6.38	1.99	10.89	37.29	14.19
35	4.38	1.53	7.02	51.81	21.42
36	4.74	0.55	0.85	46.84	24.15
37	6.41	7.43	12.44	40.45	17.05
38	3.71	3.89	0.28	46.87	28.60
39	4.03	0.01	0.19	41.65	31.88
40	3.25	0.01	0.14	43.73	31.96
41	3.82	0.19	0.59	39.78	24.88
42	3.67	0.42	0.75	44.60	28.62
43	5.41	0.57	15.64	36.60	13.89

Table 3. Continued.

ID #	Median Grain Size (μm)	%>63μm	%20-63μm	%2-20μm	%<2μm
44	3.63	0.01	0.15	49.55	29.65
45	4.76	0.42	6.30	38.75	16.58
46	2.96	2.71	4.41	33.94	18.99
47	3.58	0.26	0.32	44.32	30.50
48	4.62	1.54	2.73	37.70	23.54
49	3.43	0.55	0.56	39.43	22.90
50	4.80	0.47	3.56	42.95	17.58
51	7.72	16.74	17.07	31.62	15.30
52	4.14	0.40	0.85	48.27	22.80
53	4.41	2.35	9.19	18.84	13.90
54	4.03	0.11	0.09	10.17	6.47
55	9.73	5.96		35.06	10.50
56	17.92	71.14	9.70	4.67	1.34
57	8.93	2.60	5.00	23.56	3.50
58	4.94	1.23	2.40	43.51	17.71
59		13.78	29.20	33.21	6.49
60	3.94	1.22	1.45	34.91	24.65
61	4.04	0.07	0.34	26.41	16.94
62	6.23	0.97	5.12	39.96	15.99
63	6.60	61.41	2.70	11.93	6.50
64	4.45	3.16	1.23	44.16	26.54
65	4.12	0.10	0.54	46.96	28.44
66	4.39	0.13	4.40	42.28	15.75
67	3.87	0.15	0.45	45.26	25.77
68	4.51	0.95	2.16	46.31	15.70
69	5.22	0.33	2.46	42.02	11.92
70	8.57	0.79	11.79	44.60	18.43
71	4.06	0.70	1.07	29.57	10.85
72	6.49	1.48	1.59	36.71	16.01
73	5.50	0.15	1.87	34.50	13.63
74	3.68	0.04	0.77	38.85	17.66
75	4.75	0.80	0.49	23.14	8.88
76	22.63	0.18	25.50	21.51	3.64
77	25.16	0.57	40.19	20.40	4.15
78	5.01	0.31	0.72	30.09	9.64
79	6.22	0.32	1.98	41.12	19.10
80	5.63	3.11	0.79	27.20	10.55
81	7.22	0.79	1.10		
82	5.49	1.04	2.08	38.38	13.07
83	5.02	1.77	2.35	33.73	13.02
84	23.81	0.26	29.92	23.74	4.24
85	4.74	0.28	2.39	49.27	21.35
86	8.67	0.80	0.42		

Table 3. Continued.

[redacted]	Median Grain Size (μm)	%>63μm	%20-63μm	%2-20μm	%<2μm
[redacted]	4.37	0.34	1.92	36.06	12.46
88	5.85	0.23	3.18	36.10	16.29
89	18.77	0.92	1.46		
90	6.41	2.56	2.59	30.00	10.91
91	34.71	0.49	37.46	25.60	4.16
92	6.36	0.16	6.66	50.64	19.52
93	3.46	0.02	0.28	47.15	24.72
94	12.43	15.14	23.31	35.55	9.36
95	6.17	0.18	6.06	52.92	20.08
96	6.04	0.38	6.34	48.32	13.05
97	3.57	0.74	0.93		
98	5.08	6.79	1.56		
99	10.82	11.69	11.99		
100	10.72	0.32	10.84		
101	5.07	21.26	2.61		
102	13.19	0.46	8.97		
103	13.18	2.24	7.86		
104	3.78	0.17	0.96	44.34	19.91
105	3.18	2.90	0.78		
106	5.82	0.14	4.55	39.92	17.15
107	4.16	0.77	0.81	38.84	20.66
108	4.93	1.39	6.93	33.77	9.46
109	4.06	0.03	0.24	22.45	13.60
110	5.39	0.57	3.08	46.48	23.81
111	9.20	39.40	8.49	19.34	5.49
112	4.78	0.65	1.77	34.10	19.79
113	5.08	0.20	2.50	37.16	14.04
114	8.45	14.37	12.22	35.99	13.72
115	5.70	2.29	2.29	30.21	14.51
116	3.50	0.11	0.31	44.18	29.60
117	5.98	0.75	8.57	39.53	13.65
118	8.92	5.16	12.91	42.94	17.88
119	5.88	0.36	5.98	42.64	17.58
120	3.81	0.25	0.54	48.72	21.97
121	3.91	1.39	1.05	43.06	17.58
122	3.62	0.64	0.72	44.08	26.69
123	4.03	27.34	1.24	28.24	8.53
124	3.71	0.25	0.65	46.45	27.11
125	4.03	0.17	1.54	50.22	24.55
126	4.80	2.08	3.35	33.22	13.48
127	5.54	7.31	8.67	39.85	18.38
128	4.45	0.02	1.00	44.09	25.39
129	6.92	0.33	2.25	35.29	17.57

Table 3. Continued.

ID #	Median Grain Size (μm)	%>63μm	%20-63μm	%2-20μm	%<2μm
130	4.02	0.28	1.11	43.56	25.32
131	24.11	0.13	17.76	31.13	4.45
132	4.64	0.35	1.38	52.90	21.15
133	7.89	8.38	5.27	24.13	14.64
134	5.21	0.11	1.50	48.10	24.32
135	10.71	0.37	17.03	48.62	16.52
136	3.48	0.08	0.32	50.68	24.83
137	12.50	4.05	16.32	9.61	7.09
138	8.78	0.25	8.61	60.10	8.47
139	5.83	0.74	4.74	44.79	12.88
140	5.94	1.55	6.07	47.67	11.26
141	13.94	5.64	7.07	20.88	8.79
142	3.40	0.06	0.23	46.83	27.15
143	3.44	0.04	0.58	45.85	22.68
144	3.50	0.19	0.24	42.25	28.36
145	4.50	0.79	2.25	44.91	22.85
146	4.18	0.82	1.32	35.02	19.12
147	6.77	10.54	5.35	27.79	5.92
148	4.65	0.36	1.24	48.48	23.59
149	4.33	0.09	0.84	46.42	26.53
150	3.94	0.91	0.69	45.67	18.02
151	4.10	1.35	2.92	44.73	20.62
152	4.34	0.57	0.85	41.23	16.81
153	7.21	0.58	8.06	37.50	13.34
154		1.46			
155		19.97			
156		0.46			
157		0.30			
158		1.63			
159		0.22			
160		2.40			
161		22.59			
162		0.29			
163		5.05			
164		0.27			
165		0.27			
166		3.51			
167		5.60			

Table 4. Mineral weight percent.

ID #	<2μm Smectite	<2μm Illite	<2μm Kaolinite	<2μm Chlorite	<2μm Quartz	<2μm Plagioclase	2-20μm Smectite	2-20μm Illite	2-20μm Kaolinite	2-20μm Chlorite	2-20μm Quartz	2-20μm Plagioclase
1	4.52	66.78	5.93	2.45	6.73	13.59	2.34	41.40	2.65	5.30	14.19	34.12
2	22.15	54.06	6.73	1.83	8.02	6.08	4.07	43.94	0.00	5.10	11.19	35.70
3	1.92	71.40	16.01	2.76	4.68	3.23	1.41	37.37	2.52	1.02	29.87	26.49
4	1.41	57.26	0.00	9.47	14.06	17.79	0.00	26.47	21.89	0.00	18.54	33.10
5	1.62	39.60	31.83	6.64	8.59	9.64	2.30	37.26	1.37	2.37	16.41	40.29
6	2.93	60.20	18.21	2.62	7.71	8.33	1.40	50.54	0.00	3.94	11.47	30.40
7	13.98	22.15	55.14	2.92	1.89	3.92	4.66	23.33	7.16	1.07	15.97	47.81
8	2.84	63.11	26.57	2.06	5.42	0.00	1.33	43.15	1.55	3.79	27.18	23.00
9	6.08	68.38	11.12	3.45	7.18	3.78	1.93	25.80	5.84	5.01	19.61	40.98
10	5.67	72.29	8.55	5.86	4.03	3.61	2.81	33.42	0.00	4.30	23.30	36.16
11	2.99	59.70	21.75	3.02	3.26	9.28	1.17	46.29	4.95	4.69	20.14	22.76
12	9.27	40.29	18.55	5.57	17.04	9.29	2.00	42.18	3.83	1.81	18.38	31.81
13	8.52	53.99	16.69	3.70	8.23	7.63	3.24	34.34	5.12	1.35	23.54	31.76
14	3.20	73.09	8.74	3.26	8.55	3.16	0.47	22.17	0.00	2.93	35.44	38.99
15	3.02	73.72	9.03	5.87	5.07	3.30	2.58	51.48	1.01	1.43	13.20	30.30
16	3.66	65.78	18.78	4.11	3.97	3.70	2.39	36.36	5.27	3.59	26.91	25.48
17	2.94	61.85	24.07	1.72	6.77	2.66	2.29	41.47	6.92	3.75	14.70	30.88
18	6.99	65.82	5.48	11.97	6.72	3.03	1.60	26.69	4.75	3.40	20.54	43.03
19	4.14	48.07	32.96	3.29	4.70	6.83	2.80	33.71	0.00	2.28	9.07	52.13
20	10.38	58.66	13.43	2.67	4.99	9.86	1.20	24.40	22.64	2.53	11.06	37.26
21	3.92	61.98	17.48	4.66	3.18	8.79	0.55	32.23	4.46	1.75	31.18	29.13
22	2.12	60.28	20.42	3.58	5.30	8.29	2.51	36.38	3.78	4.03	18.65	32.19
23	1.54	52.87	17.68	2.66	8.26	16.97	1.69	51.75	9.63	3.72	12.94	20.28
24	6.57	63.21	9.46	2.57	8.65	9.55	1.08	38.55	0.00	0.98	25.97	31.99
25	4.39	35.11	35.77	2.42	10.77	11.54	1.54	38.75	7.36	0.89	22.77	28.69
26	2.92	62.27	20.40	4.76	3.41	5.85	1.14	25.93	7.26	4.76	24.18	36.73
27	19.89	27.75	6.47	11.21	7.62	25.19	3.85	40.12	5.42	1.81	10.39	38.41

Table 4. Continued.

ID #	<2µm Smectite	<2µm Illite	<2µm Kaolinite	<2µm Chlorite	<2µm Quartz	<2µm Plagioclase	2-20µm Smectite	2-20µm Illite	2-20µm Kaolinite	2-20µm Chlorite	2-20µm Quartz	2-20µm Plagioclase
28	3.15	64.19	14.99	4.53	7.87	5.27	1.78	30.77	3.56	3.26	27.19	33.44
29	5.66	60.86	16.23	3.84	6.47	6.94	1.33	25.67	0.00	2.10	20.06	50.83
30	4.86	54.28	19.70	4.05	4.93	12.17	2.26	30.38	2.65	5.44	18.01	41.26
31	3.15	52.37	22.65	2.31	8.21	11.31	1.93	39.65	4.82	3.68	29.00	19.22
32	4.31	66.24	11.21	8.27	6.26	3.70	2.12	12.89	3.55	2.54	26.85	50.71
33	2.83	58.33	26.43	3.82	2.17	6.42	3.21	34.53	4.42	3.84	21.68	32.30
34	5.81	51.54	30.08	3.93	5.54	3.09	0.46	25.82	0.00	0.00	20.80	52.92
35	1.05	60.38	18.21	2.25	11.01	5.48	1.72	38.36	3.05	3.99	9.58	43.29
36	4.61	51.27	4.38	2.67	5.00	24.76	1.82	27.61	7.42	2.89	9.51	46.64
37	6.49	66.84	0.00	11.79	3.71	11.17	1.99	12.37	3.93	3.67	26.12	49.86
38	5.18	60.90	15.49	5.42	7.24	5.03	4.47	32.76	4.15	2.66	23.70	30.00
39	7.10	33.15	46.35	3.81	6.17	3.43	2.56	36.86	2.01	4.44	13.99	36.48
40	1.92	68.87	13.12	5.87	7.76	2.46	2.89	34.79	9.92	3.51	24.49	24.41
41	6.93	34.63	20.74	8.47	11.58	17.65	1.60	28.51	0.00	3.45	15.73	50.72
42	5.60	66.49	13.59	4.87	9.45	0.00	2.07	44.33	9.44	4.05	18.45	20.98
43	4.18	72.67	11.18	7.62	4.35	0.00	0.53	13.81	1.17	0.93	30.62	51.40
44	2.63	51.70	32.66	0.73	6.85	5.43	1.40	46.85	4.02	3.06	20.83	23.84
45	4.98	44.61	20.60	6.77	2.83	20.21	1.15	31.70	3.36	1.27	12.97	44.76
46	7.67	50.73	16.19	5.23	8.26	11.91	1.88	39.34	0.00	3.73	9.26	41.39
47	9.05	64.81	6.46	3.39	10.88	4.26	6.00	33.56	8.68	2.89	15.36	31.10
48	28.70	50.02	5.29	1.06	5.82	9.12	8.38	17.98	20.90	2.03	12.28	36.95
49	22.81	27.44	11.72	7.49	10.67	19.86	2.44	31.18	11.39	4.91	10.58	39.50
50	5.40	45.25	21.18	4.28	7.17	16.03	5.82	20.78	7.05	5.71	21.48	37.01
51	11.22	46.70	7.66	10.78	3.43	16.86	4.46	17.02	13.18	2.45	14.71	43.52
52	4.28	64.98	10.50	3.30	9.00	7.95	3.86	26.08	6.09	2.15	29.90	31.92
53	10.67	39.68	0.00	1.90	3.03	44.73	3.47	30.94	1.10	0.29	3.71	60.49
54	4.18	87.04	2.39	0.57	1.27	4.55	1.65	89.60	10.12	0.00	0.00	0.00

Table 4. Continued.

ID #	<2μm Smectite	<2μm Illite	<2μm Kaolinite	<2μm Chlorite	<2μm Quartz	<2μm Plagioclase	2-20μm Smectite	2-20μm Illite	2-20μm Kaolinite	2-20μm Chlorite	2-20μm Quartz	2-20μm Plagioclase
55	5.70	62.00	13.83	3.93	7.67	6.88	2.96	47.60	6.68	3.32	9.86	29.59
56							12.42	12.26	9.63	5.93	6.14	48.19
57							21.12	13.61	9.54	1.31	10.86	42.41
58	7.80	47.97	16.96	4.54	13.19	9.55	2.32	33.96	9.86	3.44	21.81	26.93
59	21.30	28.66	32.10	8.81	2.48	6.64	3.21	32.07	0.00	0.00	21.01	43.70
60	47.94	10.51	14.36	7.31	5.50	14.37	18.30	7.67	23.49	1.67	10.88	36.19
61	8.95	34.10	44.49	1.62	3.82	7.03	2.42	5.55	26.00	0.00	22.09	39.52
62	33.19	27.30	24.57	2.97	2.50	9.48	7.57	17.86	8.93	3.29	10.57	46.90
63	24.23	20.90	37.73	0.77	6.59	4.36	7.85	14.04	10.80	0.79	14.69	51.84
64	10.22	49.39	16.68	4.78	5.50	10.29	3.27	48.18	2.80	5.47	7.71	32.57
65	7.88	44.46	24.52	2.82	7.31	12.36	3.13	33.85	10.06	3.53	16.51	30.75
66	21.58	23.85	48.80	1.98	0.86	2.93	6.80	7.78	7.91	4.44	4.06	56.42
67	3.23	49.64	19.22	2.82	8.71	16.38	3.14	41.71	3.47	5.18	18.17	28.33
68	27.06	36.36	15.65	10.00	7.28	2.79	11.45	37.22	8.04	6.22	4.84	28.05
69	12.59	48.67	0.00	7.46	16.46	14.82	1.42	44.40	2.26	4.38	27.19	20.35
70	24.73	42.73	0.00	11.49	3.38	17.66	4.22	22.77	1.29	2.57	14.72	54.42
71	43.00	8.29	28.07	3.61	6.07	10.96	23.33	6.29	8.38	3.37	16.09	40.22
72	36.24	28.15	11.87	2.84	10.36	10.54	4.35	7.63	24.70	7.87	12.45	42.00
73	5.46	54.64	17.52	4.89	7.16	10.33	3.75	31.70	13.85	2.34	15.98	32.37
74	8.80	37.33	28.02	3.92	6.86	15.07	4.69	33.20	6.98	2.65	10.43	40.40
75	35.38	39.03	3.64	0.71	8.89	12.36	6.74	17.15	8.24	1.80	18.41	40.52
76	2.93	67.84	8.71	2.54	1.00	11.68	2.29	84.98	0.00	0.87	0.25	6.05
77	41.96	39.66	0.00	3.74	1.01	13.64	19.84	36.15	9.02	0.00	0.00	23.22
78	37.28	19.07	24.67	4.33	3.71	10.94	7.67	31.27	9.97	2.33	5.23	40.13
79	40.23	13.79	16.28	3.63	3.82	20.12	0.56	2.33	37.08	0.00	2.08	57.95
80	27.75	36.05	15.65	2.84	1.83	15.88	12.11	29.28	12.34	1.03	7.44	36.15
81												

Table 4. Continued.

ID #	<2μm Smectite	<2μm Illite	<2μm Kaolinite	<2μm Chlorite	<2μm Quartz	<2μm Plagioclase	2-20μm Smectite	2-20μm Illite	2-20μm Kaolinite	2-20μm Chlorite	2-20μm Quartz	2-20μm Plagioclase
82	13.33	24.18	27.73	10.49	14.01	10.26	6.78	12.23	13.87	2.07	11.55	53.50
83	24.18	14.52	39.27	1.50	7.49	10.45	12.09	12.19	16.87	1.29	9.91	47.66
84	16.26	83.74	0.00	0.00	0.00	0.00	4.35	75.24	0.00	4.20	2.47	13.74
85	6.32	56.51	15.99	4.47	6.30	9.38	4.93	41.34	3.44	5.24	18.38	26.67
86												
87	32.57	16.64	39.93	4.96	3.15	2.76	11.42	19.80	30.15	4.25	4.17	30.21
88	13.54	34.86	19.43	3.65	10.51	18.01	4.83	31.42	7.83	3.04	19.10	33.79
89												
90	29.40	28.61	27.37	2.34	6.15	6.12	21.49	23.88	0.00	10.86	16.02	27.75
91	39.35	43.94	0.00	7.23	0.98	5.14	32.13	36.03	0.00	6.95	4.18	20.71
92	6.10	58.50	10.54	1.30	6.53	11.25	2.88	29.05	6.37	2.31	13.54	45.85
93	9.69	17.65	31.63	9.01	12.60	17.69	5.93	37.20	6.17	5.37	25.25	18.47
94	27.02	14.02	32.69	1.86	4.01	20.40	5.81	10.95	7.32	1.17	6.59	68.17
95	8.91	46.13	30.69	1.44	8.14	4.68	5.05	22.12	8.75	2.84	13.65	46.58
96	12.52	27.49	5.66	13.32	7.68	23.10	4.29	32.35	3.58	4.62	9.48	40.66
97												
98												
99												
100												
101												
102												
103												
104	13.14	46.29	24.94	4.38	3.88	2.55	6.75	42.20	6.11	6.55	14.62	23.77
105												
106	9.08	41.63	0.00	8.05	16.96	21.88	2.57	32.24	5.50	2.20	20.16	37.33
107	11.40	38.29	22.18	4.77	8.96	12.51	4.92	28.49	6.52	3.78	22.81	33.48
108	21.44	43.11	11.26	0.93	5.35	17.91	5.83	30.42	8.18	3.74	9.24	42.60

Table 4. Continued.

ID #	<2µm Smectite	<2µm Illite	<2µm Kaolinite	<2µm Chlorite	<2µm Quartz	<2µm Plagioclase	2-20µm Smectite	2-20µm Illite	2-20µm Kaolinite	2-20µm Chlorite	2-20µm Quartz	2-20µm Plagioclase
109	4.44	60.63	9.96	6.87	16.43	1.67	3.60	44.72	7.98	3.08	10.67	26.61
110	3.41	61.01	17.27	4.63	10.24	2.42	3.13	33.01	2.99	3.78	19.31	37.78
111	57.71	21.16	8.15	4.93	8.05	0.00	0.00	40.95	21.95	1.04	10.78	25.28
112	9.37	60.07	8.22	6.60	7.65	8.09	3.08	33.95	7.45	3.11	19.83	31.69
113	18.81	13.86	25.37	5.53	2.67	33.75	12.24	3.99	3.92	3.19	5.09	71.57
114	5.25	46.02	13.80	7.33	8.77	17.40	2.97	25.76	0.00	3.95	11.12	51.29
115	9.35	37.70	37.69	1.66	3.53	10.06	7.72	11.30	22.80	3.68	13.38	41.12
116	5.86	46.67	21.74	5.70	8.65	11.37	3.73	28.24	17.91	3.40	13.86	31.75
117	12.72	25.28	19.83	3.39	8.78	28.04	4.42	10.04	1.76	2.01	22.72	57.94
118	6.83	62.90	18.06	3.54	6.52	2.15	2.04	32.27	9.38	1.83	26.15	27.75
119	8.94	44.38	12.90	4.93	10.80	14.52	4.81	30.43	7.08	2.33	21.00	34.36
120	6.19	66.77	6.00	4.47	5.42	8.18	4.02	53.18	5.79	4.32	21.80	10.89
121	7.16	48.51	28.17	2.65	10.73	2.78	2.92	30.38	26.23	0.00	14.43	22.80
122	4.37	55.84	19.57	7.15	10.24	0.00	2.24	31.88	9.08	4.17	25.34	23.86
123	24.32	46.94	16.27	2.84	4.80	4.82	5.76	11.49	19.77	3.31	5.58	50.92
124	4.10	68.69	7.46	8.99	8.05	2.72	0.26	42.73	5.23	5.65	24.30	17.99
125	17.45	43.86	0.00	0.00	20.91	17.79	4.56	41.98	6.99	4.35	8.20	33.93
126	53.39	14.18	10.48	4.87	7.37	7.06	20.87	22.01	26.53	1.22	12.83	14.10
127	10.88	30.65	11.04	5.25	8.49	31.97	2.62	18.32	12.82	4.44	10.87	43.66
128	2.14	45.03	25.85	4.26	5.69	17.02	3.26	35.76	16.40	2.57	24.22	16.93
129	27.76	32.73	13.55	1.66	0.40	23.90	2.56	4.38	0.00	0.00	3.01	90.05
130	6.23	52.99	25.87	2.58	9.72	1.95	4.93	35.80	7.94	7.48	14.51	28.20
131	14.32	55.35	15.45	0.57	3.09	11.21	15.45	35.81	0.00	2.74	12.47	33.52
132	5.65	53.30	12.38	6.15	18.61	3.91	3.03	36.44	0.00	2.95	26.24	31.34
133	5.29	72.10	5.36	0.00	0.92	5.20	6.69	37.60	8.97	3.12	2.71	38.54
134	10.67	61.99	4.63	4.98	17.73	0.00	4.58	36.18	9.19	3.65	19.42	25.58
135	23.67	19.21	12.37	13.82	6.30	24.64	4.65	26.05	0.00	3.72	7.14	50.79

Table 4. Continued.

ID #	<2µm Smectite	<2µm Illite	<2µm Kaolinite	<2µm Chlorite	<2µm Quartz	<2µm Plagioclase	2-20µm Smectite	2-20µm Illite	2-20µm Kaolinite	2-20µm Chlorite	2-20µm Quartz	2-20µm Plagioclase
136	11.52	51.69	3.58	9.74	11.87	11.60	3.69	38.95	8.61	4.40	19.86	24.49
137	9.52	42.59	4.79	0.69	5.08	30.53	1.85	67.09	10.16	0.60	1.45	17.56
138	34.56	27.86	19.63	6.39	2.70	8.86	20.26	14.93	15.57	2.29	3.23	43.72
139	15.58	46.91	3.13	8.64	4.46	13.45	14.23	7.65	6.74	0.62	10.34	46.49
140	27.57	21.30	32.54	5.92	2.54	10.13	5.63	22.66	7.56	3.61	12.22	48.33
141							11.13	35.07	13.13	5.98	4.73	29.96
142	6.28	58.88	10.62	7.27	11.01	5.94	2.54	41.14	3.60	6.04	20.17	22.39
143	3.84	47.08	28.21	6.93	6.46	6.87	3.45	33.98	7.55	5.59	26.08	22.61
144	12.07	71.67	2.37	10.29	3.60	0.00	4.91	38.73	5.60	4.61	20.80	24.13
145	21.84	32.59	20.26	5.33	7.17	10.58	6.25	20.00	6.86	0.74	22.37	43.78
146	18.54	37.84	22.22	9.82	11.57	0.00	6.28	32.07	11.19	2.54	22.88	23.75
147	12.50	51.60	17.20	3.30	10.39	5.01	5.32	15.48	0.00	0.00	29.05	47.34
148	5.04	63.64	3.40	1.26	13.80	9.01	2.85	39.87	16.11	3.25	9.98	26.79
149	7.56	41.87	22.35	5.64	10.53	10.91	6.02	35.97	3.58	6.99	14.78	32.66
150	6.35	56.42	19.84	4.77	9.03	3.58	5.23	18.29	3.68	3.60	27.96	39.52
151	34.03	16.93	33.54	2.78	3.40	9.34	16.35	27.72	19.72	2.84	15.46	15.67
152	7.49	56.23	12.70	6.49	8.55	7.35	4.22	36.72	9.12	2.09	10.03	36.92
153	29.87	14.01	23.86	12.63	11.94	6.69	9.82	16.80	15.10	2.85	21.37	34.07

Figure 1. Spatial distribution of low frequency susceptibility. Units are $\mu m^3/kg$. Contour interval is 0.5 $\mu m^3/kg$.

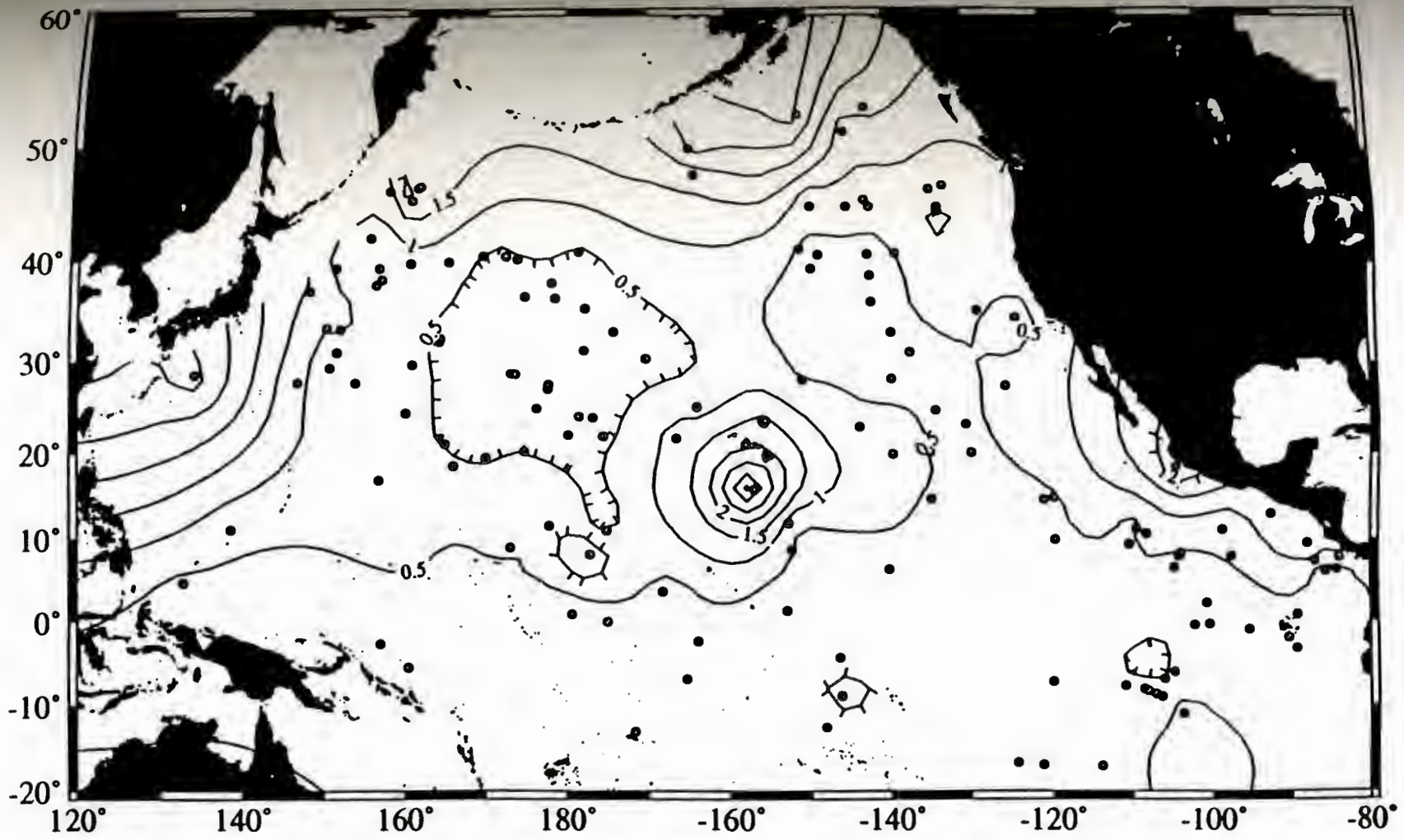
60°
50°
40°
30°
20°
10°
0°
-10°
-20°
120°
140°
160°
180°
-160°
-140°
-120°
-100°
-80°
0.5
1
1.5
2

Figure 2. Spatial distribution of SIRM. Units are $\mu Am^2/kg$. Contour interval is 10,000 $\mu Am^2/kg$.

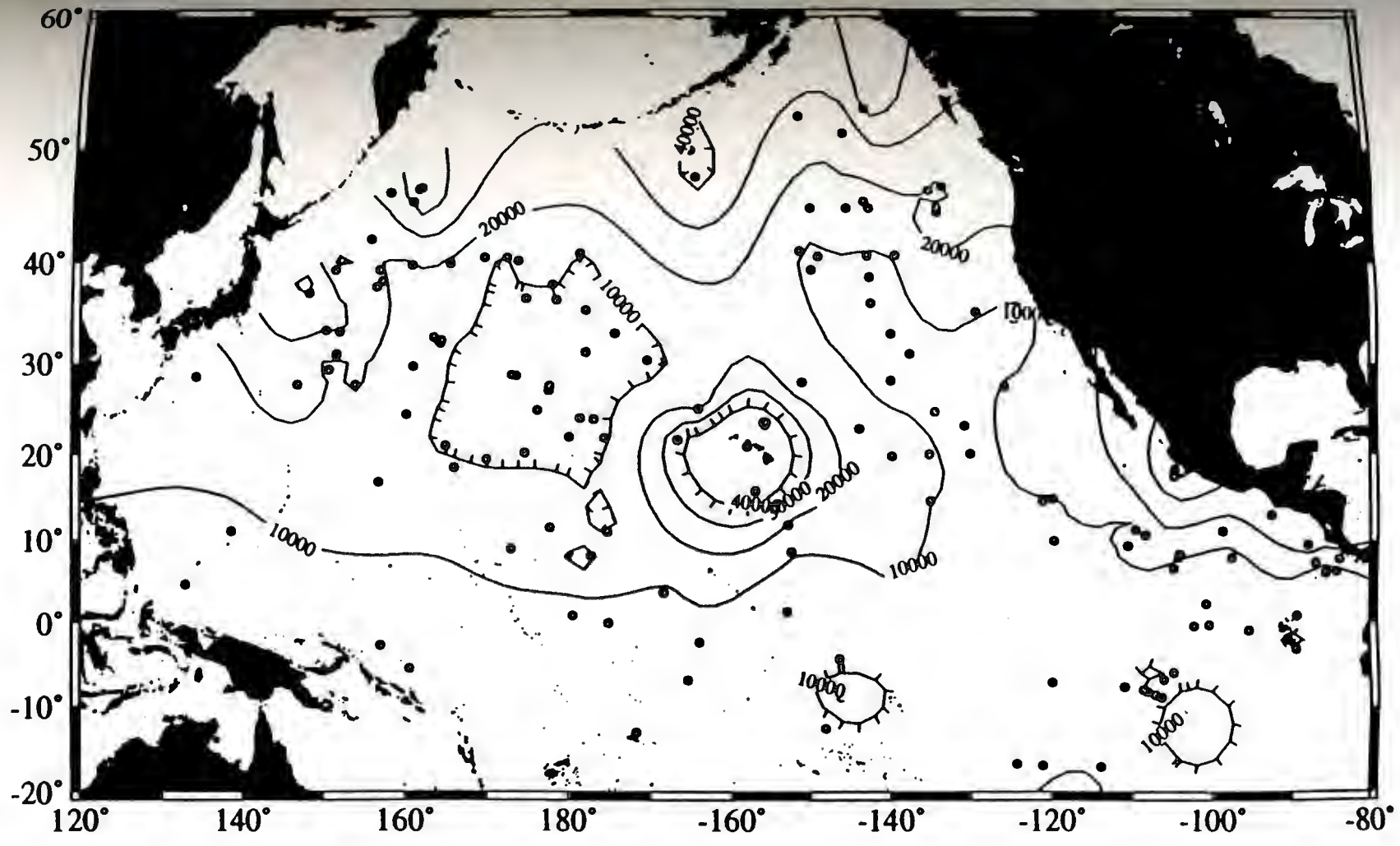
60°
50°
40°
30°
20°
10°
0°
-10°
-20°
120°
140°
160°
180°
-160°
-140°
-120°
-100°
-80°
40000
20000
10000
20000
10000
40000
30000
20000
10000
10000
10000

Figure 3. Spatial distribution of HIRM. Units are $\mu Am^2/kg$. Contour interval is 500 $\mu Am^2/kg$.

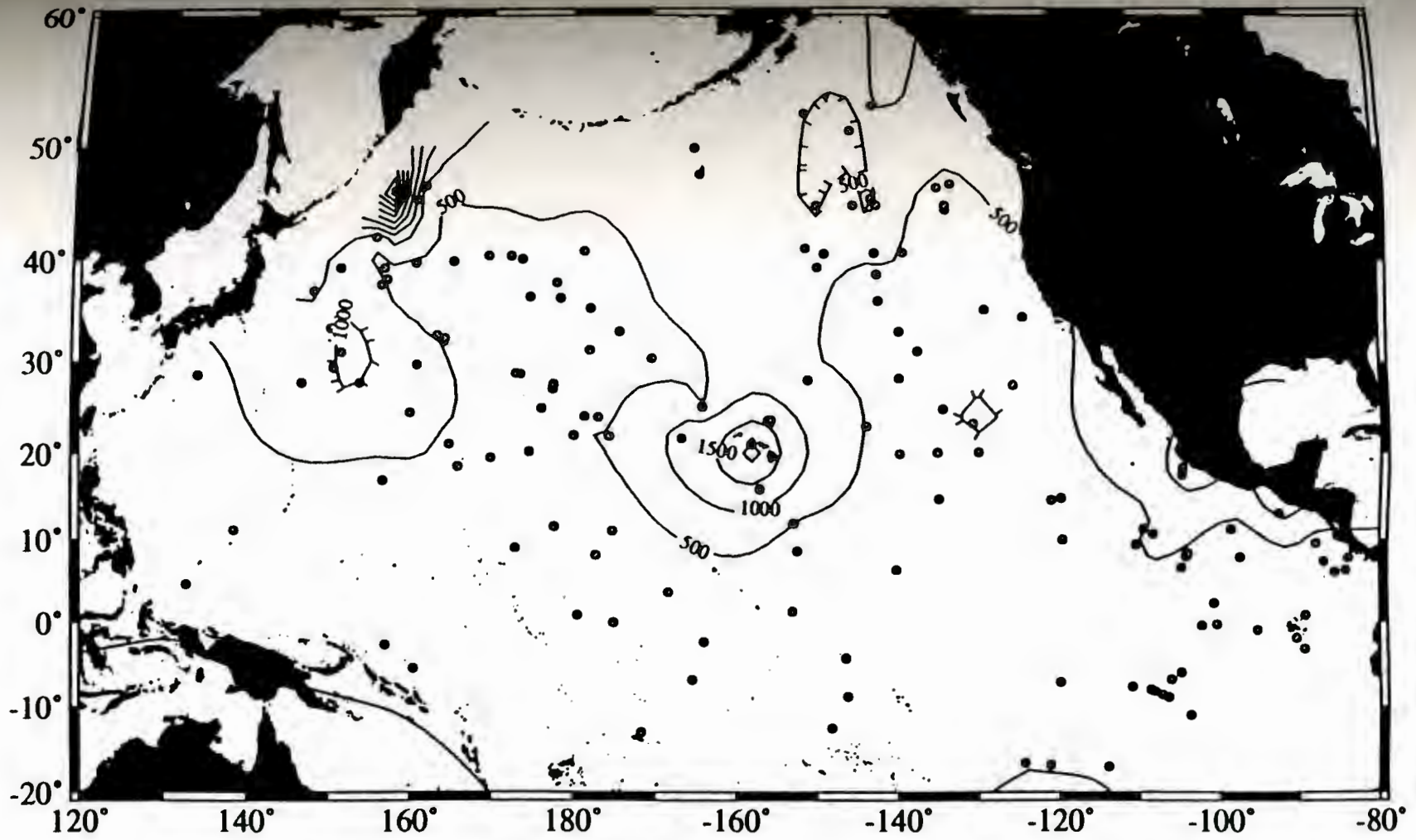
60°
50°
40°
30°
20°
10°
0°
-10°
-20°
120°
140°
160°
180°
-160°
-140°
-120°
-100°
-80°
500
1000
1500

Figure 4. Spatial distribution of X_{arm}. Units are $\mu m^3/kg$. Contour interval is 10 $\mu m^3/kg$.

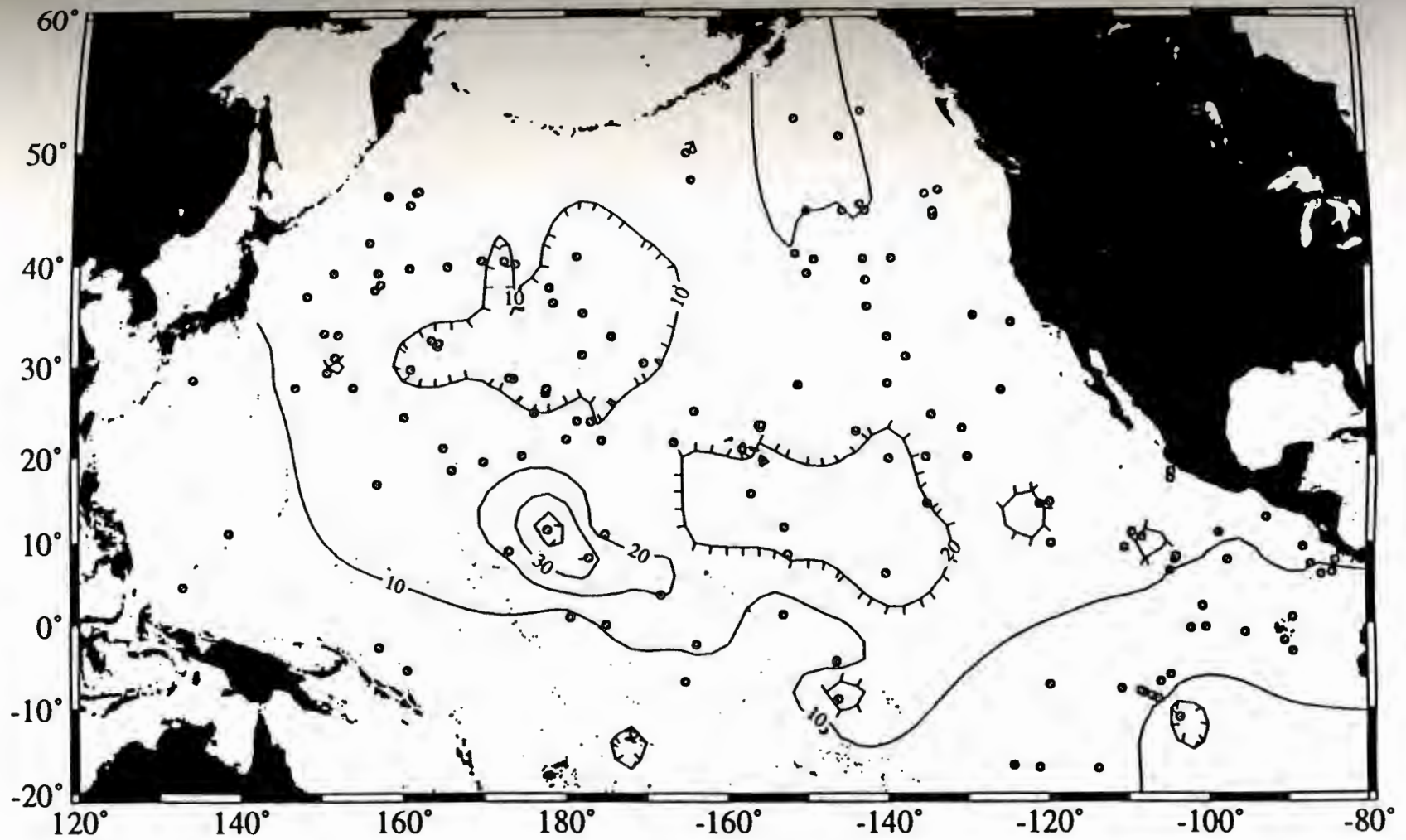
60°
50°
40°
30°
20°
10°
0°
-10°
-20°
120°
140°
160°
180°
-160°
-140°
-120°
-100°
-80°
10
10
10
20
30
20
10
10

Figure 5. Spatial distribution of Xarm/X. Contour interval is 20.

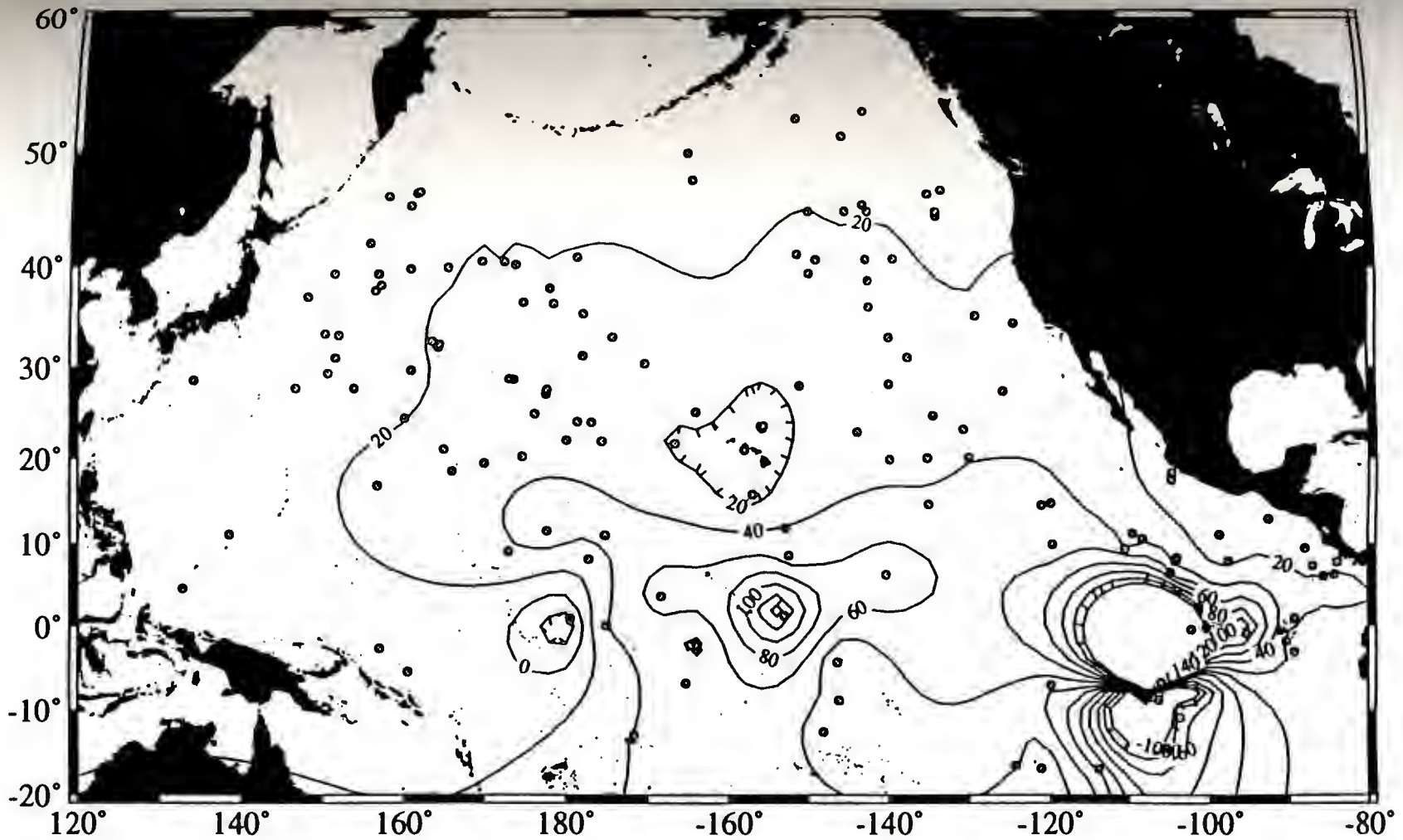
60°
50°
40°
30°
20°
10°
0°
-10°
-20°
120°
140°
160°
180°
-160°
-140°
-120°
-100°
-80°
20
20
20
40
60
80
100
0
20
40
60
80
100
120
140
-10
-10

Figure 6. Spatial distribution of S-ratio. Contour interval is 0.05.

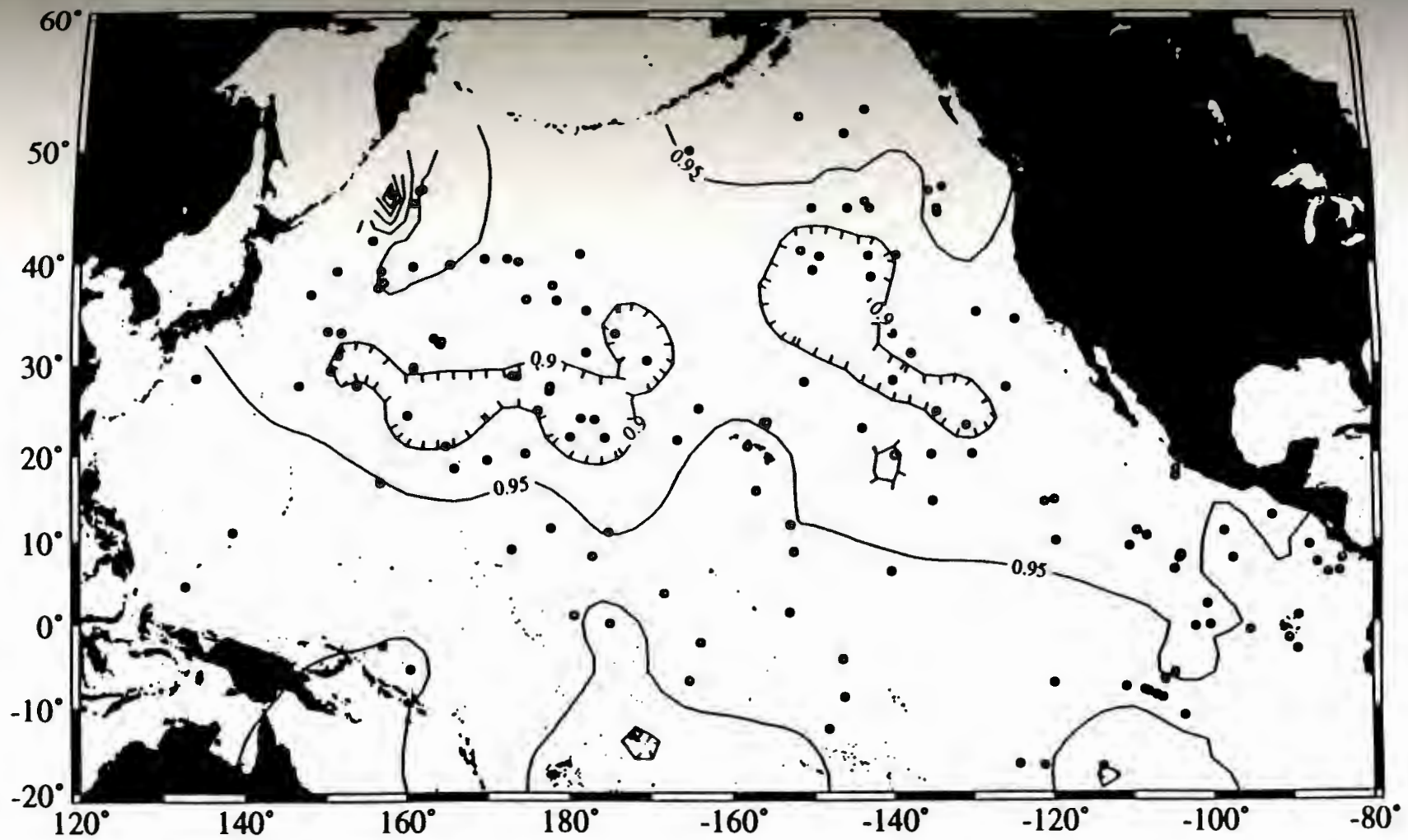
60°
50°
40°
30°
20°
10°
0°
-10°
-20°
120°
140°
160°
180°
-160°
-140°
-120°
-100°
-80°
0.95
0.9
0.9
0.9
0.95
0.95

Figure 7. Spatial distribution of median grain size. Units are μm. Contour interval is 2 μm.

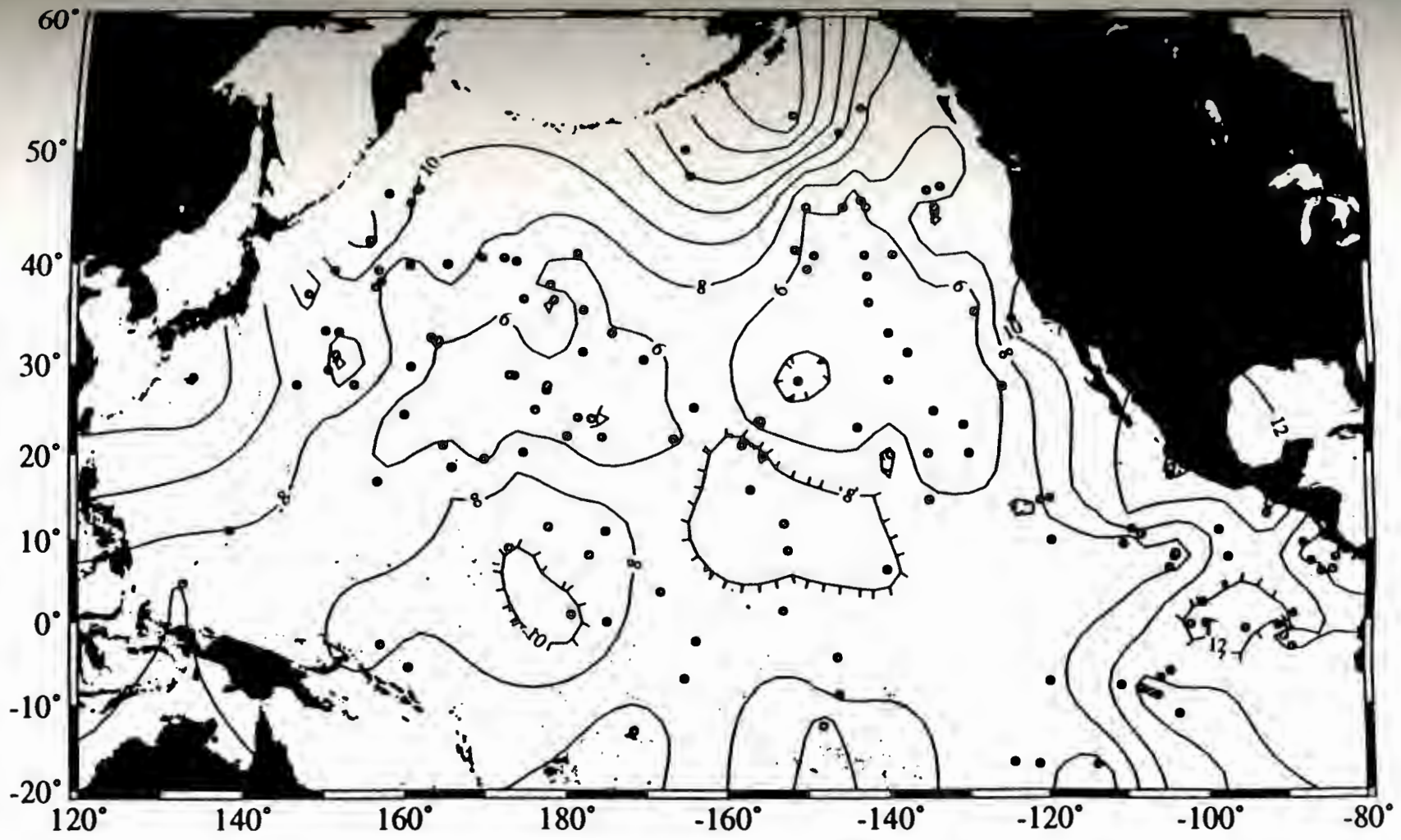
60°
50°
40°
30°
20°
10°
0°
-10°
-20°
120°
140°
160°
180°
-160°
-140°
-120°
-100°
-80°
6
8
10
12

Figure 8. Spatial distribution of >63μm size fraction weight percent. Contour interval is 10 percent.

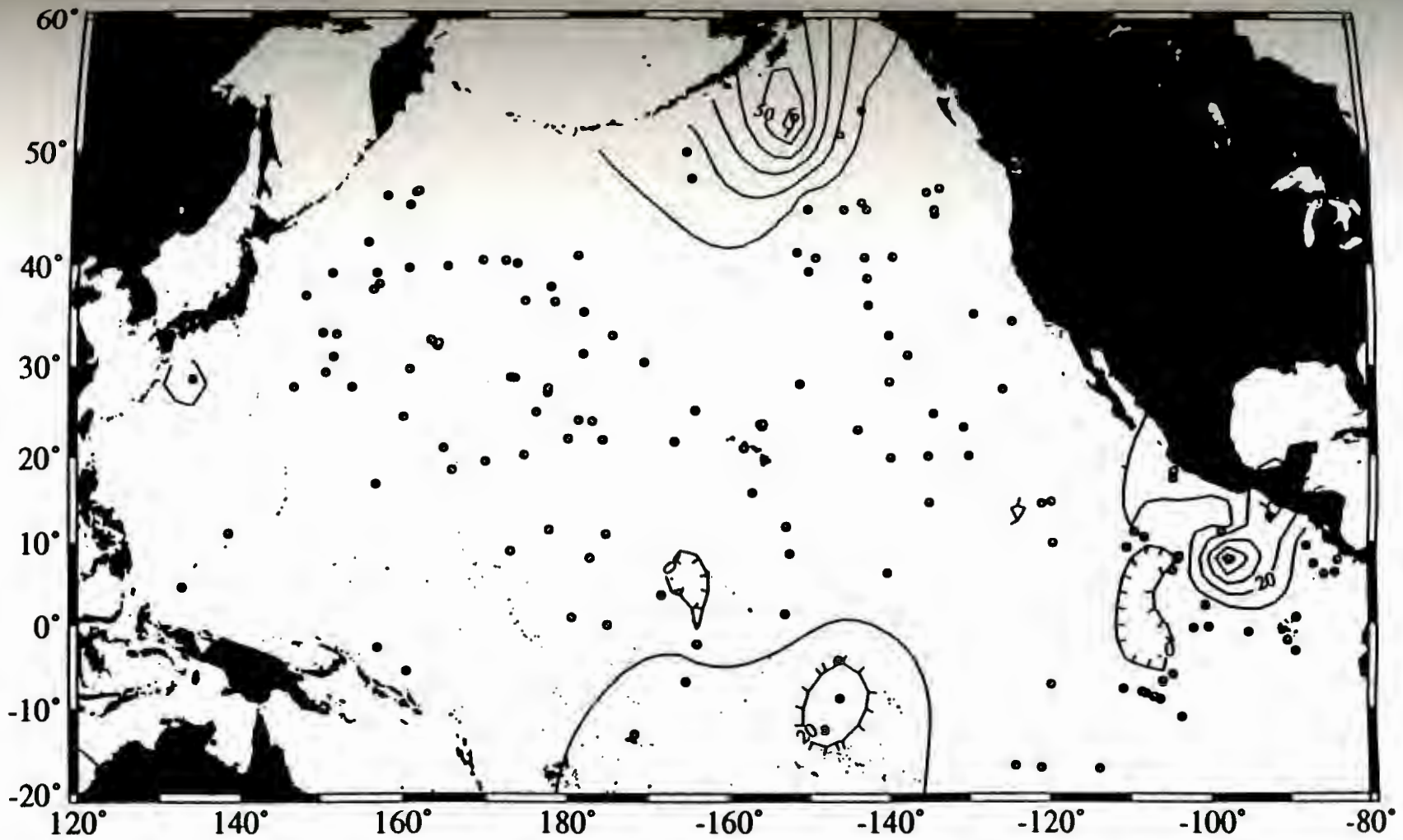
60°
50°
40°
30°
20°
10°
0°
-10°
-20°
120°
140°
160°
180°
-160°
-140°
-120°
-100°
-80°
50
20
20

Figure 9. Spatial distribution of 20-63µm size fraction weight percent. Contour interval is 5 percent.

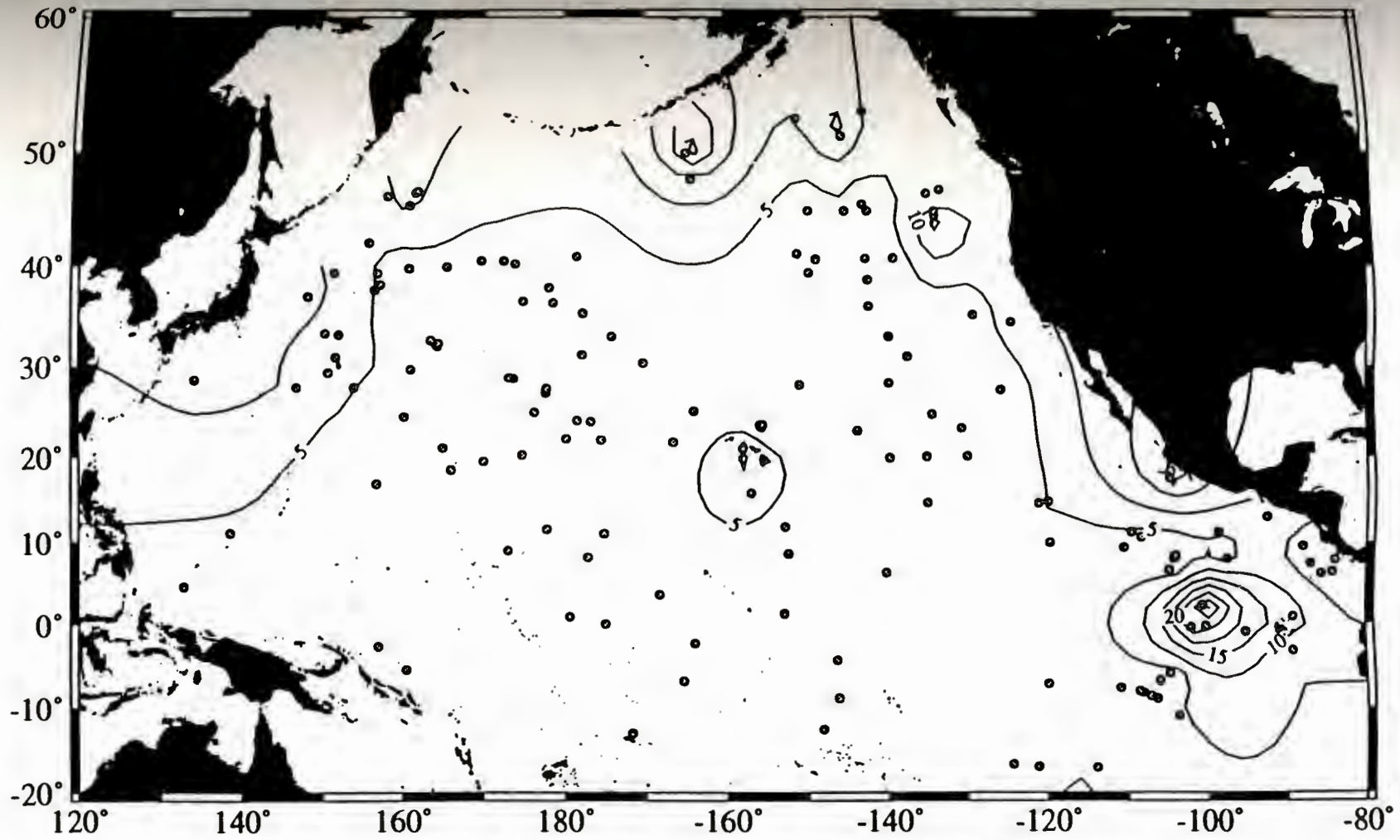
60°
50°
40°
30°
20°
10°
0°
-10°
-20°
120°
140°
160°
180°
-160°
-140°
-120°
-100°
-80°
5
10
5
5
5
20
15
10

Figure 10. Spatial distribution of 2-20μm size fraction weight percent. Contour interval is 5 percent.

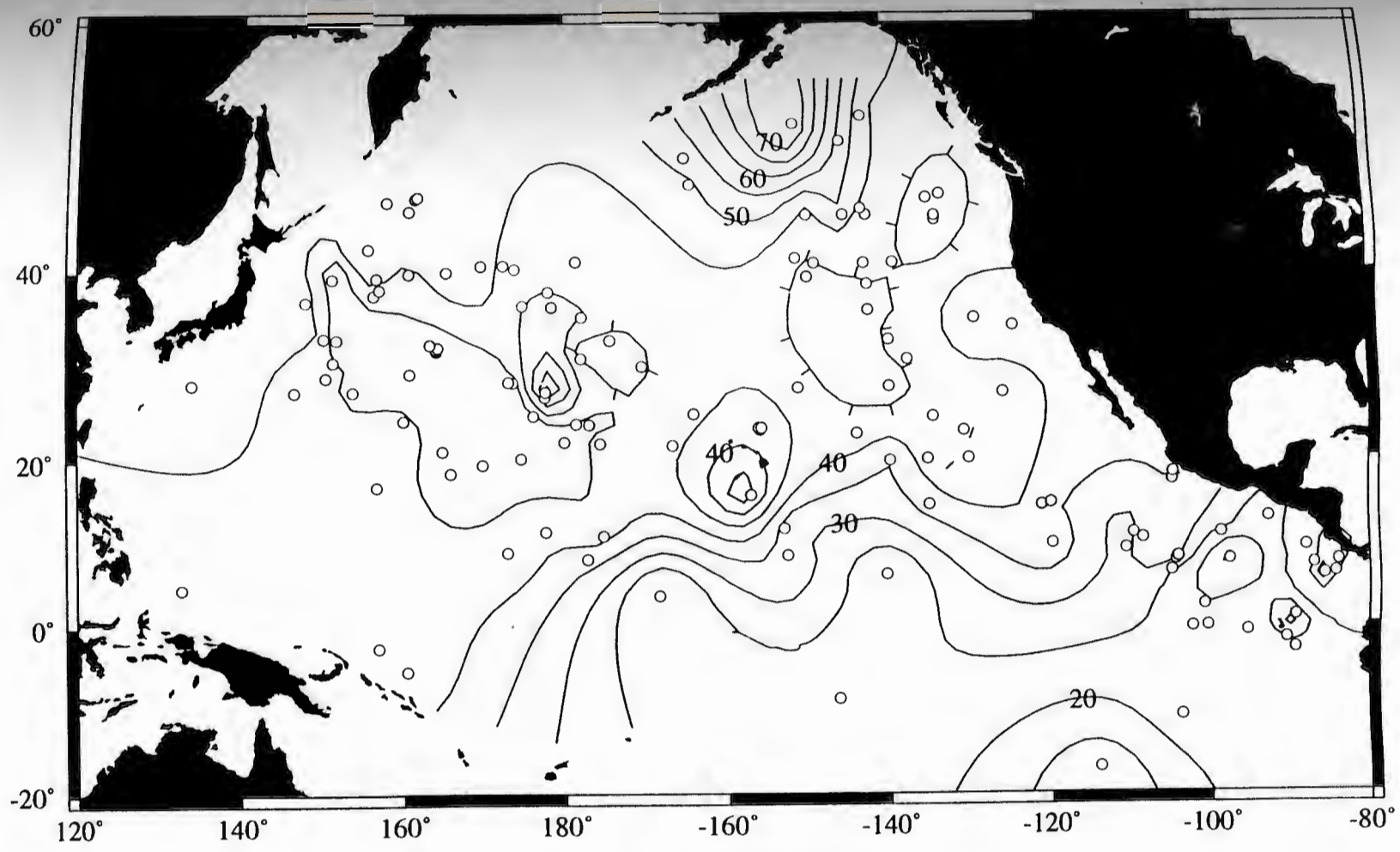
60°
40°
20°
0°
-20°
120°
140°
160°
180°
-160°
-140°
-120°
-100°
-80°
70
60
50
40
40
30
20

Figure 11. Spatial distribution of <2μm size fraction weight percent. Contour interval is 5 percent.

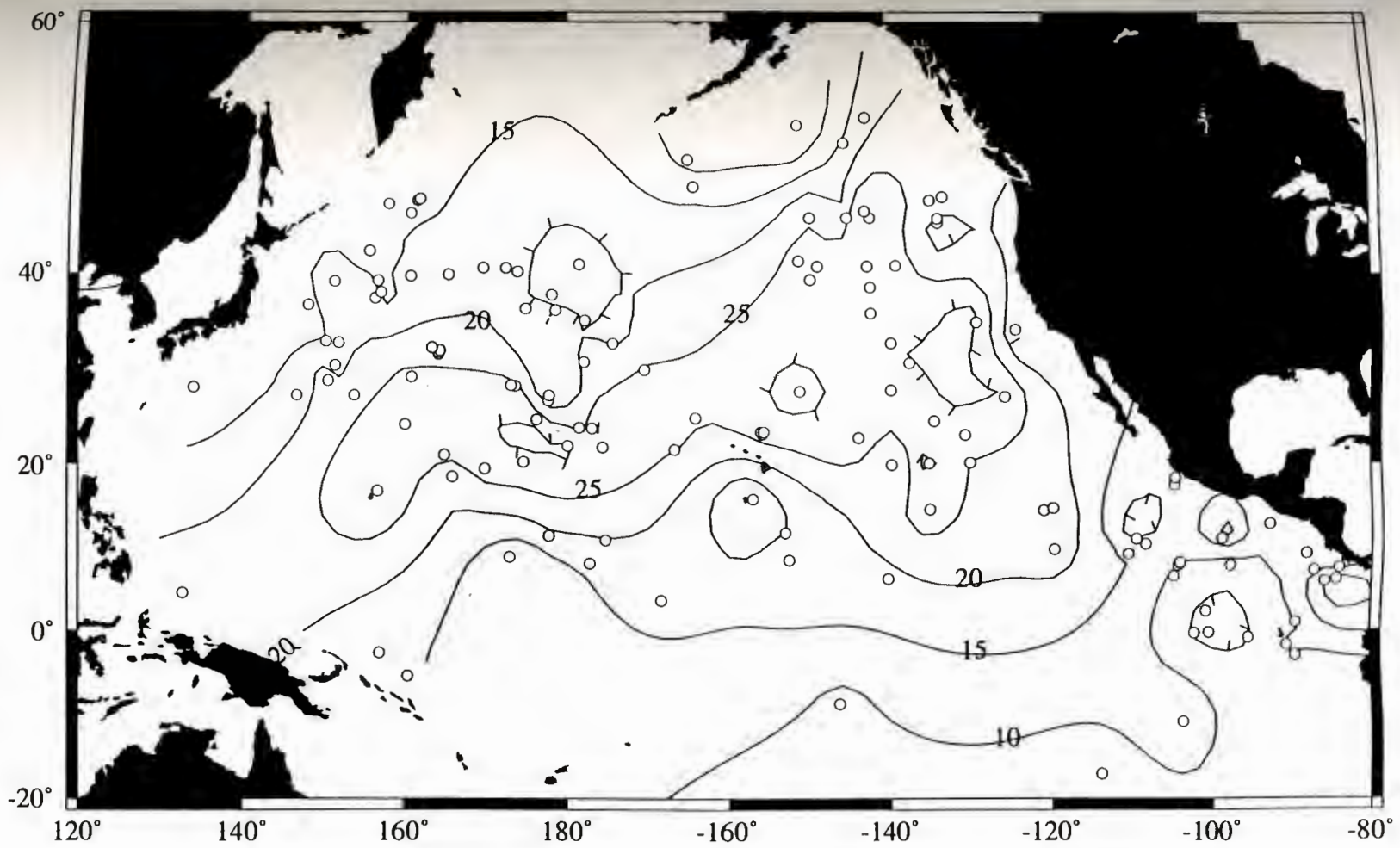
60°
40°
20°
0°
-20°
120°
140°
160°
180°
-160°
-140°
-120°
-100°
-80°
15
20
25
25
20
15
10
20

Figure 12. Spatial distribution of <2μm smectite concentration. Contour interval is 10 percent.

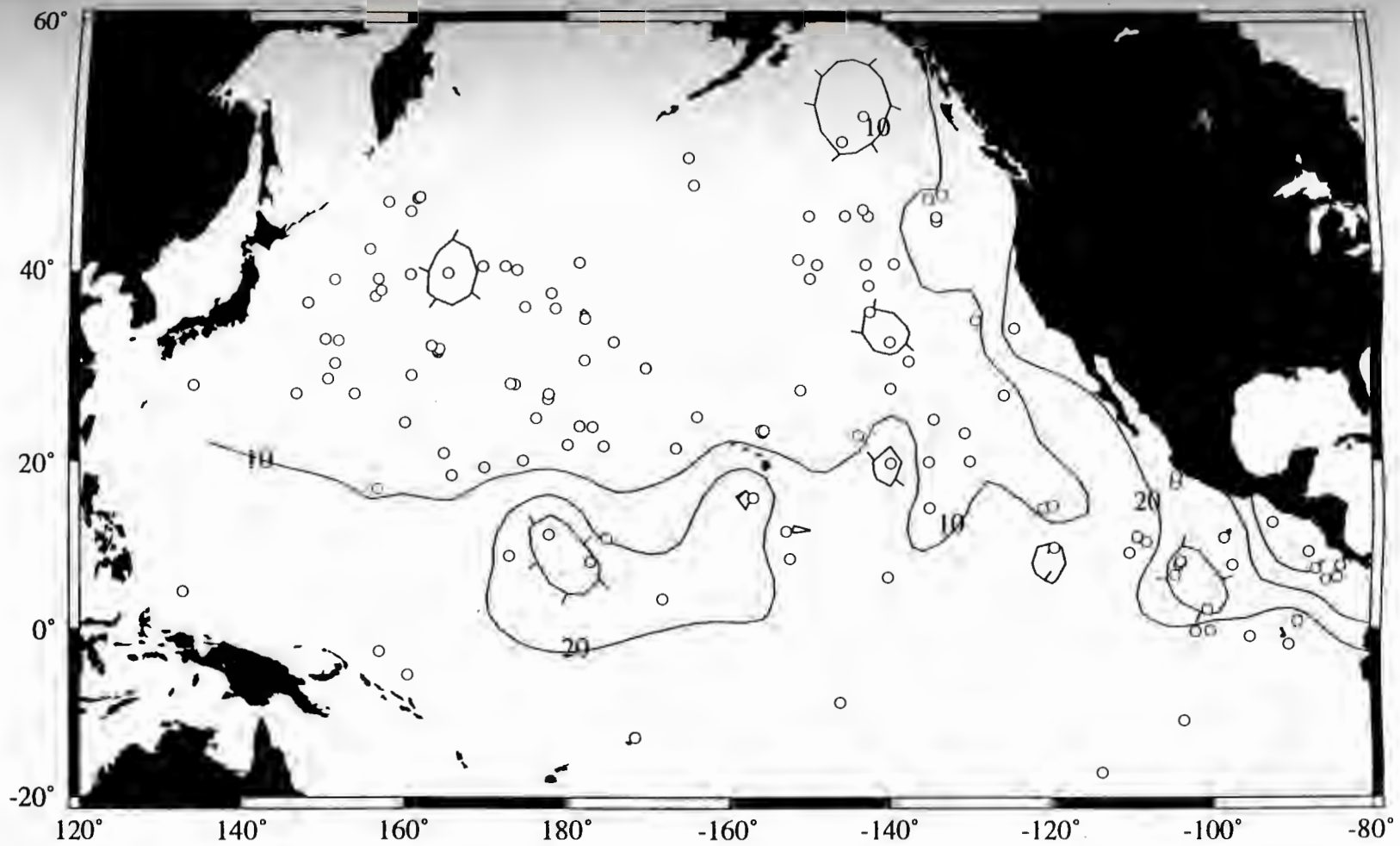
60°
40°
20°
0°
-20°
120°
140°
160°
180°
-160°
-140°
-120°
-100°
-80°
10
9
10
20
10
20

Figure 13. Spatial distribution of <2μm illite concentration. Contour interval is 10 percent.

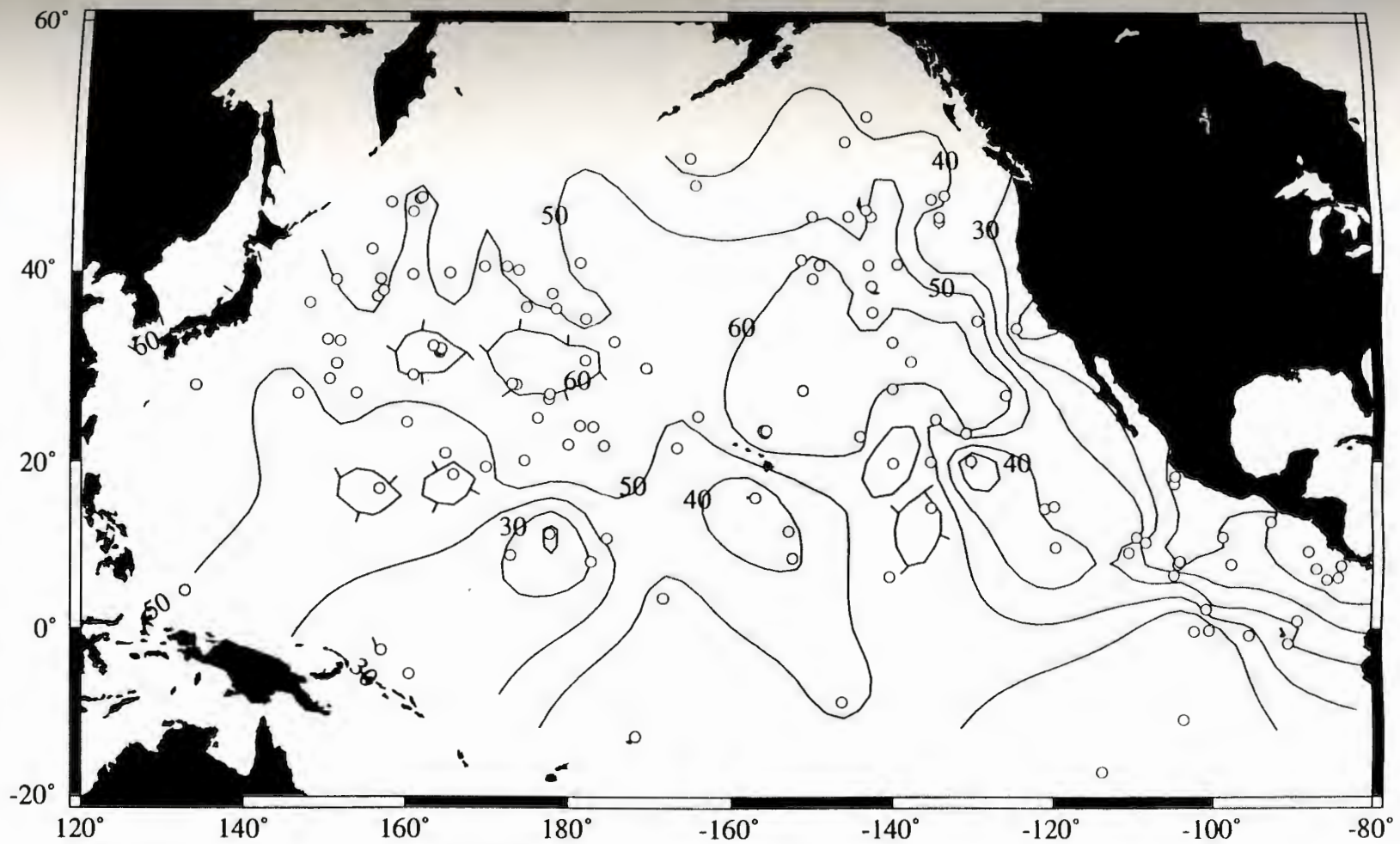
60°
40°
20°
0°
-20°
120°
140°
160°
180°
-160°
-140°
-120°
-100°
-80°
60
50
40
30
60
50
40
30
60
50
40
30
50
60
40

Figure 14. Spatial distribution of <2μm kaolinite concentration. Contour interval is 10 percent.

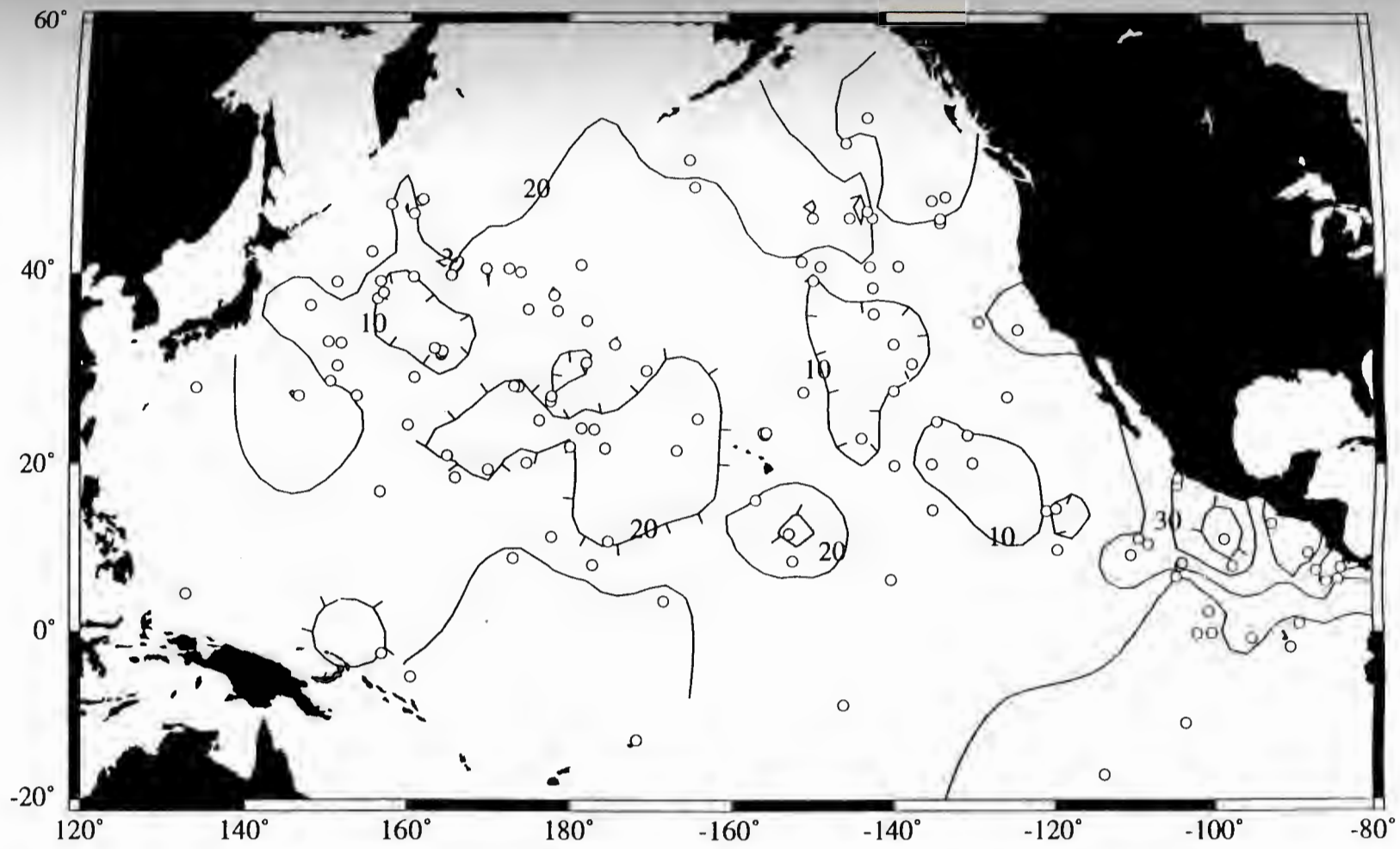
60°
40°
20°
0°
-20°
120°
140°
160°
180°
-160°
-140°
-120°
-100°
-80°
10
20
30
10
20
20
10
30

Figure 15. Spatial distribution of <2μm chlorite concentration. Contour interval is 2.5 percent.

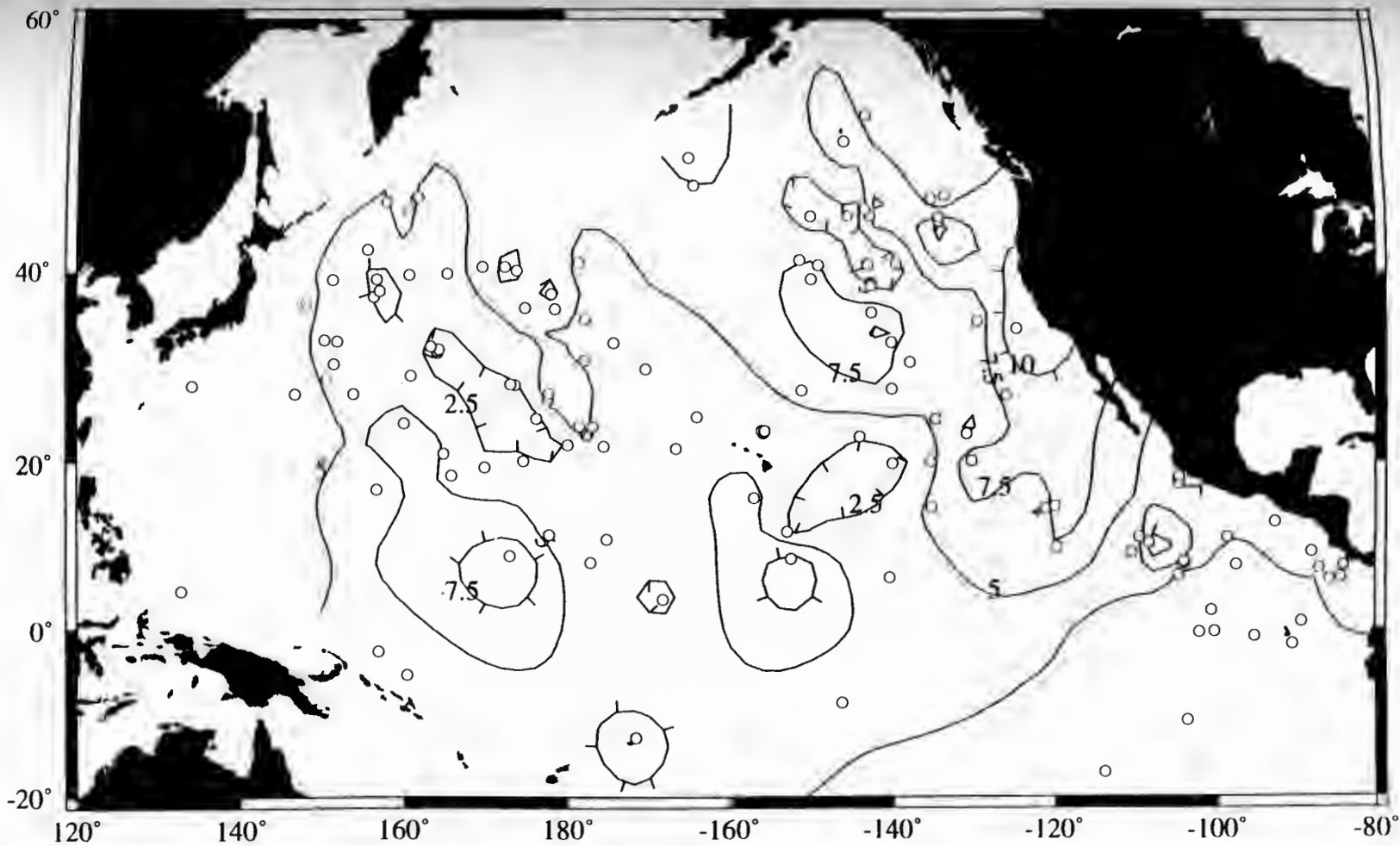
60°
40°
20°
0°
-20°
120°
140°
160°
180°
-160°
-140°
-120°
-100°
-80°
2.5
7.5
7.5
10
7.5
2.5
7.5
5

Figure 16. Spatial distribution of <2μm quartz concentration. Contour interval is 2 percent.

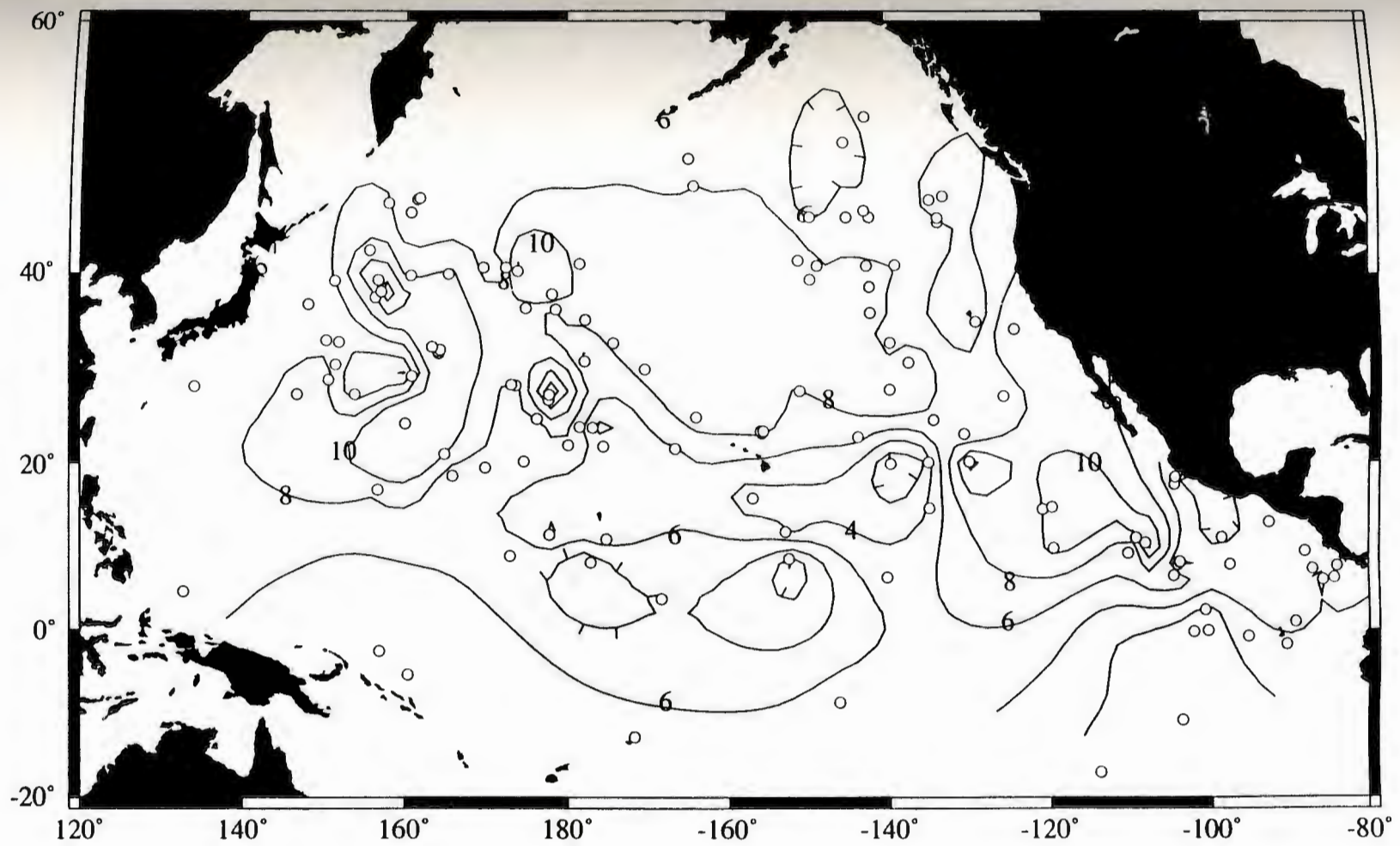
60°
40°
20°
0°
-20°
120°
140°
160°
180°
-160°
-140°
-120°
-100°
-80°
6
10
8
10
8
6
4
10
8
6
6

Figure 17. Spatial distribution of <2μm plagioclase concentration. Contour interval is 5 percent.

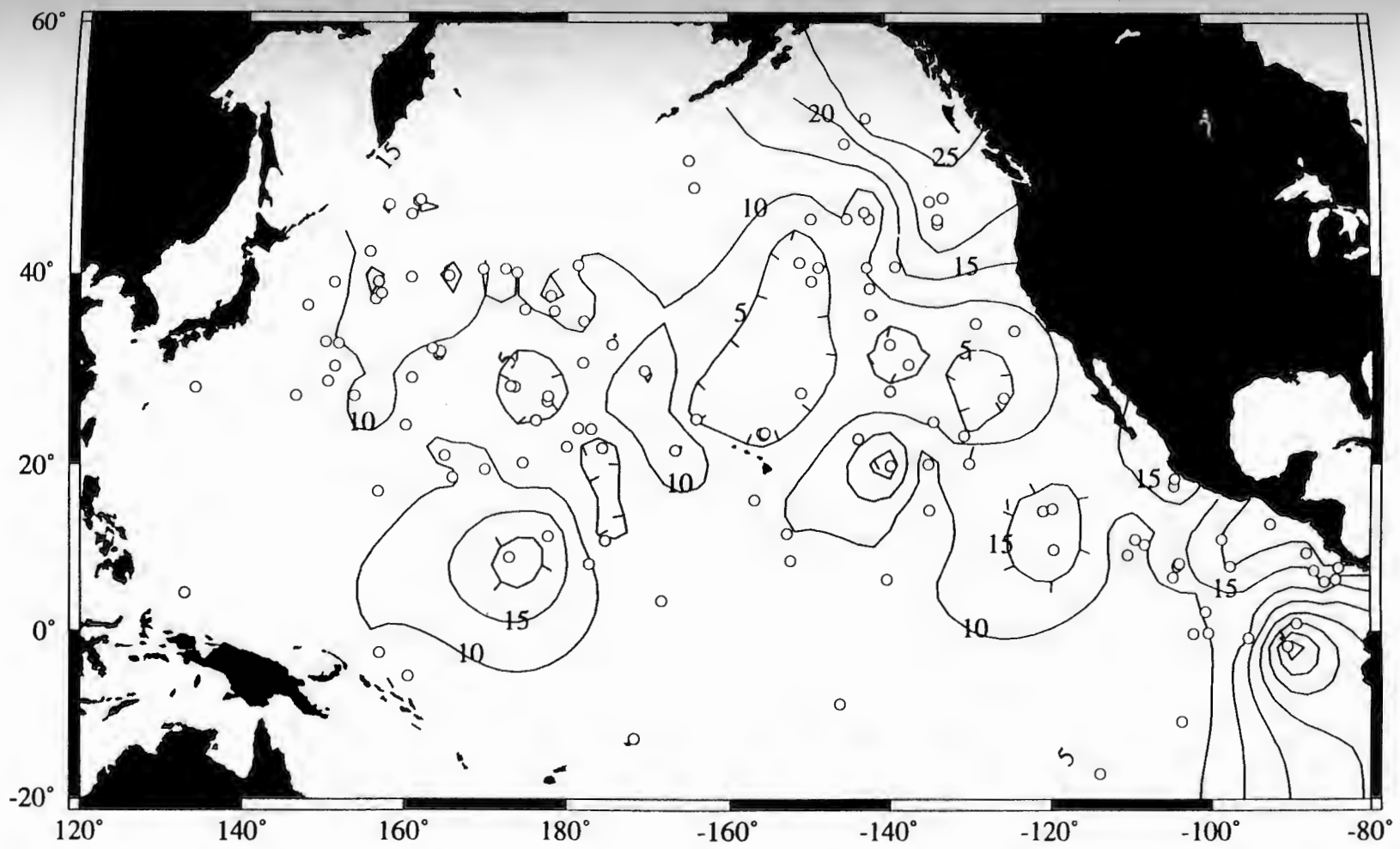
60°
40°
20°
0°
-20°
120°
140°
160°
180°
-160°
-140°
-120°
-100°
-80°
20
25
15
10
5
10
15
5
10
15
15
15
10
15
10
5

Figure 18. Spatial distribution of 2-20μm smectite concentration. Contour interval is 2.5 percent.

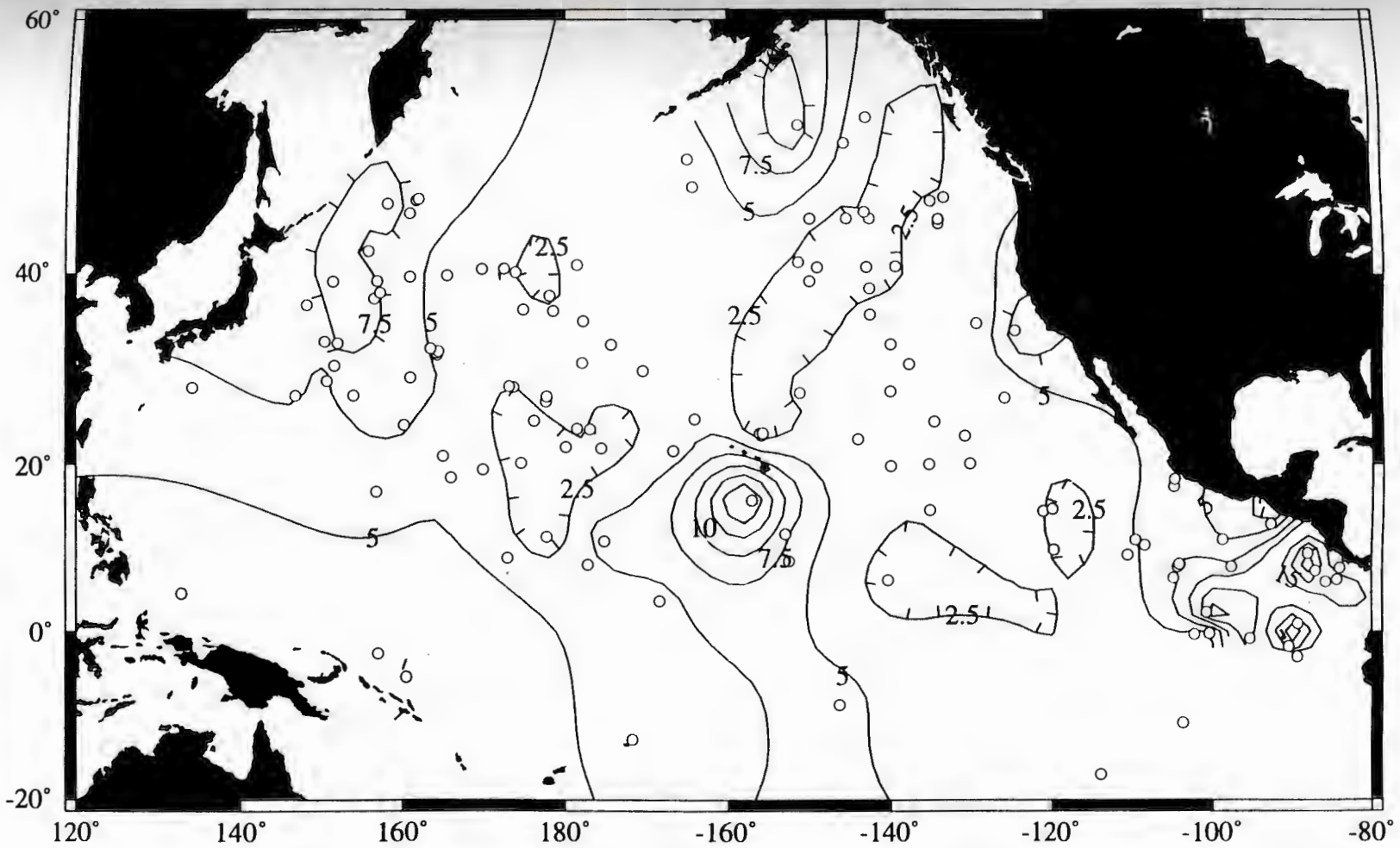
60°
40°
20°
0°
-20°
120°
140°
160°
180°
-160°
-140°
-120°
-100°
-80°
7.5
5
2.5
10

Figure 19. Spatial distribution of 2-20μm illite concentration. Contour interval is 10 percent.

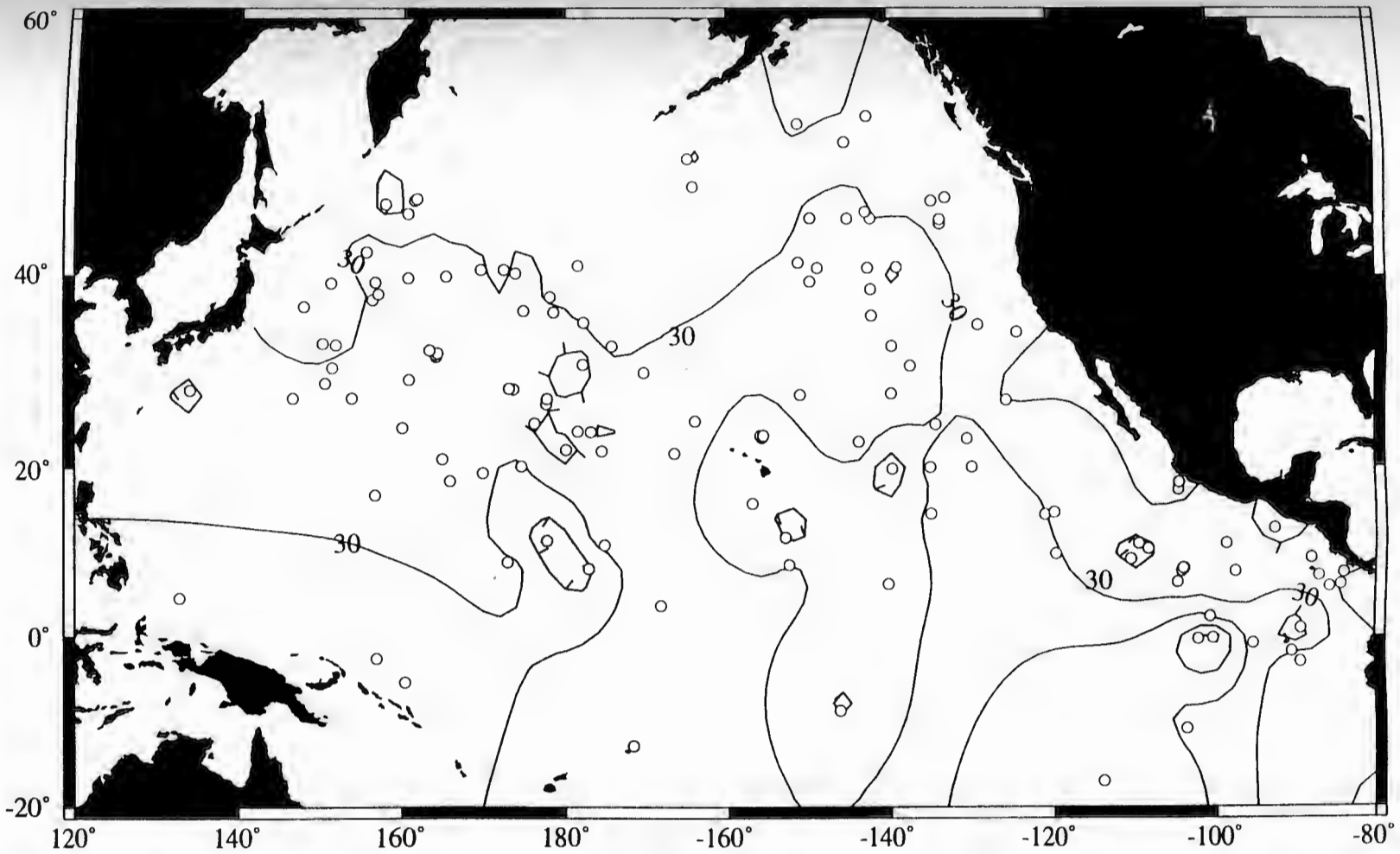
60°
40°
20°
0°
-20°
120°
140°
160°
180°
-160°
-140°
-120°
-100°
-80°
30
30
30
30
30
30

Figure 20. Spatial distribution of 2-20μm kaolinite concentration. Contour interval is 5 percent.

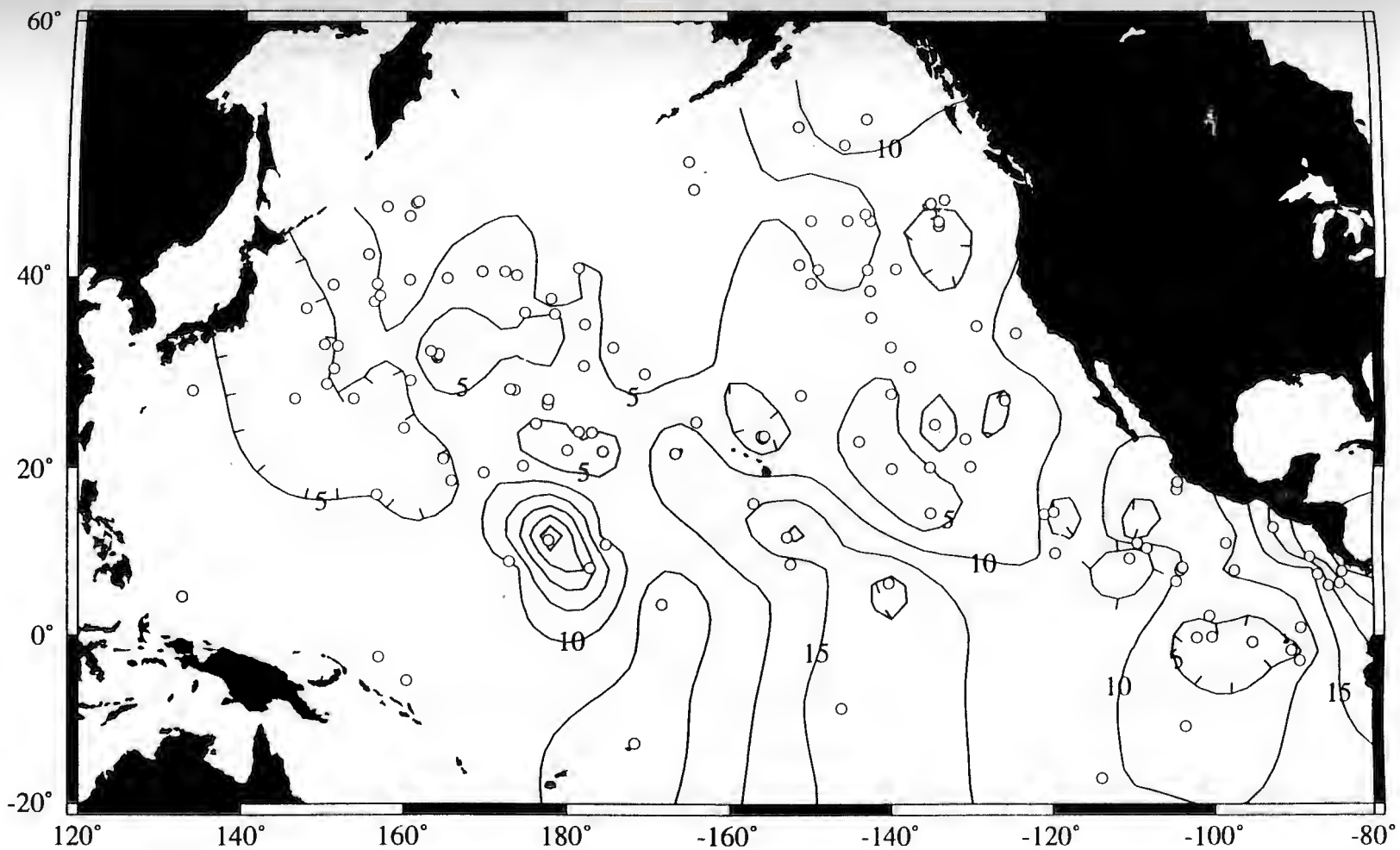
60°
40°
20°
0°
-20°
120°
140°
160°
180°
-160°
-140°
-120°
-100°
-80°
5
5
5
5
5
10
10
10
15
15

Figure 21. Spatial distribution of 2-20μm chlorite concentration. Contour interval is 1 percent.

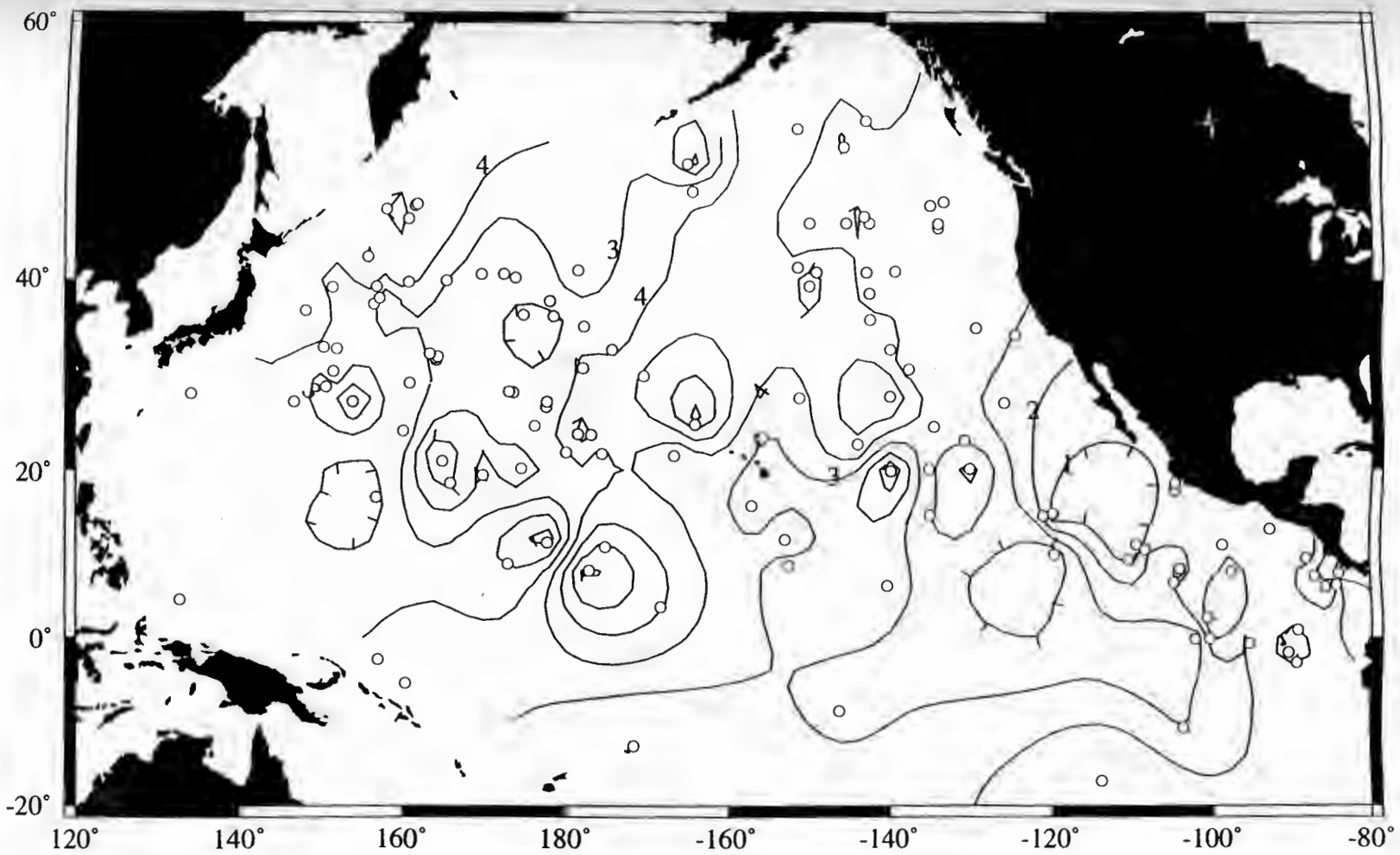
60°
40°
20°
0°
-20°
120°
140°
160°
180°
-160°
-140°
-120°
-100°
-80°
4
3
4
2

Figure 22. Spatial distribution of 2-20μm quartz concentration. Contour interval is 5 percent.

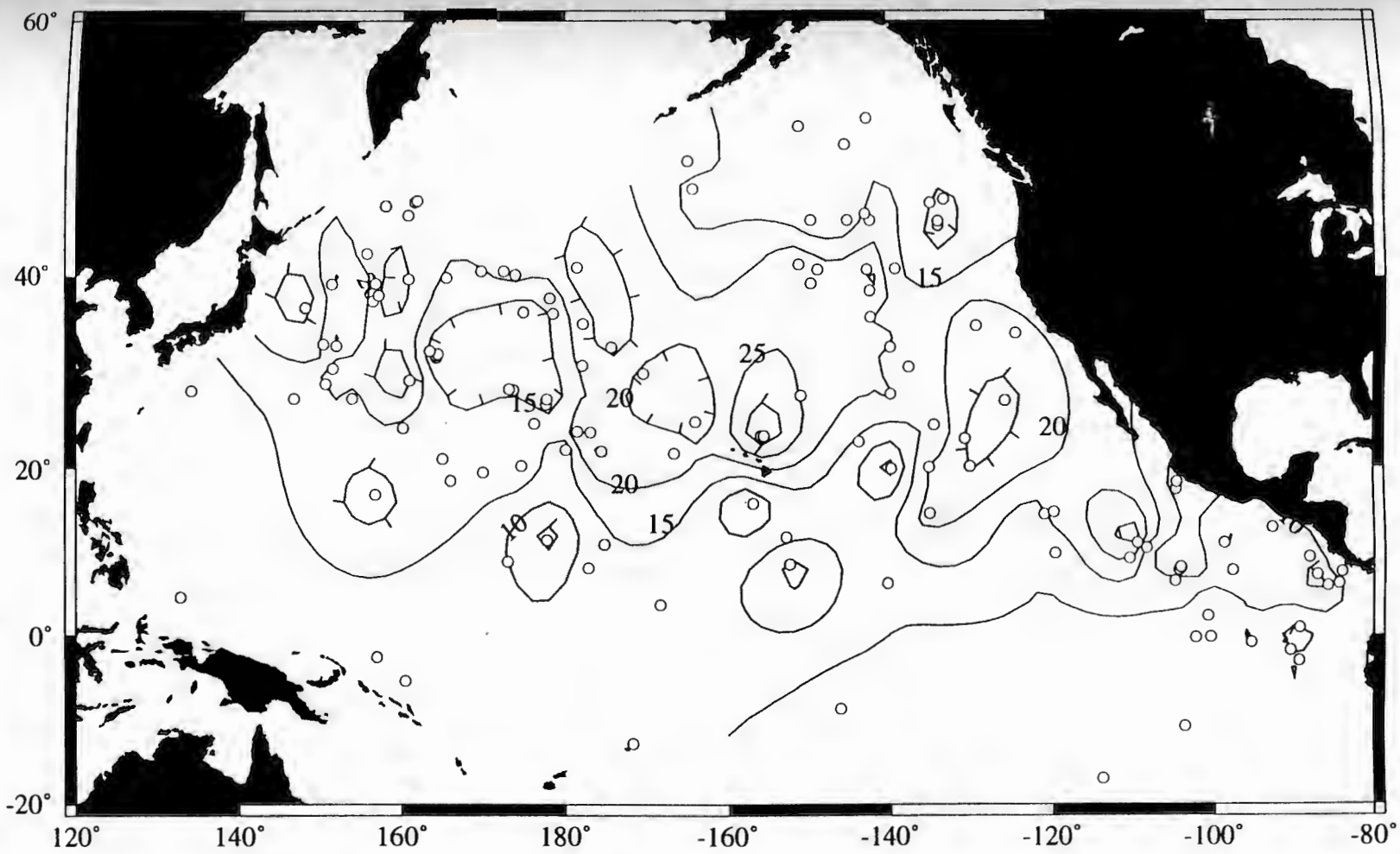
60°
40°
20°
0°
-20°
120°
140°
160°
180°
-160°
-140°
-120°
-100°
-80°
15
25
20
15
20
20
15
10

Figure 23. Spatial distribution of 2-20μm plagioclase concentration. Contour interval is 10 percent.

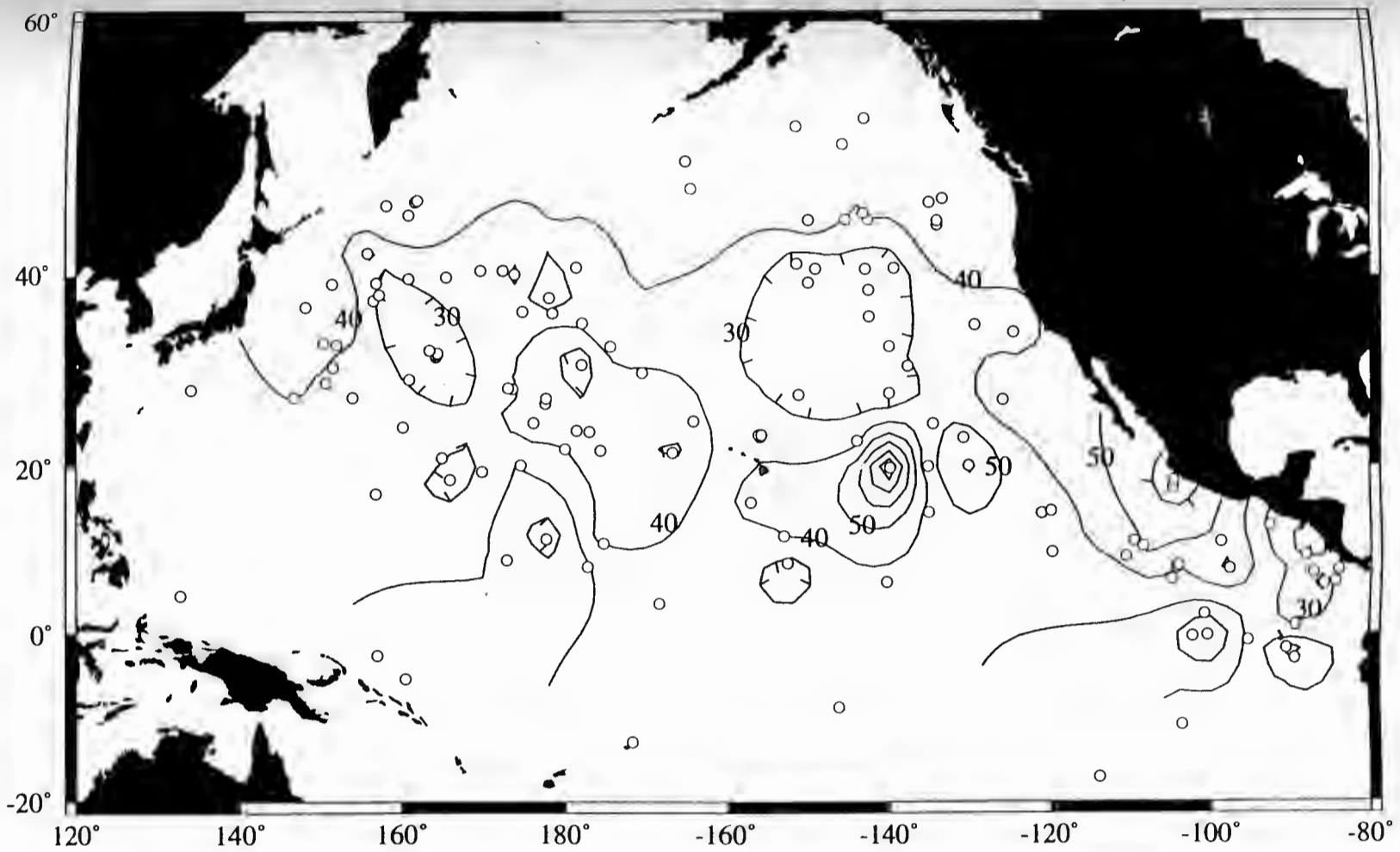
60°
40°
20°
0°
-20°
120°
140°
160°
180°
-160°
-140°
-120°
-100°
-80°
40
30
40
30
40
40
50
50
40
50
30

Figure 24. Rock magnetic concentration properties vs. longitude.

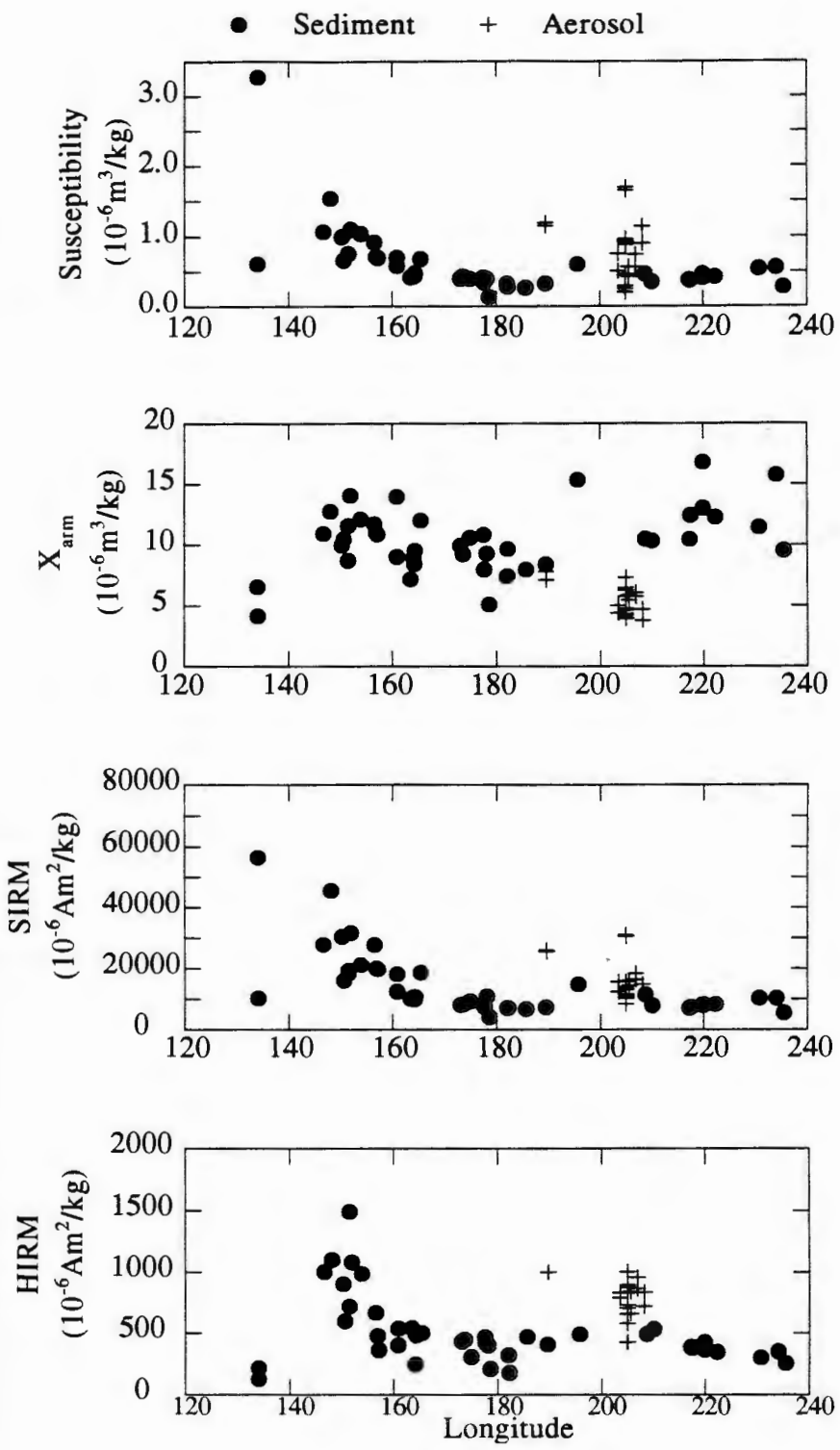
Sediment
Aerosol
Susceptibility ($10^{-6}m^3/kg$)
3.0
2.0
1.0
0.0
X_{arm} ($10^{-6}m^3/kg$)
20
15
10
5
0
SIRM ($10^{-6}Am^2/kg$)
80000
60000
40000
20000
0
HIRM ($10^{-6}Am^2/kg$)
2000
1500
1000
500
0
120
140
160
180
200
220
240
Longitude

Figure 25. S-ratio vs. longitude.

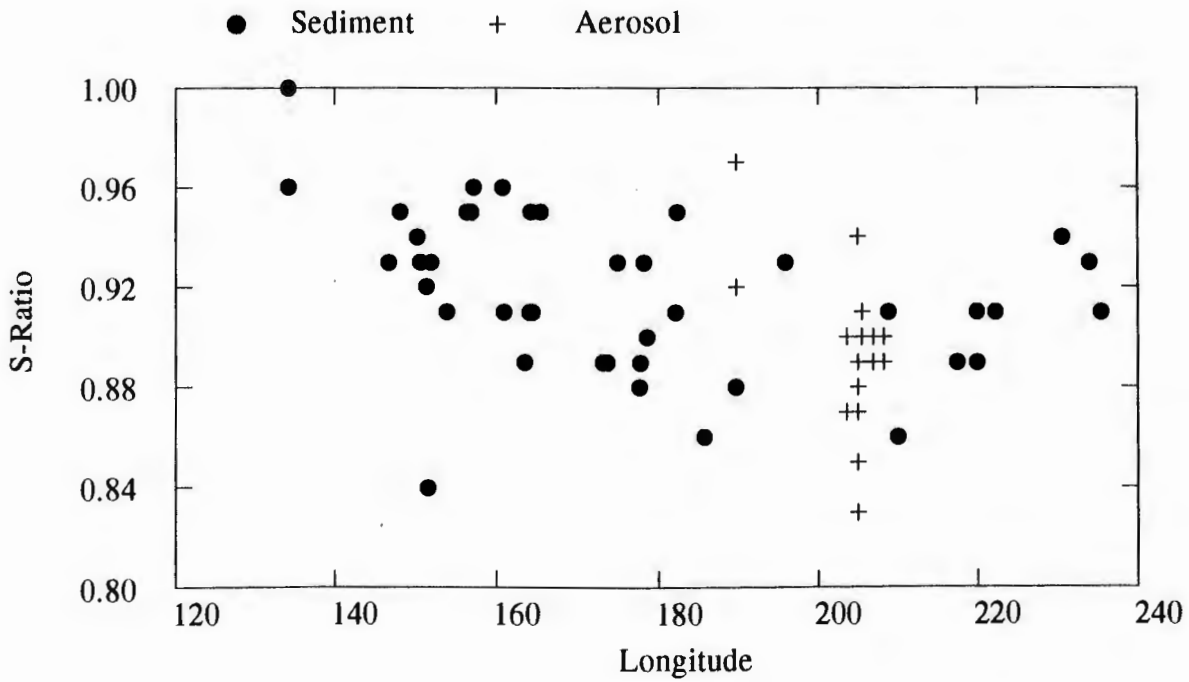
Sediment
Aerosol
1.00
0.96
0.92
0.88
0.84
0.80
S-Ratio
120
140
160
180
200
220
240
Longitude

Figure 26. Grain size parameters vs. longitude.

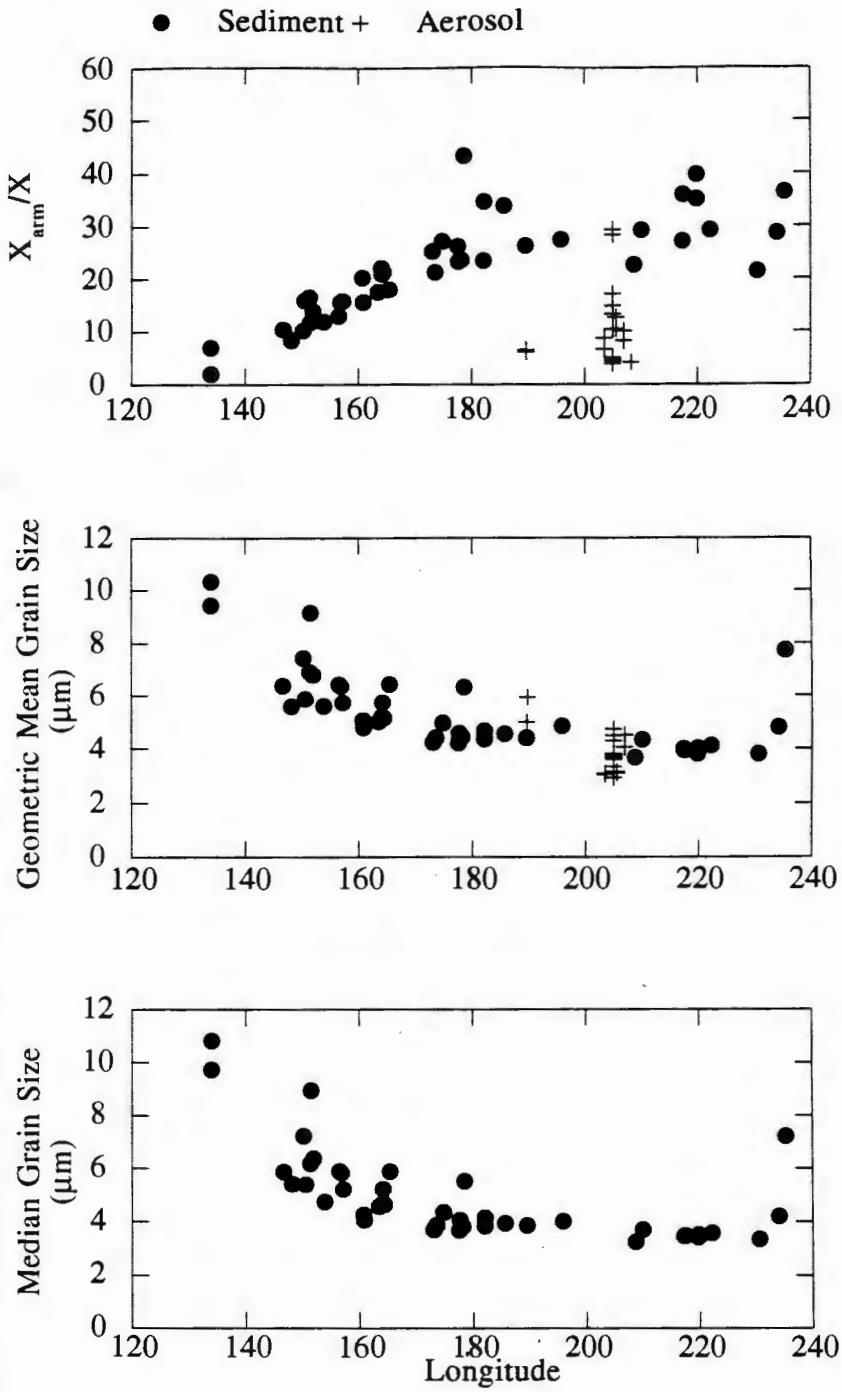
● Sediment + Aerosol
X_{arm}/X
Geometric Mean Grain Size (μm)
Median Grain Size (μm)
Longitude
120
140
160
180
200
220
240

Figure 27 Sediment weight percent by size class vs. longitude.

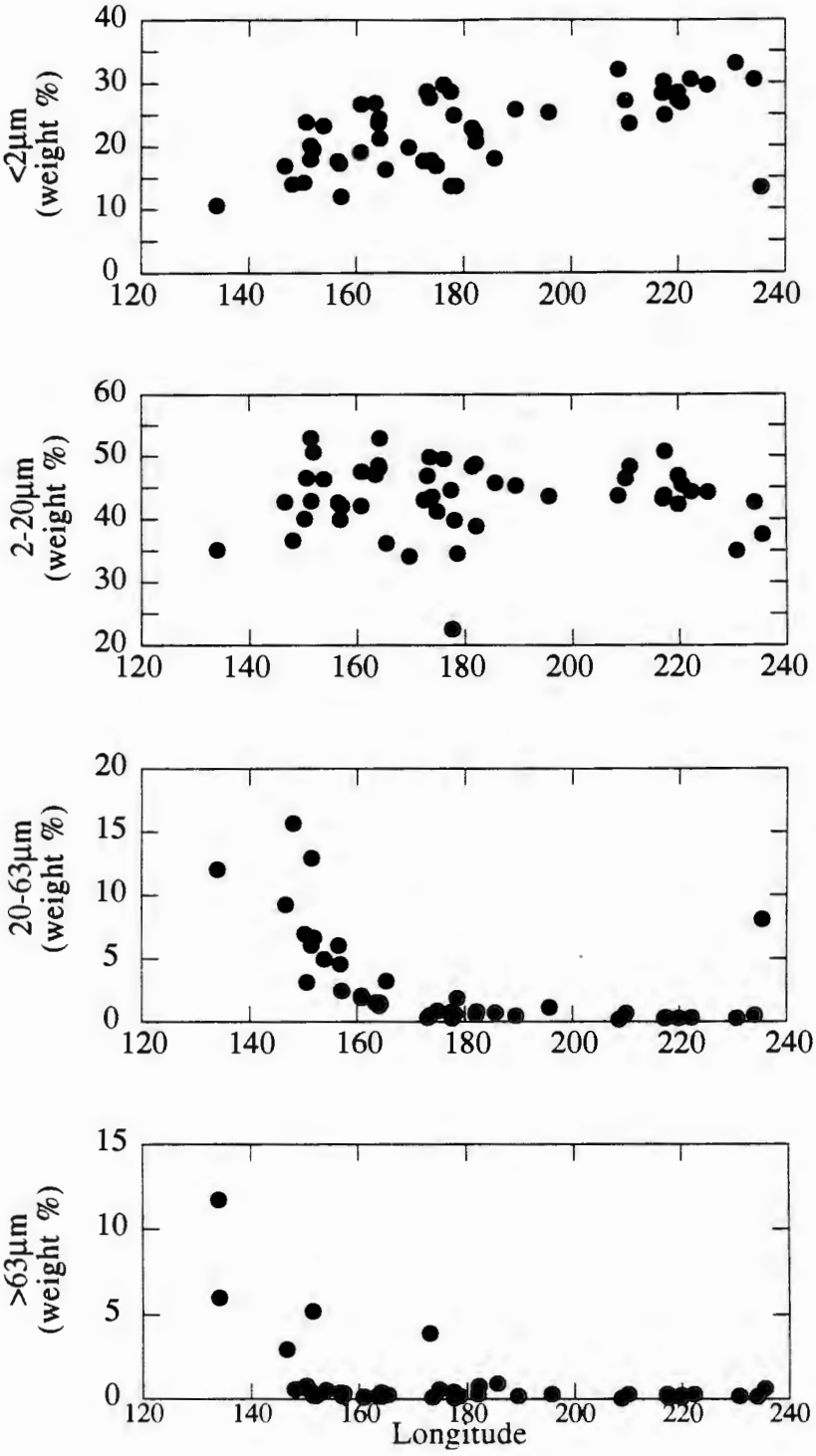
<2µm (weight %)
40
30
20
10
0
120
140
160
180
200
220
240
2-20µm (weight %)
60
50
40
30
20
20-63µm (weight %)
20
15
10
5
>63µm (weight %)
Longitude

Figure 28. <2 μm smectite, illite and kaolinite vs. longitude.

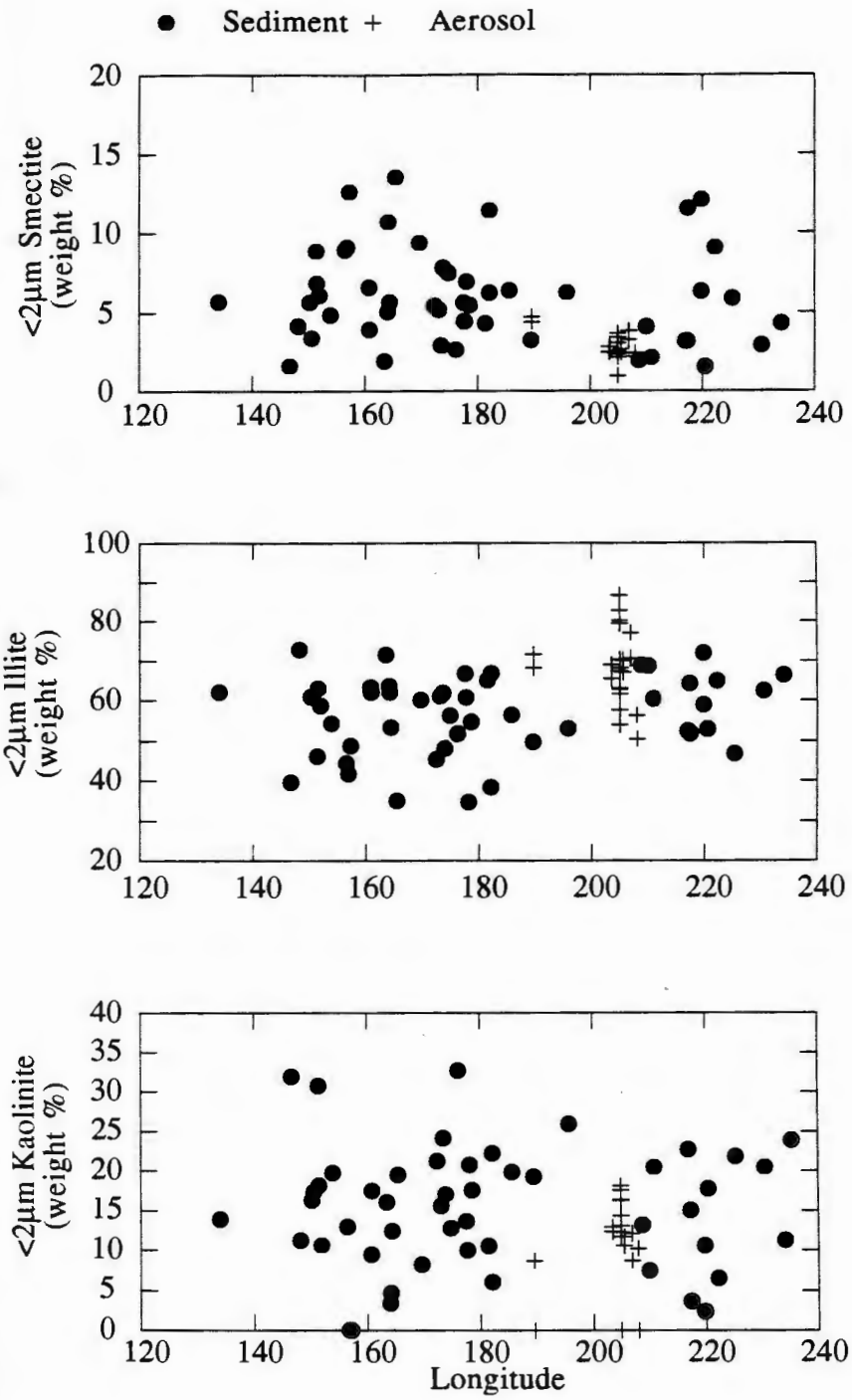
Sediment + Aerosol
<2µm Smectite (weight %)
<2µm Illite (weight %)
<2µm Kaolinite (weight %)
Longitude
120
140
160
180
200
220
240

Figure 29. <2 μm chlorite, quartz and plagioclase vs. longitude.

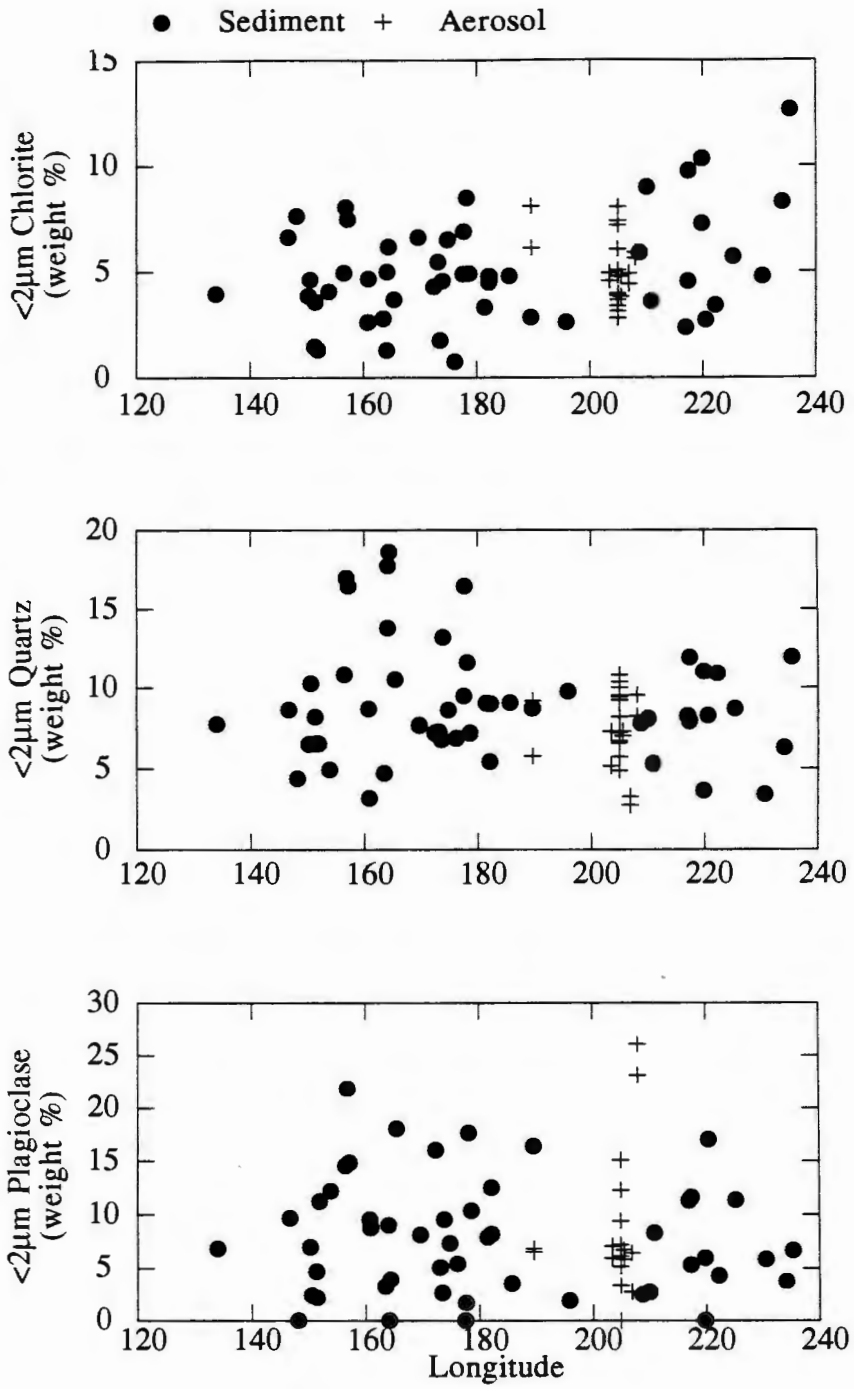
Sediment
Aerosol
<2µm Chlorite (weight %)
<2µm Quartz (weight %)
<2µm Plagioclase (weight %)
Longitude
0
5
10
15
20
25
30
120
140
160
180
200
220
240

Figure 30. 2-20 μm smectite, illite and kaolinite vs. longitude.

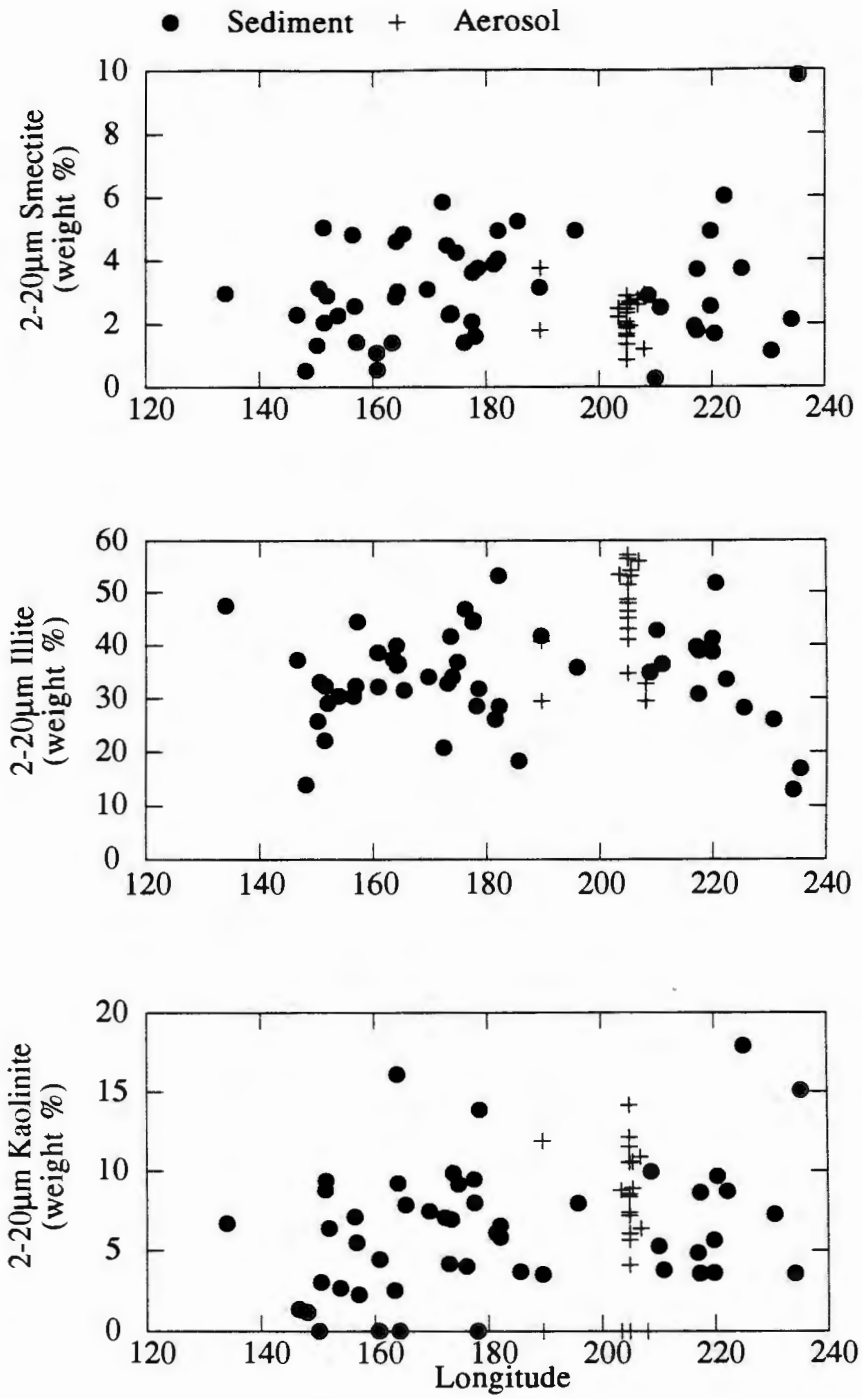
Sediment
Aerosol
2-20µm Smectite (weight %)
2-20µm Illite (weight %)
2-20µm Kaolinite (weight %)
Longitude
120
140
160
180
200
220
240

Figure 31. 2-20 μm chlorite, quartz and plagioclase vs. longitude.

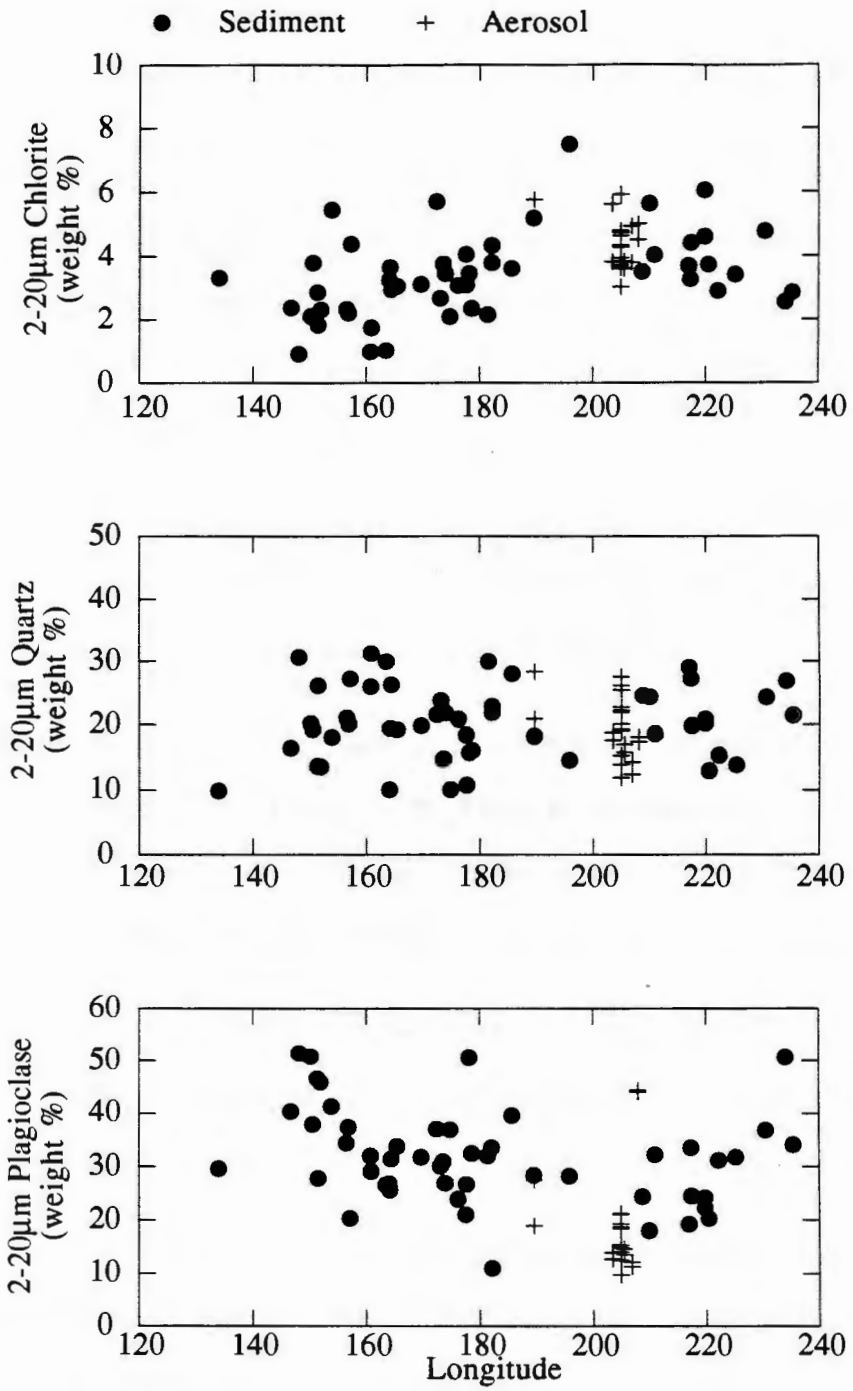
Sediment
Aerosol
2-20µm Chlorite (weight %)
2-20µm Quartz (weight %)
2-20µm Plagioclase (weight %)
Longitude
120
140
160
180
200
220
240

Bibliography

Amano, K., and Taira, A., 1992. Two-phase uplift of the higher Himalayas since 17 Ma. *Geology*, 20, 391-394.

Arimoto, R., Duce, R. A., Ray, B. J., Hewitt, A. D. and Williams, J. 1987. Trace elements in the atmosphere of American Samoa: concentrations and deposition to the tropical South Pacific. *Journal of Geophysical Research*, 92, 8,465-8,479.

Arimoto, R., Duce, R. A., Ray, B. J. and Unni, C. K. 1985. Atmospheric trace elements at Enewetak atoll: 2. Transport to the ocean by wet and dry deposition. *Journal of Geophysical Research*, 90, 2,391-2,408.

Betzer, P. R., Carder, K. L., Duce, R. A., Merrill, J. T., Tindale, N. W., Uematsu, M., Costello, D. K., Young, R. W., Feely, R. A., Breland, J. A., Bernstein, R. E. and Greco, A. M. 1988. Long-range transport of giant mineral aerosol particles. *Nature*, 336, 568-571.

Blank, M., Leinen, M. and Prospero, J. M. 1985. Major Asian eolian inputs indicated by the mineralogy of aerosols and sediments in the western North Pacific. *Nature*, 314, 84-86.

Bloemendal, J. and deMenocal, P. 1989. Evidence for a change in periodicity of tropical climate cycles at 2.4 Myr from whole-core magnetic susceptibility measurements. *Nature*, 342, 897-900.

Buat-Menard, P., Ezat, U. and Gaudichet, A. 1983. Size distribution and mineralogy of aluminosilicate dust particles in tropical Pacific air and rain. *4th*

International Conference on Precipitation Scavenging, Dry Deposition, and Resuspension, November 28-December 3, 1982. Santa Monica, California. 8 pages.

Chamley, H. 1989. *Clay Sedimentology*. Springer-Verlag. Berlin. 623 pages.

Copeland, P., and Harrison, T.M., 1990. Episodic uplift in the Himalayas revealed by $^{40}Ar/^{39}Ar$ analysis of detrital K-feldspar and muscovite, Bengal Fan. *Geology*, 18, 354-357.

Ding, Z., Rutter, N., Jingtai, H., and Tungsheng, L., 1992. A coupled environmental system formed at about 2.5 Ma in east Asia. *Palaeoceanography, Palaeoclimatology, Palaeoecology*, 94, 223-242.

Doh, S.-J., King, J. W. and Leinen, M. 1988. A rock-magnetic study of giant piston core LL44-GPC3 from the central North Pacific and its paleoceanographic implications. *Paleoceanography*, 3, 89-111.

Duce, R. A. 1989. SEAREX: The Sea-Air Exchange Program. In: Riley, J. P. and Chester, R. *Chemical Oceanography*, Volume 10, Academic Press Inc., San Diego. 404 pages.

Duce, R. A., Arimoto, R., Ray, B. J., Unni, C. K. and Harder, P. J. 1983. Atmospheric trace elements at Enewetak Atoll: 1, concentrations, sources and temporal variability. *Journal of Geophysical Research*, 88, 5321-5342.

Duce, R. A., Unni, C. K., Ray, B. J., Prospero, J. M. and Merrill, J. T. 1980. Long-range transport of soil dust from Asia to the tropical North Pacific: temporal variability. *Science*, 209, 1,522-1,524.

Ferguson, W. S., Griffin, J. J. and Goldberg, E. D. 1970. Atmospheric dusts from the North Pacific - a short note on a long-range eolian transport. *Journal of Geophysical Research*, 75, 1137-1139.

Griffin, J. J., Windom, H. and Goldberg, E. D. 1968. The distribution of clay minerals in the world ocean. *Deep-Sea Research*, 15, 433-459.

Glaccum, R. A. and Prospero, J. M. 1980. Saharan aerosols over the tropical North Atlantic-mineralogy. *Marine Geology*, 37, 295-321.

Heath, G. R. and Pisias, N. G. 1979. A method for the quantitative estimation of clay minerals in North Pacific deep-sea sediments. *Clays and Clay Minerals*, 27, 175-184.

Hovan, S., and Rea, D.K., 1992. The Cenozoic record of continental mineral deposition on Broken and Ninetyeast Ridges, Indian Ocean: southern African aridity and sediment delivery from the Himalayas. *Paleoceanography*, 7, 833-860.

Janecek, T. R. and Rea, D. K. 1983. Eolian deposition in the northeast Pacific Ocean: Cenozoic history of atmospheric circulation. *Geological Society of America Bulletin*, 94, 730-738.

Johnson, L. R. 1976. Particle-size fractionation of eolian dusts during transport and sampling. *Marine Geology*, 21, M17-M21.

King, J. W., Bloemendal, J. and Gangemi, P. 1989. Paleomagnetic and rock-magnetic stratigraphy of ESOPE core 63, southern Nares abyssal plain. 611-636. In: Schuttenhelm, R. T. E., Auffret, G. A., Buckley, D. E., Cranston, R. E., Murray, C. N., Shepard, L. E. and Spijkstra, A. E. *The ESOPE international*

expedition, geoscience investigations of two North Atlantic abyssal plains. Office for official publications of the European community, Luxembourg.

Kutzbach, J.E., Guetter, P.J., Ruddiman, W.F., and Prell, W.L. 1989. Sensitivity of climate to late Cenozoic uplift in southern Asia and the American west: numerical experiments. *Journal of Geophysical Research*, 94, 18393-18407.

Kyte, F. T., Leinen, M., Heath, G. R. and Zhou, L. 1993. Cenozoic sedimentation history of the central North Pacific: Inferences from the elemental geochemistry of core LL44-GPC3. *Geochimica et Cosmochimica Acta,* 57, 1719-1740.

Landa, E. R. and Gast, R. G. 1973. Evaluation of crystallinity in hydrated ferric oxides. *Clays and Clay minerals*, 21, 121-130.

Leinen, M. 1989. The late Quaternary record of atmospheric transport to the Northwest Pacific from Asia. In: Leinen, M., and Sarnthein, M. (Eds.), *Paleoclimatology and Paleometeorology: Modern and Past Patterns of Global Atmospheric Transport.* Dordrecht, (NATO ASI Series), 693-732.

Leinen, M. 1989. The pelagic clay province of the North Pacific Ocean. 323-335. In: Winterer, E. L., Hussong, D. M. and Decker, R. W. *The eastern Pacific Ocean and Hawaii*. Geological Society of America. Boulder.

Leinen, M. 1987. The origin of paleochemical signatures in North Pacific pelagic clays: partitioning experiments. *Geochimica et Cosmochimica Acta,* 51, 305-319.

Leinen, M., 1985. Quartz content of northwest Pacific Hole 576A and implications for Cenozoic eolian transport. In: Heath, G.R., Burkle, L.H. *Initial Reports of*

the Deep Sea Drilling Project, 86. Washington, (U.S. Govt. Printing Office), 581-588.

Leinen, M., Cwienk, D., Heath, G. R., Biscaye, P. E., Kolla, V., Thiede, J. and Dauphin, J. P. 1986. Distribution of biogenic silica and quartz in recent deep-sea sediments. *Geology*, 14, 199-203.

Leinen, M. and Pisias, N. 1984. An objective technique for determining end-member compositions and for partitioning sediments according to their sources. *Geochimica et Cosmochimica Acta*, 48, 47-62.

Leinen, M., Prospero, J. M., Arnold, E. and Blank, M. 1994. Mineralogy of aeolian dust reaching the North Pacific Ocean 1. Sampling and analysis. *Journal of Geophysical Research*, 99, 21,017-21,023.

Merrill, J., Arnold, E., Leinen, M. and Weaver, C. 1994. Mineralogy of aeolian dust reaching the North Pacific Ocean 2. Relationship of mineral assemblages to atmospheric transport patterns. *Journal of Geophysical Research*, 99, 21,025-21,032.

Merrill, J. T. 1989. Atmospheric Long-range Transport to the Pacific Ocean. 15-49. In: Duce, R. A. *SEAREX: The Sea/Air Exchange Program.* Academic Press. San Diego.

Merrill, J. T., Bleck, R. and Avila, L. 1985. Modeling atmospheric transport to the Marshall Islands. *Journal of Geophysical Research,* 90, 12,927-12,936.

Merrill, J. T., Uematsu, M. and Bleck, R. 1989. Meteorological analysis of long range transport of mineral aerosols over the North Pacific. *Journal of Geophysical Research*, 94, 8584-8598.

Murray, R. W. and Leinen, M. 1993. Chemical transport to the seafloor of the equatorial Pacific Ocean across a latitudinal transect at 135°W: tracking sedimentary major, trace and rare earth element fluxes at the Equator and the intertropical convergence zone. *Geochimica et Cosmochimica Acta*, 57, 4,141-4,163.

Oldfield, F., Hunt, A., Jones, M. D. H., Chester, R., Dearing, J. A., Olsson, L. and Propero, J. M. 1985. Magnetic differentiation of atmospheric dusts. *Nature*, 317, 516-518.

Olivarez, A. M., Owen, R. M. and Rea, D. K. 1991. Geochemistry of eolian dust in Pacific pelagic sediments: implications for paleoclimatic interpretations. *Geochimica et Cosmochimica Acta*, 55, 2147-2158.

Parrington, J. R. and Zoller, W. H. 1984. Diurnal and longer-term changes in the composition of atmospheric particles at Mauna Loa, Hawaii. *Journal of Geophysical Research*, 89, 2,522-2,534.

Parrington, J. R., Zoller, W. H. and Aras, N. K. 1983. Asian dust: seasonal transport to the Hawaiian Islands. *Science*, 220, 195-197.

Prospero, J. M. and Bonatti, E. 1969. Continental dust in the atmosphere of the eastern equatorial Pacific. *Journal of Geophysical Research*, 74, 3362-3371.

Prospero, J. M. and Nees, R. T. 1977. Dust concentration in the atmosphere of the equatorial North Atlantic: Possible relationship to the Sahelian Drought. *Science*, 196, 1196-1198.

Prospero, J. M., Uematsu, M. and Savoie, D. L. 1989. Mineral aerosol transport to the Pacific Ocean. 188-218. In: Duce, R. A. *SEAREX: The Sea/Air Exchange Program,* Academic Press, San Diego.

Rea, D. K. 1994. The paleoclimatic record provided by eolian deposition in the deep sea: the geologic history of wind . *Reviews of Geophysics*, 32, 159 - 195.

Rea, D.K., Basov, I.A., Janecek, T.R., Palmer-Julson, A.., 1993. *Proceedings of the Ocean Drilling Program, Initial Reports,* 145, College Station, Texas, Ocean Drilling Program.

Rea, D. K. and Hovan, S. A. 1995. Grain size distributions and depositional processes of the mineral component of abyssal sediments: lessons from the North Pacific. *Paleoceanography*, 10 251-258.

Rea, D. K. and Janecek, T. R. 1982. Late Cenozoic changes in atmospheric circulation deduced from North Pacific eolian sediment. *Marine Geology*, 49, 149-167.

Rex, R. W. and Goldberg, E. D. 1958. Quartz contents of pelagic sediments of the Pacific Ocean. *Tellus*, 10, 153-159.

Robinson, S. G. 1986. The late Pleistocene palaeoclimatic record of North Atlantic deep-sea sediments revealed by mineral magnetic measurements. *Physics of the Earth and Planetary Interiors*, 42, 22-47.

Ruddiman, W.F., Prell, W.L. and Raymo, M.E. 1989. Late Cenozoic uplift in southern Asia and the American west: rationale for general modeling experiments. Journal of Geophysical Research. 94:18397-18391.

Sager, W.W., and Pringle, M.S., 1988. Mid Cretaceous to early Tertiary apparent polar wander path of the North Pacific. *Journal of Geophysical Research,* 93, 11753-11771.

Schneider, B., Tindale, N. W. and Duce, R. A. 1990. Dry deposition of Asian mineral dust over the central North Pacific. *Journal of Geophysical Research*, 95, D7. 9,873-9,878.

Schramm, C.T. 1989. Cenozoic climatic variation recorded by quartz and clay minerals in North Pacific Sediments. In: Leinen, M., and Sarnthein, M. (Eds.), *Paleoclimatology and Paleometeorology: Modern and Past Patterns of Global Atmospheric Transport*, Dordrecht, (NATO ASI Series), 805-839.

Uematsu, M., Duce, R. A. and Prospero, J. M. 1985. Deposition of atmospheric mineral particles in the North Pacific Ocean. *Journal of Atmospheric Chemistry*, 3, 123-138.

Uematsu, M., Duce, R. A., Prospero, J. M., Chen, L. Q. and Merrill, J. T. 1983. Transport of mineral aerosol from Asia to the North Pacific Ocean. *Journal of Geophysical Research*, 88, 5343-5352.

Weber II, E. T., Owen, R. M., Dickens, G. R., Halliday, A. N., Jones, C. E. and Rea, D. K. 1996. Quantitative resolution of eolian continental crustal material and volcanic detritus in North Pacific surface sediment. *Paleoceanography*, 11, 115-127.

Windom, H. L. 1975. Eolian contributions to marine sediments. *Journal of Sedimentary Petrology*, 45, 520-529.